Application of Analytical Electron Microscopy to the Physical and Chemical Characterisation of Ferrihydrites

Gareth Michael Vaughan

Submitted in accordance with the requirements for the degree of Doctor of Philosophy

The University of Leeds
School of Chemical and Process Engineering

September, 2017

The candidate confirms that the work submitted is her own and that appropriate credit has been given where reference has been made to the work of others.

This copy has been supplied on the understanding that it is copyright material and that no quotation from the thesis may be published without proper cknowledgement

"Where the telescope ends, the microscope begins. Which of the two has a grander view?"

VICTOR HUGO, Les Misérables (1862)

Acknowledgements

I would like to acknowledge my supervisors, Professor Rik Brydson and Dr Andy Brown, for their continued support, guidance, insight, motivation and most of all patience. Without their commitment, this work would not have been possible. Secondly, I would like to thank Dr Kasim Sader of SuperSTEM for both his help with the use of the SuperSTEM1 microscope and the many hours of enlightening and stimulating discussions I have shared with him. Dr Ying-Hsi Pan for having provided me with such an excellent foundation from which I could start my work. I would like to acknowledge Professor Fiona Meldrum for her kind assistance with the reconstitution of ferritin mineral core. Special thanks is extended to Dr Bernhard Schaffer for imparting some of his extensive scripting knowledge upon me.

Finally, a little closer to home, I owe a great debt to my loving parents and beautiful sisters for providing me with everything.

Abstract

Ferrihydrite is a poorly crystalline iron (oxy)hydroxide which exists exclusively in a disordered nanocrystalline form. Lacking long range three-dimensional structural order, possessing a high density of defects and displaying variable composition depending on origin has meant that to date a clear consensus regarding a structural model has yet to be reached. A departure from traditional means of crystallographic investigation is therefore required prompting the exploration of hitherto unexplored and potentially novel methods in refining this elusive structure. Recent years have witnessed significant interest in the investigation of ferrihydrites formed in the presence of compounds such as phosphate and citrate. Novel forms of ferrihydrite have been reported, produced by the hydrothermal treatment of these modified ferrihydrites, which have the potential to increase understanding of ferrihydrite in general.

This work demonstrates the application of the latest generation of aberration corrected electron microscopes to the structural and chemical characterisation of ferrihydrite produced both *in vitro* and within the protein cage of ferritin. Two-line ferrihydrite (2LFh), coprecipitated in the presence of varying concentrations of phosphorus (P-doped) and subject to hydrothermal and dry air annealing heat treatments, has also been investigated. By way of a thorough characterisation additional physicochemical characterisation techniques have been applied to confirm the phase purity of specimens and benchmark them against those reported in the literature.

The effects of prolonged exposure to the 200 keV electron beam of the transmission electron microscope (TEM) has been investigated by the simultaneous acquisition of Fe-*L* and O-*K* edge electron energy-loss (EELS), EELS and energy dispersive X-ray (EDX) compositional and selected-area electron diffraction (SAED) data. A safe fluence level of 10^8 electrons nm^{-2} has been established, below which both 2LFh and P-doped 2LFh can be observed in their pristine state. Beyond the safe fluence limit alteration of both pristine 2LFh and the P-doped 2LFh proceeds by preferential loss of oxygen, reduction of iron and concomitant phase transformation to a material with characteristics similar to that of magnetite.

A novel low-electron fluence method of scanning TEM EELS acquisition (SmartAcquisition) has been developed and its applicability to the characterisation

of ferrihydrite nanoparticles proven.

Results here are consistent with independently published data which confirm ferrihydrite to be a predominantly Fe(III) bearing iron-oxide material in which the iron atoms reside in six-fold coordination with oxygens and/or hydroxyls. Fe-*L* EELS edge analysis provides support for a new and controversial model for the structure of ferrihydrite in which a significant fraction of iron is in four fold coordination.

High-angle aberration corrected scanning electron microscopy is used to investigate the morphology of ferritin mineral cores. Atomically resolved sub-unit structure is observed with individual cores comprising several crystalline units which appear to have nucleated independently of one another.

The principle aim of this work it to explore the applicability of the latest generation of analytical electron microscopes for the elucidation of chemical and structural properties of challenging nanoparticulate systems.

Table of Contents

List of Figures

List of Tables

List of Abbreviations

2D	Two-Dimensional
3D	Three-Dimensional
2LFh	Two-Line Ferrihydrite
2LFhPX	Phosphorus doped two-line ferrihydrite (defined in section 4.1.3)
6LFh	Six-Line Ferrihydrite
AC	Aberration Corrected
ADF	Annular Dark Field
ATEM	Analytical Transmission Electron Microscopy
BE	Binding Energy
BF	Bright-Field
CCD	Charge-Coupled Device
CTEM	Conventional TEM
CTF	Contrast Transfer Function
DF	Dark-Field
DSC	Differential Scanning Calorimetry
EDX	Energy Dispersive X-ray
EEL(S)	Electron Energy-Loss (Spectroscopy)
ELNES	Energy-Loss Near Edge Structure
EXFAS	Extended X-ray Fine Absorption Structure
FEG	Field Emission Gun
FMC	Ferritin mineral core
FTIR	Fourier-Transform Infrared Spectroscopy
GEM	General Materials (Diffractometer)
HAADF	High Angle Annular Dark Field
HoSF	Horse-Spleen Ferritin
NCESS	National Centre for Electron Spectroscopy and Surface Analysis
NLLS	Non-Linear Least Squares
PDF	Pair Distribution Function
PTFE	Polytetrafluoroethylene
SA	Spherical Aberration
SAED	Selected Area Electron Diffraction
SEM	Scanning Electron Microscope
STEM	Scanning Transmission Electron Microscope
TEM	Transmission Electron Microscope
TGA	Thermogravimetric Analysis
VSM	Vibrating Sample Magnetometer
WPO	Weak phase object
XAS	X-Ray Absorption Spectroscopy
XPS	X-Ray Photoelectron Spectroscopy
XRD	X-Ray Diffraction

List of Publications

1. Vaughan, G., Brown, A. P., Brydson, R., Sader, K., "A low electron fluence EELS study of Fe-coordination within ferrihydrite and phosphorous doped ferrihydrite nanoparticles*", EMC 2008 14th European Microscopy Congress 1–5 September 2008, Aachen, Germany,* 2008, 1 (I2), pp. 451-452.
2. Vaughan, G., Brown, A. P., Brydson, R., "Analytical transmission electron microscope characterisation of thermally aged two-line ferrihydrite co-precipitated with phosphorous" *Geochimica et Cosmochimica Acta*, 2010, 74 (11), Supplement 1077.
3. Vaughan, G., Brown, A. P., Brydson, R., Sader, K., "Low-electron fluence STEM-EELS analysis of ferrihydrite nano-particles approaching the Ångstrom scale", *Journal of Physics: Conference Series*, 2010, 241 (1), 012051.
4. Sader, K., Schaffer, B., Vaughan, G., Brydson, R., Brown, A., Bleloch, A., "Smart Acquisition EELS", *Ultramicroscopy (Proceedings of the International Workshop on Enhanced Data Generated by Electrons)*, 2010, 110 (8), pp. 998-1003.
5. Seabourne, C. R., Scott, A. J., Vaughan, G., Brydson, R., Wang, S-.G., Ward, R. C. C., Wang, C., Kohn, A., Mendis, B., Petford-Long, A. K., "Analysis of computational EELS modeling results for MgO-based systems", *Ultramicroscopy (Proceedings of the International Workshop on Enhanced Data Generated by Electrons)*, 2010, 110 (8), pp. 1059-1069.
6. Pan, Y-.H., Vaughan, G., Brydson, R., Bleloch, A., Gass, M., Sader, K., Brown, A., "Electron-beam-induced reduction of Fe^{3+} in iron phosphate dihydrate, ferrihydrite, haemosiderin and ferritin as revealed by electron energy-loss spectroscopy", *Ultramicroscopy (Proceedings of the International Workshop on Enhanced Data Generated by Electrons)*, 2010, 110 (8), pp. 1020-1032.
7. Vaughan, G., Brydson, R., Brown, A., "Characterisation of Synthetic Two-line Ferrihydrite by Electron Energy Loss Spectroscopy", *Journal of Physics: Conference Series*, 2012, 371 (1), 012079

The work contained within publications 2 and 7 is attributed to G. M. Vaughan under the guidance of academic supervisors Dr A. P. Brown and Professor R. Brydson. Publication 2 relates to the results discussed in Chapter 6 of this thesis, whereas publication 7 relates to the results discussed in Chapter 4. Publications 1 and 3 are again mainly attributed to G. M. Vaughan, with guidance from A. P. Brown and R. Brydson, however, could not have been published without the aid of K. Sader who also collaborated The work contained in publication 1 relates to both Chapters 4 and 5. Publication 3 relates only to Chapter. Publications 4, 5 and 6 are co-authorship papers, in which G. M. Vaughan was responsible for collaborative assistance with methods development and the acquisition and analysis of electron energy loss spectroscopy. The method developed in publication 4 was used in Chapter 4. The results contained within publication 6 are presented in this thesis

between Chapters 4, 5 and 7.

© 2013 The University of Leeds and Gareth Michael Vaughan

Chapter 1 Introduction

1.1 Electron Microscopy

Microscopy is concerned with visualising objects and structures on length scales smaller than may be perceived by the unassisted human eye: some 0.2 mm or so. Magnified images are produced by focusing radiation that has been scattered following interaction with an object. The means of focusing depends on the illuminating radiation which in turn determines the resolution or precision with which points within an object are mapped to points within an image. For the first 200 years or so, following the advent of the microscope, light of optical frequencies was the only available means of illumination. With optical frequencies features down to several hundred nanometres or so can be visualised. However, it turns out that light is far from the best choice, although this would have mattered little to the early pioneers whose groundbreaking observations truly changed our view of the world. Indeed, it is difficult to look back without the slightest envy on those, who by coincidence of their temporal existence, were the first to put a refracting glass instrument to their eye and observe without prejudice or the slightest notion of what they might find. The revolution in optics which, with Hook's discovery of cells to Galileo's equally unprecedented observation of Jovian moons, must have been quite disconcerting to the unprepared 17th-century mind.

Electron microscopy is a rich and diverse branch of microscopy which provides many unique opportunities for probing the nature of matter on length scales ranging from microns the Ångstrom level. Recent years have witnessed revolutionary breakthroughs in the ability of microscope manufacturers to produce machines of the highest stability, in which the limiting imperfections in the design and construction of their predecessors have been greatly reduced, if not entirely eliminated. Innovations in design combined with the appearance of high-powered computer-controlled optics, providing real-time management and optimisation of the lens system, have led to the elimination of spherical aberration, an inherent characteristic of electromagnetic lenses and hitherto the limiting factor in determining the degree of spatial resolution attainable. It is now becoming routine for aberration-corrected scanning microscopes to be equipped with sub-Ångstrom

probes which possess current densities one hundred times greater than machines of the pre-corrected generation.

1.2 Aims and Objectives

Ferrihydrite is a poorly crystalline iron (oxy)hydroxide which exists exclusively in nanocrystalline form. Found in both geological and biological context it is thermodynamically unstable and is known to be the precursor of a number of more stable iron oxides found in the natural environment. Exhibiting only short range atomic order, it is widely accepted to be composed of hexagonally close packed O and OH anions with ferric iron occupying octahedral interstitial sites. Lacking long range three-dimensional structure, possessing a high density of defects and displaying variable composition depending on origin (H_2O/OH either adsorbed or structural) has meant that to date a clear consensus regarding a structural model has yet to be reached. Indeed, the presence of tetrahedral iron (either at the surface or structural) has yet to be unequivocally ruled out. X-ray powder diffraction, traditionally used in atomic structure determination of crystalline materials, identifies only two to six broad peaks and consequently is of little use in refining a structural model. A departure from traditional means of crystallographic investigation is therefore required prompting the exploration of hitherto unexplored and potentially novel methods in refining this elusive structure. Recent years have witnessed significant interest in the investigation of ferrihydrites formed in the presence of compounds such as phosphate and citrate. Novel forms of ferrihydrite, produced by the hydrothermal treatment of these modified ferrihydrites have been reported, which have the potential to increase understanding of ferrihydrite in general.

In recent years aberration-corrected electron microscopy has become a mainstream technique and is now in widespread use. In the case of aberration-corrected scanning transmission electron microscopy (AC-STEM), this means that probes with extremely high current densities are in use; typically two orders of magnitude greater than previously available with pre-corrected instruments. This not only allows for real-space atomic scale analysis but also makes the likelihood of irradiation-induced specimen alteration ever more real. Consequently, any analysis conducted using such machines must given proper consideration to this if observations are to be free of artifact.

The aim of this work is to apply analytical electron microscopy to the characterisation of iron (oxy) hydroxide nanoparticulate systems with the highest degree of spatial resolution currently available. In particular, ferrihydrite produced both synthetically and by biological means within the ferritin protein are studied. Particular focus is given to the least crystalline form of ferrihydrite, so called two-line ferrihydrite. Complementing observations made within the transmission electron microscope will be measurements made using a variety of analytical techniques commonly used in materials science.

Whilst ferrihydrite has been the subject of several high-quality electron microscopy investigations in the past (Janney, Cowley, & Buseck, 2000a, 2000b, 2001), it was not until the work of Pan (2006) that the consequences of electron irradiation damage were given proper consideration. In particular the effect of 197 keV electrons on six-line ferrihydrite. This work aims to build on that of Pan (2006) by revisiting the question of ferrihydrite's sensitivity to the effects of prolonged exposure to the electron beam, however, the focus herein is on two-line ferrihydrite, the least crystalline form. Methods for obtaining artifact free observations using the analytical AC-STEM with be investigated and where developed where necessary.

The principle aim of this work it to explore the applicability of the latest generation of analytical electron microscopes for the elucidation of chemical and structural properties of challenging nanoparticulate systems.

1.3 Overview of Thesis Chapters

Following this short introductory chapter, the rest of this thesis is laid out in the following order.

Chapter 2 provides a brief overview of iron chemistry with particular reference to ferrihydrite and ferritin. An account of scientific opinion is given outlining both the historical context and the current state of affairs.

Chapter 3 discusses the analytical electron microscope describing in some detail the microscope's construction, the analytical methods it permits and the information which may be obtained using these methods.

Chapter 4 describes the synthetic routes to the samples studied herein and the analytical techniques used from which evidence has been obtained. A brief description of the underlying physics is given, as each technique is put in context within the aims of this work. The first part of this chapter describes in detail the synthesis methods used. The second part is devoted to describing those techniques which have been chosen to complement observations made within the electron-microscope.

Chapters 5 through 8 provide accounts of the experimental results of this study. They are divided in the following manner:

Chapter 5 details the characterisation of ferrihydrite as both two- and six-line types. Analytical data acquired from bulk methods is compared with peer-reviewed data in order to confirm the integrity of the product. Following this, a detailed account of observations made within the electron microscope is given and discussed in the context of those previously outlined.

Chapter 6 follows the same approach as the previous chapter in detailing the characterisation of two-line ferrihydrite synthesised in phosphate bearing solutions. This product is later described as phosphorous-doped two-line ferrihydrite or P-doped ferrihydrite for short. Observations from bulk methods and the electron-microscope are given.

Chapter 7 expands on the work of the previous two chapters by investigating the effects of the thermally induced accelerated ageing of ferrihydrite, in particular, P-doped ferrihydrite. Ageing at elevated temperature in both dry-air (annealing) and within aqueous solutions (hydrothermal) is compared, with the main focus on

the hydrothermally treated samples. In addition to the bulk analytical techniques employed in previous chapters data obtained from magnetic studies, neutron diffraction and pair-distribution data derived from total X-ray scattering experiments are given. These additional observations are presented along with data obtained from un-doped two-line ferrihydrite for comparison. This chapter concludes by presenting observations made within the electron microscope.

Chapter 8 sees a departure from synthetic ferrihydrite, with the focus turning to the iron-hydroxide core of the ferritin molecule (widely believed to be ferrihydrite). The aim here being to study the nature of the inorganic core as a function of core iron content. The iron-loading levels chosen (¼, ½, ¾ and capacity of 4500 iron atoms) were characterised in the electron microscope. Direct imaging of cores is made using aberration-corrected high-angle annular dark field STEM and correlated with core iron content.

Chapter 9 brings together the work of the previous four chapters in providing a discussion and summary of the work described. Here particular attention is given to what has been learnt and achieved. This chapter concludes by providing a speculative outlook and specific suggestions for the continuation of this research.

Following Chapter 9 Appendices are presented which provide supplementary information on particular themes encountered in the main chapters of this document.

Chapter 2 Introduction to Iron Chemistry

2.1 Overview

Iron, element number 26 in the periodic table, is the cornerstone of human technology and also plays pivotal roles in the chemistry of living organisms, being found in the active cores of many bioinorganic molecules. In the data published by Nelson (1991) elements were ranked based on their abundance in the atmosphere, lithosphere, biosphere and hydrosphere. This system also takes into account whether the elements are essential to life, their role in energy production, manufacturing and their importance in pure chemistry. In this publication, iron has an overall ranking of eight, highlighting the relevance of this element, and its compounds, to humankind.

Native iron (iron uncombined with other elements) is present on the surface of the earth in very small quantities with the majority of it being involved in the formation of iron oxides, hydroxides, carbonates and pyrites. Among the most abundant ores of iron compounds is magnetite (Fe_3O_4); hematite (Fe_2O_3); siderite ($FeCO_3$); iron pyrite (FeS_2). Iron oxides have low solubility in water, therefore the main forms of iron in water environments are ferric hydrates such as $[Fe(OH)_2]+$ and $[Fe(OH)_4]-$.

In its metal oxidation state (0), the outer electronic configuration of iron is $3d^64s^2$. Depending on the oxidation state and the number of ligands, the total number of unpaired electrons in the outer orbitals can vary from 0 to 5. This number is at the core of the chemistry of iron and its compounds, its reactivity with other elements and the electronic properties of the resulting molecules. The number of unpaired electrons and their relative orientation and distribution in the d and s orbitals dictates the spin-state of the element, which in turn influences the nature of bonding around the metal centre. The type of chemical bonding iron is involved in, its strength and the nature of elements and ligands which can take part to this bonding are a result of the electronic configuration of iron.

Known oxidation states for iron span from –II (d^{10}) to +VIII (d^0), although several of them are not well established. The common oxidation states of iron are ferrous iron II (d^6) and ferric iron III (d^5). The ferryl state IV (d^4) is now largely recognised in biological systems. Low oxidation states such as I, 0, -I and –II are stabilised by π-acceptor ligands and are therefore presents in iron carbonyls Fe(CO)x such as sodium iron tetracarbonyl $[Na_2Fe(CO)_4]$ (Collman, 1975;

Colquhoun, Holton, Thompson, & Twigg, 1984) and $Fe(CO)_5$ (Beagley, Cruicksank, Pinder, Robiette, & Sheldrick, 1969), iron nitrosyls Fe(NO)y like $[Fe(H_2O)_5NO]^{2+}$ (Griffith, Lewis, & Wilkinson, 1958) and iron phosphines such as $[Fe(PF_3)_5]$ (Taylor, Lehto, Valkiers, Bièvre, Selgrad, Flegel, & Kruk, 1998) and their derivatives. Fe(II) and Fe(III) species are widely involved in the formation of iron oxides and oxyhydroxides and will be discussed in more detail in the following sections.

Fe(IV) species are extremely reactive and therefore of transient nature. Because of this feature, only a few of them have been fully characterised. However, transient Fe(IV)O species are fully established as key intermediates in many biological catalytic cycles, including that of cytochrome P-450 (Shaik, Kumar, Visser, Altun, & Theil, 2005).

The ability of iron to adopt a variety of oxidation states is paramount to its rich chemical reactivity and versatility as co-factor of large arrays of proteins and enzymes (see next section).

2.2 Spin States of Iron

Depending on its oxidation state, iron can adopt a variety of different spin states, each of them referring to a particular configuration of its d electrons. These states can be described and understood based on the principles of the crystal field theory (CFT) (House, 2008).

CFT describes the changes of the energy levels of electron orbital states, in particular, *d* and *f*, of a metal involved in the formation of a complex, upon the effect of an electric field created by an approaching charge (an anion or a neutral ligand). The magnetic properties of transition metal complexes can be explained based on CFT.

Briefly, the base of the CTF model is the change in the energy of the otherwise degenerate *d*-orbitals of a metal upon interaction with a ligand based on the attraction between the positive charge of the metal centre and the negative charge of the non-bonding electrons of the ligand. Given the spatial orientation of the *d* orbitals, when a ligand approaches the metal centre, its electrons will be closer to some of the *d*-orbitals and farther away from others. As the electrons in the ligand will repel the electrons in the *d*-orbitals, the destabilisation of each *d*-orbital will

depend on its orientation and overlap relative to the approaching ligand, thus previously degenerate *d*-orbitals will be split into new energy levels. The *d*-electrons closer to the ligand will experience a greater repulsion from the electron pairs of the approaching nucleophile and will, therefore, populate higher energy levels. The degree of splitting between these new orbital levels is the result of the combination of the nature of the metal ion, its oxidation state, the geometry of the ligands around the ion centre and the nature of the ligand itself.

The difference between the new energy levels of the *d*-orbitals, with t_{2g} being the low energy level and e_g being the high energy level, is known as the crystal field splitting parameter Δ and its determined by the degree of π interaction (interactions above and under the plane comprising the interacting atoms) between the *d*-orbitals of the metal centre and the ligand orbitals.

High splits are caused by π-acceptor ligands such as CO and CN^-. Conversely, π-donor weak ligands like I^- and Br^-, cause a relatively smaller split of the *d*-orbitals. The higher the split, the more difficult it will be for one particular electron to be promoted from a t_{2g} to an e_g orbital. Compounds with large Δ will, therefore, have all of the electrons populating the low energy t_{2g} orbitals, before occupying the higher energy e_g. Low-spin states refer to complexes where the *d*-electrons completely populate the low energy t_{2g} orbitals with anti-parallel spin before occupying the higher energy e_g. High-spin states are on the other hand characterised by singly occupied t_{2g} and e_g orbitals with electrons with parallel spins.

The crystal field splitting parameter Δ is characteristic of the geometry of the complex, with octahedral geometries having a greater Δ value than tetrahedral. Octahedral complexes can vary between low-spin and high-spin, whereas tetrahedral complexes are always high-spin, as the gap between t_{2g} and e_g orbitals is low enough to enable occupation of both levels by electrons with the same spin orientation, before filling one single orbital with two electrons with anti-parallel spin. The number of unpaired electrons will dictate whether the compound displays diamagnetic (no unpaired electrons) or paramagnetic (one or more unpaired electrons) properties. Diamagnetic compounds are repelled by applied external electric fields as they create an induced magnetic field in the opposite direction. Paramagnetic compounds are attracted by an external magnetic field as they form

induced magnetic fields in the direction of the applied magnetic field.

An example of the electronic configuration in a low-spin and high-spin complexes is given below.

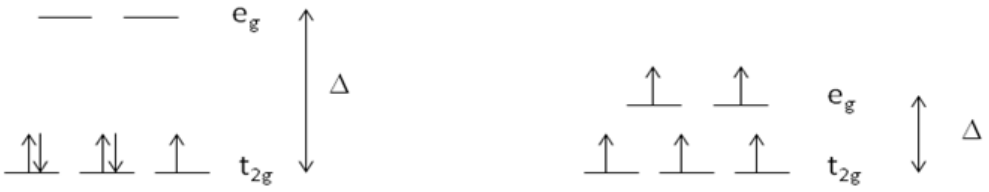

Figure 2.1 Electronic configurations of iron in low-spin (left) and high-spin (right) complexes with 5 *d* electrons.

A variety of electronic spin states can be found for iron in its complexes. Understanding the spin state in which iron is found helps in describing the nature and strength of the bonds that iron can be involved in when bound to oxygen in iron oxides and iron oxyhydroxides, as well as the magnetic properties of these compounds. A table summarising the electronic spin states of the most typical oxidation states of iron is provided below (adapted from Silver, 1993).

Table 2.1 Summary of the electronic spin states and electronic configuration of typical iron oxidation states (adapted from Silver, 1993).

(S)[a]	Spin state	Oxidation state	Electronic configuration
0	low	II	t_{2g}^6
1/2	low	III	t_{2g}^5
1	low	IV	t_{2g}^4
2	high	II	$t_{2g}^4 e_g^2$
	High	IV	$t_{2g}^3 e_g^1$
5/2	high	III	$t_{2g}^3 e_g^2$

[a] S here indicates the spin quantum number, given by the total number of unpaired electrons.

2.3 Iron Oxides and Hydroxides

Iron oxides (Fe_xO_y) and iron oxyhydroxides [$Fe_xO_y(OH)_z$] are ubiquitously present in nature as solid (for instance, rock), liquid (for instance, mineral inclusion in bacteria) and gaseous compounds (for instance, aerosols). Given their widespread presence and their rich chemistry and physics, they find applications in a vast variety of fields including steel production, earth and planetary science, physics, magnetism, medicine, biology, material science and engineering. 16 iron oxides, hydroxides and oxyhydroxides have been described so far. In all these compounds, iron (either ferrous (II), ferric (III) or a combination of both) is bound to oxygen (O^{2-}) and/or hydroxyl (OH^-) groups. They differ in their composition, iron valence and crystal

structure. The degree of crystalline order (crystallinity) is also seen to vary between different iron oxides with some displaying a high degree of (long range) atomic order (hematite, goethite, lepidocrocite, magnetite, maghemite) whilst others are poorly crystalline lacking extended structural periodicity (ferrihydrite, feroxyhite, green rust, schwertmannite). In general most iron oxides are structurally related, something which permits the thermodynamic transformation between similar types. The basic structural units are an octahedron (Fe coordinated to six O^{2-}/OH^{-} ions) and to a lesser extent a tetrahedron (Fe coordinated to four O^{2-}/OH^{-} ions). Mixed octahedral/tetrahedral may occur as in the case of the solid state solution magnetite-maghemite. The structural differences between iron oxides is manifest in the way in which these polyhedral structural units are interconnected, either by face, edge or corner sharing (Faivre, 2016).

The composition and structure of iron oxides are still the subject of a lively scientific discussion. As structural characterisation techniques advance, more details as to the atomic composition, the bonding nature and the crystal structure of these compounds are revealed and questioned. Ferrihydrite, on which this thesis is focused, raised a recent dispute in the field of inorganic chemistry. As this compound only exists in nanometer-scaled materials, its characterisation has proved challenging to traditional long-range characterisation techniques such as X-ray diffraction. A structure described as 20% tetrahedral and 80% octahedral-coordinated iron with a $P6_3mc$ space group was recently suggested based on the analysis of total X-ray scattering pair distribution function (PDF) data (Michel, Ehm, Antao, Lee, Chupas, Liu, Strongin, Schoonen, Phillips, & Parise, 2007; Michel, Barrón, Torrent, Morales, Serna, Boily & Liu, 2010). This study proposed a novel single phase interpretation of the structure of ferrihydrites. There is, however, some objection to this new model (Manceau, 2011) as discussed in (Manceau, 2012; Barrón, Torrent & Michel 2012). It has been suggested that using PDF refinement for the identification of a parent crystal structure of defective nanocrystalline materials could do what XRD did for crystalline materials (Egami & Billinge, 2003).

2.4 Ferrihydrite and its Binding with Inorganic Phosphate

Ferrihydrite, $5Fe_2O_3 \cdot 9H_2O$, is a nanoparticulate hydrated iron(III) oxide (Towe & Bradley, 1967). As opposed to other iron oxides, this compound is metastable and its structure has been described to be of low order (Cornell & Schwertmann 1996; Carta, Casula, Corrias, Falqui, Navarra, & Pinna, 2009). Ferrihydrite is ubiquitous in the near-surface environment, finds a large number of industrial applications and also constitutes the core of ferritin (Cornell & Schwertmann 2003). The absorptive capacity of this material is notably high. Along with its ability to precipitate ions from aqueous solutions, this provides ferrihydrite with the ability to sequester contaminants such as arsenate and uranium from both natural (Violante, Ricciardella, del Gaudio & Pigna, 2007; Kinniburgh, Jackson & Syers, 1976) and industrial environments (Xu, Zeng, Huang, Feng, Hu, Zhao, Lai, Wei, Huang, Xie & Liu 2012).

As previously alluded to, the structure of ferrihydrite is still the subject of intense scientific debate. Although a certain degree of disorder is generally attributed to this material, the lack of any evident crystalline order might be the consequence of the limited crystallite size which eludes any long-range order to be assessed by conventional structural techniques. A hexagonal unit cell has been reported for the ferrihydrite that aggregates in the human brain (Quintana & Gutierrez, 2010).

With regards to its formation, ferrihydrite has been described as the first product of induced ferric hydrolysis. Numerous studies have described a model for the formation and precipitation of ferrihydrite from aqueous solutions (Spiro, Allerton, Renner, Terzis, Bils, & Saltman, 1966; Knight & Sylva, 1974; Flynn 1984; Schwertmann, Friedl, & Stanjek, 1999; Rose, Blight, Collins, & Waite, 2014; Jolivet, Chanéac, & Tronc, 2004).

The classic model describes solvated Fe(III) ions which undergo hydrolysis to generate low molecular weight Fe(III) hydrated species as dimers and trimers. These species then undergo olation and oxolation (the two terms being somewhat interchangeable), in which one of the water molecules in the coordination sphere or Fe(III) ionises to hydroxide:

$$[Fe^{III}(H_2O)_6]^{3+} \rightleftharpoons [Fe^{III}(H_2O)_5OH]^{2+} + H^+$$

During olation, the displacement of one water molecule by a surrounding complex

occurs, leading to a species in which the hydroxide is bridged between the two metal centres, in the so-called μ-configuration.

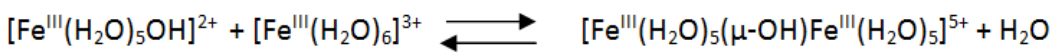

In the μ-species, the water molecules in the coordination sphere of Fe(III) can still undergo ionisation and displacement by surrounding complexes, thus leading to an extensive condensation process and ultimately to the formation of $5Fe_2O_3 \cdot 9H_2O$ nanoparticles from solution.

The details of the hydrolysis mechanism are still under debate. Due to the high reactivity of Fe(III) towards hydrolysis, the reactions involved in the formation of ferrihydrite can occur at a high rate, thus making the isolation and characterisation of the intermediates challenging. Recently, the μ-oxo Fe(III) species has been reported as the main component in partially hydrolysed ferric solutions (Zhu, Puls, Frandsen, Kubicki, Zhang, & Waychunas, 2013). Detection of Fe(III) trimers (Lopes, de Laat, & Legube, 2002; Vilgé-Ritter, Rose, Maison, Bottero, & Lainé, 1999) tetramers (Melikhov, Kozlovskaya, Berliner, & Prokofiev, 1987) and larger aggregation states have also been reported. The exact composition of the larger polymers is yet to be univocally defined. Some studies also have considered these larger polymers to be already ferrihydrite phase.

Based on the similarity between aqueous Al(III) and Fe(III), the involvement of the so-called Al_{13} Keggin cations in the formation of ferrihydrite has been suggested. These species are composed of central tetrahedral metal units surrounded by octahedral metal units (Casey 2006; Bradley, & Kydd, 1993). Fe_{13} Keggin clusters have recently been synthesised (Sadeghi, Zakharov, & Nymann, 2015), posing the question as to whether Fe_{13} clusters might actually be the precursor to ferrihydrite formation (Gebauer, Kellermeier, Gale, Bergström & Cölfen, 2014).

After the nucleation and growth of individual ferrihydrite nanoparticles, aggregation may occur (Yuwono, Burrows, Soltis, Do, & Penn, 2012). Aggregates of ferrihydrite nanoparticles can adopt low mass fractal dimensions, thus enabling the formation of larger low-density structures that exist as stable colloidal suspensions on micrometer scale (Legg, Mengqiang, Comolli, Gilbert, & Banfield, 2014A; Legg, Mengqiang, Comolli, Gilbert, & Banfield, 2014B). These structures can then collapse to form denser aggregates upon a change in solution conditions, such as increased ionic strength. The final structure of the resulting ferrihydrite

aggregates dictates their stability, reactivity, transport behavior (Legg et al., 2014A; Legg et al., 2014B; Gilbert et al., 2007) and usage as a sequester in the treatment of wastewater (Loan, Parkinson, Newman, & Farrow, 2002).

As mentioned before, ferrihydrite plays a crucial role in the binding and sequestering of contaminants and nutrients, including the ubiquitous phosphate. Phosphate's environmental relevance stems from its involvement as a nutrient for plants and crops. The absorption of phosphate onto ferrihydrite could be used as a model to study and predict the behaviour of toxic species such as arsenate $H_2AsO_4^-$. Additionally, phosphate plays a crucial role in the biochemistry of iron mineralisation in the ferritin protein family (see next section).

Although the reactions of phosphate towards iron hydroxides have been detailed, the entire process is yet to be fully understood, as is the configuration adopted by phosphate on the surface of the mineral (Khare, Martin, & Hesterberg, 2007; Antelo, Fiol, Pérez, Mariño, Arce, Gondar, & López, 2010; Lindegren & Persson, 2010).

Phosphates are known to form innersphere complexes with iron hydroxides, as evidenced by numerous experimental techniques (Khare, Hesterburg, Beauchemin, & Wang, 2004; Tejedor-Tejedor & Anderson, 1990). However, the interpretation of surface complex structures spectroscopic data is not straightforward, and questions such as whether monodentate or bidentate complexes between phosphate and ferrihydrite are formed are still under debate.

In a theoretical study by Kwon and Kubicki (2004), six possible surface complexes were modeled by quantum mechanical calculations: deprotonated, monoprotonated, and diprotonated versions of bridging bidentate and monodentate complexes (see Figure 2.2). The results suggested that the surface complexes change depending on pH. Four possible species were suggested, including a diprotonated bidentate complex at pH 4-6, a deprotonated bidentate or a monoprotonated monodentate complex at pH 7.5-7.9, and a deprotonated monodentate complex at pH 12.8. Reaction energies were also calculated for adsorption from aqueous solution to determine the relative stability of a monoprotonated monodentate complex and a deprotonated bidentate complex. According to these results, the monoprotonated monodentate complex should be favoured (Kwon & Kubicki, 2004).

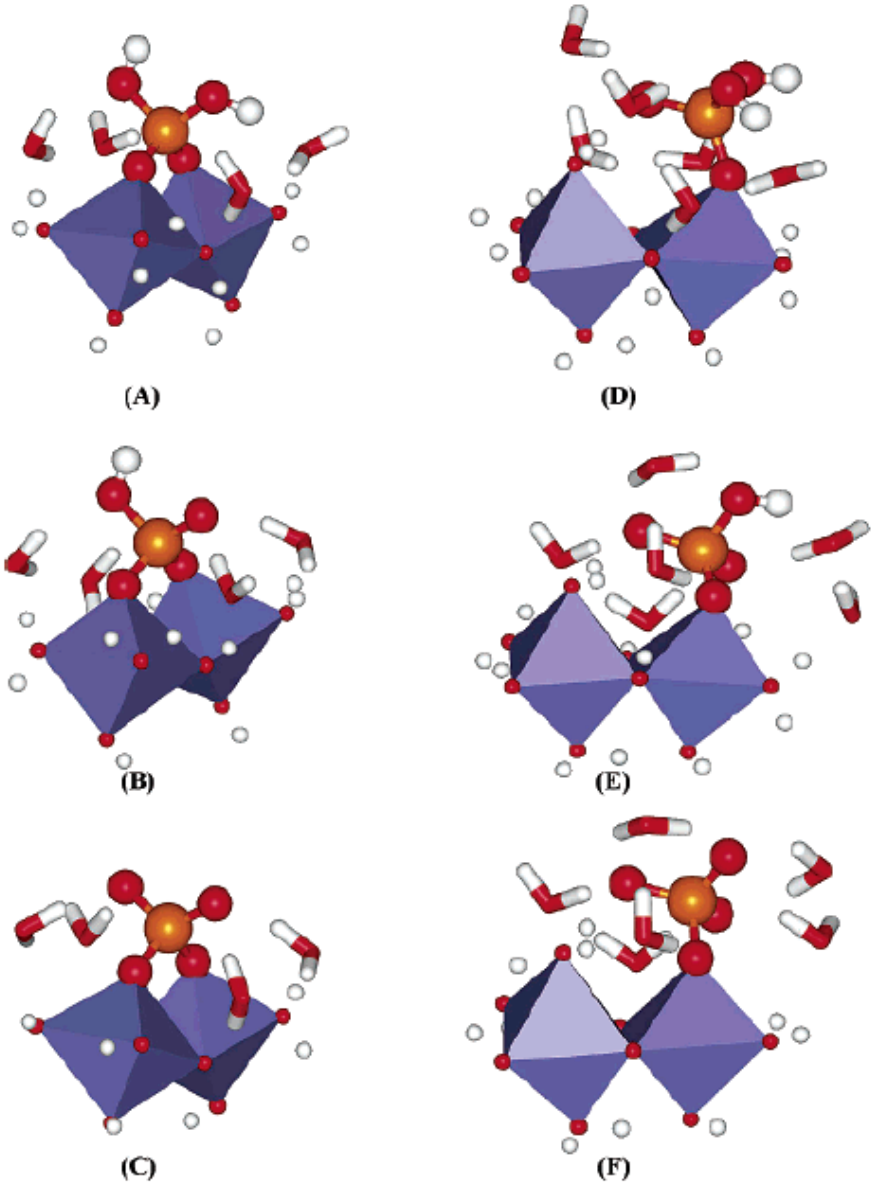

Figure 1. Possible bidentate ($2C2^E$) and monodentate ($1C2^E$) surface complexes of phosphates/iron hydroxides: (A) diprotonated bidentate (BD-H_2); (B) monoprotonated bidentate (BD-H_1); (C) deprotonated bidentate (BD-H_0); (D) diprotonated monodentate (MD-H_2); (E) monoprotonated monodentate (MD-H_1); (F) deprotonated monodentate (MD-H_0). H_2O molecules are H-bonding to the phosphate−iron clusters. Red, oxygen; white, hydrogen; orange, phosphorus; blue, iron octahedra.

Figure 2.2 Possible surface complexes between phosphate and ferrihydrite showing bidentate and monodentate configurations. Reproduced from Kwon & Kubicki, (2004).

A recent X-ray diffraction and transmission electron microscopy study indicated that both the adsorption capacity and relative adsorption reactivity toward phosphate significantly decrease with increasing crystallite size. The absorption kinetics could be divided into three successive first-order stages: relatively fast adsorption, slow adsorption, and a very slow stage. With decreasing crystallite size,

ferrihydrite absorption of inorganic phosphate exhibited increasing rate constants per mass in all of the stages. Additionally, the smaller ferrihydrite crystals have higher rate constants, and more phosphate is adsorbed and more OH^- is released over time per mass basis. The initial step in the overall process was shown to be that of a phosphate binding to two Fe-OH groups to form a binuclear bidentate surface complex on ferrihydrites with a ~3.25 Å Fe−P coordination distance (Wang, Harrington, Liu, Parise, Feng, & Sparks, 2013).

2.5 Bioinorganic Relevance of Ferrihydrite: Structure and Function of Ferritin

As mentioned in the introduction to this chapter, iron plays a vital role in a variety of biological processes, including respiration, photosynthesis, nitrogen fixation and DNA synthesis (Andrews, Robinson, Rodriguez-Quinones, 2003). High intracellular levels of iron, however, can result in high toxicity because of its competition with other essential metal ions and its ability to induce oxidative damage. The latter is usually the result of the naturally occurring Fenton redox reaction, in which ferrous iron(II) reacts with hydrogen peroxide H_2O_2 to produce highly reactive hydroxyl radicals $^{\bullet}OH$. These reactive oxygen species, generally known as ROS, are able to react with any nucleophile presents in biological molecules, including protein, lipids and DNA, eventually resulting in the possible onset of cellular malfunction and DNA damage.

Cellular systems have evolved to be able to control the eventuality of this toxic reaction by developing the ability to control cellular iron homeostasis by sequestering excess iron into the insoluble form of ferrihydrite within proteins known as ferritin.

Ferritin can be described as a protein nanocage with a specific size and shape which is optimal for iron binding and for hosting a core in which the excess ferrous iron(II) can be oxidised to ferric iron(III) and then converted into ferrihydrite. Each ferritin is composed of 24 homomers or structurally related heteromers with an octahedral symmetry. This results in a macromolecular assembly with a diameter of ~12 nm and a mineral core of ~8 nm (Bou-Abdallah 2010; Chasteen & Harrison, 1999; Mann, Bannister, & Williams, 1986; May & Williams, 1980). Ferritin is ubiquitous, being found in all higher animals, bacteria, fungi and plants (Harrison

& Arosio, 1996; Massover, 1993)

Ferrous iron(II) enters the ferritin core through conserved pores located on the protein shell. Once transported into the core, ferritins are able to promote the oxidation of Fe(II) to Fe(III) using molecular oxygen or hydrogen peroxide as the oxidant, in a reaction catalysed by a ferroxidase centre. The resulting Fe(III) is then used to biomineralise a core of crystalline ferrihydrite in the absence of phosphate. If phosphate is present in the surrounding crystallisation core, an amorphous mineral is obtained. The inner surface shell of ferritins is a conserved structural region which allows for the accommodation of up to ~3500 iron atoms within the ferritin cavity (Chasteen & Harrison, 1999).

A ferritin monomer (see Figure 2.3) usually comprises a sequence of ~180 amino acids folded into five helices (A – E). The N-termini is located on the outside of the ferritin shell whereas the C-term is within the ferritin core. Helices A to D are roughly ~4.2 nm in length and assembled together into a bundle with parallel and antiparallel helices. Helices B and C are connected via a loop that acts as one of the interacting surfaces between two monomers. Helix E is oriented at 90 degrees to the bundle and is one of the main interaction points between four monomers within the protein shell. In helix D a break into the network of hydrogen bonds is present around residue 136, allowing the loop between helices B and C to point outwards from the protein surface, taking part in the formation of the threefold axis pore.

The overall structure of human ferritin, depicting the five helices and the B-C loop is given in Figure 2.3.

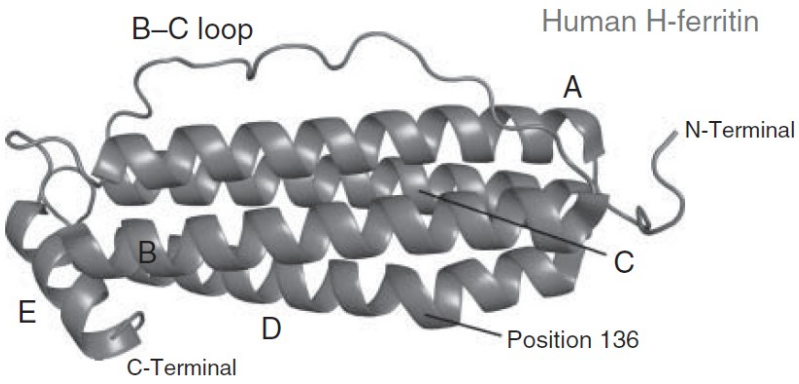

Figure 2.3 Ribbon diagram illustrating the protein backbone structure of monomeric human H-ferritin showing helices A-D in a sequential way from N- to C-terminals. Position 136 indicated the residue at which a break in the hydrogen bonds allows the C-D loop to kink outwards in forming the threefold axis pore. Reproduced from Faivre (2016).

Each subunit can be described as an elongated cylinder with a length of ~5.2 nm and a width of ~3 nm. Hydrophobic interactions characterise the ends of the cylinder, whilst the centre is predominantly maintained by hydrophilic interactions.

In mammalian systems, two distinct polymers are observed, of roughly 21 and 19kDa molecular weight. These two polymers are usually referred to as heavy (H) and light (L) chain, respectively. The heavy subunit hosts the ferroxidase centre, while the light subunit contains the nucleation surface where crystal formation is induced and displays electron transfer capacity. Depending on the ratio between H- and L-chain, the predominant function of the resulting ferritin can either be oxidation activity or iron storage (Clegg, Fitton, Harrison, & Treffry, 1980; Grady, Zang, Laue, Arosio, & Chasteen, 2002; Levi, Santambrogio, Cozzi, Rovida, Corsi, Tamborini, & Spada, 1994).

The H-chain in mammalian ferritin contains the redox ferroxidase centre in the helix bundle. The centre is able to bind two ferrous Fe(II) cations and oxidise them to ferric Fe(III) cations with concomitant reduction of molecular oxygen. Once oxidised, ferric cations migrate from the bundle to the inner core of ferritin where biomineralisation occurs, leading to formation and growth of ferrihydrite nuclei (Bou-Abdallah 2010).

Two iron sites are present in the ferroxidase, namely FeA and FeB, bound to the rest of the protein via coordination bonds with histidine and glutamic acid residues. FeA is also bound to a water molecule which is in turn coordinated to a glutamine and a glutamic acid residue. Another site, FeC, is present but unlikely to be essential for the redox properties of ferritin. This site might play a role in iron movement within the inner core of the protein.

The inner surface of ferritins host the nucleation site, a binding site that coordinates iron ions (Wade, Levi, Arosio, Treffry, Harrison, & Mann, 1991). The protein backbone surrounding the nucleation site is folded in such a way that leaves space for additional coordination spheres around the iron, thus allowing the growth of the mineral and formation of one or more polynuclear ferrihydrite crystallites.

Multiple nucleants can form on numerous nucleation sites, thus ferritins can nucleate and hold polynuclear iron clusters of up to 4500 iron atoms (Treffry, Zhao, Quail, Guest, & Harrison, 1998; Towe & Bradley, 1967), however, isolated proteins usually contain ~1000 to 3000 iron atoms. At high iron loading, slow mineralisation

kinetics are observed, thus resulting in oxidation of ferrous Fe(II) outside the protein ferroxidase site to be in kinetic competition with the intraprotein oxidation.

L-ferritin, which lacks the active ferroxidase centre, is still able to promote biomineralisation to ferrihydrite, suggesting that core mineralisation can occur by direct deposition of iron on the surface of the mineral. A core of at least ~200 ferrous Fe(II) cations seems to be required for the surface mineralisation reaction (Zhao, Bou-Abdallah, Arosio, Levi, Janus-Chandler, & Chasteen, 2003).

The oxidation of Fe(II) to Fe(III) and the subsequent formation of ferrihydrite crystallites are the result of three main chemical reactions, usually referred to as ferroxidation reaction (a), mineralisation reaction (b) and detoxification reactions (c).

$$\text{(a)}\quad 2Fe^{II} + O_2 + 4\,H_2O \longrightarrow 2FeOOH + H_2O_2 + 4H^+$$
$$\text{(b)}\quad 4Fe^{II} + O_2 + 6\,H_2O \longrightarrow 4FeOOH + 8H^+$$
$$\text{(c)}\quad 2Fe^{II} + H_2O_2 + 2\,H_2O \longrightarrow 2FeOOH + 4H^+$$

Depending on the iron intake into the ferritins, Fe(II) is either processed via ferroxidation or a mixture of ferroxidation, mineralisation and detoxification for low and high iron uptakes, respectively. Fe(II)/protein ratios higher than ~800 promotes mostly the mineralisation reaction, whereas the detoxification reaction is predominant for Fe(II)/protein ratios of ~100 to 500.

Iron mineralisation within ferritins is also largely influenced by the presence of phosphate, an abundant anion in living systems. Phosphate can be incorporated and released by ferritins (Trefry & Harrison, 1978) and can form a layer on the mineral core surface. Addition of phosphate/Fe(II) mixture under anaerobic conditions leads to the formation of a layer consisting of one iron atom per three phosphates (Heqing, Watt, Frankel, & Watt, 1993). Additional Fe(II) entering the inner core of ferritins can bind the phosphate layer and then undergo oxidation to Fe(III), which then migrates to the iron core under the phosphate layer, leading to more Fe(II) binding and oxidation (Johnson, Cannon, Watt, Frankel, & Watt, 1999).

Addition of phosphates to ferritins has been shown to accelerate the oxidation of Fe(II) to Fe(III) and the uptake of Fe(II), along with aiding the migration of oxidised Fe(III) from the redox centre of ferroxidase to the ferritin core, where nucleation occurs (Watt, Hilton, & Graff, 2010).

Ferritin has a long history of analysis by electron microscopy (Farrant, 1954; Haydon, 1969; Isaacson & Ohtsuki, 1980). A long-standing question has existed as to the nature and role the apparent low central density of cores as seen in electron micrographs (for example see Figure 2.4). Recently the group here at Leeds demonstrated that ferritin mineral cores within human liver tissue possess distinct subunit morphology. It was postulated by Pan et al., (2009) that the sub-unit structure results from the eight channels in the protein shell that are known to facilitate the transport of iron ions into the protein cavity (Pan, Sader, Powell, Bleloch, Gass, Trinik, Warley, Li, Brydson, & Brown, 2009; Chasteen & Harrison, 1999). Figure 2.4 shows a bright-field transmission electron microscope image in which ferritin molecules appear to exhibit subunit structure and apparent low density cores.

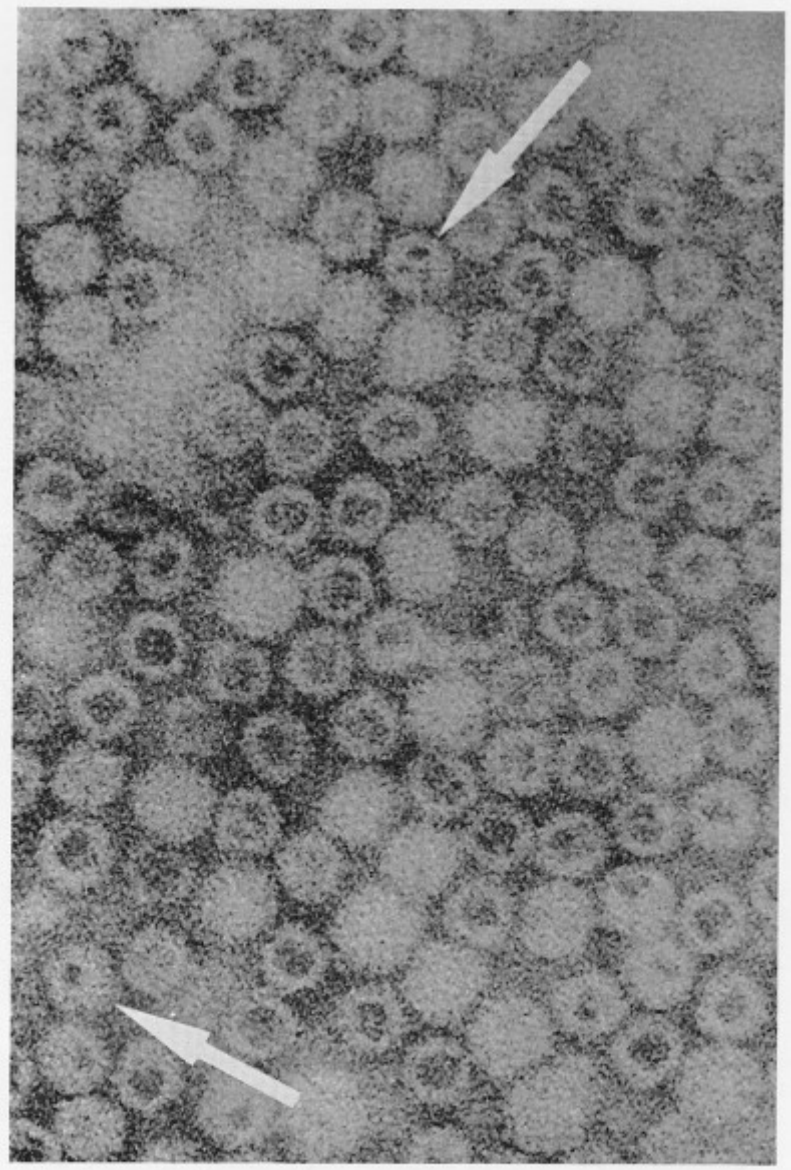

Fig. 1. Apoferritin and ferritin molecules of variable iron content negatively stained with sodium phosphotungstate at pH 7. This electron micrograph shows substructures (arrowed) in the iron cores which are independent of phase-image granularity. Twice-recrystallized horse spleen ferritin supplied by Mann Research Laboratories, New York. Philips EM-200; 80 kV. × 800,000.

Figure 2.4 BF-TEM micrograph of negatively stained horse spleen apoferritin and ferritin molecules of variable iron content illustrating iron core subunit structure. Reproduced from Towe (1969).

Chapter 3 Analytical Transmission Electron Microscopy

Transmission Electron Microscopy is a rich and diverse branch of microscopy which provides many unique opportunities for probing the nature of matter on length scales ranging from microns to nanometers and in more recent years beyond this to the Ångstrom level. Various imaging modes combined with a range of *in situ* analytical techniques provide information pertaining to atomic structure, chemistry, electrical and magnetic properties of materials.

Recent years have witnessed revolutionary breakthroughs in the abilities of microscope manufacturers to produce machines of the highest stability. In refining their art they have greatly reduced, if not entirely eliminated, the limiting imperfections inherent in the design and construction of their predecessors. The arrival of computer controlled optics, providing real-time management and optimisation of the lens system, has led to the elimination of spherical aberration: an inherent characteristic of all lenses and hitherto the limiting factor determining the degree of spatial resolution attainable. Electron microscopy sits firmly in the arsenal of characterisation techniques at the cutting edge of materials science. Providing both a unique window on the atomic world and complementing the information derived by other techniques, electron microscopy has been pivotal in bringing about the nanotechnology revolution.

Numerous texts exist on the subject many of which offer unique perspectives. In no particular order here are a few which cover most of the bases (Amelinckx, Dyck, Landuyt, & Tendeloo, 1997; Egerton, 2011; Egerton, 2005; Fultz & Howe, 2012; Spence, 2002; Williams & Carter, 2009; Brydson 2001).

3.1 The Basics

In the transmission electron microscope an ultra thin specimen (<100 nm), is examined by means of a high-energy beam of electrons. The majority of these illuminating electrons will pass directly through the sample unaffected, however, a small proportion will interact with the atoms which make up the specimen.

Two distinct types of transmission electron microscope may be defined: the conventional transmission (TEM) and the scanning transmission microscope (STEM). In the first instance, a broad beam illuminates the sample and a post sample objective lens is used collect the transmitted electrons to form images and diffraction

patterns. On the other hand in the STEM, the objective lens sits prior to the specimen and is used to form a highly focused probe at the specimen's surface. This probe is scanned across the surface in a raster fashion and information is collected serially point-by-point. Of the two, the STEM tends to be the most versatile for analytical proposes since its focused probe allows signals to be localised with a higher degree of spatial resolution. Accordingly, STEMs are almost always equipped with a spectrometer (EDX or EELS) whereas for TEM this is not always the case.

More will be said about the particulars of TEM and STEM later, but for now the components they share in common will be discussed.

3.2 The Electron as an Illumination Source

The electron, a fundamental particle of mass, $m_0 = 9.109 \times 10^{-31}\ kg$, possessing electronic charge, $e = 1.602176 \times 10^{-19}\ C$, the electron is a constituent part of the atom and provided sufficient energy it may travel freely. Originally thought to be of ethereal origins, in 1897 J. J. Thomson dispelled this by verifying its particle nature by proving it possesses charge (Thomson, 1897). However, a quarter of a century later in 1924, Louis de Broglie proposed that all matter is inherently undulatory depending on its energy and how it's observed (de Broglie, 1924). According to de Broglie, all particles have an associated wavelength related to their momentum by $\lambda = h/mv$, where m and v are the relativistic mass and velocity respectively, and h is Plank's constant. Just three years later Davisson and Germer provided evidence for electron diffraction thus providing experimental backing for de Broglie's apparently contradictory hypothesis (Davisson & Germer, 1928). In 1927, Hans Busch showed that a magnetic coil can focus an electron beam which led to Ruska and Knoll constructing the first transmission electron microscope with which they obtained the first images with 17x magnification in 1931 (Hawkes, 1990). Only two years later they had surpassed the resolution of light microscopes.

With the energies of electrons in the TEM being of the order of several hundred thousand electron volts, relativistic effects cannot be ignored. Correcting for relativistic effects the de Broglie wavelength is given by

$$\lambda = \frac{h}{(2m_0eV(1 + \frac{eV}{2m_0c^2}))^{1/2}}$$

where *h*, *m* and *e* are described above, *V* is the accelerating potential and *c* is the speed of light in the vacuum. This relationship is tabulated for selected energies typical of electron beams used in the TEM (Table 3.1).

Table 3.1 Selected energies typical of electron beams in TEM along with corresponding electron wavelengths (uncorrected and corrected for relativistic effects), and relativistic values of mass and velocity. Reproduced from Williams & Carter (2009).

Accelerating voltage (kV)	Nonrelativistic wavelength (nm)	Relativistic wavelength (nm)	Mass ($x\, m_0$)	Velocity ($x\, 10^8$ m/s)
100	0.00386	0.00370	1.196	1.644
120	0.00352	0.00335	1.235	1.759
200	0.00273	0.00251	1.391	2.086
300	0.00223	0.00197	1.587	2.33
400	0.00193	0.00164	1.783	2.484
1000	0.00122	0.00087	2.957	2.823

Being wavelike the electron exhibits all the characteristics of classical waves such as refraction, interference and diffraction as illustrated below in Figure 3.1.

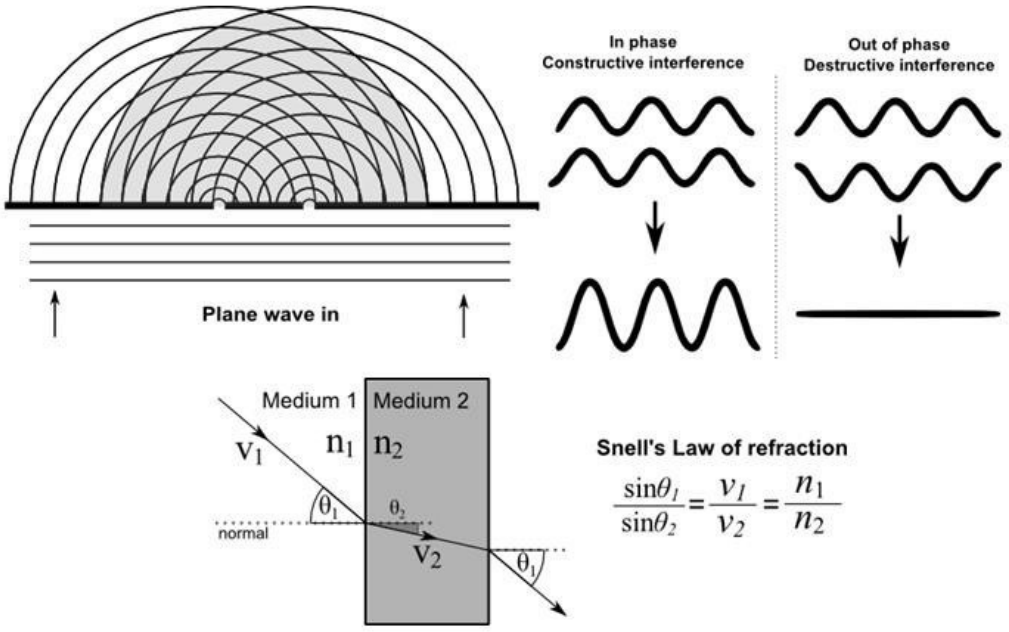

Figure 3.1 Illustration of some characteristics of classical waves: diffraction from an aperture and subsequent interference; the phase relation between two waves and the resultant wave from their superposition; refraction at a boundary between two media with dissimilar refractive indices and Snell's law of refraction.

3.3 Microscope Construction

As already alluded to there are two different types of transmission electron microscope: the conventional (TEM) and the scanning type (STEM). Regardless of the type, the fundamentals are the same. Electrons, produced in a source or *gun*, are

accelerated towards a specimen held in a high vacuum. Their trajectory is manipulated by a series of lenses and apertures. Electrons pass through the specimen and their interaction is detected in one of several ways.

3.4 The Electron Source (Gun)

The electron gun sits at one extreme of the optical system and provides the electrons for imaging and analysis. Electron emission from the cathode ('*tip*') is achieved by either *thermionic* emission, *field-emission* or a combination of the two as is the case for *Schottky* sources. Thermionic sources were traditionally made of tungsten wire, however, these have been superseded by lanthanum hexaboride, LaB_6, in modern TEMs. Figure 3.2 compares the emission characteristics of these sources.

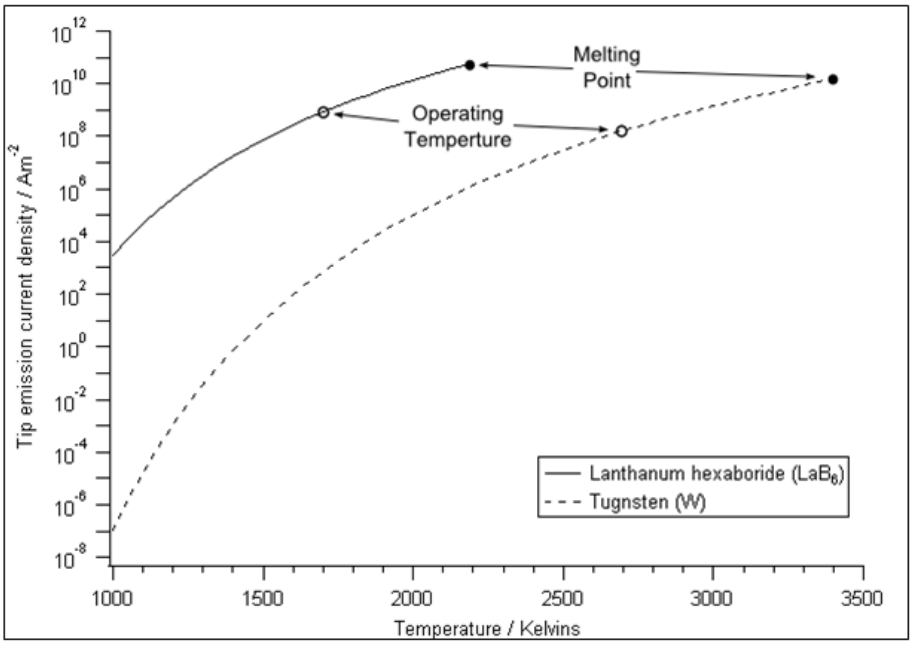

Figure 3.2 Emission current densities (Am^{-2}) for thermionic emitters comparing tungsten and lanthanum hexaboride as a function of operating temperature.

Field emission, or FEG, sources rely on the enhancement of the electric field (>10^7 V/cm) about the sharp point of a tungsten rod, which is held at a potential V of several kV with respect to the first (extracting) anode. This bias applied to this lens is thusly termed the *extraction voltage*. The point radius (r) is typically < 100 nm and in the idealised case of a spherical point the electric field scales as $E = V/r$. The tip must be kept ultra clean which requires ultra-high vacuum (UHV) conditions (< 10^{-7} Pa). Operated at ambient temperatures, FEG sources are said to be "cold" FEGs, however, they do require temporarily heating (*flashing*) from time to time to drive

off debris attracted by the strong field in the vicinity of the tip which would otherwise impair emission. The problem of contamination build-up, as well as the requirement for UHV conditions, may be avoided if the tip is heated during operation as is the case for *thermally assisted* FEGs. Semiconductor surface coatings (e.g. ZrO_2) may be applied to the tip in order to lower the work function thus enhancing emission. The reduction $\Delta\Phi$ is equal to the Schottky barrier between the metal-semiconductor from which such sources derived their name.

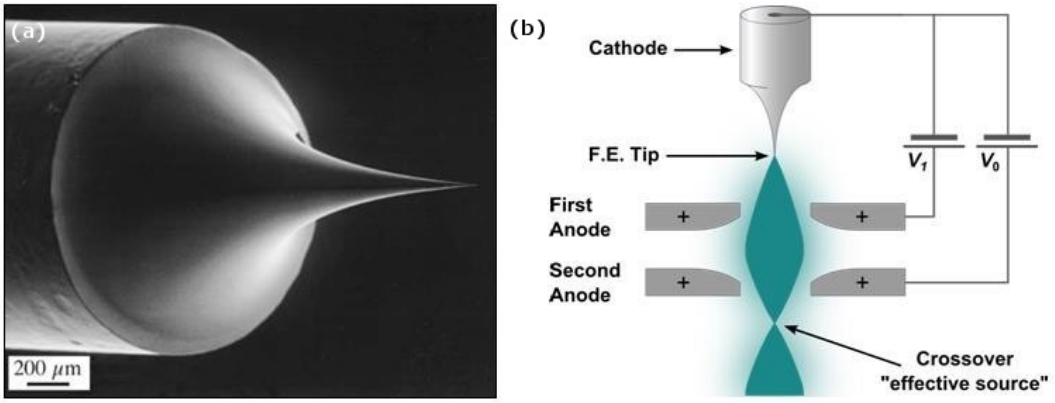

Figure 3.3 Scanning electron microscope image of a FEG tip, illustrating it's extreme sharpness and a schematic of a field-emission source showing the relative positions of the tip, anodes and first beam crossover point. Reproduced from Williams & Carter, (2009).

Electrons drawn from the tip by the first anode pass through it's centre towards the second anode with 100 kV or so accelerating voltage to define the electron beam. The overlap of the field from the two anodes has a lensing effect on the beam which produces a crossover point beyond the second anode (see Figure 3.3b). The diameter of this crossover is the effective source size the rest of the microscope 'sees' and is important for the subsequent formation of the beam. A large (or bright) effective source size facilitates forming a parallel beam of electrons since the demagnification of the source, occurring in the optical elements directly preceding the source, will serve to condense and blur variations across the source's surface as seen at the specimen. Larger source sizes necessarily have a larger spread in the distribution of electron energies and a greater degree of incoherency. This causes problems when focusing due to chromatic aberration in the lenses and makes the beam less viable for use in energy-loss spectroscopy.

Some of the defining characteristics of electron sources (see Table 3.2) are as follows. The *brightness* of the source, measured in A/m^2sr, is the ultimate limiting factor in determining the maximum achievable beam flux. The gun's *emission*

current stability can vary from fractions of seconds to days. A stable source (on short time scales) is especially desirable in scanning techniques where the incident flux will necessarily determine the intensity of the signal being measured. The *coherency* of the source is a factor determining the diffraction limited spatial resolution and is especially important in situations where interference between electrons provides analytical information such as in *phase contrast* imaging.

The field emission gun (FEG) offers an improvement in brightness over thermionic emitters (cold-FEG 10^{13} A/m^{2}sr and Schottky ~10^{12}A/m^{2}sr) and also offers an order of magnitude reduction in energy spread (CFEG 0.3 eV and Schottky 0.7 eV). The cold-FEG operates with a stability of ~5% whereas the Schottky is capable of greater than 1% stability.

Table 3.2 Comparison of the principle characteristics of electron sources used in electron microscopy. Reproduced from Williams & Carter (2009).

	Units	Tungsten	LaB_6	Schottky FEG	Cold FEG
Work function, Φ	eV	4.5	2.4	3	4.5
Richardson's constant	A/m^{2}K^2	6 x 10^9	4 x 10^9		
Operating temperature	K	2700	1700	1700	300
Current density (at 100 kV)	A/m^2	5	10^2	10^5	10^6
Crossover size	nm	>10^5	10^4	15	3
Brightness (at 100 kV)	A/m^{2}sr	10^{10}	5 x 10^{11}	5 x 10^{12}	10^{13}
Energy spread (at 100 kV)	eV	3	1.5	0.7	0.3
Emission current stability	%/hr	<1	<1	<1	5
Vacuum	Pa	10^{-2}	10^{-4}	10^{-6}	10^{-9}
Lifetime	hr	100	1000	>5000	>5000

3.5 Electron Lenses and Apertures

After leaving the gun's assembly the electron beam is guided along the column of the microscope by a series of apertures and electromagnetic lenses. Apertures provide a means of selecting individual electron trajectories and the lenses serve to redirect and focus these trajectories. The similarity between electron optics (charged particle optics in general) and traditional light-based optics is such that, in considering the trajectories of electrons in passing through an optical apparatus and ultimately image forming lenses, the same approach may be used: that of *geometric optics*. More precisely, provided the refractive index does not change significantly over a distance of a few wavelengths then on paper light optics and electrons optics are indistinguishable. The only difference is that in electron optics the influences of

the lenses extend beyond the physical material from which it is constructed, gradually diminishing with distance. In light optics, however, lenses generally constitute abrupt changes in refractive index (Rose, 2008).

The lenses of both TEM and STEM, with the exception of those within the gun housing, are electromagnetic. A direct current I is passed through a coil of wire and the magnetic field B produced (see Figure 3.4) is used to manipulate the trajectories of the electrons as they pass through. The Biot-Savart law predicts that B will be directed along the axis of the coil and for a given radial distance R its magnitude will be proportional to I. A cross-section through a "top entry emersion lens" typically found in TEM is shown in Figure 3.5. The iron cladding serves to concentrate the magnetic field in the vicinity of the pole-piece where the specimen sits immersed in the field.

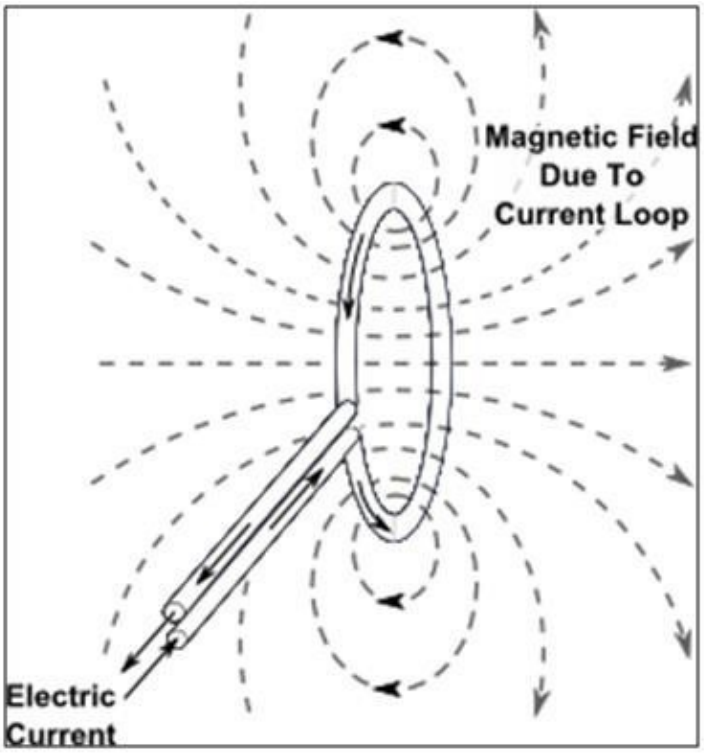

Figure 3.4 Schematic illustrating the geometry of the magnetic field produced by a current carrying coil of wire.

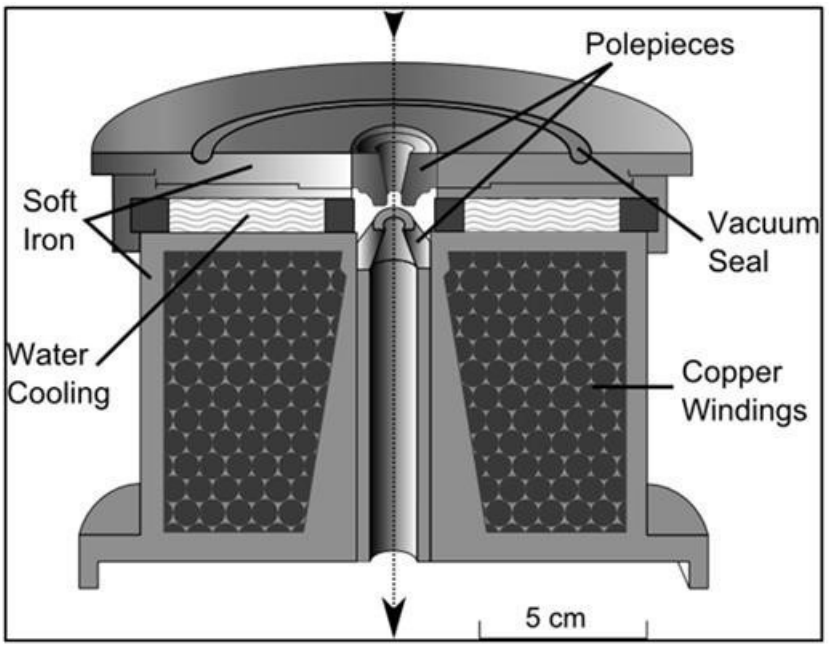

Figure 3.5 A cross-section through a "top entry emersion lens" typically found in the transmission electron microscope. The iron cladding serves to concentrate the magnetic field in the vicinity of the pole-piece where the specimen sits immersed in the field. Redrawn from Egerton (2005).

In the general case of an electron travelling at velocity $\vec{v}$ within a uniform magnetic field $\vec{B}$ it will experience a force given by:

$$\vec{F} = -(\vec{v} \times \vec{B})$$

If $\vec{v}$ and $\vec{B}$ are parallel then $\vec{F}$ will be zero and the electron will continue according to Newton's first law. However, if $\vec{v}$ subtends an angle θ with respect to $\vec{B}$ then the electron will experience a force F proportional to $v_{\perp} = \sin(\theta)$. This force acts in a direction mutually orthogonal to $\vec{B}$ and $\vec{v}$. The resulting motion of the electron describes a helix propogating along the direction of the field line $\vec{B}$ with velocity $v_{\parallel} = \vec{v}\cos(\theta)$. Ignoring relativistic effects and considering only the perpendicular velocity component $v_{\perp}$the radius of the electron's helical motion is given by

$$r = \frac{mv_{\perp}}{Be} = \frac{mvsin(\theta)}{Be}$$

The focussing action of the electromagnetic lens is achieved by adjusting I which varies B, which in turn alters the radial distance r of the electrons from the optical axis about which they spiral. Since r also depends on v it is apparent why (as mentioned previously) electrons of a single wavelength are desirable for electron beams in the TEM.

The geometry in the electron microscope is chosen such that $\vec{B}$ is ideally

symmetrical about the optical axis to which the electron trajectory will be near parallel: i.e. θ will be small meaning that $sin\theta \approx \theta$. In optics this condition is known as the paraxial approximation and in both light and electron optics means that geometric optics may be used for determining the beam paths through an optical system by simple ray-tracing.

3.6 Idealised Image Formation in the TEM

An imaging system aims to map points in an object to points in an image with a one to one correspondence. Focusing with a thin lens results in rays scattered from an object in the object plane, a distance u from the lens, being brought to focus in the image plane a distance *v* on the opposite side of the lens. These rays pass through the lens and converge to cross in the back focal plane from where they continue (unless detected as a diffraction pattern) to be projected to a point in the (Gaussian) image plane (Figure 3.6). The image thus produced is inverted and linearly scaled (magnified) with respect to the object.

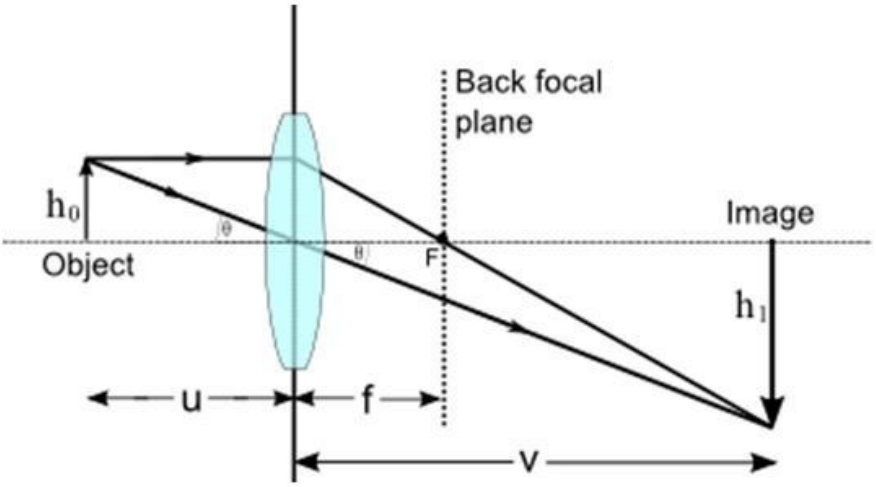

Figure 3.6 Ray diagram illustrating focusing using a thin lens. Rays from an object in the object plane a distance u from the lens pass through the lens and converge to focus in the back focal plane from where they continue (unless detected) to be projected as a upside-down image in the image plane.

The action of the lens is to Fourier transform the object to reciprocal space in the back focal plane which is then transformed back to real space in passing to the image plane. It is obvious that the transformation is not total in that not all spatial frequencies in the object pass through to the image and therefore the image is a filtered representation of the real space object. The finite diameter of the lens ultimately determines the angular range of scattered rays coming from the object

which make it through to the image much like a top-hat filter used in signal processing. The angular acceptance of the lens can be further limited by using an aperture to select specific beam paths about the optical axis (Figure 3.7). This may be used to enhance contrast in BF images resulting in strongly diffracting/scattering regions appear darker in the resulting image. The aperture can also be displaced from the optical axis resulting in dark-field images in which diffracting regions are brighter. The further from the optical axis the higher the spatial frequencies that are accepted.

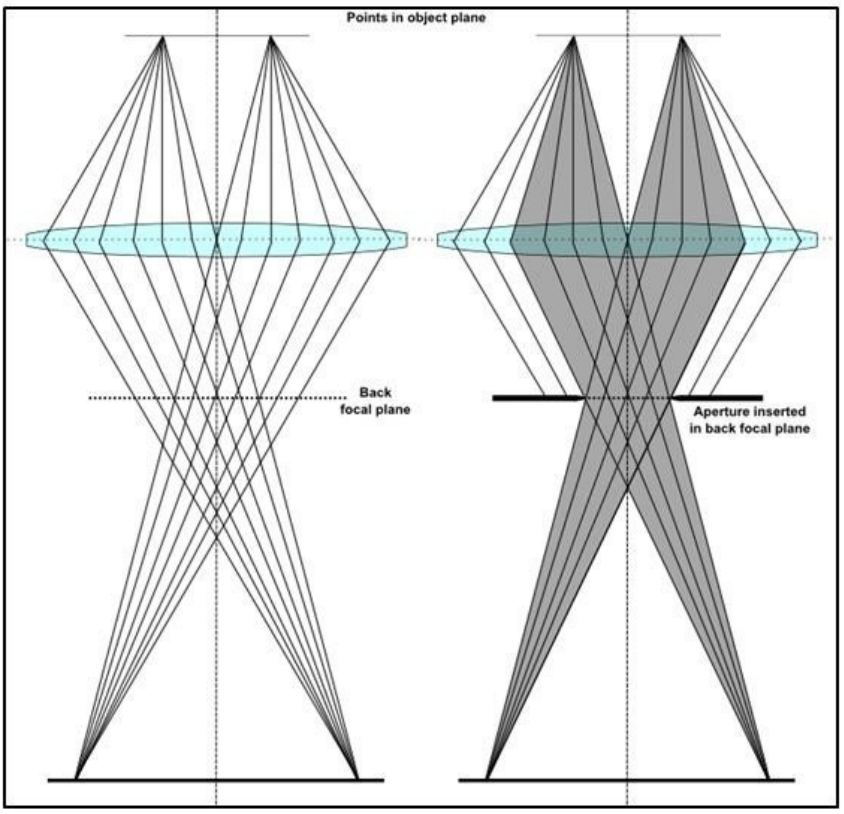

Figure 3.7 The use of an aperture in the back focal plane of a transmission electron microscope to limit the effective angular acceptance of its objective lens.

The resolution of any optical imaging system is ultimately limited by the wavelength of radiation it employs as illumination. Essentially any image forming lens, by virtue of a finite diameter, limits the angular range of illumination that passes through it to be focused in forming an image. Diffraction, which invariably occurs when a wave passes through such a limiting aperture, results in point sources in the object plane being transferred by the lens to an extended region in the image plane. Provided the focal length f of the lens is large compared with the lens diameter d the phenomenon is known as Fraunhoffer diffraction, which for a circular lens predicts that a point source object will have an intensity distribution in the image plane known as an Airy

pattern the form of which is depicted in various ways in Figure 3.8.

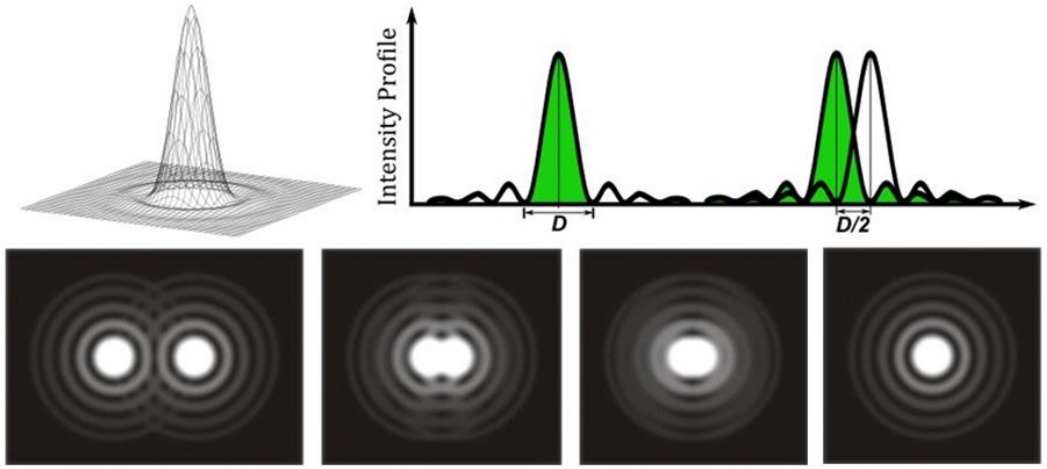

Figure 3.8 Various depictions of an Airy or Fraunhofer diffraction pattern showing a 3D wire mesh model of the Airy pattern (top-left), a 2D profiles through the centre of the Airy pattern (top-right) defining D the width of the Airy disk (83.8% total power) and the closest approach of two Airy patterns used in defining the Rayleigh criterion for spatial resolution. A sequence of projections of two Airy patterns progressively overlapping (bottom).

By the Fourier relation, the diameter of the Airy disk (i.e. the Fraunhofer pattern) varies inversely with the diameter of the lens (or limiting aperture) and proportionally with wavelength (λ). This is encapsulated in the so-called Rayleigh criterion which defines the spatial resolution of an imaging lens.

$$\delta = \frac{0.61\lambda}{\mu \sin(\beta)} \qquad \text{(Williams \& Carter 2009)}$$

where μ is the refractive index of the of the medium and β is the acceptance angle of the lens. The Rayleigh criterion requires that in order for two point objects to be distinguishable in the image plane their Airy disks must be separated such that the first minimum of one corresponds to the maximum of the other, as shown in Figure 3.8.

3.7 Lens Aberrations

Electron lenses, like their optical counterparts, suffer from aberrations which degrade the performance of the lens. Some of the most important aberrations are represented in Figure 3.9.

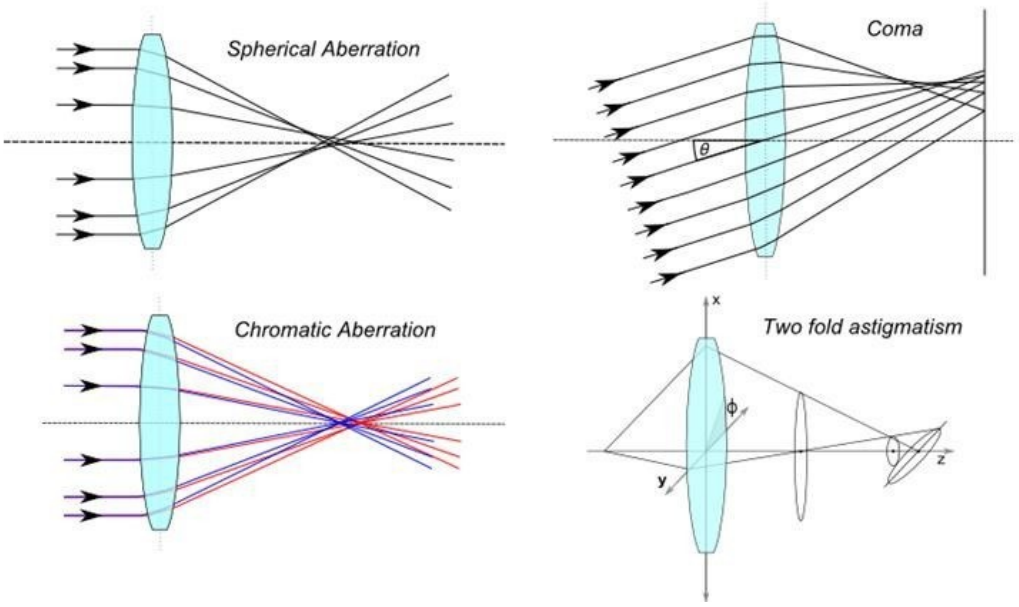

Figure 3.9 Graphical ray diagram depictions of some of the most important aberrations of electron optical lenses. Diagrams illustrate spherical-aberration, off-axis coma, chromatic aberration and two-fold astigmatism.

The most important of these imperfections are *chromatic* and *spherical aberration*. Chromatic aberrations result in lenses having a wavelength dependent focal length, an effect which can be minimised with the use of monochromated sources or energy filtered imaging. Spherical aberration (C_s) – which is the most significant in TEM – results in a lens with a radially varying focal length, with the lens being optically stronger moving radially out from the optical axis. Electrons travelling off axis will be brought to focus closer to the lens than those which travel close to, or on, the axis. One way to minimise the effect of spherical aberration is to use an appropriately small aperture to select only those electrons which travel close to the optical axis. This, however, limits the resolution by increasing the size of the Airy disk. Coma is an aberration which is a result of the electron beam travelling along a path which is not coincident with the true optical axis of the lens. This can be corrected for by appropriately tilting the beam so as to achieve alignment with the optical axis. Astigmatism is an aberration which results from a departure from radial symmetry of the lens' magnetic field. First order astigmatism is corrected for by using a series of electromagnetic coils immediately preceding the objective lens. Other, high-order, aberrations (i.e. C_s-3rd) can be corrected for, or at least partially compensated for, by offsetting their effect against other aberrations. This is done by using a series of multipole lenses immediately following the lens. Such configurations are known as aberration correctors and are used to provide

sub-Ångstrom probes and image resolution in the latest machines (Egerton, 2003; Krivanek, Corbin, Dellby, Elston, Keyse, Murfitt, Own, Szilagyi, & Woodruff, 2008; Lupini & Pennycook, 2002).

In an optically perfect lens, all ray paths travelling parallel to the optical axis will be focused exactly at the focal point. However, in real lenses, the net effect of chromatic and spherical aberrations gives rise to what is known as the disk of least confusion. The size of this disk (in the image plane) is the size of the smallest 'focused' spot which can be achieved and is an indication of the overall resolution of the microscope set up (Williams & Carter, 2009).

3.8 Optical Element Configurations (TEM)

The Condenser Lens System

Immediately following the anode is the condenser lens system. This comprises up of one or more (typically two) lenses and an aperture centered about the optical axis. The condenser system demagnifies the beam crossover from the gun system and, together with the pre-field of the objective lens, projects the beam onto the sample. By over-focusing the lens system (i.e. using it as a weak lens) near parallel illumination can be achieved at the sample. The area of illumination in this mode can be up to ~ 25 μm and is suitable for low magnification imaging. A convergent beam can be achieved by using the condenser system as a strong lens as well as using the condenser's aperture to control the convergence angle of the beam. The condenser aperture can also be used to limit the beam current by cropping electrons from it.

The Objective Lens

Immediately following the specimen is the objective lens and its aperture. This lens is used to produce a high-quality image in its image plane and a diffraction pattern (DP) in its back focal (diffraction) plane (BFP). The diffraction pattern is formed by the objective lens focusing electrons at positions in the BFP according to their angle of incidence on the lens (i.e. the scattering angle with which they have left the specimen). If these electrons are followed past the BFP they are recombined in the image plane to form an image (typically 60-1,000,000x magnification in TEM). The objective aperture is used to select which scattering angles of the transmitted electrons which contribute to the final image, something which is important for

generating diffraction contrast in phase contrast imaging to be discussed later in this chapter.

The Projector Lens System

Following the objective system is a series of intermediate lenses which further magnify the image or DP, and project this (with the projector lens) onto the viewing screen, camera or detector system. Contained in this section of the optical system is the selected area diffraction aperture (SAD) which can be used to limit the effective area of illumination (typically 10 - 0.2 μm depending on the size of aperture used) at the sample (projected backwards) from which a DP or an EELS spectrum are obtained

Correctors and Stigmators

In addition to the main lenses outlined above, there are a series of alignment coils and astigmatism correctors (stigmators). The alignment coils provide control over the tilt and shift of the beam with respect to the optical axis. This is necessary for the proper alignment of the microscope (e.g. coma correction). The astigmatism correctors, as their name suggests, are used to compensate for astigmatism in the objective lens and are essential in the formation of high-quality high-resolution lattice images.

3.9 Optical Element Configurations (STEM)

The STEM's lens arrangement is similar to that of TEM, however, in STEM the objective sits prior to the specimen and there are no post objective lenses for imaging purposes and a set of scan coils are used to raster scan the beam across the sample. Post specimen coupling lenses may be used to compress the beam in order that it may be efficiently transferred to a post-column EELS spectrometer. In STEM magnification is achieved by appropriately choosing the area over which the beam scans and varying the objective lens' excitation (beam convergence angle).

The Objective Lens

The objective lens in STEM is highly excited, when compared to TEM, and is used to form an extremely small (~0.1 nm) probe of high current density (~10^{-10} A). The sample in STEM sits very close to the objective lens and is in fact immersed in its post lens field. This allows for highly convergent probes (20 - 25 mrads).

Scan Coils

After the objective-condenser lens system comes two pairs of scan coils which are arranged to be mutually orthogonal to the optical axis. This arrangement allows them to act in cooperation scanning the beam over an area of the sample in a raster fashion.

3.10 Signal Detection

There are many possible signals which may be produced when the electron beam of a (S)TEM interacts with a sample. The most commonly exploited of these are the scattered transmitted electrons - both indirectly (BF) and directly (DF) - and the X-rays produced by electron-beam excited sample atoms. The scattered electrons carry a wealth of information about the sample which can be extracted by proper measurement of their scattering angle, phase and energy loss (EELS). X-rays provide information on the elements present in the sample and can be used to determine relative concentrations of different atomic species.

Electron Detection for Imaging

Electrons are generally detected either by using photographic plates, charge-coupled devices (CCD) or photomultipliers. In TEM the CCD is either located below the viewing screen in a dedicated post column imaging/EELS system or above the viewing screen in a 35 mm port. The CCD itself is not actually exposed directly to the electrons but is coupled to a phosphorescent (scintillator) screen via a series of fibre optical cables. Photons produced by electron bombardment in this screen travel down the optical cables and are detected in the CCD.

In the STEM, a scintillator material is used to convert an electron's kinetic energy into light. This light is then detected by a photomultiplier system and its intensity recorded as a function of beam position to construct an image. STEM is capable of not only detecting those electrons which have been scattered through small Bragg angles (~1^{o}) but also those which have suffered relatively large (> 5^{o}, Rutherford or nuclear) changes in their direction of propagation. This is accomplished by using several (on and off-axis) detectors to simultaneously detect electrons from various scattering angles. The off-axis detectors are called *annular* dark-field (DF) detectors. DF imaging is possible in the TEM and is accomplished by either tilting the beam or by offsetting the objective aperture.

Electron Detection for EELS

Electron energy loss spectroscopy in the analytical (S)TEM involves analysing the kinetic energy distribution of the forward scattered electrons emerging from the sample (Brydson, 2001). For this a dedicated spectrometer is used which usually consists of an energy discriminating element and an electron detector. The first element, which is usually a magnetic prism, is used to disperse the electrons, according to their kinetic energies, across a detector. The detector can either count electrons serially (SEELS), with the aid of a slit to select an energy window, or in parallel (PEELS) as is the case for CCD detectors. In front of the prism element is the spectrometer entrance aperture, this is used to define the angular range of scattered electrons accepted by the spectrometer (typically < 30 mrads). Between the prism and the CCD there are usually a series of electromagnetic multipole lenses and electrostatic correctors. These are used to modify the electron paths leaving the prism and achieve focus in the detector plane. The whole EELS detector system is usually mounted post column in both TEM and STEM. Another EELS system, which is less frequently employed, is the so-called Omega Filter. This is an in-column energy discriminating element which is made up of four magnetic prisms arranged in the shape of the Greek letter Ω.

In PEELS the magnetic prism projects the spectrum across a CCD. The spectrum is then recorded in parallel by vertically summing the CCD pixel values across the CCD. That is, in a direction perpendicular to the energy dispersive plane. PEELS has the major advantage of short acquisition times (~ 0.5 - 100s) which are generally only limited by the time taken to collect sufficient electron counts for good statistics. One major disadvantage of PEELS is that CCDs give rise to added noise and in some cases a fixed pattern gain variation (a problem for STEM) in spectra: this is in contrast with the SEELS detector system in which the same detector is used for all energy-losses.

X-Ray Detection for Chemical Analysis

X-rays emitted from the sample are collected by a dedicated detector which is mounted on the side of the column just above the sample stage. The sample is usually presented to the detector during acquisition by tilting it through an angle of ~15^{o} to avoid absorption by the specimen holder.

The detector its self is generally one of two types: Wavelength Dispersive (WDX) or

Energy Dispersive (EDX). The former consists of a collimator system and several (curved) crystals of well know Bragg spacings. The collimated X-rays are diffracted by the crystals and are serially collected as a function of angle, usually by a photomultiplier system. WDX detectors are capable of energy resolutions of ~ 10 eV and can detect all elements down to lithium (Egerton, 2009). EDX systems, which are capable of parallel recording, employ a semiconductor material (Loretto, 1994) to convert the X-ray photon's energy into a corresponding voltage pulse. This pulse is then analysed by the detector's electronics and passed to dedicated software to create a spectrum. EDX systems perform less well at detecting soft X-rays than WDX and are limited, in the best case, to elements above boron. EDX also performs worse in terms of energy resolution (~ 100 eV) when compared to WDX. These drawbacks are however compensated for by the short acquisition times inherent in parallel recording. This has meant that EDX has become the X-ray detection method of choice in most modern analytical (S)TEMs (Egerton, 2009).

3.11 Imaging Modes and Contrast Mechanisms

There are two grand regimes of imaging in the TEM: Bright Field (BF) and Dark Field (DF). BF images are produced using on-axis apertures and detectors (a position which would give 'bright' image regions in the absence of a specimen). DF images are acquired by either tilting the beam, using off-axis apertures (in the case of TEM) or by using off-axis annular detectors (in the case of STEM). Depending on their angular location, these detectors are termed either annular dark-field (ADF) or high-angle ADF (HAADF) detectors.

Amplitude Contrast

As electrons pass through a specimen they will be scattered by the atoms within the sample. The amount of scattering will depend upon the atomic density (in projection) of a given region of the specimen. The greater this density the more scattering will occur. In TEM, with a suitable choice of objective aperture, regions of high density in a specimen will result in intensity deficient regions in BF images. This mechanism is called *mass-thickness-contrast*. The inelastic scattering power of an atom, at high angles (> 5°), is proportional to the square of its atomic number (Z) and as such imaging using only electrons scattered through these large angles or greater is called Z-*contrast-imaging* (i.e. HAADF imaging) (Goodhew, 2008).

In the case of crystalline samples, electrons will be strongly, and preferentially, diffracted in specific directions (up to ~ 1° off axis) depending on the nature of the unit cell being probed. This will affect both BF and DF images by removing electrons from BF images and transferring them into DF ones (ADF not HAADF in the case of STEM) or *vice versa*. This mechanism is termed *diffraction-contrast* and will occur along with *mass-thickness-contrast*, as outlined above. When diffraction contrast is present it will tend to dominate the image contrast for crystalline materials in TEM.

It is common to group the above contrast mechanisms together under the umbrella name of *Amplitude contrast* since they result in direct changes in the amplitude/intensity of the transmitted signal.

Phase Contrast

Phase contrast results from the phase change ($\pi/2$ in the case of Bragg diffraction) suffered by electrons which have been diffracted by atoms within the sample. If the specimen is sufficiently thin so that transmitted electrons can be considered to have experienced zero or a maximum of one scattering event the specimen is said to be a *phase-object*. In cases where the sample is extremely thin, so that the transmitted beam's intensity is almost unchanged when compared to the primary beam, the specimen is said to be a *weak- phase-object* (WPO) (Goodhew, 2008).

In TEM, if a WPO is illuminated with coherent illumination the Bragg scattered electrons will be phase shifted by $\pi/2$ with respect to the unscattered electrons. The contrast in an image is formed by selecting an appropriately sized objective aperture so as to allow both the unscattered and (some specific) diffracted electrons through. Superposition of the respective electron waves, when they are reconstructed in a conjugate image plane, will result in contrast by virtue of these phase differences. Contrast may be further enhanced in these images by adding an additional $\pi/2$ phase shift to the diffracted electrons by operating the objective lens at an appropriate level of defocus. This is the principle behind the formation of atomic lattice images in TEM.

Lattice Imaging

Images may be obtained, in both TEM and STEM, which are capable of resolving crystal lattices and individual atomic columns. For this the microscope must be well aligned, the objective aperture must let through only those diffracted electrons which

correspond to spatial distances resolvable by the microscope and the objective lens must be correctly defocused (see below). If these conditions are met atomic columns will appear dark in BF images and between the columns will appear bright (Williams & Carter, 2009).

Focusing with the objective lens introduces phase shifts in electron-waves which vary with the angle with which they pass through. The relationship between phase shift and angle for a given lens is determined by its contrast transfer function (CTF). The optimum level of defocus alluded to above is determined by the objective lens' CTF and is known as *Scherzer defocus*. For an objective lens of a given C_s (spherical aberration coefficient) and electrons of wavelength λ the value of *Scherzer defocus* is given by:

$$\Delta f_{Scherzer} = -1.2(C_s\lambda)^{1/2}$$

(Williams & Carter, 2009)

3.12 Electron Diffraction

When a collimated beam of electrons, such as that of the TEM, is incident on a periodic spatial arrangement of atoms, such as those of a crystalline material, interference between the diffracted electron-waves will give rise to a diffraction pattern (DP). The DP of single crystals, as viewed in the back focal plane (BFP) of the TEM's objective lens, consist of a series of spots whose intensity and relative position are characteristic of the scattering atoms' spatial arrangement. By analysing this pattern it is possible to deduce the real space configuration of atoms within a crystalline material. Amorphous and polycrystalline materials also give rise to a diffraction pattern, however here the pattern consists of rings rather than spots. In the case of polycrystalline samples, these rings are composed of many thousands of individual diffractions spots which, because of the random orientation of the individual crystallites, blur together to create rings. The position of these rings, in the BFP, can be used to calculate the inter-lattice spacings of the material. For amorphous samples, the position of these rings represents the average interatomic spacings.

When performing electron diffraction in the TEM it is common to use an aperture to select the area of the sample which is allowed to contribute to the diffraction pattern. This is known as a selected area aperture (SAD) and the mode of acquisition is

known as selected area electron diffraction (SAED).

3.13 Electron Energy Loss Spectroscopy (EELS)

Electron Energy Loss spectroscopy (EELS) is one of the major analytical techniques used in this study and accordingly this section is dedicated to a discussion of EELS in the TEM. The aim is to provide and outline the most relevant aspects since the subject is addressed in greater detail elsewhere (Amelinckx et al., 1997; Brydson, 2001; Egerton, 2011; Egerton, 2012).

In the context of the (S)TEM, EELS involves analysing the kinetic energy distribution of the transmitted electrons which, in passing through a specimen, have lost energy due to inelastic interactions. The amounts of energy exchanged and concomitant angular deflection is characteristic of the type of interaction process and in turn the solid state nature of the specimen. Of practical interest are energy losses up to several thousand eV which include the excitations of phonons, plasmons, inner-shell and valence electrons. Therefore, EELS probes the chemical and electronic properties of materials and may provide information pertaining to: sample thickness, valence electron density, optical properties, elemental distributions/concentrations, oxidation state, coordination environment and specific bonding characteristics (Brydson, 2001; Egerton, 2012; Egerton, 2009). Fine-structure spectral details are often sufficiently distinct making EELS an effective fingerprinting method and in many cases can be used for quantitative analysis of mixtures. Outlined in Table 3.3 is a summary of the different type of information available from a detailed analysis of an EEL spectrum.

Table 3.3 Summary of the different types of information available from detailed analysis of an electron energy loss spectrum. After Amelinckx et al., (1997).

Spectrum domain	Information accessible	Required processing technique	Field of application
Whole spectrum and zero loss in particular	Thickness, total inelastic scattering	Measurement of unsaturated zero-loss peak	Very general
Low-loss region	Average electron density	Measurement of plasmon line properties	Microanalysis in metallic alloys
Low-loss region	Interband transitions/joint density of states	Kramers–Kronig transformation; calculation of dielectric constants (critical-point modeling)	Optical and transport properties; comparison with VUV spectra; intergranular van der Waals forces
Low-loss region	Interface/surface properties	Study of the interface plasmon modes	Interface and boundary structure and chemistry
Core-loss region	Qualitative and quantitative elemental analysis	Measurement of core-edge weight	Nanoanalysis of any type of material
Core-loss region	Site symmetry; bonding type; bond lengths	Analysis of core-ELNES; comparison with fingerprints; molecular orbital, multiple scattering or band structure calculations	Site-selected valence state; charge transfer; bonding and structural environment
Core-loss region	Radial distribution function	Analysis of core-EXELFS	Site-selected crystal coordination
Core-loss region	Density of holes on local states	Measurement of white-line intensities	Electron configuration in intermetallics, insulators, and superconductors; magnetic properties

ELNES, energy loss near edge structure; EXELFS, extended electron energy loss fine structure; VUV, vacuum ultraviolet.

Performed in the conventional TEM, EELS provides bulk averaged information from areas of approximately 100 nm in extent, whereas using a dedicated STEM the probe-size limits EELS spatial resolution to around 1 nm. The use of C_s correcting optics in the case of STEM dramatically increases the spatial resolution attainable as well as the current density of the probe. AC-STEM EELS data is now routinely acquired using sub-Ångstrom probes allowing chemical and compositional information to be obtained with atomic-resolution (Allen, Findlay, Lupini, Oxley, & Pennycook, 2003; Egerton, 2007; Klie & Zhu, 2005; Kujawa, Freitag, & Hubert, 2005; Muller & Silcox, 1995; Pennycook & Varela, 2011; Pennycook, Varela, Lupini, Oxley, & Chisholm, 2009; Zhou, Pennycook, & Idrobo, 2012).

Acquisition and Persistence of Energy Loss Spectra

The energy loss signal is collected and recorded using either a dedicated spectrometer or a hybrid energy-filter-come-spectrometer which, may be used for spectroscopy. Historically, numerous designs have been proposed for electron energy analysers of which many have made the transition from the hypothetical to

their practical realisation and subsequent use. Despite this, the current market for EELS hardware is dominated by Gatan *Inc.* with their flagship post column spectrometer design (Gubbens, Barfels, Trevor, Twesten, Mooney, Thomas, & Menon, 2010; Krivanek, 1989). An example of this design is illustrated in Figure 3.10 where it adorns the top of a dedicated STEM column.

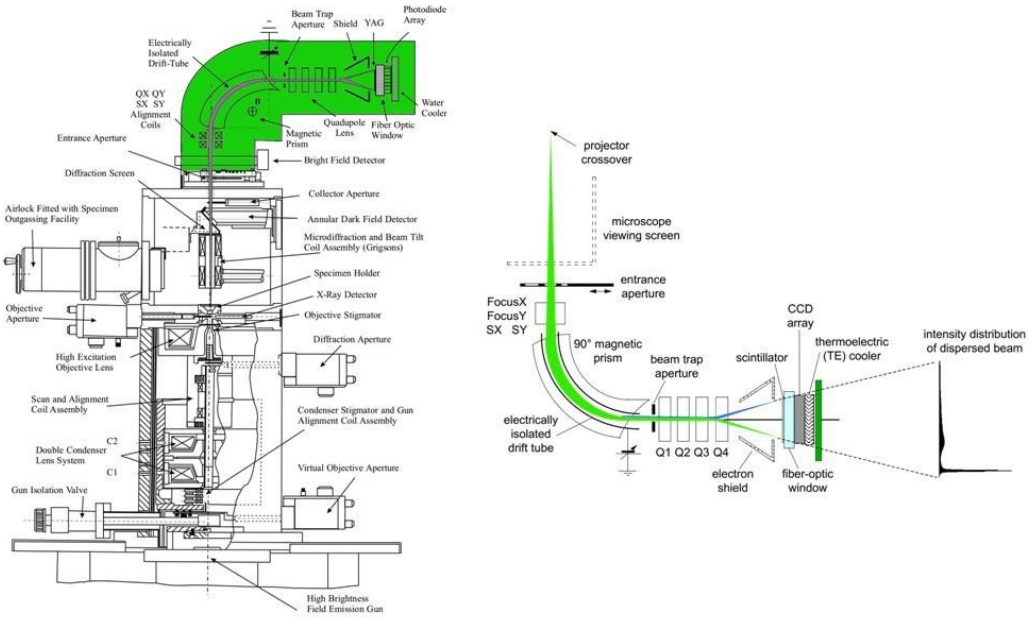

Figure 3.10 A dedicated scanning transmission electron microscope fitted with a Gatan post-column energy filter (left) and a detailed view of a Gatan post-column energy filter (right) illustrating the path of the electron beam in passing through the main components of the spectrometer.

In producing the energy loss spectrum the spectrometer must accept a small portion of the beam coming from the projector cross over just outside the entrance aperture. The spectrometer entrance aperture is variable and is used to determine the angular range of electrons entering the spectrometer. This allows aberrations, associated with off-axis beam paths, to be balanced against larger collection angles which provide more signal. Passing through the entrance aperture the electron beam is finely adjusted by passing through a set of pre-spectrometer multipole tuning lenses (FocusX, FocusY, SX and SY). It then passes through the uniform magnetic field of the prism which constitutes the main dispersive element and is ultimately responsible for producing the energy loss spectrum. The geometry of the prism is such that electrons travel along a direction perpendicular to the magnetic field *B*. The resultant force experienced by the electron is in a direction mutually orthogonal to both the magnetic field and their direction of propagation. This translates the electron path through the 90˚ of the prism's curve. The trajectory of electrons is such that those with lower energies are deflected to a greater extent such that upon

leaving the prism the beam will be spread out. Following the prism are a series of quadrupole lenses which transform the spectrum by magnifying and project it across the scintillator which is optically coupled to a CCD for parallel detection (Krivanek, 1989; Krivanek, Ahn, & Keeney, 1987; Shuman, 1981).

Optimising the Acquisition Process for Quality EELS

In conventional TEM EELS can be performed either in imaging mode or diffraction mode. In the first instance, the spectrometer is said to be diffraction-coupled to the microscope since in the spectrometer plane there will be projected a DP of the sample. In image-coupled mode, in which the microscope is operated in diffraction mode, the opposite is true (Egerton, 2011). Image coupling should be preferred over diffraction coupling as this reduces the effects of chromatic aberrations in the objective and projector lenses which can lead to spectrometer collection efficiencies being dependent on scattering angle (Brydson, 2001). When the microscope is image coupled to the spectrometer a selected-area diffraction aperture can be used to (approximately) define the area of the sample from which the EELS signal originates. In this way, EELS data from spatially resolved regions may be obtained in TEM (typically areas of ~ 200 nm in diameter).

The angular distribution of the forwards scattered electrons collected for EELS may be approximated by a Lorentzian distribution for which a characteristic scattering angle may be defined. The angle increases proportionally with the energy loss of the feature in question. If the collection angle of the spectrometer is too small then only a fraction of the signal will be collected. On the other hand beyond the characteristic angle, further increasing the collection angle results in little extra gain of signal but instead increases the background contribution. Additionally, at large angles (> 30 mrads) the dipole selection rule no longer holds. The characteristic scattering semi-angle is given by

$$\theta(mrads) = \frac{E(eV)}{2E_o(keV)} \qquad \text{(Brydson 2001)}$$

As a rule of thumb collection angles should not exceed 2-3 times θ.

The Energy Loss Spectrum

The energy loss spectrum is a discrete approximation of the continuous probability distribution describing inelastic electron scattering as a function of increasing energy

loss. The independent variable is energy-loss which is divided into discrete intervals of equal width in energy loss. The dependent variable is simply the frequency ($N(E + \Delta E)$) with which electrons are observed with energy in the interval E to $E+\Delta E$. In principle this covers a large range of energy loss, however, due to practical considerations values from 0 to several keV are normally considered accessible. The actual range covered in a single spectrum acquisition depends on the total number of channels, the energy-dispersion and any energy-offset used by the spectrometer.

With numerous energy loss mechanisms contributing to the EELS signal it is natural to define several regions of energy-loss (see Figure 3.11)

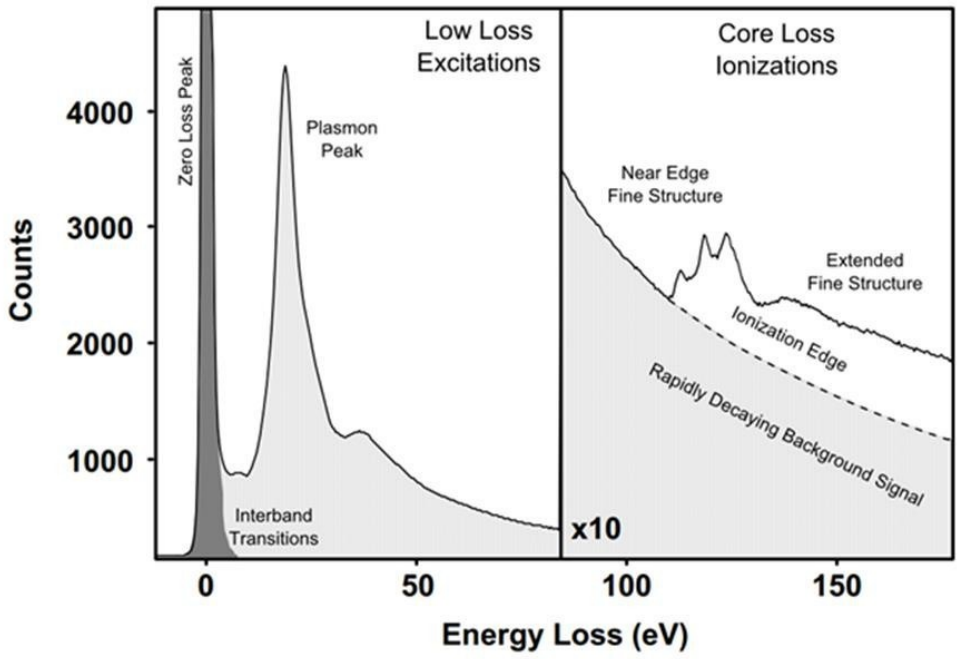

Figure 3.11 Electron energy loss spectrum showing the zero-loss peak, plasmon and core-loss regions of an idealised electron energy-loss spectrum with electron-counts on a logarithmic scale. After Egerton (2011).

The Zero-Loss Peak

At zero energy loss, we find the *zero-loss peak* (ZLP) which represents all those electrons which have been either elastically scattered or not at all. In a properly prepared (i.e. thin) TEM sample, the ZLP will be by far the most intense feature in the spectrum. By definition, the ZLP is due to electrons having incurred zero energy loss and as such it provides a known reference for calibration of the energy-loss scale (Egerton, 2011).

The width of the ZLP is determined by the energy spread and stability of the electron source as well as the spectrometer focusing and aberration effects in the

microscope. Typically ΔE is between 0.3 - 0.8 eV for field-emitters and below 0.2 eV for monochromatic sources (Egerton, Qian, & Malac, 2006). This width is the commonly used *yardstick* for measuring and comparing the energy resolution of an EELS setup.

The integrated signal intensity of the ZLP with respect to the rest of the spectrum is related to the thickness of the specimen by

$$\frac{t}{\Lambda} = n\left(\frac{I_t}{I_0}\right)$$

(Brydson, 2001)

where t is the specimen thickness, Λ is the electron's mean free path for inelastic scattering, I_t is the integrated intensity of the whole spectrum and I_0 is the integrated intensity of the ZLP. In the case of an ideal specimen, for which multiple scattering is not an issue, the relative thickness, t/Λ will ideally be ≤ 0.3.

Plasmon Losses

From around 5 - 50 eV energy loss is in the *plasmon* region. This is populated by peaks due to electrons having lost energy in exciting collective resonant oscillations of valence and/or conduction-band electrons (Egerton, 2011). With relatively large interaction cross sections, this is by far the most intense region of the inelastic EELS spectrum. Corresponding mean free path values for fast electrons (~100 keV) interacting with plasmons are of the order of 100 nm – close to the thickness of a typical TEM specimen. Accordingly, there is a significant likelihood that in passing through the specimen such an electron will excite a plasmon and lose energy E_p in the process. The position of the plasmon peak is proportional to the square root of the valence electron density, and its width is governed by the damping mechanisms which tend to quell these oscillations (Brydson, 2001).

In the case of thick samples, in which multiple scattering is significant, multiple plasmon peaks may be observed spaced evenly in energy loss (see Figure 3.12). In terms of thickness, an ideal low-loss spectrum is one which exhibits only one clearly visible plasmon peak. In general EELS data require treatment for multiple scattering effects and this is typically done using Fourier deconvolution methods which rely on an accurate measurement of the low-loss spectrum (Egerton, 2011).

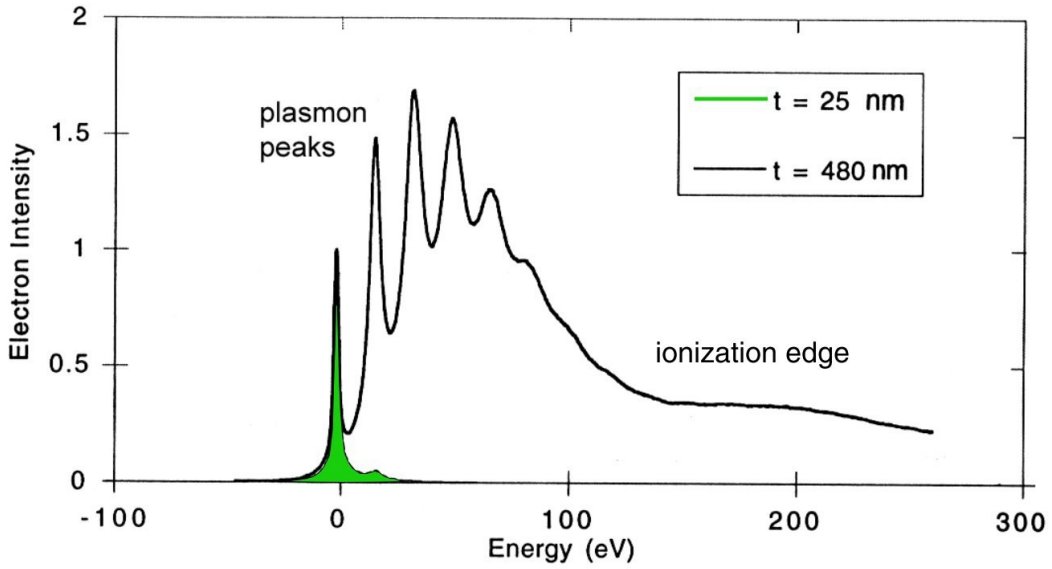

Figure 3.12 Composite electron energy loss spectrum comparing a thin region (25nm) of silicon (solid) with that of a thicker (480nm) area (line). Multiple plasmon peaks starting at ~16.7 eV, can clearly be observed for the thicker spectrum. The broad feature starting around 100 eV is a silicon L_{23} ionisation edge. Adapted from Egerton (2009).

Core Losses

Extending from the low-loss region up to several thousand eV is the *core-loss* region. Peaks, or edges, found here are due to electrons having lost energy in exciting atomically bound electrons from inner shell core-levels to previously unoccupied (yet still bound) final-states just above the Fermi level (Brydson, 2001). This energy-loss mechanism is analogous to absorption edges in X-ray absorption spectroscopy (XAS).

The spectroscopic notation used for identifying EELS core-loss edges is broadly similar to that used in X-ray absorption spectroscopy (XAS), however, in the case of EELS, edges are identified by the initial state core-level rather than the final state as in XAS. Initial state orbitals where n = 1, 2, 3… are designated *K, L, M* etc. For each value of *n,* the *orbital angular momentum* number *l* may assume integer values between 0 and (n-1) inclusive. The *total orbital angular momentum* number *j*, is given by $j = l + s$, in which *s* is the spin quantum number equal to ± 1/2 and identifies two distinct electrons for each combination of n & l as predicted by the Pauli exclusion principle. This relationship is illustrated graphically in Figure 3.13.

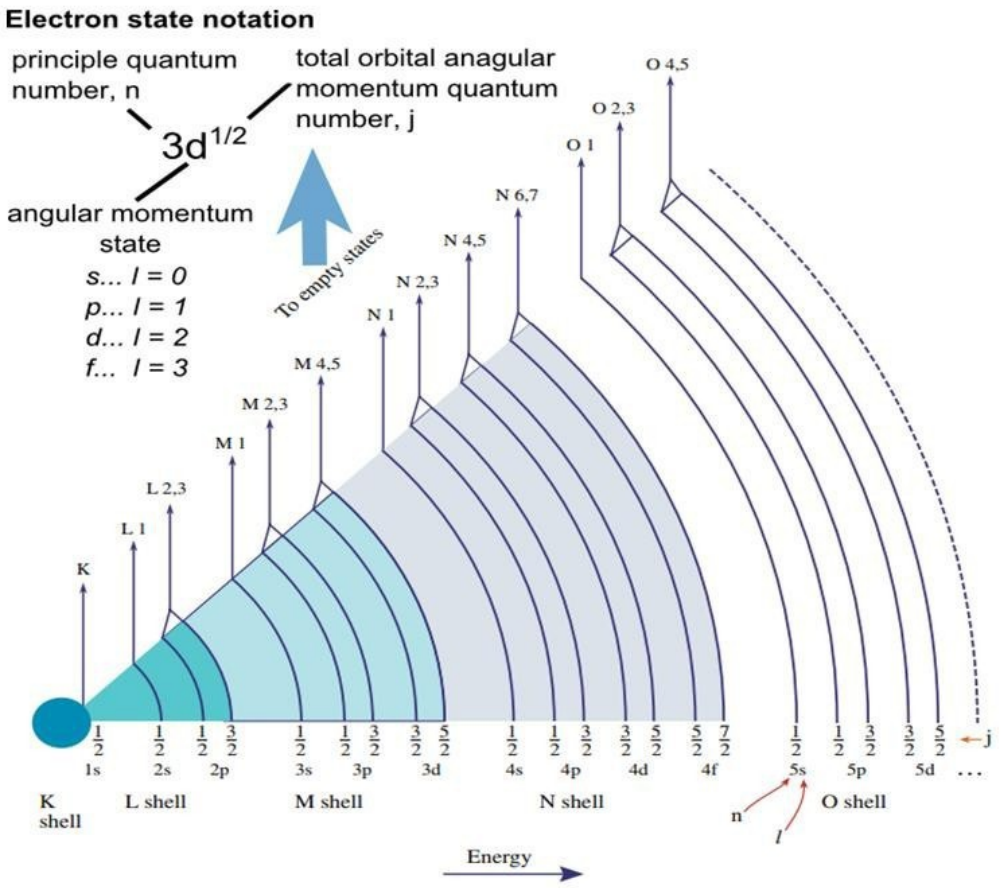

Figure 3.13 The full range of possible edges in an electron energy-loss spectrum due to core-shell ionisation along with a description of the associated nomenclature. Adapted from Williams and Carter (2009).

Core-loss edges are superimposed on a slowly decaying background signal. This background signal is primarily due to the high-energy tail of the plasmon region and to a lesser extent contributions due to core-loss features lying at lower energy-losses. At an energy-loss E, sufficiently beyond (> 40 eV) the next nearest energy-loss feature, the analytical form of the background signal is that of a power-law

$$AE^{-r} \qquad \text{(Egerton, 2011)}$$

where A and r may be determined by fitting to a region of background.

Provided the energy loss associated with a particular transition is negligible compared to that of the primary beam transitions between core-levels and previously unoccupied (yet still bound) states will be subject to the dipole selection rule. This limits the range of observed (allowed) transitions to those for which the change in orbital angular momentum between initial and final states is $\Delta l = \pm 1$ (Brydson, 2001). In general, this condition is true provided the spectrometer collection angle (β) used is relatively small permitting electrons scattered by <30–40 mrads (Egerton, 2011).

Energy Loss Near Edge Structure (ELNES)

In EELS, core-loss edges correspond to electron transitions from core-level initial states to previously unoccupied (yet still binding) final-states just above the Fermi level. The edge-onset corresponds to the energy required to promote the transition of a core-level initial state electron to the lowest (allowed) state just above the Fermi level.

The actual position of this onset will vary with formal charge (oxidation state), something which is known as a *chemical* shift (Brydson, 2001; Garvie & Buseck, 1998). These chemical shifts will typically be of the order of a few eV across different chemical states. For example, in the case of iron, there is an approximate ~2 eV increased between oxidation state Fe^{2+} and Fe^{3+}. Unlike XPS in which such shifts may be rationalised in terms of a combination a reduction of nuclear screening and the corresponding increased attraction, the nucleus has on the 25 electrons of Fe^{3+} compared to the 26 of Fe^{2+}. In EELS additional consideration must be given to the final state which is most probably a 3*d* state for which the occupancy is one less in Fe^{3+} than Fe^{2+}.

3.14 Beam Damage

The high energy electron beam of the TEM has the potential to seriously alter a specimen to such an extent that it no longer can be considered to be representative of the parent material. Typically referred to as *beam damage* often there is a compromise between the information sought and what is permitted before damage is so significant it can no longer be ignored. This is all the truer in the case of aberration-corrected STEM where the reduced probe size (0.1 nm compared to pre-corrected 1–2 nm) contains the same total number of electrons as pre-corrected only now concentrated over an area one hundredth of the size. Damage has been studied and discussed numerous times in the literature (Egerton, 2013; Egerton, Li, & Malac, 2004; Egerton, McLeod, Wang, & Malac, 2010; Humphreys, 1991; Jiang & Spence, 2012).

Damage results from the inelastic interaction between the specimen and electron beam and can take several forms. *Knock-on* damage results from interaction between beam electrons and the nuclei, in which the electron's direction may deflected by up to 180°. *Radiolysis* refers to the breaking of chemical bonds due to the ionising

effects of electron irradiation. The excitation of phonons results in the beam energy being dissipated as heat throughout the specimen (Williams & Carter, 2009).

In strict radiation physics terms, the amount of energy absorbed by a substance is measured in joules per kilogramme (or grays), however, in the TEM it is difficult to gauge the extent of the third dimension and therefore fluence is the preferred units of measure. Fluence refers to the amount of radiation passing through an area presented perpendicular to it. This is extended to electron microscopy where the number of electrons passing through a given area is considered. In SI units this would be the number of electrons per meter squared, however, due to the reduced dimension typically considered in the TEM, units of electrons per nm or Coulombs per centimetre are used since these give a more sensible number.

There are a number of methods for minimising the effect of beam damage such as reducing the beam energy in order that is below the threshold for a specific damage mechanism. Cryo-fixation, in which the specimen is embedded in vitreous ice, is also used. This may help with heating, but in other cases, it simply fixes the damage products in place. Carbon coating the specimen can help but again this does not solve the problem. The best way is to reduce the overall fluence that the specimen receives, however this cannot be done indefinitely (Egerton et al., 2010).

Part of this work involved the development of a low-fluence EELS method in collaboration with Dr Kasim Sader of SuperSTEM (see Appendix A). This involved customised control of the electron beam in order that signal can be averaged over extended “equivalent” areas of the specimen (Sader, Schaffer, Vaughan, Brydson, Brown, & Bleloch, 2010).

3.15 Electron Microscopes Used During This Study

The following microscopes were used extensively throughout this study. Additional information pertaining to the simulation of microscope images is presented in Table 4.2.

NION UltraSTEM™

The Nion Company was founded in 1997 by Ondrej Krivanek and Niklas Dellby and is dedicated to the research, design and manufacture of cutting-edge aberration-corrected STEM microscopes, correctors and their constituent parts. Built

from scratch the UltraSTEM 100 was designed as a dedicated aberration-correction machine rather than being a retro-adapted design. Imaging may be performed using three imaging detectors: bright field, medium angle dark field and high-angle annular dark field. EELS is carried out using a Gatan Enfina spectrometer. A fast readout 1k x 1k CCD detector allows for Ronchigram and diffraction pattern acquisition. The microscope combines a high-brightness 100 kV cold-field emission gun capable providing around 200 pA beam currents with an energy spread of 0.3 eV. The gun vacuum is extremely low, being typically 10^{-11} Torr, meaning the tip remains clean for longer providing extremely reliable emission. A 3rd generation NION aberration-corrector (12 quadrupole and three combined quadrupole-octopoles) corrects all aberrations up to fifth-order. A fully bakeable modular column design which provides ultra-high stability whilst minimising contamination. The microscope is fully remotely computer controlled (e.g. insertion of apertures, detectors, etc).

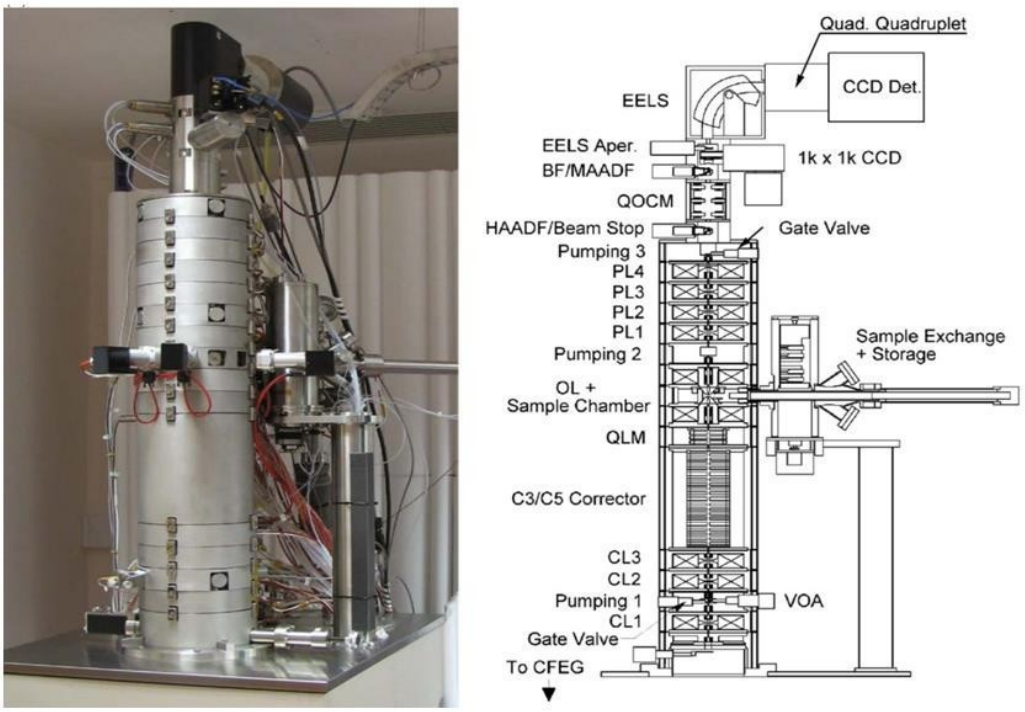

Figure 3.14 The column of the NION UltraSTEM2 "An electron microscope for the aberration-corrected era" at SuperSTEM (UK) (left) and a schematic of the column (right) taken from Krivanek et al., (2008).

This microscope was used over a five day period (a significant part of which was unsupervised) during a visit to the STEM groups are Oak Ridge national laboratories in the USA. Additionally, the same model has been used numerous times at the SuperSTEM facilities at Daresbury Laboratory, UK.

SuperSTEM1

SuperSTEM1 (see Figure 3.15) is a VG HB501 column retrofitted with a Mark II Nion quadrupole-octopole C_s corrector providing 1.0 Å probes with 80pA current. It is fitted with a cold-FEG emitter with a 40-100keV operating voltage and a 0.3 eV energy spread. Detectors consist of BF, medium and high angle annular detectors collecting over angles of 0-6, 35-100, and 70-210 mrads respectively.

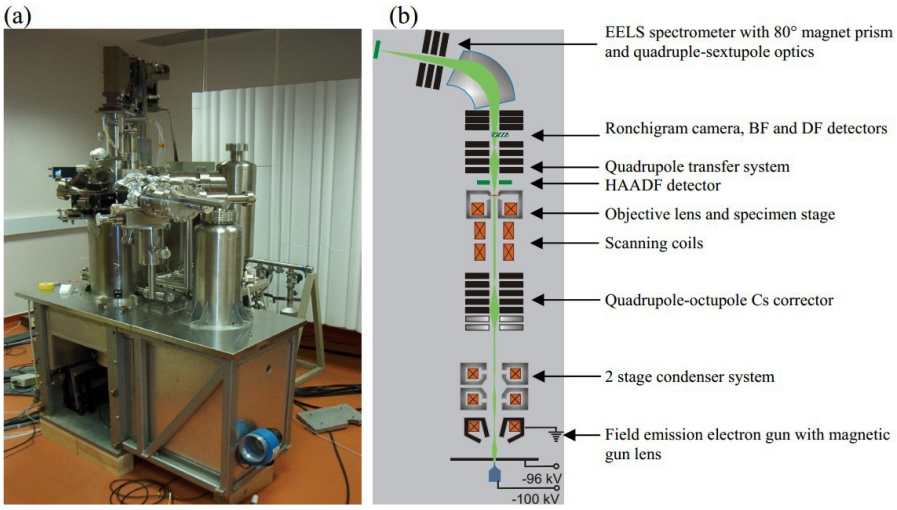

Figure 4.5 (a) The SuperSTEM facility at Daresbury Laboratory, UK; (b) Schematic diagram of the microscope column.

Figure 3.15 (a) The SuperSTEM1 microscope at Daresbury Laboratories, UK along with a (b) schematic diagram of the microscope column. Taken from Pan (2006)

Philips CM200 at the University of Leeds (UK)

TEM analysis was carried out using a Philips Model CM200 TEM operating at 197kV. This microscope is fitted with a Gatan Imaging Filter (GIF) which was used for bulk EELS investigations and all other TEM imaging based work. An Oxford Instruments UTW ISIS X-ray detector was used for EDX spectrum acquisition. This microscope has a point resolution of 0. 1nm.

Figure 3.16 The Philips CM200 transmission electron microscope housed at the University of Leeds, UK.

Chapter 4 Materials Synthesis and Characterisation Methods

This chapter provides a detailed description of the preparation methods used for each of the synthetic compounds examined in this report. A brief synopsis of each of the major techniques used in their characterisation is given in terms of what is measured and how this is measured. It is not the intention here to be exhaustive in describing or provide the histories of technique development as that has already been covered in many textbooks. What is intended however is that the reader be convinced of what information a particular technique can provide and how the measurements may be repeated. Split into three parts, the first section covers the methods used in synthesising various ferrihydrites and the iron storage protein, ferritin. Second, the techniques which provide what is traditionally termed bulk information as acquired from macroscopic areas of a sample are described. Third, the experimental parameters used for each analytical technique are provided.

4.1 Synthesis Methods

This chapter details the samples synthesised during this study providing a description of the sample, the synthesis methods used and abbreviated sample names used throughout this document for the sake of brevity. Table 4.1 provides a concise summary of all samples used during this study.

Table 4.1 Details of samples synthesised and examined during this study. Sample Full Names, Abbreviated Names and Description are provided along with appropriate sign posting to the sections where a fuller description of corresponding synthesis methods may be found.

Sample Full Name	**Abbreviated Name(s)**	**Sample Description**
Synthetic two-line ferrihydrite	2LFh	Two-line ferrihydrite synthesised *in vitro* according to the method provided in section 4.1.1.
Synthetic six-line ferrihydrite	6LFh	Six-line ferrihydrite synthesised *in vitro.* according to the method provided in section 4.1.2.
Phosphorus doped synthetic two-line ferrihydrite	2LFhPX, P-doped 2LFh 2LFhP0 ≡ 2LFh 2LFhP1 or P1, 2LFhP3 or P3, 2LFhP5 or P5, 2LFhP10 or P10, 2LFhP20 or P20, 2LFhP30 or P30	2LFh coprecipitated *in vitro* in the presence of phosphorus according to the method provided in section 4.1.3. Molar quantities of PO_4 were chosen to achieve a range of P/Fe levels (0.01, 0.03, 0.05, 0.10, 0.20 & 0.30). X is the atomic percent P with respect to Fe. e.g. for P/Fe = 0.20, X = 20 and the sample is denoted 2LFhP20.
Hydrothermally treated (phosphorus doped) two-line ferrihydrite	PXhY (P3h12, P5h5, P5h11)	2LFh coprecipitated *in vitro* in the presence of phosphorus according to the method provided in section 4.1.3 was subject to hydrothermal treatment at 175°C according to the method provided in section 4.1.4. X in the abbreviated sample name is as defined above and in section 4.1.3 and Y is the time in hours the sample was subject to hydrothermal treatment.
Thermally annealed (phosphorus doped) two-line ferrihydrite	PXaY (P5a12)	2LFh coprecipitated *in vitro* in the presence of phosphorus according to the method provided in section 4.1.3 was subject to hydrothermal treatment at 175°C according to the method provided in section 4.1.5. X in the abbreviated sample name is as defined above and in section 4.1.3 and Y is the time in hours the sample was subject to thermal treatment.
Reconstituted (*in vitro*) Ferritin mineral cores	F1125, F2225, F3375, F4500	Horse spleen ferritins were reconstituted *in vitro* from apo-ferritins prepared from commercially bought horse spleen ferritin according to the method provided in section 4.1.6. Iron-to-protein ratios of 4500, 3375, 2225 and 1125 were chosen since these values correspond to cores filled to *maximum, ¾, ½* and *¼* of their nominal capacity for iron.

The methods described below for the preparation of end-member crystalline forms of ferrihydrite are based upon those described in Schwertmann & Cornell, (1993).

Apo-ferritin was prepared from horse spleen ferritin following the method outlined

in Meldrum et al., (1991) (Meldrum, Wade, Nimmo, Heywood, & Mann, 1991).

4.1.1 Preparation of Two-Line Ferrihydrite

Ten grams of $Fe(NO_3)_3 \cdot 9H_2O$ were weighed and dissolved in 250 ml of twice-distilled water and placed on a magnetic stirring plate set for rapid stirring. Approximately 165 ml of 1M $NaOH_{(aq)}$ was added to the solution raising the pH from an initial value of pH 3 - 4 to a final target value of pH 7 - 8. Above pH 5 the base was added dropwise with sufficient time between additions allowed for the solution's pH to re-equilibrate.

Washing of the precipitate was achieved by a combination of centrifugation, exchange of the supernatant with fresh distilled water and re-agitation by vortex to bring the sediment back into suspension. This was repeated five times. After each successive wash the supernatant was observed to become increasingly cloudy indicating a decrease in the electrolytic content of the solution. For storage the samples were freeze-dried, ground using a mortar and pestle and stored as a dry powder at 4 °C to prevent both bacterial growth and the possibility of thermodynamic transformations. This method produces approximately 2.5 grams of 2LFh.

4.1.2 Preparation of Six-Line Ferrihydrite

One litre of twice-distilled water was preheated in an oven to 75 °C and its temperature maintained. Twenty grams of $Fe(NO_3)_3 \cdot 9H_2O$ were added to the preheated water with rapid stirring producing a golden coloured solution. The resulting solution was returned to the oven for approximately 11 minutes – by which time it had become reddish brown in colour – before being rapidly cooled by plunging in an ice bath until the solution's temperature was approximately equal to ambient temperature. The sample was then transferred to dialysis tubing and dialysed against excessive distilled water for four days with the dialysis water being changed twice daily. Following this the sample was freeze-dried, ground using a mortar and pestle and stored as a dry powder at 4 °C to prevent both bacterial growth and the possibility of thermodynamic transformations. This method produces approximately 5 grams of 6LFh.

4.1.3 Coprecipitation of Two-Line Ferrihydrite with Phosphorus

2LFh was coprecipitated in the presence of phosphorous following a protocol based on a modification of the method previously described for *pure* 2LFh. The source of phosphorous was potassium phosphate monobasic (KH_2PO_4, MP Biomedicals Europe) which was added to 1M $NaOH_{(aq)}$ prior to their addition to the ferric nitrate solution. Molar quantities of KH_2PO_4 were chosen to achieve a range of P/Fe levels from 0.01 to 0.30. From this point forward these sample are referred to as 2LFhPX, where X represents the atomic percent P with respect to Fe. For example, a sample with P/Fe = 0.10 will be denoted 2LFhP10 (or simply P10 for brevity).

Washing and storage of the products were carried out as per the method used for *pure* 2LFh (section 4.1.1).

4.1.4 Hydrothermal Treatment of Phosphorous-Doped Two-Line Ferrihydrite

Phosphorous-doped two-line ferrihydrite (P-doped 2LFh) was synthesised and the product washed according to the protocol for 2LFh as outlined in section 4.1.1. Freeze-drying of the product was omitted, with the precipitate being kept as an aqueous suspension prior to ageing.

Fresh suspensions of P-doped 2LFh were taken and hydrothermally aged according to the protocol described in the literature for the hydrothermal treatment of 2LFh in the presence of citrate (Michel, Barrón, Torrent, Morales, Serna, Boily, & Liu, 2010). A polytetrafluoroethylene (PTFE) lined high-pressure reaction vessel (Parr Instruments Co., Model 4748) was filled with freshly prepared P-doped 2LFh suspensions and placed in an oven, which had been previously preheated to 175 °C, for times ranging between 0 to 14 hours. Once the ageing time had elapsed the reaction vessel was removed from the oven and allowed to cool naturally to ambient laboratory temperature which typically took several hours. The solution was then freeze-dried, ground to a fine powder and stored at 4 °C prior to further analysis. Samples prepared in this manner are subsequently referred to as PXhY where X represents the target atomic P level with respect to Fe and Y the time in hours the samples spent at 175 °C.

It should be noted here that although Y represents the time the samples spent in the oven at 175 °C this is not the total time they were subject to temperatures elevated

above ambient. The large thermal mass of the reaction vessel (3750 g of stainless steel) dictates that the heating up and cooling down periods necessarily add some degree of ambiguity when defining a time spent at a given temperature.

4.1.5 Thermal Annealing of Phosphorus-Doped Two-Line Ferrihydrite

Phosphorus-doped 2LFh was prepared and dried according to the method outlined in section 4.1.1. For heat treatment in air, approximately 1 gram of the dry powder was placed on a clean alumina plate and placed in an oven which had been preheated to 175°C. Treatment time ranged from 0 to 14 hours after which time the samples were removed and allowed to cool to ambient laboratory temperatures before being stored at 4°C prior to further analysis. Samples produced in this manner are subsequently referred to as PXaY; where X represents the target atomic P level with respect to Fe and Y the time in hours the samples spent in the oven at 175 °C.

In another experiment, a small amount of each of the P-doped 2LFh samples were heat treated in air for XRD analysis, the results of which are presented in chapter 7. Each was placed on an alumina plate and heated in a furnace to 700˚C where it was held for one hour before being removed and allowed to cool to ambient temperatures.

2LFhP3 was also subject to heat treatment in air, however, this was performed *in situ*, combined with XRD analysis and so the method can be found in section 7.6.

4.1.6 *In vitro* Reconstitution of Horse Spleen Ferritin Mineral Cores

Horse spleen holo-ferritins were reconstituted *in vitro* from apo-ferritins prepared from commercially bought horse spleen ferritin (HoSF) (Sigma-Aldrich, UK). The native mineral cores were removed using the procedure outlined below. Once obtained, the cores of the apo-HoSF were reconstituted with ferrihydrite *in vitro* with controlled amounts of iron available for uptake so as to obtain a series of ivHoSF samples each with a different iron-to-protein ratio. Four ivHoSF samples were prepared with iron-to-protein ratios of 4500, 3375, 2225 and 1125. These values correspond to HoSF cores filled to *maximum, ¾, ½* and *¼* of their nominal capacity for iron. (4500 iron atoms is usually taken to be the ferritin molecule's capacity for Fe(III) atoms Treffry and Harrison (1978)). From here on the ivHoSF samples are referred to as F4500, F3375, F2225 and F1125 thus denoting the target

iron level used for each reconstitution.

All work was carried out at room temperature (23°C) and following reconstitution the ivHoSF solutions were stored at 4°C prior to analysis. Special thanks are given to Professor Fiona Meldrum who was kind enough to provide practical assistance with initial attempts at reconstitution.

Preparation of Apo-Ferritin

Apo-ferritin was prepared from horse spleen ferritin (Sigma-Aldrich U.K. Type 1 Equine Spleen, Cd ≤ 1% of ferritin, CAS: 9007-73-2) following the method outlined in Meldrum et al., (1991).

A 20 ml aqueous solution containing 50 mg of HoSF was prepared and dialysed, with constant stirring and nitrogen bubbling, against three portions of a 0.6 % w/v solution of thioglycollic acid in a 0.1 M buffer solution of sodium acetate which had been pH adjusted to 4.5 by the addition of sodium hydroxide. Two hours were allowed to elapse between successive changes of dialysate and during this time the ferritin solution was observed to change from reddish to clear and colourless, indicating the reduction and removal of the ferric iron core to leave only the iron-free apo-ferritin in solution. Next, the (apo)ferritin solutions were washed by dialysis against four portions of 0.15M saline solution, with constant stirring and nitrogen bubbling, over a period of twenty-four hours. Finally, the ferritin solutions were dialysed for three hours against a preservative solution of 0.15M saline and 0.015M sodium azide, in order to prevent unwanted bacterial growth, prior to storage in solution at 4 °C.

The residual iron content present in the apo-ferritin solution was determined using atomic absorption spectroscopy (AAS). Calibration of the equipment was carried out using solutions of known iron concentration (1, 5 and 10 ppm). With this method, the residual iron content was determined to be no more than 0.1 ppm (which is close to the detection limits of iron by AAS), or in other words equivalent to approximately one iron atom per apo-ferritin molecule.

The protein concentration of the apo-ferritin solution was determined via UV-Vis spectroscopy by measuring the absorbance at 280 nm for which $A_{280n}{}^{1\%,\ 1cm} = 9.6$ (May & Fish, 1978). Assuming a molecular mass for apo-ferritin of 443 kDa (Richter & Walker, 1967) the protein concentration was found to be 2.2 x 10^{-9} mol

ml^{-1} of apo-ferritin.

Reconstitution of Apo-Ferritin

For reconstitution of HoSF cores from apo-HoSF the following reagents were prepared. All water used here was of ultra pure (MILLI-Q) grade and had been de-aerated by constantly bubbling nitrogen through it over a period greater than twelve hours (i.e. overnight). A 0.021 M stock solution of ferrous ammonium sulphate (Sigma-Aldrich) was used as the soluble source of iron. Reconstitution was carried out in a 0.1 M MOPS (4-Morpholine-propanesulfonic acid) buffer solution (Sigma-Aldrich, UK) which was adjusted to pH 6.5 by the addition of sodium hydroxide.

For the preparation of ivHoSF samples, 1 ml of apo-ferritin solution was taken and diluted up to 2.3 ml by the addition of the 0.1M MOPS buffer solution. An appropriate volume of ferrous ammonium sulphate solution was added to achieve the desired iron-to-protein ratio: i.e. 0.47 ml for 4500 iron atoms per protein. Following this the solution was gently mixed by slight agitation before being set aside for a period of several hours in order that the uptake and sequestration of iron may take place. Following preparation, the samples were transferred to a refrigerator (4°C) for storage prior to analysis.

4.2 Characterisation Methods and Experimental Parameters

The following section provides a brief overview of the methods used for sample characterisation during this study.

4.2.1 Diffraction Based Techniques

Diffraction is a wavelike phenomenon that occurs on all length scales. It is most pronounced when the wavelength of the incident wave is comparable to the dimensions of the repeating structure of the diffracting object. In the case of a crystalline solid the regular spatial-repeat of the columbic atomic potential provides both the geometry and perturbation necessary for diffraction to occur. A collimated beam of monochromatic radiation incident on such a structure will scatter such that it becomes spread over a wide angular range. At a given distance from the diffracting object the interference between waves scattered from various points within the object result in an intensity distribution dependent on the angle with respect to the incident beam. For certain angles, constructive interference between

diffracted waves gives rise to intensity maxima known as Bragg 'reflections'. These reflections occur at angular positions determined by the wavelength, λ, of the incident wave and the lattice plane spacing, *d*. It is by the analysis of these peaks, in terms of their angular position, intensity, breadth and asymmetry, that the spatial arrangement of the atoms in a crystalline solid may be deduced. This is the concern of crystallography (Cullity, 1956). The Bragg condition for diffraction is given by:

$$2dsin\theta = n\lambda$$

where *d* and λ are defined above, *n* is an integer and θ is the angle between the incident beam and the diffracting planes.

In this study diffraction (polycrystalline/powder) has been carried out using three different experimental probes: the X-ray, the neutron and the electron. Electron diffraction will be addressed in the dedicated TEM section of this chapter. The specifics of the related techniques of X-ray and neutron diffraction are given below.

Powder X-Ray Diffraction

In interacting with matter X-rays are scattered by the charge distribution associated with atomic electrons. The scattering power or *atomic factor* for X-rays is observed to vary monotonically in proportion to the *Z*-number of the scattering atom or ion (Shmueli, 2007). For this study, two different forms of X-ray scattering were explored for which the methods are described separately below.

Powder X-ray diffraction (XRD) is a widely used laboratory technique which provides a quick, easy and powerful means of probing the atomic structure of crystalline materials. It can be used in the determination of crystal structures, but is now more commonly used for the identification of crystal phases and finds application in a wide variety of disciplines from materials science to protein biology.

As used here powder XRD provides a method for validating the phase purity of samples by comparison with patterns already reported in the literature. The nanocrystalline and defective nature of the ferrihydrite samples results in an excessive broadening of the Bragg reflections preventing the identification of isolated Bragg peaks and the possibility of meaningful structural refinement.

Powder XRD data was acquired using a PANalytical X'Pert Bragg-Brentano (θ - 2θ) diffractometer equipped with a PW3373 Cu-*K*α source (1.54 Å) operating at 40 kV and 30 mA. Diffractograms were acquired over an angular range of 5 - 70° (2θ) with

a scan speed of 0.0016 °/s resulting total acquisition times of just over 11 hours. Approximately 1 gram of dry powder was ground in a mortar and pestle prior to mounting. A rotating stage with a rotation period of 4 seconds was used to reduce preferred orientation effects. XRD data was collected with a 2θ resolution of 0.01° which is far beyond the resolution required for the analysis presented in subsequent sections.

In situ Heating and Combined Powder X-Ray Diffraction

In situ heating and combined XRD analysis of 2LFhP3 was performed in air between 25-1000 °C using a HTK-1200 heating stage (Anton Paar), the results of which are presented in section 7.6. Diffractograms were collected over 10 to 110° 2θ in increments of 0.05° 2θ. First, a diffractogram was collected at room temperature (~ 25°C), following which the stage was heated to 100 °C and a diffractogram acquired. Subsequent diffractograms were then collected in 50 °C steps up to and including 1000 °C. Finally, the sample was allowed to cool to room temperature before the final scan was made. Temperature calibration of the heating stage has been carried out by Roger Molinder (Ph.D. student Leeds UK) using materials for which phase-transition temperatures are well known (KNO_3 130 °C, KSO_4 583 °C and $BaCO_3$ 810 °C).

No post-acquisition reduction of the data has been performed other than the manual removal of the occasional counting-spikes by setting channel intensities equal to the average of the two immediately adjacent ones.

Total X-ray Scattering & Pair Distribution Function Analysis

In general there are two components to the diffracted signal intensity – the Bragg reflections and the diffuse background. The sharp Bragg peaks are reciprocally related to extended regions of order in real-space. Whereas the slowly varying diffuse signal is due to order occurring on much shorter scales. Traditional crystallography, such as XRD, is concerned only with the coherent Bragg like intensities which it extracts from the total signal by discarding the background. As such, information pertaining to short range structure is lost. On the other hand, so called total-scattering methods use the entire diffracted signal for analysis.

The atomic pair distribution function (PDF) describes 3D atomic structure in terms of the radial distance between pairs of atoms. It may be experimentally determined only from data for which Qmax (i.e. momentum transfer) is sufficiently high (~30

Å^{-1}). Such data is obtainable in synchrotron X-ray beam lines and neutron source facilities (Billinge & Kanatzidis, 2004; Billinge, 2008; Egami & Billinge, 2003)

In obtaining the PDF the 2D total scattering signal is first corrected accounting for instrument and sample effects. The PDF is then arrived at by calculating the Fourier transform of the corrected data. Once obtained the PDF may be used in the refinement of structural models.

The total X-ray scattering data presented here was very kindly collected by Dr. M. Michel who is also responsible for the post-acquisition reduction of the data to obtain the PDFs following the protocol used in (Michel et al., 2007). The procedure involved in refining the crystallographic parameters specific to the Drits (1993) and Michel models, which was also investigated using PDFgui by myself (Drits, Sakharov, Salyn, & Manceau, 1993). This has been used to benchmark this work against the current literature.

High-energy X-ray total scattering data was collected at 11-ID-B beamline (S4) at the Advanced Photon Source, Argonne National Laboratory. Total scattering data for PDF analysis were collected with a beam energy close to 90 keV (λ = 0.13702 Å) with a sample-to-detector distance of ~21 cm. The radiation scattered by the sample and calibrant (cerium) was collected with a Perkin-Elmer amorphous-Si area detector. Conversion of data from 2D to 1D was done using the program Fit2D (Hammersley, 1997). A polarisation correction was applied during integration of the data. The experimental total scattering structure function S(Q), reduced experimental structure function f(Q), and PDF, or G(r), were obtained using PDFgetX2 (Qiu, Thompson, & Billinge, 2004) and standard corrections were applied (Chupas, Qiu, Hanson, Lee, Grey & Billinge, 2003). The true background intensity of an empty sample holder was measured and subtracted from each sample. PDFs were calculated from the Fourier transform of the reduced structure function truncated at 30 +/- 1 Å^{-1}.

Neutron Diffraction

Neutron diffraction is a complementary technique to X-ray diffraction and provides unique information in its own right. Unlike X-rays, which scatter due to interactions with atomically bound electrons, neutrons are scattered from atomic nuclei. This results in a scattering power which varies irregularly with atomic number (and mass number, i.e. isotopes) – unlike X-rays and electrons which vary smoothly with

atomic number. This means that in certain cases neutrons are able to easily distinguish between species of similar atomic number: for example, important elements such as H, N, O, F, C. Additionally, unlike X-rays, neutron scattering factors do not fall off with increasing (2θ) and are therefore more reliable for higher angle peaks. Neutrons have an intrinsic magnetic moment (unlike X-ray and electrons) and therefore are sensitive to the magnetic lattice arrangement of magnetic materials. The penetration depth of neutrons is much greater than that of either X-rays or electrons and therefore they are less susceptible to absorption and surface effects. Neutrons do have their own drawbacks, however, and therefore are complementary to other scattering techniques.

Neutron diffraction data was collected using the General Materials (GEM) diffractometer located at Target Station 1 on the ISIS beamline at the Harwell Science and Innovation Campus, Oxfordshire, UK. The GEM time-of-flight (TOF) instrument has a highly stable detector array with six large solid angle detectors covering an angular range of 1.1-169.3˚. The maximum measurable momentum transfer of 55 $Å^{-1}$ gives GEM high spatial resolutions approaching 0.1 Å.

Beamtime was granted via the Gem Express measure-by-courier service. Reduction of the raw total scattering data was carried out following the guidelines provided by ISIS.

Electron Diffraction

Selected area electron diffraction (SAED) patterns were obtained using a Philips CM200 TEM using an aperture of approximate diameter 180 nm and a camera length of 30 mm. Patterns were recorded on photographic plates and digitised for subsequent persistence and analysis. Lattice spacings, d, were deduced from the radial location R of spots/rings within recorded patterns using

$$Rd = L\lambda$$

where $L\lambda$ = 23.1Åmm and is a calibrated constant. A script routine was also developed which produced radially averaged diffraction patterns for the analysis of extremely spotty patterns.

4.2.2 Vibrational Spectroscopy

Infrared absorption and Raman scattering are related structural-chemical techniques

which measure transitions primarily between the vibrational energy levels associated with chemical bonds. Bonds vibrate by stretching, contracting and bending about their equilibrium position. The precise energy associated with a given vibrational mode depends on the bond strength and atomic masses involved. The differences between the techniques lie in the nature of the resulting molecular transition. Because they are subject to different selection rules, often an infrared active transition is Raman inactive (and *vice versa*). Both give information on the structural and chemical make-up of a sample, however, since strong bands in the IR spectrum of a material often correspond to weak bands in the Raman, the two make for complementary analysis tools.

Fourier-Transform Infrared Spectroscopy

The selection rule for infrared absorption dictates that allowed transitions are those which are accompanied by a change in the electric dipole moment of the molecule (Barbara, 2004). The majority of molecules exhibit bands in the mid-infrared (4000 - 400 cm^{-1}), and as a general rule the region < 1800 cm^{-1} will be the most populated. In the case of iso-structural molecules, the precise energy associated with a particular vibrational mode depends on the bond strength and atomic masses involved.

FTIR spectra were obtained using a Thermo Scientific Nicolet iS10 FTIR spectrometer, fitted with an attenuated total reflectance (ATR) accessory. This setup provides superior data quality along with increased repeatability compared to traditional transmission methods. The ATR accessory was a Thermo Smart iTR Diamond designed to overcome specific difficulties encountered by traditional methods when measuring transmission data of opaque materials. For analysis the sample is pressed hard against a diamond stage to ensure close contact. Infrared radiation approaches the sample from within the crystal only to suffer totally internal reflection at the crystal sample interface by virtue of the large decrease of refractive index that travelling outside this boundary would otherwise imply. With this arrangement, the interaction between the radiation and sample is possible via its evanescent wave which rapidly decays to zero within 0.5 to 5 μm distance from the stage.

All spectra were recorded as the sum total of thirty-six scans, between 4000 – 600 cm^{-1}, at a resolution of 4 cm^{-1}.

Raman Scattering Spectroscopy

Raman scattering is the name given to the inelastic scattering of light upon interacting with the normal vibrational modes of molecular and crystal structures. The probability of this interaction is vanishingly small, accounting for around one in ten million of the scattering events attributed to its elastic counterpart, Rayleigh scattering. It is the change, or *shift*, in the energy of the scattered photons, compared to the incident radiation that give rise to the Raman signal. The selection rule for Raman scattering dictates that allowed transitions are those with are accompanied by a change in the polarisability of the electron cloud about the molecule (Smith & Dent, 2004).

In this study, Raman spectra were acquired using a dedicated Renishaw® inVIva Raman microscope equipped with a 514 nm, 25mW laser. Calibration of the measured shift was achieved using the 520 cm^{-1} line of an internal silicon standard.

For observation, a small amount of dry powder was placed on a standard glass microscope slide (76 x 26 x 1 mm) and placed on the microscope's stage. A suitably flat area of the sample was selected and brought to approximate focus using one of the low magnification objective lenses. A 50x objective lens was used for final optimum focusing by adjusting the height of the sample stage to minimize the diameter of the laser spot.

In a preliminary experiment, it was determined that a laser power of 1.25 mW (~3.5 x 10^3 W/cm^2) was required to avoid thermally driven phase transitions observed at higher laser powers. Using this value all spectra were collected using six accumulations each of thirty seconds duration. All spectra are presented as acquired.

4.2.3 X-Ray Photoelectron Spectroscopy

In X-ray photoelectron spectroscopy (XPS) the binding energies of core-shell electrons within a sample are determined. By illuminating the sample's surface with an intense beam of monochromatic X-rays the emission of photoelectrons is stimulated. These electrons, having been excited from atomically bound core-shell orbitals, exit the sample's surface where they are detected and analysed according to their kinetic energy.

Photoemission process involving a valence electron initially at or close to the Fermi energy E_f may be described by:

$$E_{k,max} = h\nu - \Phi$$

where $E_{k,max}$ is the is the maximum photoelectron energy for a given material of work function Φ (and X-ray source energy), h is Planck's constant and ν is the frequency of the illuminating radiation. In the case photoelectrons of core-shell origin the effective binding energy of the initial state must be taken into account.

$$E_B = h\nu - E_k - \Phi$$

where E_B is the binding energy and E_k is the kinetic energy of the photoelectron.

From the above equations, the binding energy of the core-shell state from which the photoelectron originated is thereby inferred from the difference between the energy of the incident illumination and the kinetic energy with which it exited the sample. The binding energy of core-shell states are sufficiently distinct to permit elemental identification and consequently XPS is used for quantitative compositional analysis. The environment immediately surrounding an atom affects the binding energies of its electrons and it is by these 'chemical shifts' that the detection of the presence of particular molecular species is achieved. However, it is the initial state which predominates in determining the measured binding energy with final state effects being minimal. Therefore the resulting spectrum is not as information-rich as EELS or X-ray absorption spectroscopy for example (Watts & Wolstenholme, 2003).

The mean free path of the photoelectron is of the order of a few nanometres, therefore, in most cases XPS is considered a surface-sensitive technique, however, applied to ferrihydrite crystallites of approximately 5 nm in diameter, the technique can be considered to be probing the entirety of the sample, i.e. the surface and bulk of the material.

During the course of this study X-ray photoelectron spectroscopic (XPS) data was acquired using two different dedicated spectrometers.

Time was successfully applied for at the National Centre for Electron Spectroscopy and Surface Analysis (NCESS) located at the Daresbury Laboratories (UK), via the "NCESS call for proposals". Housed at this facility is a VG Scienta ESCA300 photoelectron spectrometer, equipped with a high intensity monochromated aluminium X-ray source (Al-$K\alpha$ λ = 8.338(6) Å (1486.7 eV)) with an energy width of 0.26 eV, allowing for the rapid acquisition of high quality spectroscopic data, in

terms of both spectral resolution and signal-to-noise statistics. The detector system is a hemispherical analyser combined with a multi-channel detector which gives the entire system an overall energy resolution of 0.30 eV.

The second XPS system used was a VG Scienta Escalab 250 housed in the Physics department of the University of Leeds (UK). This instrument is also equipped with a monochromated Al-$K\alpha$ source.

For both systems, samples were prepared for analysis from dried powders by pressing a holder stub, which had a piece of double sided carbon impregnated sticky tape on it, into the powder. A smooth analysis surface was made by scraping the surface with a clean razor blade to remove excess material. Energy calibration was done by setting the 1*s* peak of (adventitious) carbon to 284.5 eV (Wagner, Riggs, Davis, Moulder, & Muilenberg, 1979). In addition to low energy resolution survey spectra (0 - 1300 eV), high- resolution spectra were acquired specific to the C 1*s*, Fe 2*p*, O 1*s* and P 2*p* energy- levels. In order to compensate for charging of the sample, which occurs as photoelectrons are lost from the sample's surface, an electron flood gun was used to uniformly illuminate the sample and was set such that the measured O 1*s* signal was maximised.

All data was processed using the CasaXPS™ software. In CasaXPS three mathematical profiles are available to the user to model the background contribution to the measured signals, these are; a simple linear, Shirley and Tougarrd profiles. Fitting regions are set over a given binding energy range and resonant peaks extracted from the background by choosing one of the model functions. Displayed in Figure 4.1 is a comparison of the Shirley and Tougarrd background functions as applied to the O 1*s* signal as measured from six-line ferrihydrite using the VG Scienta ESCA300 spectrometer at the NCESS facility.

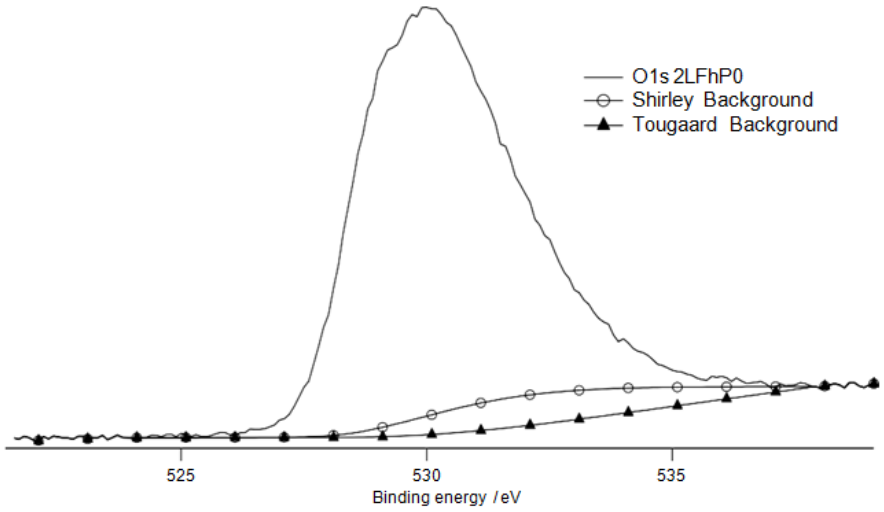

Figure 4.1 X-ray photoelectron spectrum of the oxygen 1s peaks comparing Shirley and Tougarrd background model functions as described in section 4.2.3. Measurement made using the VG Scienta Escalab 250 spectrometer at the University of Leeds (UK)

Analysis of the O 1*s* XPS peaks was carried out as follows. Energy calibration of the binding energy scale was set relative to the C 1*s* peak (284.5 eV) and the measured signal was extracted from the underlying background by means of a Shirley-type background fitted over the binding energy range 524 to 538 eV. The envelope of the O 1*s* peak was then subsequently modelled by fitting a number of synthetic peaks using the Marquardt least-squares method. In order to account for the combined effect of instrumental (Gaussian) and lifetime broadening (Lorentzian) on the measured spectrum, a Voigt profile (product of Gaussian with a Lorentzian) with a 30% Gaussian-like component was chosen as the mathematical function for the fitting peaks. During fitting, the areas and centroid positions of the peaks were allowed to vary freely and independently, whereas the full-width-half-maxima of the peaks, whilst being allowed to vary freely, were coupled such that they were equal for all fitted peaks for a given specimen.

The same peak fitting analysis, as described above for the O 1*s* signal, was performed on the P 2*p* signal with the background being fitted over the binding-energy range 129 to 136 eV. The Fe 2*p* peaks, being less simple to interpret, were simply compared to those from literature over the binding energy range 710-750 eV.

Elemental quantification was performed by first calibrating the binding-energy scale, as outlined above before extracting the element specific signals from the underlying background using one of two profiles to model the background contribution; i.e. those of Shirley and Tougarrd. Ratios of elemental concentrations

were then calculated using the measured element specific signal intensities and comparing those with interaction cross-sections which reside in CasaXPS' internal library.

Quantitative elemental analysis of XPS spectra is a multistep approach which involves the extraction of inner shell photoelectron signals and the determination of appropriate photoelectron cross-sections or Scofield factors (van der Heide, 2011). Quantitative accuracy depends on several parameters such as the accuracy of relative sensitivity factors, corrections for electron transmission function, surface-to-volume homogeneity, estimates of the energy dependence of the electron mean free path and signal-to-noise ratio. Additionally the topology of the specimen surface can lead to bias due to photoelectron absorption. Typically errors in compositional estimates are considered to be of the order 5-10%. Data presented here has been derived using the peak positions and Scofield factors contained within the standard CasaXPS library (Fairley, 2001).

4.2.4 Thermal Analysis

Thermal analytical methods involve monitoring the physical properties (or changes in) of a sample in response to being heated in a given atmosphere, according to a controlled heating regime (Brown, 1988; Speyer, 1994). Atmospheres can be chosen to be inert (vacuum, nitrogen, helium, argon) or reactive (air, oxygen, hydrogen) depending on the specific experimental requirements at hand (Rowland & Lewis, 1951).

Thermogravimetric analysis (TGA) involves monitoring the mass of a sample as a function of temperature, whilst it is subject to a controlled heating protocol (Speyer, 1994). With variable atmospheres, the sample can be protected from oxidation or made to react. Typical applications include observing decomposition, absorption, adsorption, desorption and dehydration as well as chemical reactions such as oxidation and reduction (Speyer, 1994).

Differential scanning calorimetry (DSC) is used in the study of phase transitions and chemical reactions in terms of heat flow to and from a material. In the power-compensated DSC each crucible has its own dedicated temperature sensor and heater. The temperature difference between the sample and reference material is maintained close to zero by varying the power to each of the heaters. DSC is

commonly used for studying heat capacities, phase changes, chemical reactions and crystallisation (Kaufmann, 2003; Tanaka, 1992).

Thermal analysis was performed using a Mettler-Toledo TGA/DSC 1 Star system in which both TGA and DSC measurements were executed simultaneously. The scan program was set to increase from ambient to 700 °C at a fixed heating rate of 0.17 °C s^{-1}. Measurements were conducted in atmospheres of both air and helium. Thermal analysis data presented here typically measures mass with an accuracy of accuracy to ± 0.1% and temperature to within ± 1°C.

4.2.5 Magnetic Analysis

The vibrating sample magnetometer, or VSM, is an instrument that measures the magnetic moment *m* of a sample as a function applied magnetic field strength *H* and temperature *T* (Cullity & Graham, 2011). The technique is described in further detail by Foner (1959) who is widely considered responsible for its development (Foner, 1959, 1967).

Determination of the magnetic moment *m* involves vibrating a sample sinusoidally along a direction perpendicular to an externally applied field, *H*. If the sample is magnetised then this oscillatory motion will result in a varying flux which is then measured as an induced electromotive force within a set of inductive pick-up coils located in close proximity to the sample. Given that *m* is the net moment for the whole of the sample it is common to define the specific moment per unit mass, *M*.

The magnetic measurements reported here were made using an Oxford Instruments 3001 vibrating sample magnetometer (VSM) which is the property of the Condensed Matter Physics group at the University of Leeds (UK). This instrument is capable of producing applied fields between ± 5 T and operating with temperatures ranging from 4 - 300 K. The VSM was used in this study to acquire *magnetisation curves* (M *vs*. H) and temperature dependence (M *vs.* T) measurements. All samples were fine grained dry powders of which approximately 100 mg was used for the analysis of each.

M *vs.* H data was recorded at a fixed temperature of 5 K for applied field values between ± 5 T with a fixed rate of 0.033 T s^{-1}. The scan pattern was a 5-quadrant loop in which applied fields were scanned as follows:

$$0\ T \rightarrow +5\ T \rightarrow 0\ T \rightarrow -5\ T \rightarrow 0\ T \rightarrow +5\ T.$$

M *vs.* T measurements were recorded with the applied field strength fixed at 5mT over the temperature range 5 – 250 K. Demagnetization of the sample was accomplished by a series of alternating field strengths, each 180˚ out of phase and each successively lower in magnitude.

4.2.6 Electron Energy Loss Spectroscopy

Bulk energy loss spectra were acquired using a Philips CM200 TEM in diffraction mode (image coupled) using an approximately 0.18 mm diameter selected area aperture. The EELS collection and convergence semi-angles were defined as 6 mrad and approximately 1 mrad, respectively. A thin area was examined for each sample with the relative sample thickness being estimated from the low-loss spectrum. In each case all were less than 0.3 inelastic mean free path lengths. EELS spectra were acquired with an energy dispersion of 0.1 eV/channel and an energy resolution of 0.8 eV as estimated from the width of the zero-loss peak. The probe current was estimated using an FEI calibration curve based on the measured brightness (i.e. exposure time) incident on the fluorescent viewing screen of the TEM. The value derived from the FEI curve had been independently verified by (indirectly) measuring the current incident on the drift tube of the GIF when exposed to the image coupled beam and with the spectrometer magnet switched off (Pan, 2006).

Core-loss EELS spectra were extracted from the underlying background using a power-law function fitted over 20 eV prior to the edge onset. The effects of plural scattering were removed using the Fourier-ratio deconvolution technique using the low-loss profile.

Quantitative elemental analysis of EELS spectra is a multistep approach which requires the extraction of elemental inner shell signals and the determination of appropriate cross-sections for these interactions (Williams & Carter, 1996). Extraction of the signal intensity involves separating signals from the background which is done here by extrapolating a power-law background fitting over 20 eV prior to the edge onset. The effects of plural scattering in the measured signal are accounted for by Fourier deconvolution using the low-loss spectrum as reference. Hydrogenic cross-sections are used to model interaction cross-sections. Each of these steps may introduce bias in measured elemental concentrations and therefore quantitative elemental EELS results presented here, although-self consistent, may differ from actual compositions. It is commonly accepted that the magnitude of

these discrepancies may be as large as 5-10% depending on the elements under consideration.

Analysis of the Fe-*L* edge ELNES was performed using two different methods. The first, which provides an estimate of the ratio $Fe^{3+}/\Sigma Fe$, was the white-line intensity ratio method (van Aken, Liebscher & Styrsa, 1998). A DigitalMicrograph script was developed for this method and is provided in Appendix C. The second method, which, in addition to estimating iron's oxidation state, also provides an estimate of iron's coordination (octahedral *vs.* tetrahedral). This method was first proposed in the EELS literature by Garvie and Buseck (1998) and uses linear least squares fitting to estimate an experimentally acquired spectrum in terms of a linear combination of the spectra of several well characterised reference standards. The reference minerals, originally measured in the thesis of Pan (2006) are: hematite $^{[6]}Fe^{3+}$; hedenbergite $^{[6]}Fe^{2+}$; Fe-orthoclase $^{[4]}Fe^{3+}$ and hercynite $^{[4]}Fe^{2+}$. A fuller description of these reference minerals along with information regarding their origins and a more in depth description of the fitting routine can be found in the thesis of Pan (Pan, 2006) and in subsequent publications of her work (Pan, 2006; Pan, Vaughan, Brydson, Bleloch, Gass, Sader, & Brown, 2010). Fitting of experimental Fe-*L* edges was performed using IGOR Pro™ data analysis software, the fitting engine of which is based upon the Levenberg-Marquardt method of least-squares fitting (Wavemetrics, 2007). Errors quoted within this document for linear-least squares fitting of Fe-*L* edge data have been derived from the estimated errors associated with each of the free fitting parameters as provided by the Igor Pro software. Typically these errors are a few tens of percent and are thought to be rather pessimistic estimates and that in fact actual errors may indeed be less.

Smart EELS Acquisition

One of the chief aims of this project is to investigate low fluence methods of EEL spectrum acquisition. To this aim a novel method of EELS acquisition, dubbed "Smart Acquisition" (SA), was developed in collaboration with the team at the SuperSTEM facility in Daresbury (UK). The method is described in detail elsewhere (Sader, Schaffer, Vaughan, Brydson, Brown & Bleloch, 2010) as such only a brief description will be given here. Computer code for implementing Smart Acquisition EELS specifically geared towards nanoparticulate systems is provided in Appendix A. Briefly SA uses the fine probe of STEM to integrate EEL signals from

spatially extended regions of a sample. It allows the independent control of probe scanning procedures and the simultaneous acquisition of EELS signals. The original motivation for this work arose from the need to control the electron dose experienced by beam-sensitive specimens whilst maintaining a sufficiently high signal-to-noise ratio in the EEL signal for the extraction of useful analytical information (such as energy loss near edge spectral features) from relatively undamaged areas. Obtaining a sufficient SNR in EELS to detect and analyse the core-ionisation edges usually requires many orders of magnitude greater electron fluence than imaging (because only a fraction of the incident electrons produce core-ionisation events). Consequently specimen damage is the major limitation when under-taking EELS of beam-sensitive materials.

In traditional STEM EELS data is usually collected either from a single position using a stationary beam or from a series of equally spaced points across a sample. In the first case a single spectrum is generated and in the second case multiple spatially resolved spectra are acquired in what is known as a spectrum image. In each case the beam dwell time must be sufficiently long for adequate signal statistics to be collected. In the case of core-loss EELS features seconds to tens of seconds are typical. In the case of SA, dwell times are limited only by the scanning hardware which currently permits dwell times of a few milliseconds.

The practical execution of SA is a multistep process which in the simplest terms is as follows. Using a reduced beam dwell time the sample is searched and a target area is found. A preview HAADF image of the area is acquired with sufficient signal to noise statistics to permit subsequent image processing. The beam is then blanked to avoid further illumination of the specimen. The area from which the EELS signal is to be collected is then defined using appropriate image processing and masking functions and the scan coordinates are generated. The beam is then unblanked, a preview scan is acquired and any sample drift which may have occurred is corrected. Finally, the SA-EELS data is acquired using an appropriate dwell time per mask pixel.

4.2.7 Energy-Dispersive X-ray Analysis

When the high energy electron beam of TEM is incident upon a specimen, an inner shell electron may be ejected thus creating an electron hole. The resulting electron vacancies are then filled by electrons from a higher energy level, and an X-ray is

emitted with energy equal to the difference of the two states. These energies are characteristic of the element from which it was emitted, and therefore may be used for compositional analysis. In EDX analysis the relative intensity of X-ray emitted is measured as a function of their energy. The EDX spectrometer used in this study was an Oxford Instruments UTW ISIS system mounted on the column of the Philips CM200 housed at the University of Leeds (UK).

Quantitative elemental analysis of EDX spectra performed here relies on the Cliff-Lorimer relation which relates measured signal intensities to values of relative atomic concentrations via so called *k*-factors (Garratt-Reed & Bell, 2003; Cliff & Lorimer, 1975; Lorimer, 1987). The Cliff-Lorimer *k*-factors are not constant but depend on the accelerating voltage of the TEM, the detector efficiency amongst other parameters. Additional factors affecting the accuracy of elemental quantification by EDX include the method used for background (*bremsstrahlung*) removal, specimen topology, X-ray absorption within the specimen and florescence. The accuracy of EDX elemental analysis can be improved if *k*-factors are determined experimentally by measuring spectra from standard reference samples for which precise composition is known. This has not been done here and therefore EDX compositional estimates are expected to have associated errors of 10-15% (relative atomic) in the worst case.

4.2.8 (S)TEM Micrograph Simulations

Image simulations of both BF-TEM and HAADF micrographs were performed using Christoph Koch's Quantitative TEM/STEM simulation (QSTEM) software (Koch, 2002). This software uses the multislice method as described in Kirkland (2009). For BF-TEM image simulation parameters were chosen to best replicate imaging in the Philips CM200 TEM and for HAADF STEM image simulation parameters were chosen to simulate imaging using the Nion UltraSTEM. Table 4.2 summarises the simulation parameters used in each case. Where simulations are presented (Figure 7.24 & Figure 7.28) the crystal structure, relative sample orientation and thickness are given.

Table 4.2 Summary of (S)TEM image simulation parameters used in multislice image calculations.

Parameter	**Philips CM200**	**Nion UltraSTEM**
Electron Energy (kV)	200	100
Defocus (nm)	-86.7 (Scherzer)	0.0
Astigmatism (nm)	0.0	0.0
Spherical Aberration, C_3 (mm)	2.0	0.0
Chromatic Aberration, C_c (mm)	1.0	1.0
Convergence Angle (mrads)	15	25
Beam Tilt, (deg.)	0	0
Thermal Diffuse Runs	30	30
Temperature (K)	300	300

Chapter 5 Characterisation of Two-Line and Six-Line Ferrihydrite

Synthetic samples of both two- and six-line ferrihydrite were prepared by the methods described in sections 4.1.1 & 4.2.1 respectively. X-ray powder diffraction (XRD) data for the respective products confirms success in each case. FTIR and Raman spectroscopy data acquired here is discussed with reference to the literature. Analytical electron microscopy, in particular BF-imaging, SAED, EELS, EDX, is used to assess the beam damage susceptibility of 2LFh. TEM and AC-STEM images along with EELS, EDX data and SAED patterns are acquired under low fluence conditions and presented. Smart acquisition EELS is applied to the surface and bulk of individual 6LFh crystals and comparison made. Table 5.1 provides an overview of the samples examined in the current chapter.

Table 5.1 Details of samples examined in Chapter 5.

Sample Full Name	**Abbreviated Name(s)**	**Sample Description**
Synthetic two-line ferrihydrite	2LFh	Two-line ferrihydrite synthesised *in vitro* according to the method provided in section 4.1.1.
Synthetic six-line ferrihydrite	6LFh	Six-line ferrihydrite synthesised *in vitro* according to the method provided in section 4.1.2.

5.1 X-Ray Powder Diffraction

XRD data from synthetic 2LFh and 6LFh is displayed in Figure 5.1. For both samples there is excellent agreement between the data acquired here and the previous work of others, confirming both the success of synthesis and the purity (phase) of the samples (Eggleton & Fitzpatrick, 1988; Drits et al., 1993).

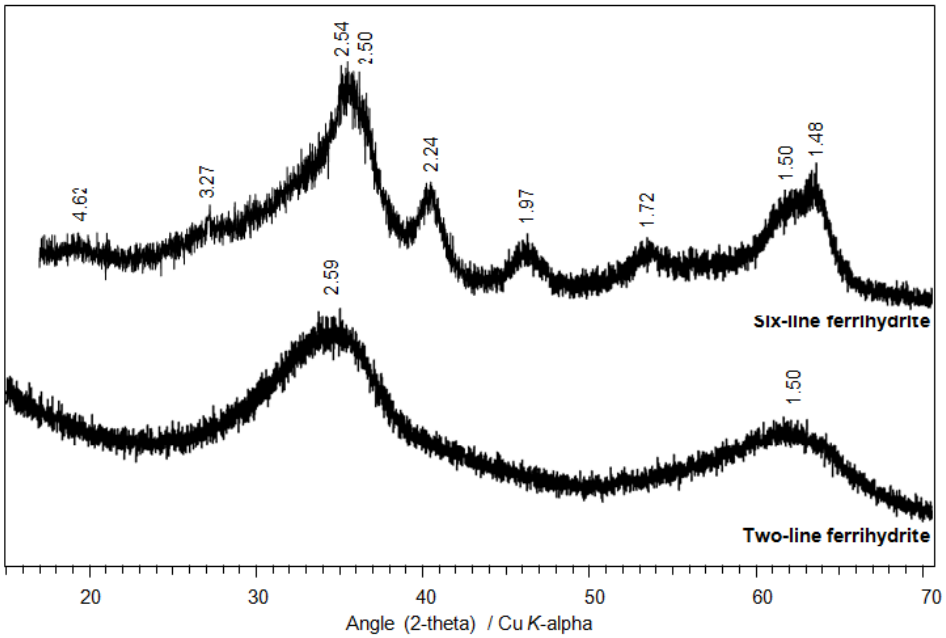

Figure 5.1 Powder X-ray diffraction data of synthetic two-line ferrihydrite and synthetic six-line ferrihydrite acquired using Cu-*K*α radiation (1.54 Å). Characteristic peaks are marked with *d*-spacings given in Ångstroms.

The XRD pattern for 2LFh is composed of two very broad maxima at *d*-spacings of 2.59 Å and 1.50 Å (35˚ and 62˚ 2θ Cu-*K*α). The extreme width of these peaks is indicative of the nanocrystalline nature and poor crystallinity of the sample (Cullity, 1956). The positions of the two main peaks, at 2.59 Å and 1.50 Å, are in good agreement with previous work of others (Eggleton & Fitzpatrick, 1988; Towe & Bradley, 1967).

The XRD pattern of 6LFh is composed of six broad peaks which lie between 1.48 and 2.54 Å. The two main peaks, residing at approximate *d*-spacings of 1.5 and 2.5 Å, can each be seen to consist of poorly resolved doublets. The lower *d*-spacing doublet corresponds to, in order of increasing interplane separation, the {330} and {115} atomic planes whilst the other is due to the {110} and {111} (Drits et al., 1993). Between these two principle maxima are the remaining three less intense peaks, at *d*-spacings of 1.72, 1.97, 2.24 Å, which are attributed to, in order of increasing *d*-spacing, the {144}, {133} and {122} planes (Drits et al., 1993). The presence of the weak broad peaks at approximate *d*-spacings of 3.3 and 4.6 Å – not normally considered when identifying this mineral – are thought to indicate that the unit cell parameter a = 5.08 Å (Towe & Bradley, 1967; Drits et al., 1993).

5.2 Fourier Transform Infrared Spectroscopy

The FTIR spectra of 2LFh and 6LFh are presented in Figure 5.2. The results of the IR measurements for both forms of ferrihydrite are broadly similar to those previously published in the literature (Russell, 1979; Cornell & Schwertmann, 2003). Russell (1979), with reference to the IR spectrum of 6LFh, noted that the background in the range 2,000 to 4,000 cm^{-1} can be attributed to strong scattering of the IR radiation which results from the "small size" particles and aggregates of ferrihydrite.

As observed here, the signal intensity within this region is somewhat more pronounced for 2LFh than for 6LFh. On the one hand, this may reflect the decreased particle size of 2LFh *vs.* 6LFh. However, it may also indicate an increased H_2O content of the 2LFh sample (Russell, 1979). This last point may be supported by the increased intensity of the band around 1622 cm^{-1} (OH bending) for 2LFh when compared to the corresponding band in the 6LFh spectrum noted by Russell (1979) to be proportional to the extent of hydration of the sample. This band, along with one at 3450 cm^{-1} (stretching vibrations of OH^- groups and H_2O molecules), was noted by Towe and Bradley (1967) to be associated with molecular water in "hydrogen-bonded association" (Ristić, De Grave, Musić, Popović, & Orehovec, 2007; Towe & Bradley, 1967).

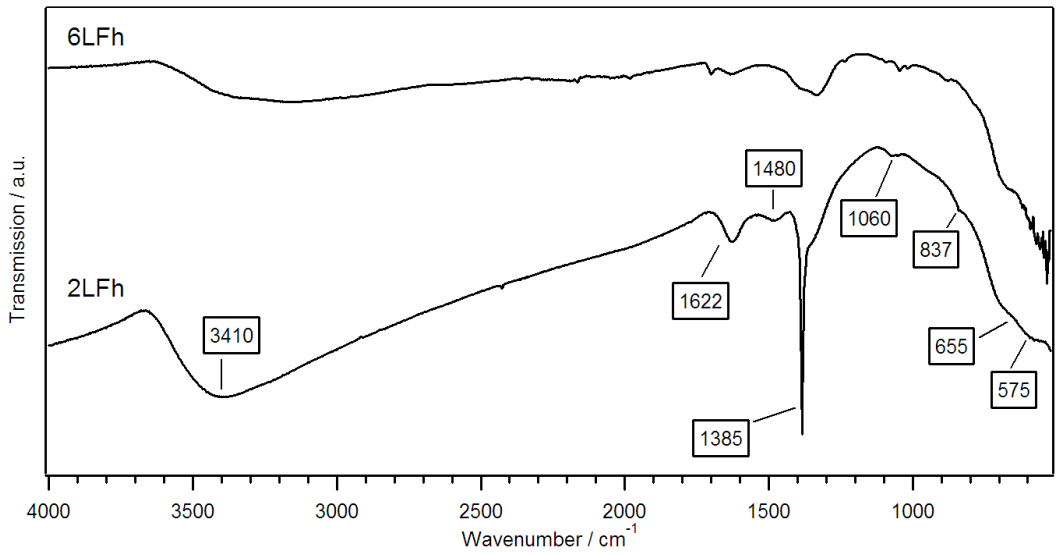

Figure 5.2 Fourier transform infrared spectra obtained from synthetic two-line ferrihydrite and synthetic six-line ferrihydrite. Labeled are the positions of important features which are discussed in the text.

Cornell and Schwertmann (2003) attribute bands at 3615 cm^{-1}, 3430 cm^{-1} and 650 cm^{-1} to be due to free surface OH, bulk OH stretch and bulk OH deformations, respectively. The sharp spike at 1385 cm^{-1} as observed for 2LFh may be attributed to NO_3^- from the ferric nitrate reagent used during synthesis (Cornell & Schwertmann, 2003; Miller & Wilkins, 1952). The absence of this feature in the 6LFh spectrum indicates the increased efficacy of the dialysis method of washing over that used for the 2LFh sample. The weak bands at 1480 and 1060 cm^{-1}, seen more prominently for 2LFh, may indicate the presence of carbonates (i.e. adsorbed CO_2 from the air) of atmospheric origin associated with samples (Ristić et al., 2007).

5.3 Raman Spectroscopy

Under the Raman optical microscope both forms of ferrihydrite (2LFh and 6LFh) were seen to be composed of two distinct surface types, each distinguished by their colour. Figure 5.3 displays the optical micrographs taken from the surface of 6LFh during the alignment of the optical system. The smoother of the two surfaces was a shiny dark black/brown whilst the rougher surface was seen to be a more orange. These different surface types have been previously noted and attributed to the surfaces and interiors of aggregates respectively (Mazzetti & Thistlethwaite, 2002). Both types of surface gave identical spectra, however, the darker of the two surfaces was slightly more susceptible to alteration under the laser; consistent with the fact that that optically darker surfaces absorb more strongly.

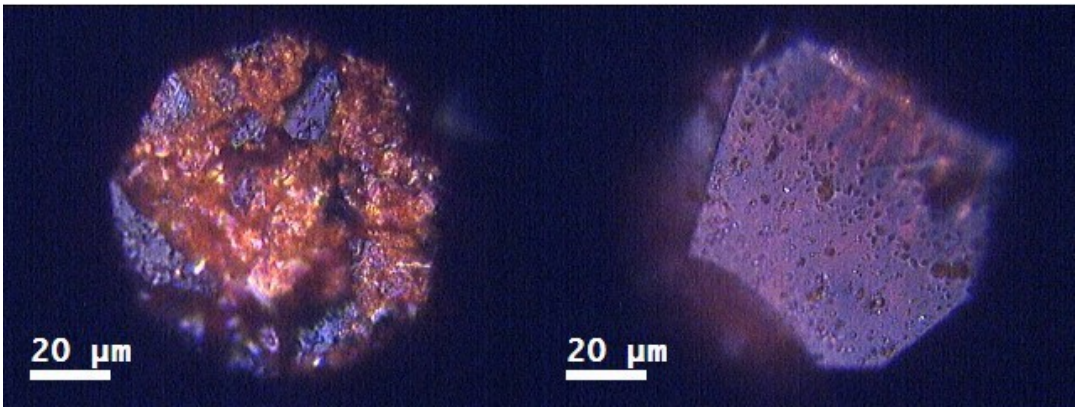

Figure 5.3 Optical micrographs taken from the surface of synthetic six-line ferrihydrite whilst focusing the Raman microscope. Two distinct surface types can be seen: a rougher orange surface (left) and a smoother darker surface (right).

Figure 5.4 compares the Raman spectra acquired from 2LFh and 6LFh. For both materials, the spectra are very similar exhibiting broad bands around 510, 710 and

1380 cm^{-1}. The positions and relative intensities of these bands are consistent with previously reported data for 6LFh (Hanesch, 2009) and also both forms of ferrihydrite (Mazzetti & Thistlethwaite, 2002). In a systematic Raman spectroscopic study of various iron oxides and (oxy)hydroxides, Hanesch (2009) suggests that the 710 and 510 cm^{-1} bands (in addition to one at 370 cm^{-1}) are sufficiently distinct to permit unambiguous identification of ferrihydrite provided sufficient care has been taken to avoid transformation under the Raman laser (Hanesch, 2009).

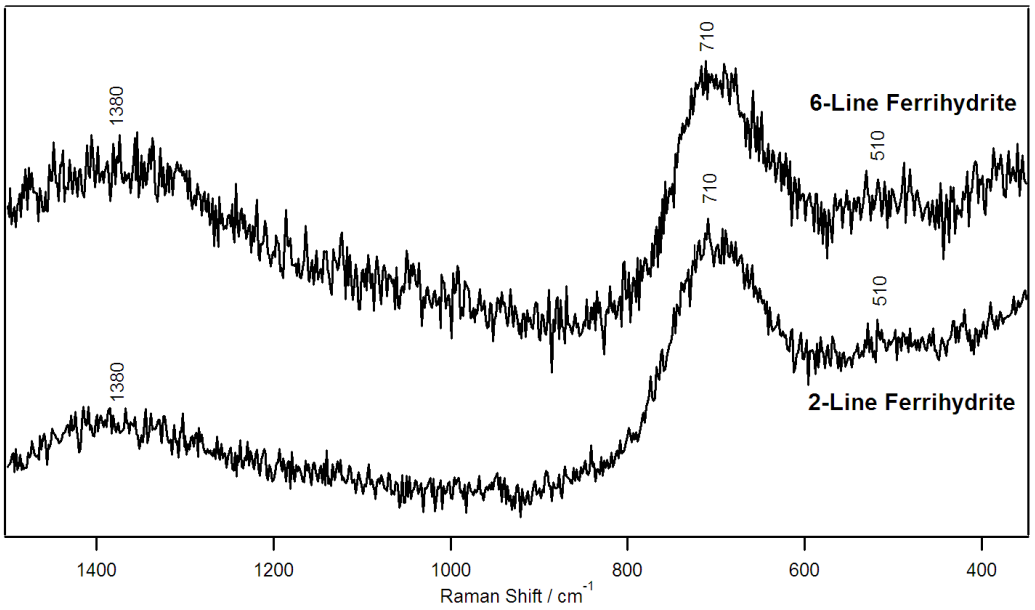

Figure 5.4 Raman spectra comparing the typical damage free signals of synthetic two-line ferrihydrite and synthetic six-line ferrihydrite. The three main features characteristic of ferrihydrite are labeled 1380, 710 and 510 cm^{-1}.

5.4 Analytical Electron Microscopy

5.4.1 Electron Beam Damage Assessment of 2LFh

Whilst both 2LFh and 6LFh have been the subject of high-quality electron microscopy investigations in the past (Janney, Cowley, & Buseck, 2000a, 2000b; Janney, Cowley, & Buseck, 2001), it was not until the work of Pan (2006) that the consequences of electron irradiation damage were given proper consideration (Pan, 2006; Pan, Brown, Brydson, Warley, Li, & Powell, 2006; Pan et al., 2010). This section aims to build from where Pan left off by revisiting the question of ferrihydrite's sensitivity to the effects of prolonged exposure to the electron beam only this time the focus is on two-line ferrihydrite, the least crystalline form.

The fluences discussed here are for 197 keV electrons belonging to the broad-beam illumination of a Philips CM200 transmission electron microscope.

Fe-$L_{2,3}$ ELNES

Displayed in Figure 5.5 are the ferric iron content estimates derived from Fe-*L* ELNES fitting analysis as a function of accumulated electron fluence for 2LFh, using the method described in section 4.2.6 and Pan (2006). Error bars shown have been derived from the errors of fitting coefficient values which were provided by the fitting routine and may be somewhat over cautious.

For fluences ranging from 1.3 x 10^5 to approximately 1.0 x 10^8 electrons nm^{-2} the ferric iron content remains fairly constant at around 87 ± 27% of the total iron present. At 1.0 x 10^8 electrons nm^{-2} the onset of change is marked by a decrease in the ferric iron signal. By the experiment's end, at which point the cumulative fluence has reached 3.5 x 10^9 electrons nm^{-2}, the ferric iron content has been reduced to ~30% of its starting value (~30 ± 15%). The same trend is identified by the van-Aken EELS Fe-*L* White-Line Ratio method (see Appendix C) which estimates the initial and final ferric iron contents to be 95 ± 5% and 18 ± 5%, respectively (van Aken at al., 1998; van Aken & Liebscher, 2002).

Fitted to the data are exponential functions which, when extrapolated back to the zero-electron fluence limit, estimate the ferric iron content to be 91 ± 27% of the total iron present in the case of the NLLS fitted data and 92 ± 5% using the van Aken method. Over the course of the experiment the average valence of iron has been reduced from an initial starting value of 2.9 $\pm$ 1 to a final mean value of 2.3 $\pm$ 1.

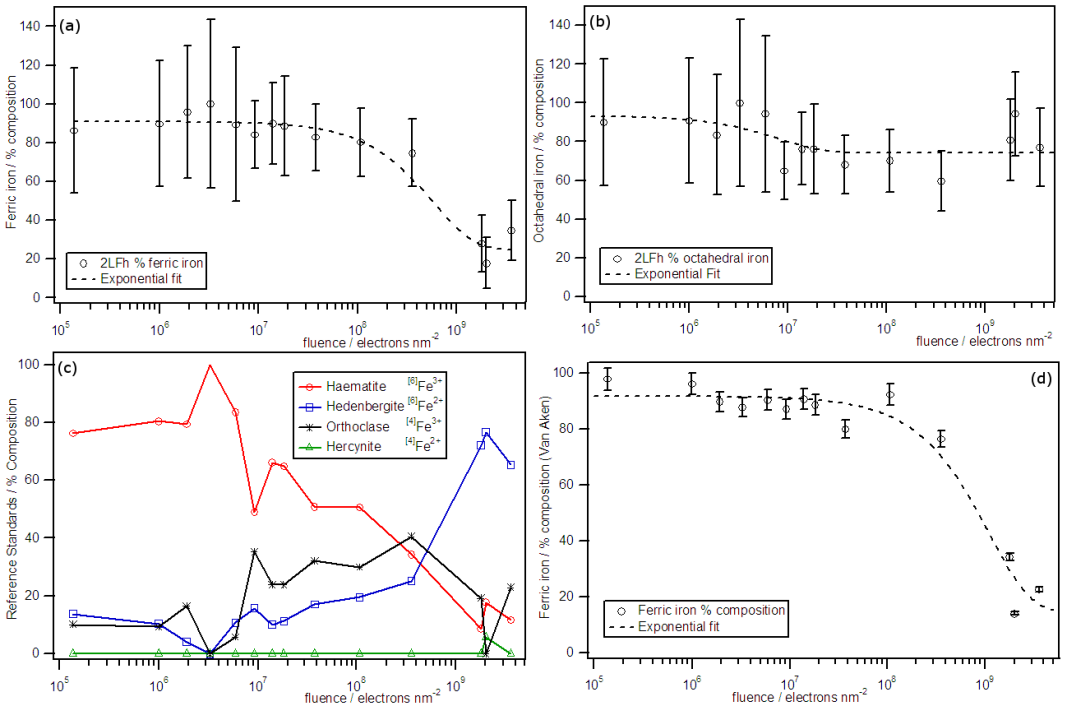

Figure 5.5 Summary of Fe-$L_{2,3}$ electron energy-loss near edge structure fitting analysis as a function of electron fluence applied to synthetic two-line ferrihydrite. (a) the percentage ferric iron derived from NLLS peak fitting; (b) the percent octahedral iron derived from NLLS peak fitting; (c) the percentage contribution of each of the four reference compounds used in NLLS fitting and (d) the percentage ferric iron contribution derived using the van Aken white-line intensity ratio method. Exponential best fit lines are displayed in a, b & d for illustrative purposes.

O-K ELNES

The evolution of the EELS O-*K* edge of 2LFh as a function of increasing electron-fluence is displayed in Figure 5.6. There are four features of interest, which in order of increasing energy-loss are as follows. Firstly, there is an intense *pre-peak* at approximately 529 eV, the intensity of which remains a constant 80% of the main-peak maximum over the entire fluence range. Moving up in energy-loss the next significant feature encountered is what will be referred to as the main peak. Having maximum intensity at some 539 eV the main peak is the most intense feature of the O-*K* ELNES and is also most typical of O 2*p* character in the absence of hybridization with Fe 3*d*. Two subtitle modifications of its fine structure can be observed. Firstly, the gradient, or slope, on its high energy-loss side is seen to increase slightly upon on increasing fluence. Secondly, at high fluences there is some evidence for a low-energy loss shoulder appearing around 536 eV. The next feature, or rather energy-loss range, to consider lies between 544.0 eV and 549.5 eV. At low fluences (below ~10^8 electrons nm^{-2}) this region is conspicuous by the absence of intensity and there is little to report. However, when fluence exceeds 2 x

10^8 electrons nm^{-2} increasing intensity is observed with the appearance of a small peak at approximately 546.5 eV. A peak at this position and with similar relative intensity is also observed in the O-*K* ELNES of hematite, maghemite, magnetite and wüstite (Brown, Moore, Evans, & Brydson, 2001). Beyond 550 eV the O-*K* edge is rather featureless save for a broad peak around 561 eV, for which a slight negative shift (~2 eV) in energy-loss may be observed to occur as the accrued fluence is increased between ~10^5 and 10^9 electrons nm^{-2}.

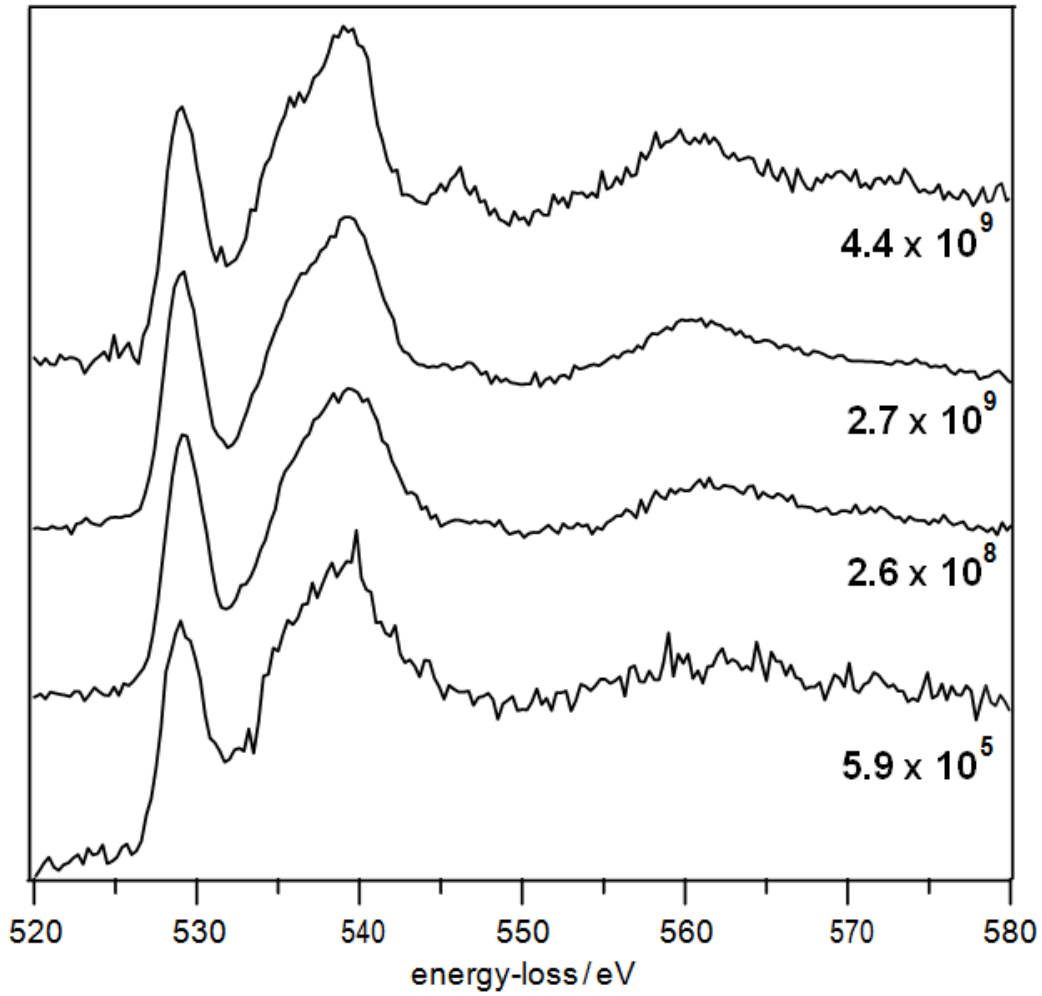

Figure 5.6 Electron energy-loss near edge structure (ELNES) of the oxygen-*K* edge for synthetic two-line ferrihydrite. Bold typeface numbers above the curves indicate cumulative electron-fluence in units of electrons nm^{-2}. The low-fluence spectrum (bottommost) is typical of both forms of ferrihydrite.

Figure 5.7 shows the change in oxygen content of 2LFh as a function of accumulated electron-fluence, derived from both EELS and EDX measurements. Error bars plotted in Figure 5.7(a) represent 10% of the base value. Within the fluence range, 1.3 x 10^5 to 3.5 x 10^8 electrons nm^{-2} the oxygen signal remains approximately constant at some 61 ± 10%. Beyond this, the oxygen signal drops to

approximately 45 ± 10%; by which time the fluence is 3.5 x 10^9 electrons nm^{-2}. Figure 5.7(b) traces the percentage change in the absolute iron and oxygen EDX signals (normalised by the copper signal) as a function of electron fluence. The absolute iron EDX signal shows little variation, whereas the oxygen specific signal is seen to drop significantly beyond approximately 10^9 electrons nm^{-2}, suggesting the preferential loss of oxygen from the material. The point at which the oxygen signal is first seen to decrease corresponds well with the observed drop in the ferric iron content as estimated by EELS. Additionally, Figure 5.7(a) displays the results of fitting an exponential function to the data, which when extrapolated back to zero-electron fluence estimates 2LFh is composed of 61% oxygen relative to iron.

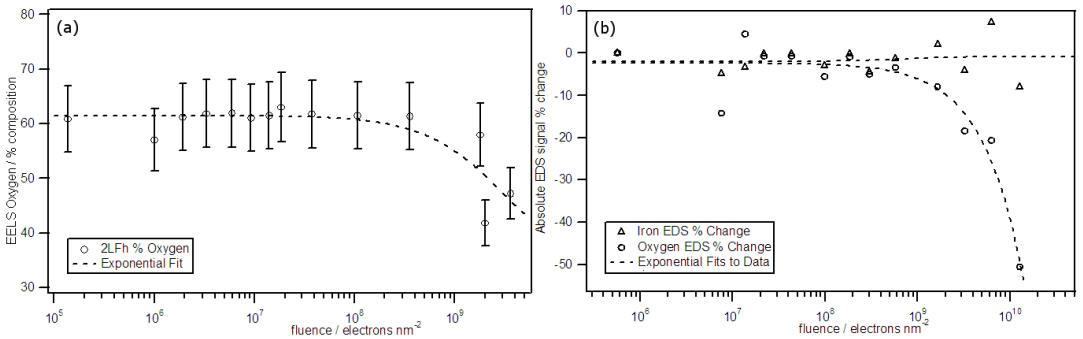

Figure 5.7 (a) Oxygen content of synthetic two-line ferrihydrite as a function of cumulative electron fluence as determined by electron energy-loss spectroscopy (EELS); (b) the change in absolute oxygen and iron signals as normalised by the copper signal using energy-dispersive X-ray spectroscopy (EDX). In both datasets preferential loss of oxygen can be seen for fluences above 10^8 electrons nm^{-2}.

A selection of high-resolution BF-TEM micrographs of 2LFh acquired at a fluence of approximately 10^{10} electrons nm^{-2} are displayed below in Figure 5.8. The effect of this exposure is quite striking, especially so when compared with *pristine* 2LFh (see Figure 5.12). Significant structural reordering has given rise to enhanced crystallinity, in terms of both the degree and extent of atomic order evident from lattice fringes now extending over many tens of nanometres. Lattice fringe spacings of approximately 4.9, 3.0 and 2.5 Å can be clearly seen in the high-resolution micrographs.

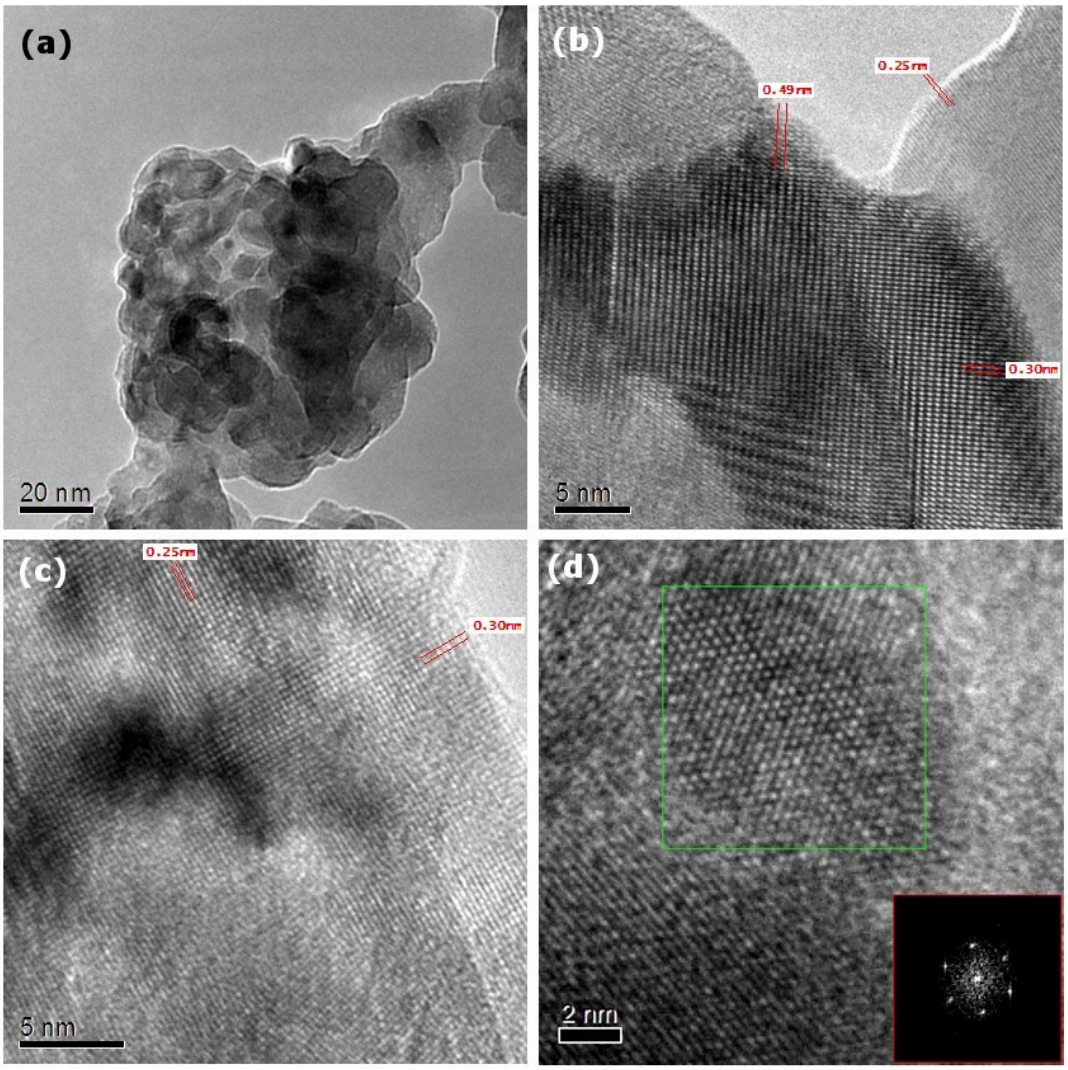

Figure 5.8 Bright-field transmission electron micrographs of synthetic two-line ferrihydrite (2LFh) after exposure to an accumulated electron–fluence of $4x10^9$ electrons nm^{-2}. Annotations in b & c show lattice spacings of 0.30 and 0.49 nm which are not characteristic of 2LFh in its pristine undamaged state. Inset in (d) is the FFT of the area in the boxed region (green) showing regular hexagonal symmetry.

SAED patterns were acquired periodically throughout the duration of the experiment. In order to aid interpretation of these patterns, especially in the case of those collected at higher fluences, one-dimensional rotationally-averaged radial-intensity profiles of the diffraction patterns have been produced, a selection of which is shown in Figure 5.9. It should be noted that the relative intensities of the peaks in the radial intensity profiles are meaningless, especially in the cases of the higher fluence, more *spotty* patterns.

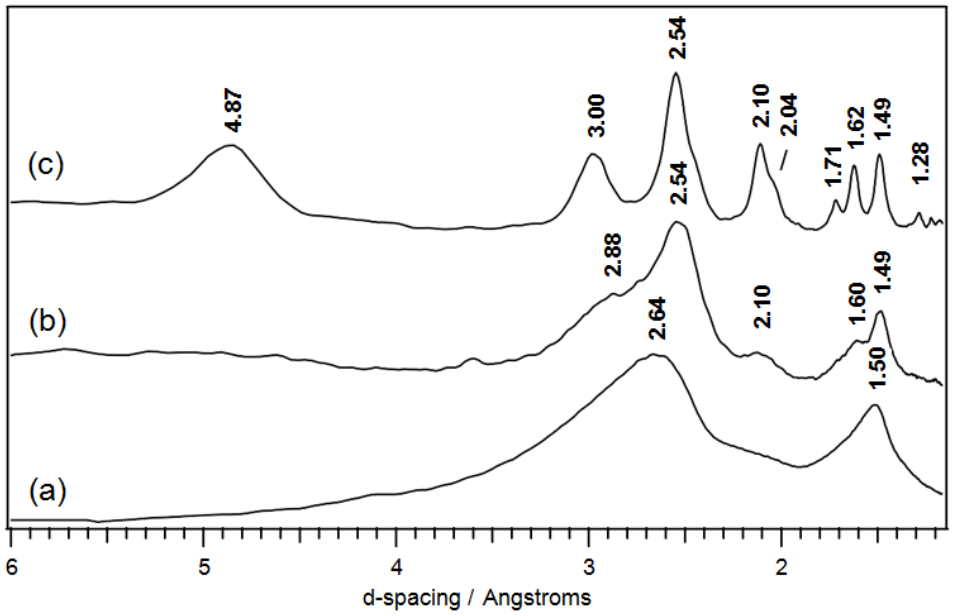

Figure 5.9 Radially averaged selected area electron diffraction patterns of synthetic two-line ferrihydrite acquired at fluences of (a) 4 x 10^6, (b) 1.5 x 10^9 and (c) 4.4 x 10^9 electrons nm^{-2}. Numbers above the curves indicate *d*-spacings given in Ångstroms. The effect of accumulated electron fluence can be seen by the appearance of additional reflections.

Upon increasing fluence, the SAEDs were observed to evolve from ones containing two diffuse rings, at *d*-spacings of approximately 1.5 and 2.6 Å, typical of 2LFh, into patterns which included additional rings and eventually into those containing discrete spots. This indicates electron irradiation induced crystallisation of the sample, resulting in an increase in both order and size (coarsening) of crystallites. It can be seen that upon increasing fluence the maxima around 1.5 Å deviates little from its original position, whilst that at 2.64 Å shifts toward slightly smaller *d*-spacings. It should be noted that, in the case of iron oxides and hydroxides, the 2.5 - 2.6 and 1.5 Å spacings are non-diagnostic, being common to many of the oxides and therefore, alone, cannot be used as a means of phase identification. The second point to note is that those *d*-spacings which offer hope of uniquely identifying a crystal structure are to be found at *d*-spacings larger than say 2.7 Å. Bearing these two last points in mind there is little we can say about the diffraction pattern collected at 4.0 x 10^6 electrons nm^{-2} other than that its general form – two broad maxima at 2.6 and 1.5 Å – is typical of 2LFh and corresponds well with powder XRD measurements. At a fluence of 1.5 x 10^9 electrons nm^{-2} three extra peaks have appeared, of which two (2.88 and 2.10 Å), confirm the presence of extra mineral phases in addition to the precursor 2LFh. At the highest fluence of 1.5 x 10^9 electrons nm^{-2} three additional maxima appear at 4.87, 1.71 and 1.28 Å. Of these new peaks the largest

d-spacing may corresponds to either maghemite, magnetite or goethite, however, these are relatively weak reflections for each these phases (12%, 6% and 8%, respectively). The large breadth of this 4.87 Å maximum is due to this reflection being somewhat oversaturated in the original diffraction pattern.

Plotted in Figure 5.10 are the radial intensity profiles of 2LFh as acquired at 1.5 x 10^9 electrons nm^{-2} and 4.4 x 10^9 electrons nm^{-2} along with the stick patterns of the most intense reflections (≤9% relative) of hematite and magnetite for comparison (JCPDS: 00-025-1402 and 39-1349 respectively). The X-ray diffraction patterns of magnetite are almost identical to those of maghemite and are therefore not shown. It can be seen that there is a good correspondence between the maghemite stick pattern and the experimental diffraction patterns.

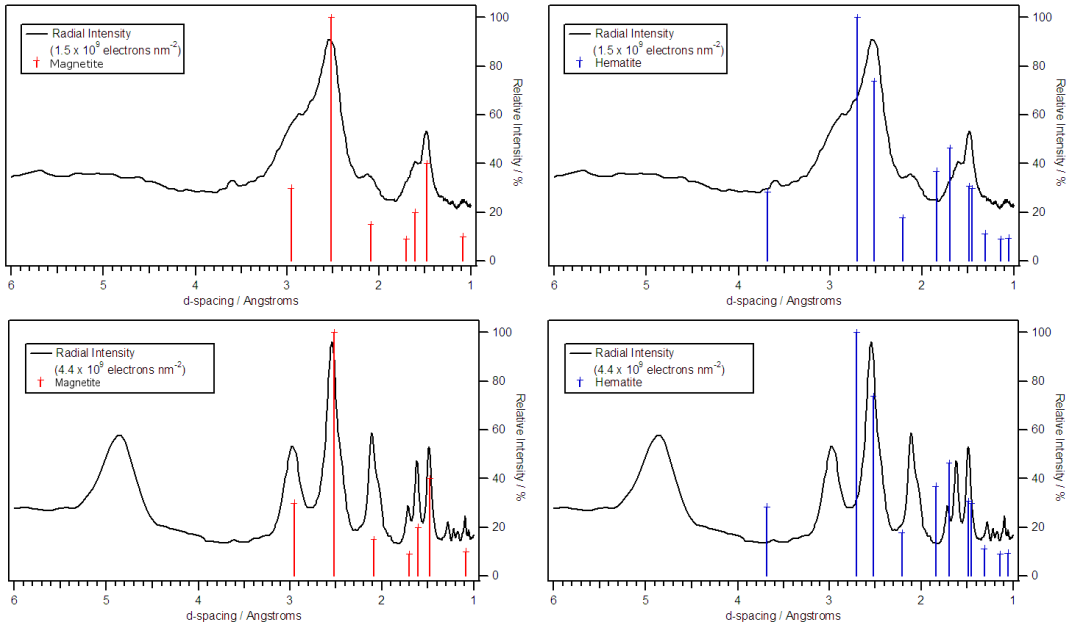

Figure 5.10 Radial averaged selected area electron diffraction intensity profiles of acquired from synthetic two-line ferrihydrite after exposure to 4.4 x 10^9 (197keV) electrons nm^{-2}. For comparison stick patterns of the most intense features (≥9% relative) are superimposed and relate to the corresponding JCPDS files for magnetite (JCPDS card 39-1349) and hematite (JCPDS card 33-0664).

In light of the above discussion, it can be concluded that magnetite is the most likely candidate for the conversion product of 2LFh when subjected to around 4.4 x 10^9 (200 keV) electron nm^{-2} in the vacuum of the TEM. This is supported by the following observations. Firstly the signals acquired from the Fe-*L* EELS edge suggest reduction of iron under the electron beam. Reduction of iron is consistent with the loss of oxygen (and/or hydroxide ions) which in turn is supported by EELS and EDX spectroscopy compositional analysis. Crystallographic data (SAED)

suggests the presence of extra phases, in addition to precursor 2LFh, being present at elevated fluences. Of these phases magnetite (oxygen% = 57) and wüstite (oxygen% ≈ 53) are ferrous-iron bearing minerals, however the latter is not highly ranked according to the crystallographic data. Finally, the O-*K* EELS edges acquired at 4.4 x 10^9 electrons nm^{-2} are very similar – both in terms of peak intensities and positions – to those measured from magnetite and maghemite, which have been measured on the same microscope (Brown et al., 2001).

In conclusion, it would appear that, up until an accumulated electron fluence of approximately 10^8 electrons nm^{-2}, 2LFh can be observed by a TEM using 197 keV beam electrons, in its *pristine* (undamaged) state with minimal alteration being observed in chemical and structural signals.

5.4.2 Bright-Field (S)TEM and HAADF STEM Imaging

Low-resolution (S)TEM imaging of 2LFh (Figure 5.11) reveals aggregation of the sample on scales ranging from tens of nanometres to several microns. Even following extended periods of ultrasonication isolated crystals were not observed.

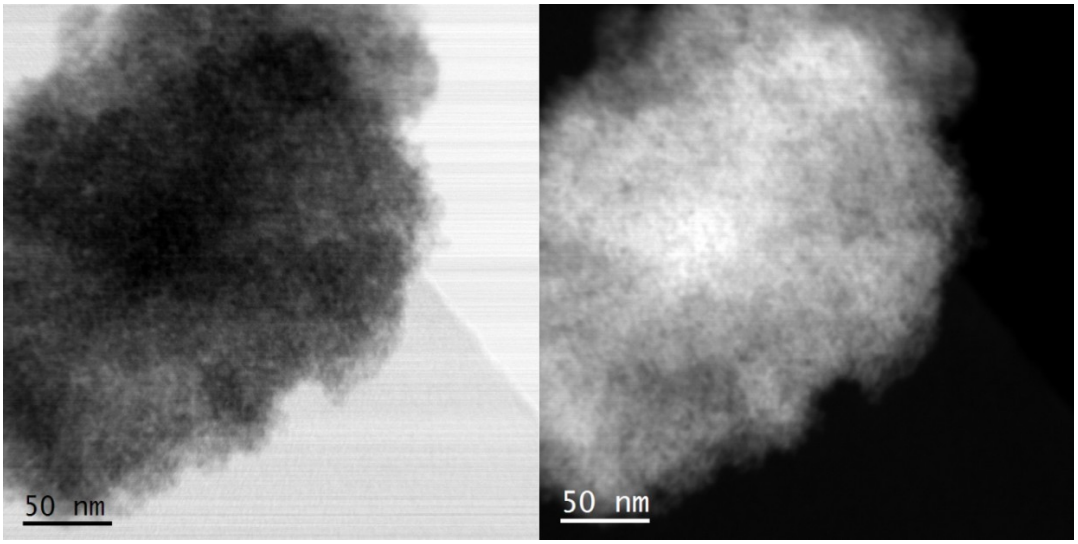

Figure 5.11 Low magnification bright-field and HAADF aberration corrected STEM micrograph pairs showing a typical aggregate of synthetic two-line ferrihydrite. Electron fluence is estimated to be of the order of 1.5 x 10^6 electrons nm^{-2}.

High-resolution BF-TEM imaging (Figure 5.12) is only possible on the electron-transparent edges of aggregates, where occasionally individual crystallites may be seen to extend from the aggregate mass. These crystals have poorly defined edges (being faceted when seen), which combined with their propensity to aggregate, makes the estimation of their full extent difficult. Therefore, the possibility of any

real statistical assessment of crystal morphology and size is precluded. Despite this by making observations at the fringes of aggregates it can be estimated that crystals no greater than 4 nm in extent is present as per previous TEM work on 2LFh (Janney et al., 2000a). Lattice fringes corresponding to *d*-spacings of approximately 2.5–2.6 Å can occasionally be observed confirming the crystallinity of the sample. However, these spacings being common to many of the iron oxides and hydroxides are not a unique diagnostic of ferrihydrite.

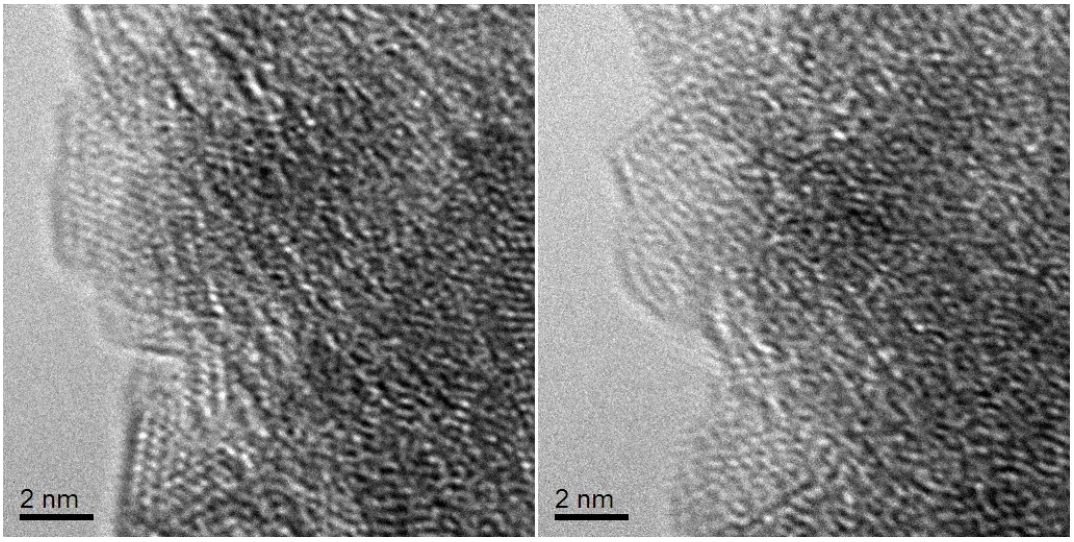

Figure 5.12 High-resolution bright-field TEM micrographs of the edge of a synthetic two-line ferrihydrite aggregate taken close to Scherzer defocus. Atomic ordering and faceting can be seen extending over regions ~4nm in extent.

HAADF AC-STEM imaging of 2LFh (Figure 5.13) more often than not yields *fuzzy* images. This is most probably due to a combination of the instability of aggregates during electron-beam irradiation and relatively large variations in sample height which make achieving perfect defocus difficult. However, in rare instances, hints of crystallinity may be observed revealing *d*-spacings of 2.5 - 2.6 Å.

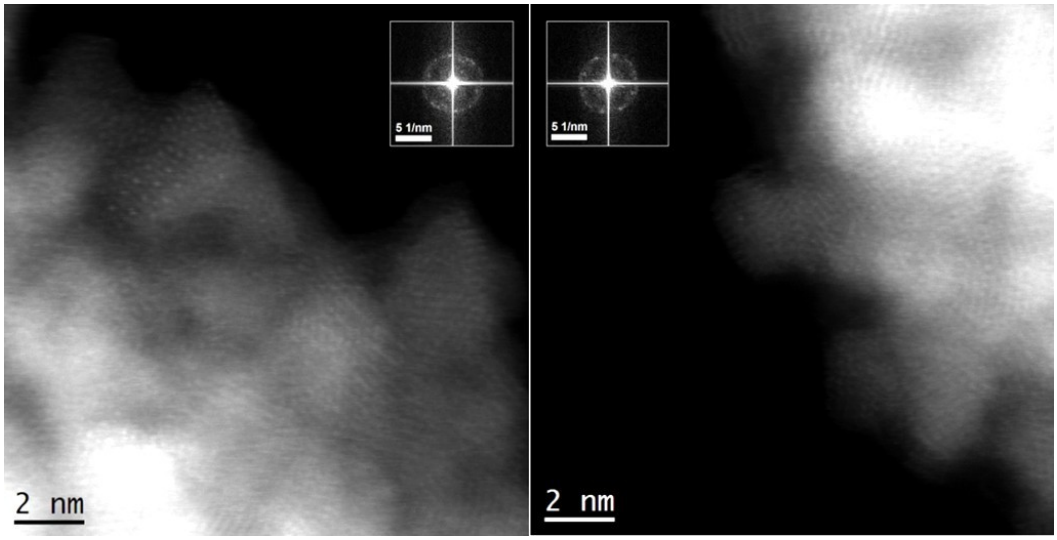

Figure 5.13 High-magnification (1,000k times) HAADF aberration corrected STEM images of synthetic two-line ferrihydrite. A high degree of crystal aggregation can clearly be seen. FFT inserts indicate periodicity of 2.5 – 2.6 Å. Electron fluence is estimated to be of the order of 10^7 electrons nm^{-2}.

As was observed for 2LFh, the 6LFh form also exhibits a tendency to aggregate, however, here the extent is far less pronounced (Figure 5.14). Single isolated crystals which may often be observed have faceted edges and sizes of approximately 4.9 ± 1.0nm (based on an average of forty crystallites).

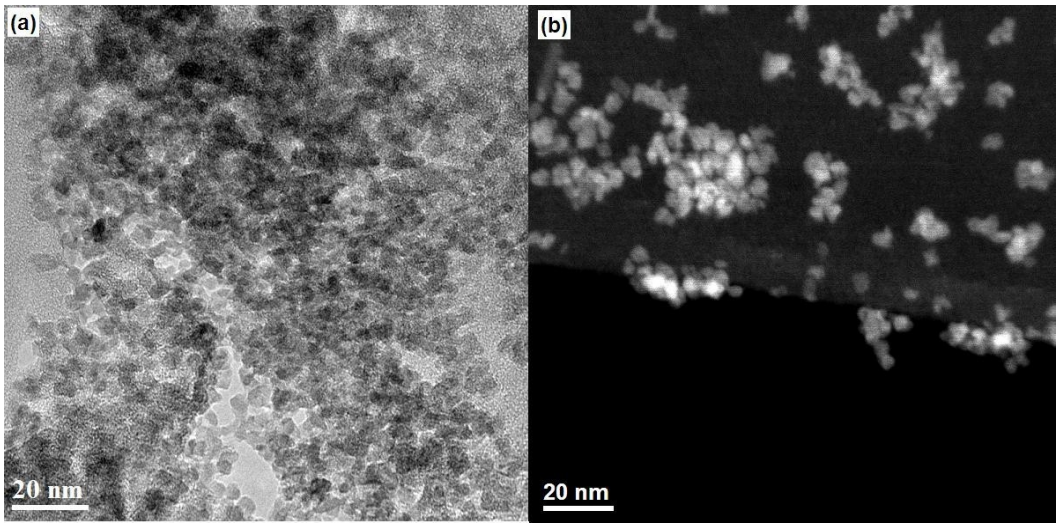

Figure 5.14 (a) Bright-field TEM and (b) HAADF aberration corrected STEM images of synthetic six-line ferrihydrite showing small aggregated clusters of well defined individual crystallites.

HAADF AC-STEM imaging of 6LFh (Figure 5.15) reveals irregular-shaped single crystal particles with aspect ratios in the image plane close to unity. Fourier analysis of the HAADF images (inset, Figure 5.15) reveales spatial frequencies corresponding to *d*-spacings of 1.8 Å in addition to the 2.5 – 2.6 Å spacings, typical of both forms of ferrihydrite.

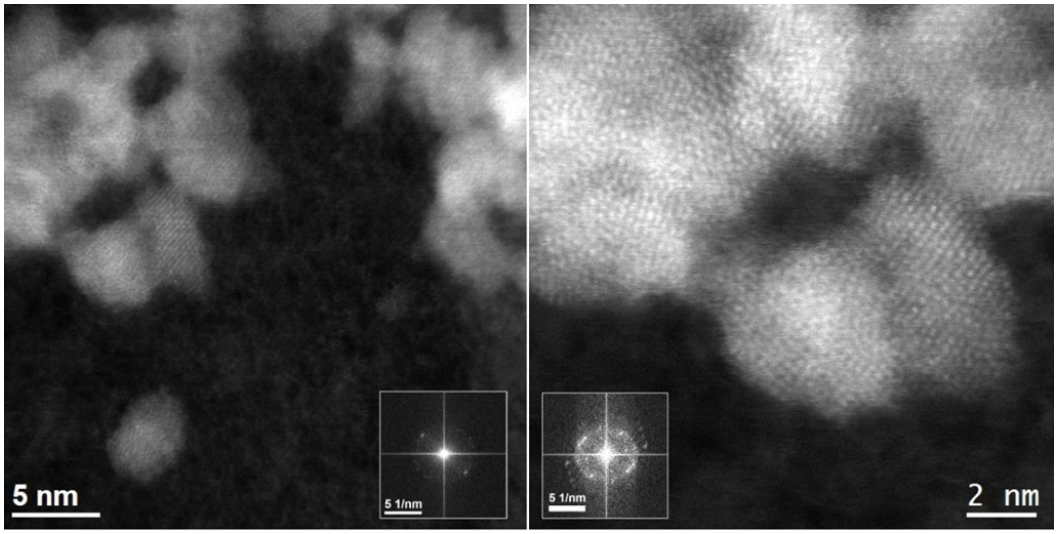

Figure 5.15 High-magnification (500k and 1000k times) HAADF aberration corrected STEM microscope images of synthetic six-line ferrihydrite showing well defined single crystals. Inset: FFTs indicate periodicities of 2.5 - 2.6 Å for the left-hand side image and 1.8 Å, 2.5 - 2.6 Å for the right-hand side image. Electron fluence is estimated to be of the order of 10^7 electrons nm^{-2}.

5.4.3 Selected Area Electron-Diffraction

SAED patterns of 2LFh (Figure 5.16, left) exhibit two diffuse rings at *d*-spacings of 2.5 – 2.6 Å and 1.5 Å, consistent with previous TEM-SAED work on the same material (Janney et al., 2000b) and also with the powder XRD data acquired in this study (section 5.1). SAED patterns of 6LFh (Figure 5.16, right) display six-rings corresponding to approximate *d*-spacing values of 1.51, 1.57, 1.81, 2.06, 2.28 and 2.60 Å, which again is consistent with previous TEM-SAED observations of this material (Janney et al., 2000b; Janney, Cowley, & Buseck, 2001).

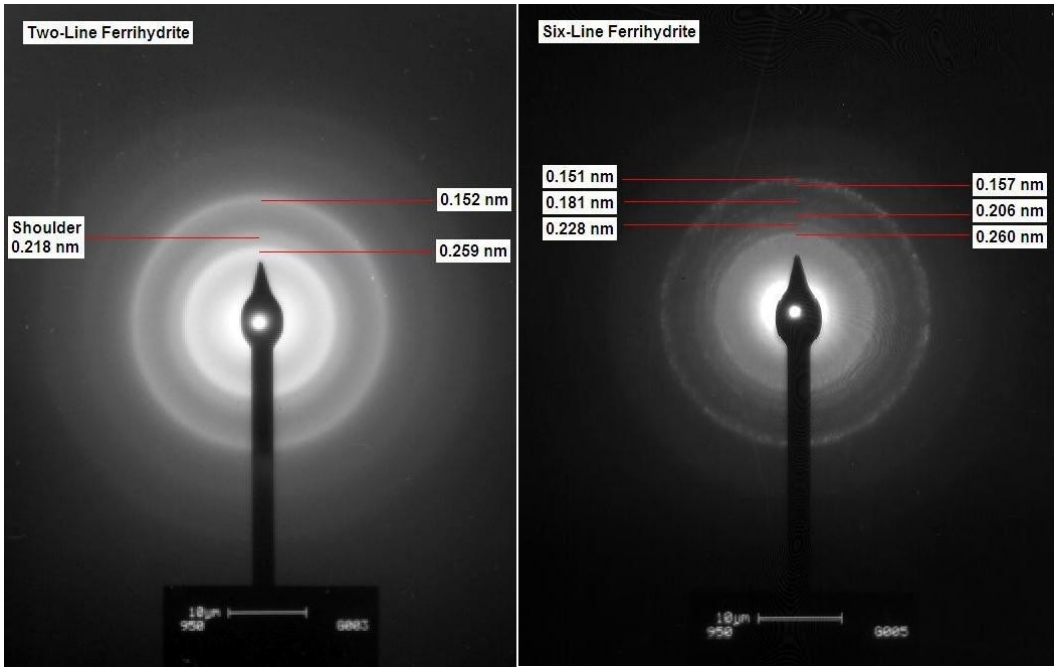

Figure 5.16 Selected-area TEM electron diffraction patterns typical of synthetic two-line ferrihydrite (left) and synthetic six-line ferrihydrite (right).

5.4.4 Energy Dispersive X-Ray Spectroscopy

EDX analysis as applied to 2LFh is shown in Figure 5.17. The carbon and copper signals are due to the sample support film and the supporting grid. No elements other than iron and oxygen are observed (EDX is not capable of hydrogen detection), thereby confirming the chemical purity of the sample. Elemental quantification, based on the Fe-*K* and O-*K* signals, in this case, gives a ratio Fe:O of 3:7 which is consistent with any one of the suggested formulae: $Fe_2O_3 \cdot 3.5H_2O$; $FeOOH \cdot H_2O$ or $5FeOOH \cdot H_2O$ (Jambor & Dutrizac, 1998). Identical results were obtained for 6LFh and on this basis are not shown here.

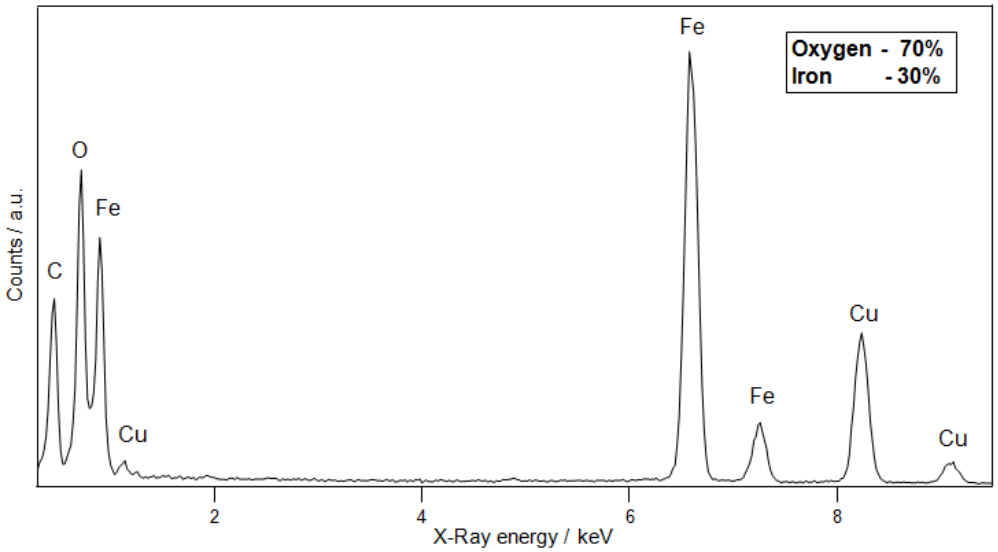

Figure 5.17 Energy dispersive X-ray spectra of synthetic two-line ferrihydrite as acquired in the TEM. Inset the relative percentage composition of iron and oxygen estimated from the integrated intensity of the respective *K* peaks.

5.4.5 Electron Energy Loss Spectroscopy

TEM EELS

EELS measurements of the Fe-*L* and O-*K* specific signals for both 2LFh and 6LFh are shown in Figure 5.18. It can be seen that for both the materials the Fe-*L* and O-*K* signals are almost identical making distinct identification impossible. Firstly, the O-*K* edge (Figure 5.18a) is characterised by an intense pre-peak feature (85% of main-peak maximum) situated at some ~529 eV. The main peak at ~538 eV is fairly broad (~10 eV) and asymmetric. A broad hump which extends from approximately 548 eV to 575 eV has its maximum intensity (~ 80% of main peak intensity) at around 561 eV. Of the major iron-oxides and hydroxides, the ELNES of the O-*K* edge of ferrihydrite is most similar to that of either maghemite or magnetite, however, there is the conspicuous absence of a peak at around 547 eV which is common to both (Brown et al., 2007).

Figure 5.18b compares the Fe-*L* signals for both forms of ferrihydrite. The signal is typical of a predominantly Fe(III) bearing iron-oxide material in which the iron atoms reside in six-fold coordination with oxygens and/or hydroxyls.

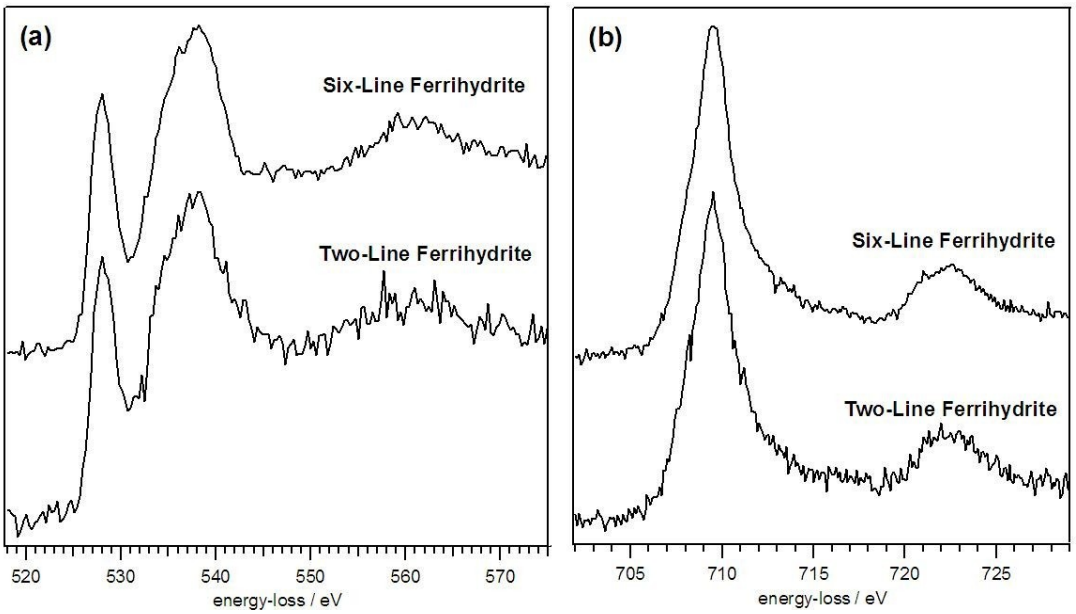

Figure 5.18 Comparison of (a) oxygen-*K* and (b) iron-*L* electron energy-loss signals from synthetic two-line ferrihydrite and synthetic six-line ferrihydrite as acquired in the TEM. Electron fluence is estimated to be below 10^7 electrons nm^{-2}.

"Smart Acquisition" EELS

The smart EELS acquisition method was applied to both 2LFh and 6LFh in order to compare the *surface* and *bulk* specific signals of each sample with high spatial-resolution and low electron fluence. Before continuing it should be made clear that *surface* and *bulk* can be somewhat misleading concepts when discussing nanoparticles, especially in the case of those, which like ferrihydrite, exhibit the propensity to aggregate. In this study an attempt was made to isolate the surface-specific EELS signals by scanning around the edge of particles as seen in HAADF images. The bulk-signal was isolated by scanning the probe over the top of a particle as seen in HAADF images. In the case of 6LFh, where it was trivial to find isolated crystallites, defining a mask to isolate the "surface" of a particle could be done with a fair degree of confidence (see Figure 5.19). However, in the case of 2LFh which invariably forms large aggregates, an attempt to isolate the surface-specific signal could only be made by scanning along the edge of aggregates. This is clearly less preferable than scanning the perimeter of a single crystallite especially considering the size typical of 2LFh particles.

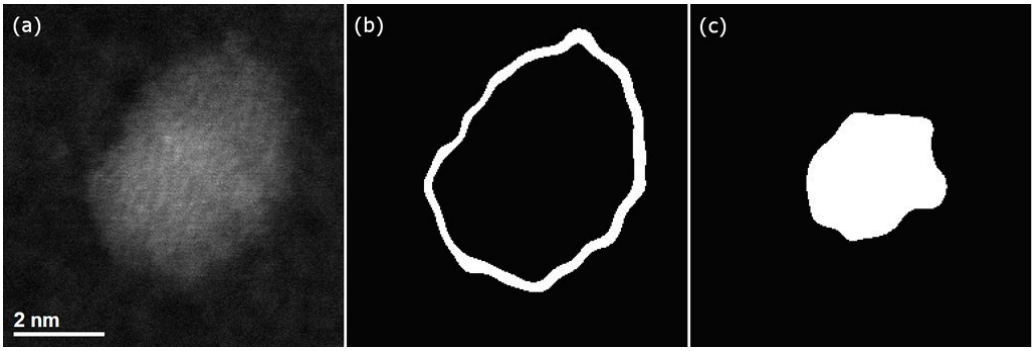

Figure 5.19 (a) High magnification aberration corrected HAADF STEM micrograph of a single isolated crystal of synthetic six-line ferrihydrite. Examples of SmartAcquisition EELS acquisition masks isolating (b) the surface and (c) the bulk signals from the crystal shown in (a).

The final data set used for surface to bulk analysis consists of the following: For 2LFh, seven *surface-bulk* mask pairs were selected for the measurement of the Fe-*L* ELNES and nine *surface-bulk* pairs were selected for the analysis of the O:Fe atomic ratio. For 6LFh the corresponding number of pairs were five and eight, respectively. In all cases only data sets containing *surface-bulk* mask pairs have been chosen to allow for comparison on a particle-to-particle (or aggregate-to-aggregate-bulk) basis. Only Fe-*L* spectra having a SNR better than 5 (as estimated from the ratio of the Fe-L_3 peak maximum to the R.M.S. of the noise in the spectrum) were selected. In addition to these constraints, an assessment of the quality of the masking was made by overlaying the masks with the HAADF images from which they were derived. By analysis of the pixel intensity distribution about the masked regions spectra have been selected which best isolate the *surface* signal. Surface masks sampling a distance greater than 0.5 nm into the sample's *bulk* were rejected from analysis. The same was true for masks which were found to have a significant offset with respect to the targeted regions or for those in which drift of the sample was observed during acquisition. Therefore, based on these selection criteria we are confident that the *surface* spectra are taken from the outer 0.5 nm of the particles analysed and the respective *bulk* from further within.

Table 5.2 Summary of the SmartAcquisition EELS least squares fitting *surface-bulk* analysis as applied to synthetic two-line ferrihydrite (2LFh) and synthetic six-line ferrihydrite (6LFh). Error values represent the standard-deviation of the measured values.

	Fe ELNES fitting for both surface and bulk				Van Aken	Fe:O - EELS Quant.	
	($^{[6]}Fe^{3+}$) Haematite	($^{[4]}Fe^{3+}$) Fe-Orthoclase	($^{[6]}Fe^{2+}$) Hedenbergite	($^{[4]}Fe^{2+}$) Hercynite	$Fe^{3+}/\sum Fe$	*Surface*	*Bulk*
2LFHY	36 ± 14%	18 ± 12%	47 ± 17%	-	0.8 ± 0.10	0.65 ± 0.08	0.63 ± 0.02
6LFHY	93 ± 2%	1 ± 2%	7 ± 2%	-	0.93 ± 0.05	0.59 ± 0.06	0.67 ± 0.03

Table 5.2 provides a summary of the *surface-bulk* smart-acquisition EELS analysis as applied to both 2LFh and 6LFh. During the analysis, it was apparent that there was no statistical difference between the Fe-*L* signals acquired from the *surface* and *bulk* of individual particles (or aggregates as the case may be). As such, results of the Fe-*L* ELNES analysis for both *surface* and *bulk* measurements have been combined so as to compare between the two forms of ferrihydrite.

Uncertainties in the Fe-*L* ELNES fitting results for 2LFh are an order of magnitude greater than those of 6LFh. Additionally, the breadth of the Fe-L_3 for 2LFh was increased when compared to that of 6LFh. This result is anomalous since when measured using TEM-EELS, the Fe-*L* edges of both forms of ferrihydrite are almost indistinguishable from one another. The increased width of the 2LFh Fe-*L* edge meant that when performing NLLS fitting, satisfactory and indeed faithful reproduction of the ELNES was often not achieved. The origin of this increase in width is thought to be due to a degradation of the EELS spectral resolution caused by a problem inherent to STEM-EELS. That is the lateral movement of probe position not being fully compensated for by the de-scanning coils resulting in electrons entering the EELS spectrometer at a range of angles (see Appendix B). This effect is more pronounced when large areas are being scanned which was necessarily the case for 2FLh scan masks.

For the 6LFh sample no statistical difference between *surface* and *bulk* Fe:O ratios were observed, being for the *surface* (0.67 ± 0.03) when compared to the *bulk* (0.59 ± 0.06). The same was observed for the 2LFh sample.

5.4 Concluding Remarks

2LFh and 6LFh were synthesised according to the methods outlined in Chapter 4. Powder XRD data for both samples confirms the success of the synthesis and their phase (purity). The two broad diffraction peaks observed in the 2LFh diffractogram are indicative of the nanocrystalline nature and poor crystallinity of this sample. The diffractograms obtained for both forms of ferrihydrite are consistent with those previously reported in the literature (Towe & Bradley, 1967; Eggleton & Fitzpatrick, 1988; Drits et al., 1993).

The FTIR spectra acquired here for 2LFh and 6LFh are in good agreement with those previously reported in the literature (Russell, 1979; Cornell & Schwertmann,

2003; Ristić et al., 2007). The decreased particle size of 2LFh, compared to 6LFh, is reflected in the strong signal intensity in the 2,000 to 4,000 cm^{-1} region. The increased intensity of the OH-stretching band at 1622 cm^{-1} in the 2LFh spectrum may be indicative of an increased water content of this sample compared to 6LFh. The absence of the sharp band at 1385 cm^{-1} (attributed to NO_3^-) for 6LFh highlights the efficacy of the dialysis method of washing over that used for 2LFh.

The positions and relative intensities of the broad bands around 510, 710 and 1380 cm^{-1} in the Raman spectra of both forms of ferrihydrite are consistent with data previously reported in the literature (Mazzetti & Thistlethwaite, 2002; Hanesch, 2009).

The effects of prolonged exposure to the 200keV electron beam of TEM has been investigated by the simultaneous acquisition of Fe-*L* and O-*K* edge EELS data, EELS and EDX compositional data and SAED. A safe fluence level of 10^8 electrons nm^{-2} has been established, below which both 2LFh and P-doped 2LFh can be observed in their pristine state. The same safe fluence level has previously been established for 6LFh under the same conditions (Pan, 2006; Pan et al., 2006; Pan et al., 2010). Beyond the safe fluence limit alteration of both pristine 2LFh and the phosphorus associated 2LFh specimens proceeds by preferential loss of oxygen, reduction of iron and concomitant phase transformation to a material with characteristics similar to that of magnetite.

Results here demonstrate that of the major iron-oxides, the EELS ELNES of the O-*K* edge of ferrihydrite is most similar to that of either maghemite or magnetite (Brown et al., 2007). The Fe-*L* signal is typical of a predominantly Fe(III) bearing iron-oxide material in which the iron atoms reside in six-fold coordination with oxygens and/or hydroxyls (Grunes et al., 1982; Colliex et al., 1991; van Aken at al., 1998; van Aken & Liebscher, 2002; Brown et. al, 2001). Support for the newly proposed Michel model for ferrihydrite (Michel at al., 2007) comes from Fe-*L* edge EELS analysis which allow for a significant proportion ($93 \pm 25\%$) of tetrahedrally coordinated iron in the pristine structure of 2LFh.

BF-TEM imaging and SAED are in good agreement with previous TEM investigations of ferrihydrite (Janney et al., 2000a, 2000b; Janney et al., 2001)

Chapter 6 Characterisation of Phosphorus-Doped Two-Line Ferrihydrite

This chapter details the characterisation of synthetic two-line ferrihydrite (2LFh) coprecipitated in the presence of phosphorous (P-doped) prepared by the method outlined in section 4.1.3. First the results of bulk measurements using X-ray powder diffraction (XRD), Fourier transform infrared (FTIR) spectroscopy, Raman spectroscopy, combined thermal gravimetric analysis (TGA) and differential scanning calorimetry (DSC) and X-ray photoelectron spectroscopy (XPS) are presented and each discussed accordingly. Following on from this the results of characterisation using analytical electron microscopy are presented for selected P\Fe levels. Emphasis here is on establishing a safe electron fluence value with which these samples may be observed. Table 6.1 provides an overview of the samples examined in the current chapter.

Table 6.1 Details of samples examined in Chapter 6.

Sample Full Name	**Abbreviated Name(s)**	**Sample Description**
Synthetic two-line ferrihydrite	2LFh	Two-line ferrihydrite synthesised *in vitro* according to the method provided in section 4.1.1.
Phosphorus doped synthetic two-line ferrihydrite	2LFhPX, P-doped 2LFh 2LFhP0 ≡ 2LFh 2LFhP1 or P1, 2LFhP3 or P3, 2LFhP5 or P5, 2LFhP10 or P10, 2LFhP20 or P20, 2LFhP30 or P30	2LFh coprecipitated *in vitro* in the presence of phosphorus according to the method provided in section 4.1.3. Molar quantities of PO_4 were chosen to achieve a range of P/Fe levels (0.01, 0.03, 0.05, 0.10, 0.20 & 0.30). X is the atomic percent P with respect to Fe. e.g. for P/Fe = 0.20, X = 20 and the sample is denoted 2LFhP20

6.1 X-Ray Powder Diffraction

Displayed in Figure 6.1 are the powder XRD profiles for the 2LFhPX series. In order to facilitate comparison, the profiles have been: (1) subtracted from the underlying background signal; (2) normalised by the respective profile intensity maximum and (3) smoothed using a Gaussian of appropriate width that information (Bragg) was neither lost or introduced. The XRD profile acquired for iron(III) phosphate dihydrate ($FePO_4 \cdot 2H_2O$), used as a reference mineral, is also displayed here.

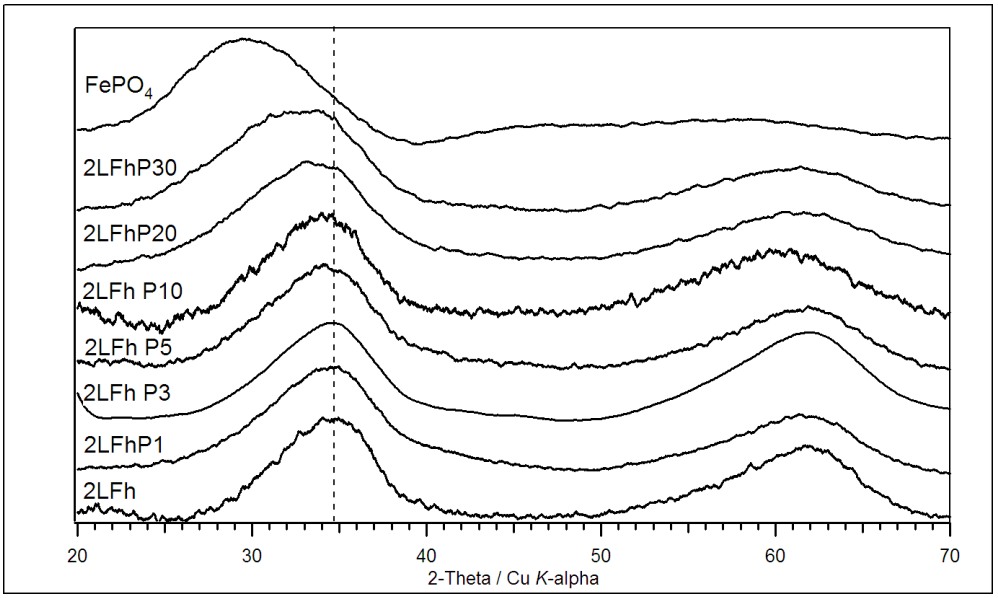

Figure 6.1 Comparison of powder X-ray diffraction patterns for the synthetic two-line ferrihydrite phosphorus doping series. Also shown for comparison is the XRD pattern of $FePO_4 \bullet 2H_2O$. With increasing P/Fe levels it can be seen that the general form of the undoped two-line ferrihydrite (2LFh) profile is preserved.

It can be seen from Figure 6.1 that with increasing P/Fe levels the general form of the undoped 2LFh profile is preserved: that is, two broad maxima at approximate *d*-spacings of 2.5 - 2.6 Å and 1.5 Å (35˚ and 62˚ 2θ CuKα) suggesting extremely small scattering domains (Towe & Bradley, 1967). For P/Fe levels of 0.10 and above there is a noticeable shift in the position of the peak maximum of the low-angle reflection to larger *d*-spacings (lower angles). Accompanying this shift is a broadening of both peaks with increasing P/Fe: this effect is most pronounced for the high-angle peak. Both effects have been previously observed for 2LFh coprecipitated in the presence of $NaH_2PO_4 \cdot H_2O$ (Thibault, Rancourt, Evans, & Dutrizac, 2009). Here the authors suggest two possible causes either: incorporation of PO_4 in the structure of the coprecipitated particles or a reduction in overall particle size due to surface poisoning by PO_4 inhibiting growth or a combination of both.

6.2 Fourier Transform Infrared Spectroscopy

Presented in Figure 6.2 is a comparison of the FTIR spectra acquired from the series of 2LFhPX samples for the spectral range 600-4000 cm^{-1} and (right) a detailed (zoomed) view of the 850-1160 cm^{-1} region. The FTIR profile of the reference mineral, $FePO_4 \cdot 2H_2O$, is also shown on the left.

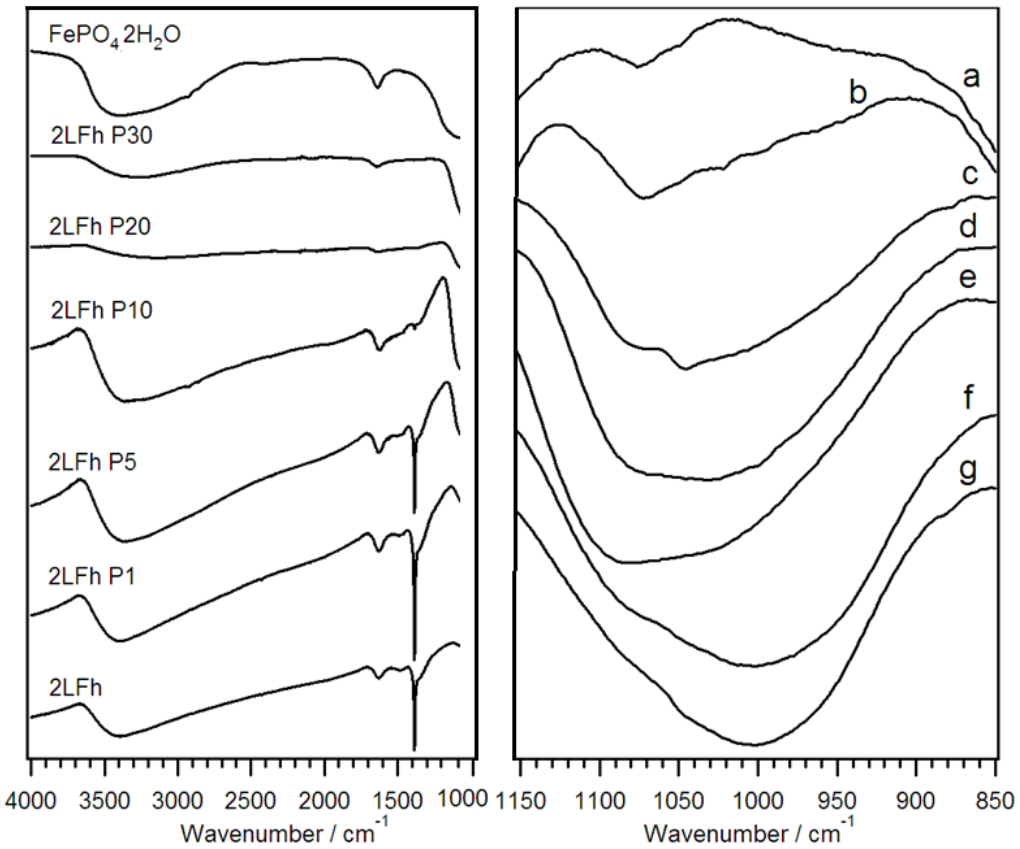

Figure 6.2 A selection of Fourier transform infrared spectra for the synthetic two-line ferrihydrite phosphorus doping series (2LFhPX defined in section 4.1.3.) and $FePO_4 \bullet 2H_2O$ (left) and a zoomed view of the P-O stretching region for phosphorus-doped two-line ferrihydrite samples (right). In the right hand pane letter annotations above each curve correspond to P/Fe levels of (a) 0.00(P0), (b) 0.01(P1), (c) 0.03(P3), (d) 0.05(P5), (e) 0.10(P10), (f) 0.20(P20) and (g) 0.30(P30) as defined in section 4.1.3.

The first observation to make is that the NO_3^- peak (1385 cm^{-1}) (Parfitt, Atkinson, & Smart, 1975) is present for P/Fe levels of 0.10(P10) and lower but not present in the spectra of samples with higher P levels. This may, on the one hand, reflect the increased efficacy of the washing procedure on the removal of NO_3^- from the samples of higher P levels. However, since 2LFhPX samples were subject to a consistent method of washing, this most likely indicates the replacement of the NO_3^- anion with the relatively more strongly binding phosphate during hydrolysis (Parfitt et al., 1975).

The relative intensity of the absorption signal between 2500 - 3600 cm^{-1} shows significant variation across the P-doping series, being least prominent for P/Fe $\geq$ 0.20(P20) when compared to lower P levels. As noted in chapter 5, this region along with the absorption feature at 1622 cm^{-1} are due to the hydroxyl (OH^-) anion and can be attributed to the extent of hydration or water content of the sample (Russell, 1979).

Shown in the right hand panel of Figure 6.2 is a detailed view of the raw signal in the 850-1160 cm^{-1} region which contains the various vibrational modes of the phosphate anion which by simple comparison are seem to be broadly similar to those observed elsewhere for P absorbed at the ferrihydrite surface (Arai & Sparks 2001; Frost, Martens, Williams & Kloprogge, 2002). An attempt was made to decompose the phosphate absorption band into a linear combination of Gaussian profiles as to assess the molecular configurations of the phosphate anion as per Arai and Sparks (2001). This analysis was unsuccessful as it was difficult to consistently determine the background in this region so as to properly extract the phosphate band for analysis. Modeling the background on that of the underlying 2LFh signal did not produce satisfactory results. Also attempted was a linear baseline background extraction between 835 cm^{-1} and 1188 cm^{-1} this appeared to work well for the 2LFhP20 and 2LFhP30, for which the phosphate band could be satisfactorily decomposed into three Gaussian peaks, however, for P/Fe levels of 0.10(P10) and lower a combination of three Gaussian peaks did not describe this feature well, leaving a significant residual signal between the experimental data and the fitted envelope. This residual signal may be due in part to the underlying 2LFh-like signal which, as can be seen from Figure 6.2, is not entirely featureless within this spectral interval. In addition, for P/Fe < 0.10(P10), the proportion of phosphate that is either surface bound or in close association with 2LFh is likely to constitute an increasing fraction of the total phosphate present as the P/Fe decreases. This phosphate would result in a P-O region which is fundamentally different to that of an amorphous iron-phosphate phase. Indeed Gálvez et al., (1999) noted, whilst studying the IR spectra of phosphated hematite, that when a hematite surface is phosphate saturated the P-O region of the spectrum is composed of two broad bands at 1015 cm^{-1} and 1105 cm^{-1} (Gálvez, Barrón, & Torrent, 1999). This is also apparent in Figure 6.2 and is consistent with the fact that 2LFhP20 and 2LFhP30 could be decomposed into two bands.

6.3 Raman Spectroscopy

Figure 6.3 compares the Raman spectroscopic data collected for the 2LFhPX series. For P/Fe > 0.1(P10), the Raman signal is essentially identical the that observed from 2LFh (as discussed in section 5.3) and therefore provides no indication of the presence of phosphate.

For P/Fe = 0.05(P5) and greater, there is an increase in relative signal intensities for both the 900 - 1200 cm^{-1} and < 600 cm^{-1} intervals which is seen to increase with P/Fe. Between 900 - 1200 cm^{-1} the extra intensity is due to the v_1 P-O stretching excitations of phosphate (Nakamoto & Brown, 2003; Mayo, Miller, & Hannah, 2004). In the case of 2LFhPX, this broad phosphate-band appears around 1045 cm^{-1} whereas the corresponding feature for $FePO_4 \cdot 2H_2O$ (see Figure 6.4) has a similar profile but is shifted slightly, peaking instead around 1025 cm^{-1}. This shift likely reflects the difference in the precise bonding environments about the phosphate ion between these compounds. The precise origin of the extra intensity in the region < 600 cm^{-1} for 2LFhPX is unknown, however, it is similar to that observed for $FePO_4 \cdot 2H_2O$ (see in Figure 6.4).

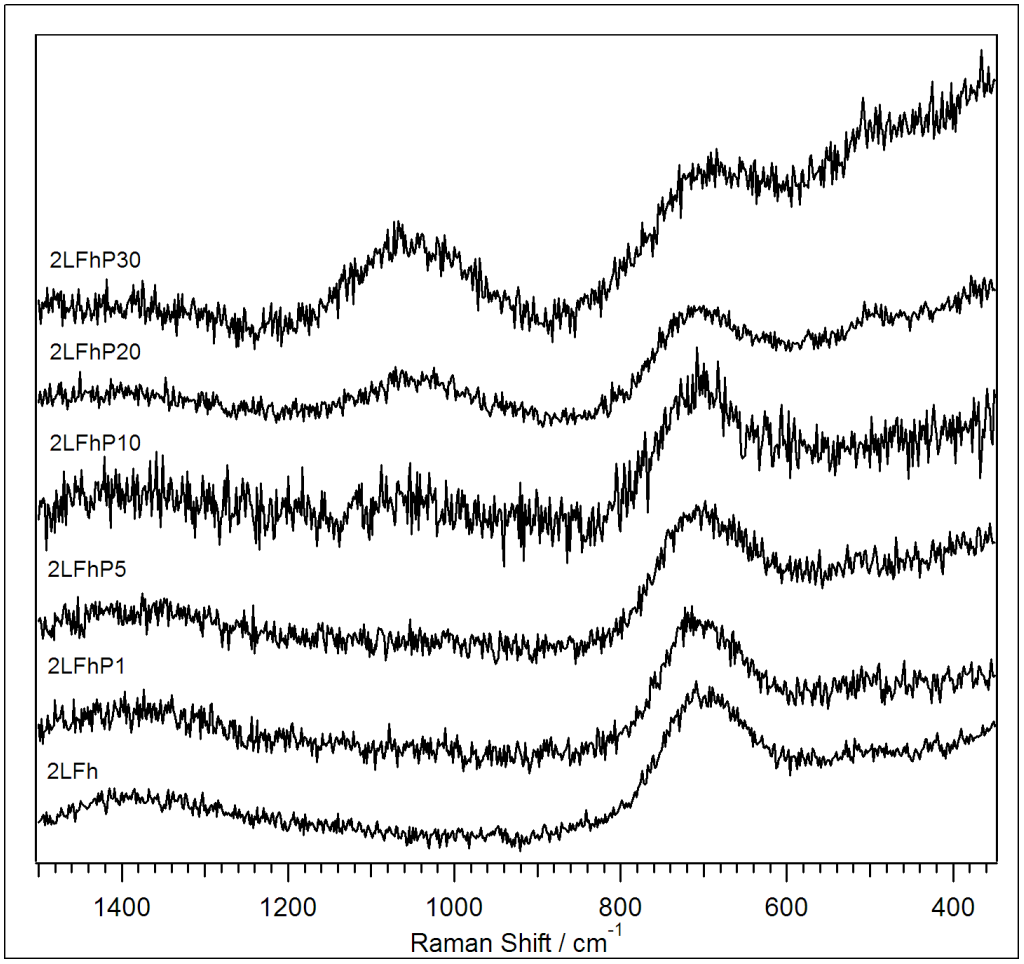

Figure 6.3 Comparison of Raman scattering signals of the synthetic two-line ferrihydrite phosphorus doping series (2LFhPX defined in section 4.1.3.) with P/Fe levels of 0.00, 0.01(P1), 0.05(P5), 0.10(P10), 0.20(P20) and 0.30(P30) as defined in section 4.1.3.

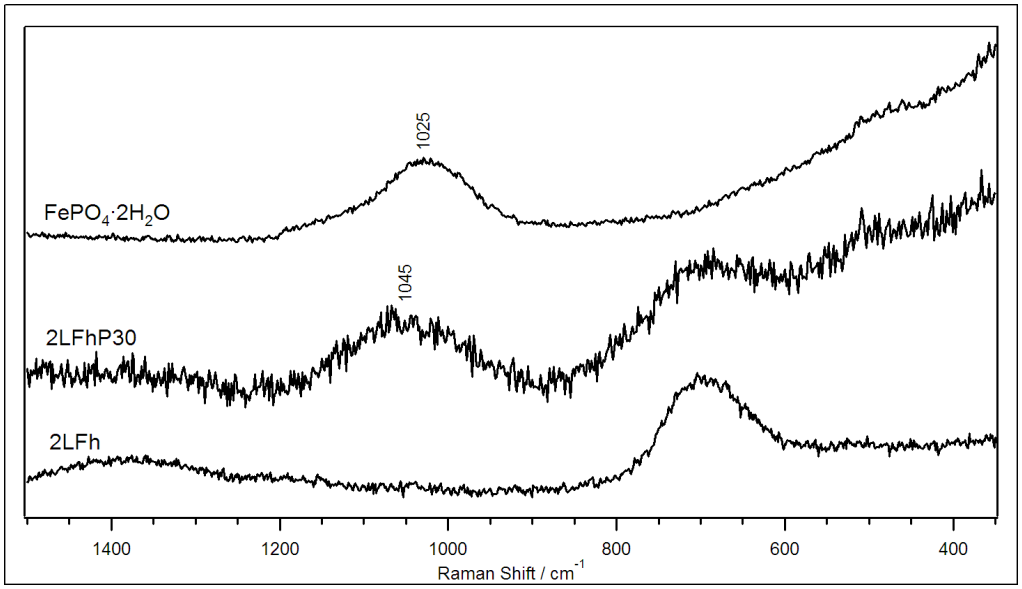

Figure 6.4 Comparison of Raman scattering signals of synthetic two-line ferrihydrite, synthetic phosphorus doped two-line ferrihydrite (2LFhP30 (P/Fe = 0.30)) and $FePO_4 \cdot 2H_2O$.

It is apparent from inspection of Figure 6.3 that for P/Fe levels of 0.10(P10) and greater the Raman signals appears to be composed of a linear mixture of *pure* 2LFh and iron-phosphate signals. In order to assess whether these spectra of the 2LFhPX series could indeed be decomposed into two such components, a two-component linear least squares fitting procedure was applied to the 2LFhPX curves. For this, the 2LFh and $FePO_4 \cdot 2H_2O$ were used as reference signals which, in the absence of a more suitable method, were normalised by setting the respective signal intensity maxima equal to unity. A fitting region between 480–1360 cm^{-1} was chosen to cover the main spectral features of each reference spectrum (i.e. the phosphate band at ~1030 cm^{-1} and the 2LFh band at ~700 cm^{-1}).

Figure 6.5 displays the fractional $FePO_4 \cdot 2H_2O$ contribution to the fitted profile which was found to linearly increase with P/Fe. As was the case for the XRD linear fitting, this result is purely qualitative since the reference spectra signals were normalised somewhat arbitrarily by setting the intensity of the major spectral feature in each case equal to unity. If a quantitative estimation of the relative phase fractions is desired the fitting procedure would need calibrating by the measurement of standards for which the ratio 2LFh:iron-phosphate is well known.

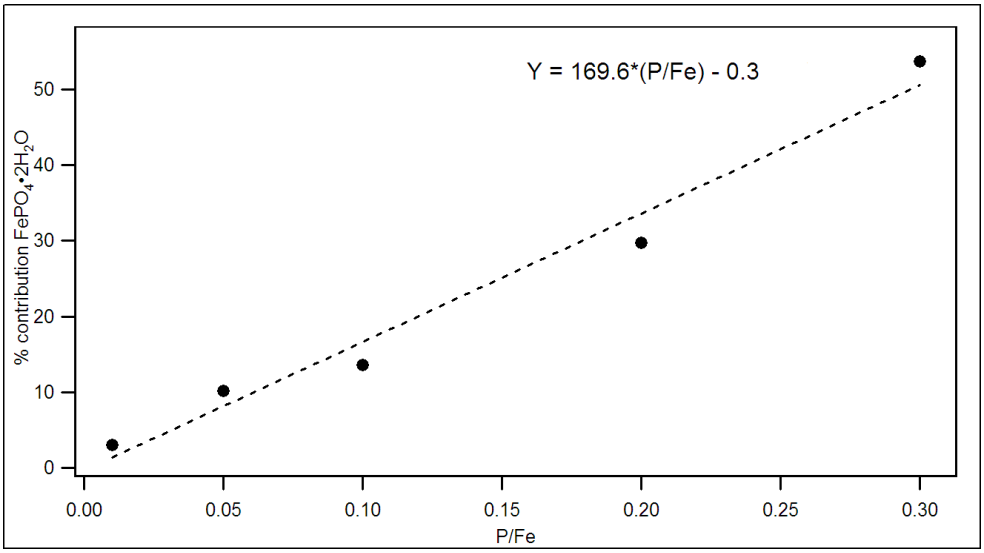

Figure 6.5 Fractional contribution of $FePO_4•2H_2O$ reference Raman spectrum to the best-fit linear combination of $FePO_4•2H_2O$ and synthetic two-line ferrihydrite to synthetic phosphorus doped two-line ferrihydrite (2LFhPX defined in section 4.1.3.) as a function of phosphorus-doping. The dashed line represents a linear fit to the data points, indicating doping results in an increased contribution of $FePO_4•2H_2O$ character.

6.4 Thermal Analysis

Thermal analysis was applied to both 2LFh and a series of six 2LFhPX's with P/Fe's between 0.01 and 0.30. For 2LFh combined DSC and TGA results are presented in Figure 6.6, whereas for the 2LFhPX series TGA and DSC results are given separately in Figure 6.7 and Figure 6.8 respectively.

Data is presented *as acquired* without correction and consequently, beyond ~300 °C, all DSC data presented here are seriously affected by (negative) baseline drift which has not been corrected for (since a background profile was not recorded) and should not be interpreted as an endothermic event.

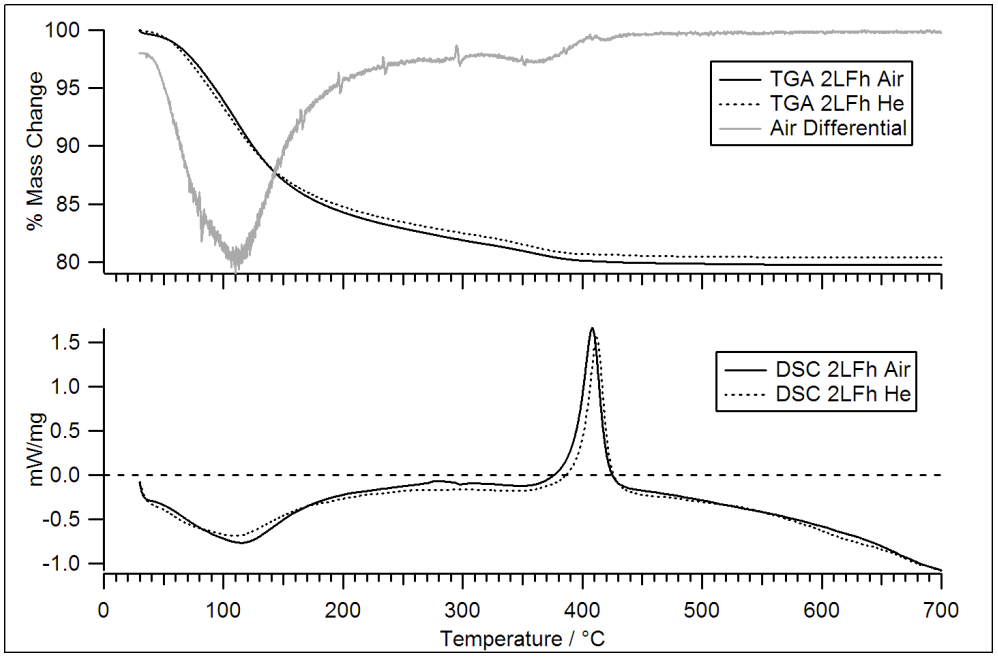

Figure 6.6 Thermogravimetric analysis (top) and differential scanning calorimetry (bottom) of synthetic two-line ferrihydrite as acquired under air and He atmospheres. The grey curve (top) represents the differential of the percent mass-change for synthetic two-line ferrihydrite as measured in air. The corresponding differential mass-loss curve for He purge gas (not shown) is almost identical.

As can be seen from inspection of Figure 6.6 there is little difference between the TGA results for 2LFh heated in air and helium. In both cases, the sample lost approximately 20 ± 0.1% of its initial mass by the experiment's end. This figure is slightly less than the 25.6 ± 0.1% mass-loss quoted by Wenqian et al. (2011), for 2LFh that had been synthesised by the same protocol used here, however, having been dried at room temperature (Wenqian, Hausner, Harrington, Lee, Strongin, & Parise, 2011). The region of continuous mass-loss corresponds well with the endothermic peak in the DSC data, an event which is known to accompany OH loss and/or loss of structural water from iron-(hyd)oxides (Schwertmann, 1991). The maximum rate of mass-loss occurs at around 110 °C corresponding to the minima (most endothermic event) in the DSC data. The DSC endothermic event extends from approximately 28 - 250 °C, as has previously been observed for 2LFh (Wenqian et al., 2011). The other prominent feature in the DSC data is an exothermic event occurring at approximately 410 °C, which is not accompanied by mass-loss, and which may be due to the phase transition to 2LFh → hematite, which has been previously noted to occur at ~ 425 °C for 6LFh (Towe & Bradley, 1967) and 415 °C for 2LFh (Wenqian et al., 2011) using a similar heating protocol as employed here. This 410 ± 1°C DSC event corresponds well with the point at which the rate of mass-loss, as seen in the differential mass-loss curve, tends to zero.

Hematite (α-Fe_2O_3) is a pure oxide in that it ideally contains no OH or H_2O. As such it can, therefore, be assumed that by 410 °C 2LFh has lost all its OH/H_2O.

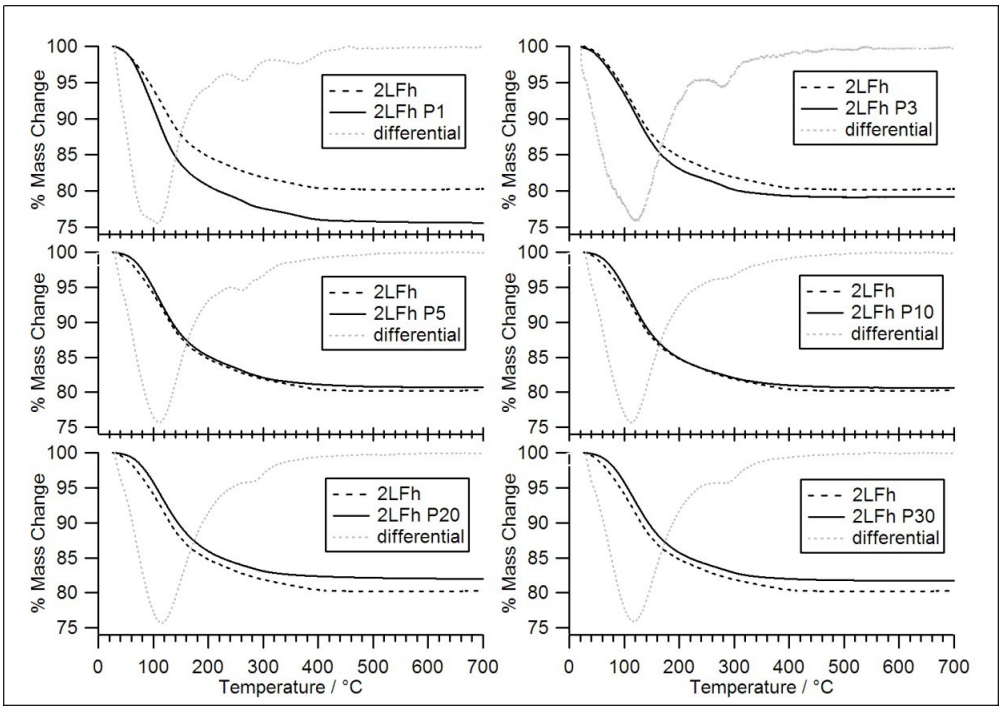

Figure 6.7 Comparison of thermogravimetric analysis data for synthetic phosphorus doped two-line ferrihydrite series (2LFhPX defined in section 4.1.3.) acquired over the range 3 to 700ºC using air as a purge gas. For comparison, the thermal mass loss curve of pure synthetic two-line ferrihydrite (dashed) and the differential-mass-loss of each respective sample (grey-dashed) are shown.

The TGA mass loss curves for the 2LFhPX samples are broadly similar to that of 2LFh (see Figure 6.7). There is some variation in the total mass lost at 700 °C, however, the difference is only a few percent and may reflect the degree of dryness of the samples since there is no systematic variation observed with P/Fe. Subtle differences, emphasised in the differential mass-loss curves, can be observed between the 2LFhPX mass-loss curves and that of 2LFh. The first difference is that there is a secondary mass-loss event which takes place at 260 °C for the 2LFhPX samples, which is not observed for 2LFh. This event is coincident with two subtle exothermic peaks in the DSC data for all 2LFhPX samples, with the exception of 2LFhP3 (Figure 6.8). These minor exotherms lie in the 210 – 300 °C region and their intensity is seen to vary approximately in proportion to P/Fe. As such these may be associated with the decomposition of iron phosphate phase.

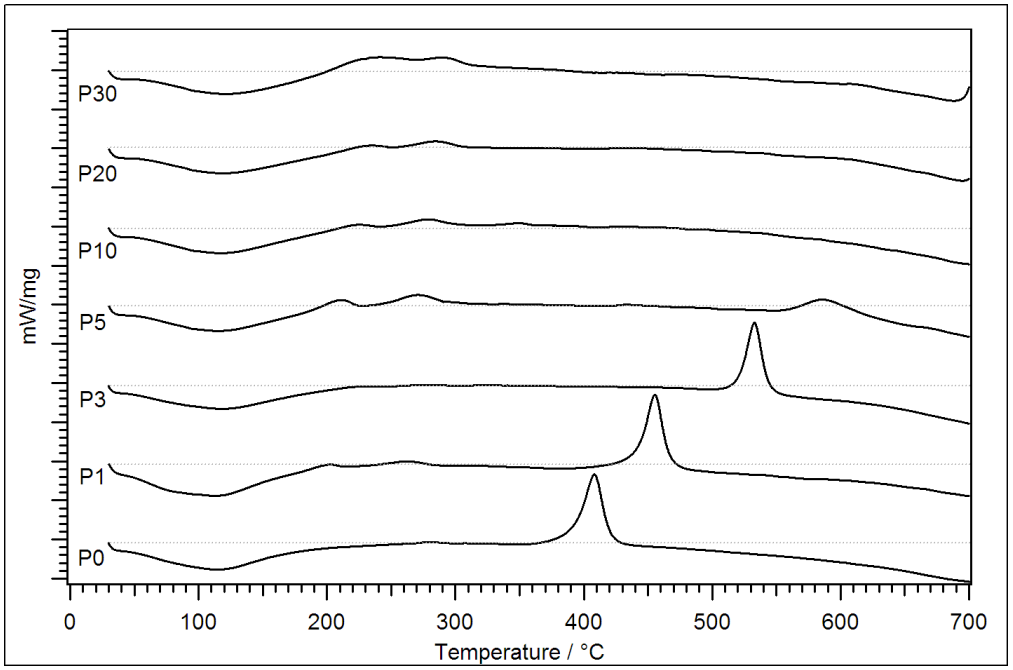

Figure 6.8 Differential scanning calorimetry data for the synthetic phosphorus doped two-line ferrihydrite series (2LFhPX defined in section 4.1.3.) acquired over the range 3 to 700ºC under oxic conditions. With increasing phosphorus content the delay and suppression of the exothermic phase transformation peak can be clearly seen.

The DSC curves show that the exothermic event, which formally lay at 410 ± 1°C for 2LFh, has been delayed to 455, 533, 587 °C for P/Fe levels of 0.01(P1), 0.03(P3) and 0.05(P5), respectively (Figure 6.8). For P/Fe levels of 0.10(P10) and beyond, this exotherm is not present indicating suppression of the phase transformation 2LFh to hematite. It can also be seen that for 2LFhP5 this feature is suppressed to approximately 15% the intensity of that of the other samples of lower P/Fe. This most probably indicates that for 2LFhP5 a reduced proportion of the sample has undergone transformation when compared to samples of lower P/Fe. A similar delay and suppression of the DSC exothermic event has been observed for a series of synthetic 2LFhs coprecipitated in the presence of silica (Carlson & Schwertmann, 1981).

Tabulated in Table 6.2 is a summary of the TGA data presented in Figure 6.7. The estimate of OH/Fe given in the table has been calculated assuming that up to 400 °C, i.e. before the hematite transition temperature, all mass-loss can be attributed solely to the loss of adsorbed water and that beyond this temperature structural OH and H_2O is lost. This estimate of OH/Fe is close to that of 0.18 which has recently been given for *pure* 2LFh based on TGA measurements (Wenqian et al., 2011). Compared to the *ferrihydrits* (Drits et al., 1993) and the revised Michel (*ferrifh*) (Michel et al., 2007) models for ferrihydrite, for which OH/Fe = ~1 and 0.90

respectively, this estimate calculated herein is OH poor. Better agreement, however, is found with the *Fhyd2/3/6* Michel models for which OH/Fe = 0.20 (Drits et al., 1993; Michel et al., 2007; Michel et al., 2010).

Table 6.2 Summary of thermogravimetric analysis data for the synthetic phosphorus doped two-line ferrihydrite series (2LFhPX defined in section 4.1.3.) as acquired under oxic conditions

Sample	Original Mass / mg	% Mass-loss between:			Total % lost @ 700°C	Estimated initial OH/Fe
		0-200°C	200-400°C	400-700°C		
2LFh	21.76	15.2	4.3	0.1	19.7	0.25
2LFh P1	33.17	19.3	4.7	0.4	24.4	0.30
2LFh P3	33.58	16.9	3.8	0.1	20.8	0.22
2LFh P5	31.11	14.8	4.0	0.4	19.3	0.25
2LFh P10	31.81	15.1	3.9	0.4	19.4	0.23
2LFh P20	32.44	14.1	3.6	0.4	18.0	0.21
2LFh P30	30.72	14.3	3.7	0.3	18.3	0.22

6.5 X-Ray Photoelectron Spectroscopy

Elemental Quantification

Displayed in Table 6.3 are the elemental concentrations for the various ferrihydrite samples used in this study as determined by XPS analysis. The concentrations calculated are slightly different depending on the model function used for removal of the background contribution. In all cases, the Tougarrd profile provides P % atomic values which are closer to the target P concentrations used during sample synthesis.

Table 6.3 Comparison of the measured elemental concentrations of synthetic six-line ferrihydrite (6LFh), synthetic two-line ferrihydrite (2LFh), synthetic phosphorus doped two-line ferrihydrite series (2LFhPX defined in section 4.1.3.) and $FePO_4.2H_2O$ as determined by X-ray photoelectron spectroscopy. Elemental concentration values are quoted as atomic percent. Data was measured using the VG Scienta ESCA300 spectrometer at the NCESS facility.

Sample	Shirley Background			
	Fe	O	P	P/Fe
6LFh	38.8	61.2	-	-
2LFh	31.1	68.9	-	-
2LFhP3	31.1	67.2	1.7	0.05
2LFhP5	31.1	66.5	2.4	0.08
2LFhP10	28.8	66.9	4.4	0.15
2LFhP20	23.7	68.8	7.5	0.32
2LFhP30	17.2	71.1	11.7	0.68
$FePO_4 \cdot 2H_2O$	7.6	73.5	19.0	2.50
Sample	Tougarrd Background			
	Fe	O	P	P/Fe
6LFh	39.4	60.6	-	-
2LFh	39.5	60.5	-	-
2LFhP3	39.1	59.4	1.6	0.04
2LFhP5	38.8	59.4	1.8	0.05
2LFhP10	36.4	59.9	3.7	0.10
2LFhP20	31.3	62.2	6.5	0.21
2LFhP30	25.2	64.9	9.9	0.39
$FePO_4 \cdot 2H_2O$	13.3	69.4	22.6	1.70

Core-Level XPS: Fe 2p

The Fe 2*p* peaks from the 2LFhPX series are displayed in Figure 6.9. In each case the maxima of the Fe $2p_{3/2}$ and Fe $2p_{1/2}$ peaks are at approximate binding energies of 710.6 and 724.5 eV, respectively, consistent with previously reported values for synthetic ferrihydrite (Descostes, Mercier, Thromat, Beaucaire, & Gautier-Soyer, 2000; Frau, Addari, Atzei, Biddau, Cidu, & Rossi, 2011). At binding energies of some 8 eV, above each of the main Fe 2*p* peaks lie corresponding "shake-up" satellite peaks. These peak positions, along with the relative separation between the principle peak and their satellites are typical of ferric iron (McIntyre & Zetaruk, 1977; Descostes et al., 2000; Frau et al., 2011). The Fe 2*p* spectrum measured from 6LFh, not shown here, was indistinguishable from that of 2LFh.

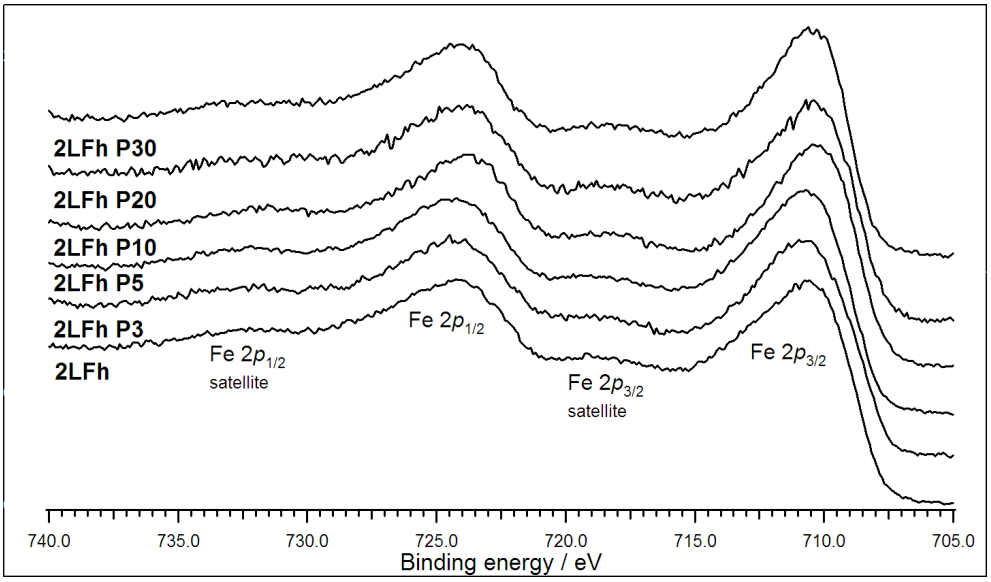

Figure 6.9 Comparison of the iron 2p X-ray photoelectron peaks for the synthetic phosphorus doped two-line ferrihydrite series (2LFhPX defined in section 4.1.3.) as measured using the VG Scienta Escalab 250 spectrometer at the University of Leeds (UK).

Core-Level XPS: O1s

Analysis of the O1*s* XPS peaks were carried out following the fitting method outlined in section 4.2.3. In all cases the O1*s* peak was found to be well fitted by three peaks, an example of such a fit is shown in Figure 6.10 and the results of the fitting are summarised in Table 6.4.

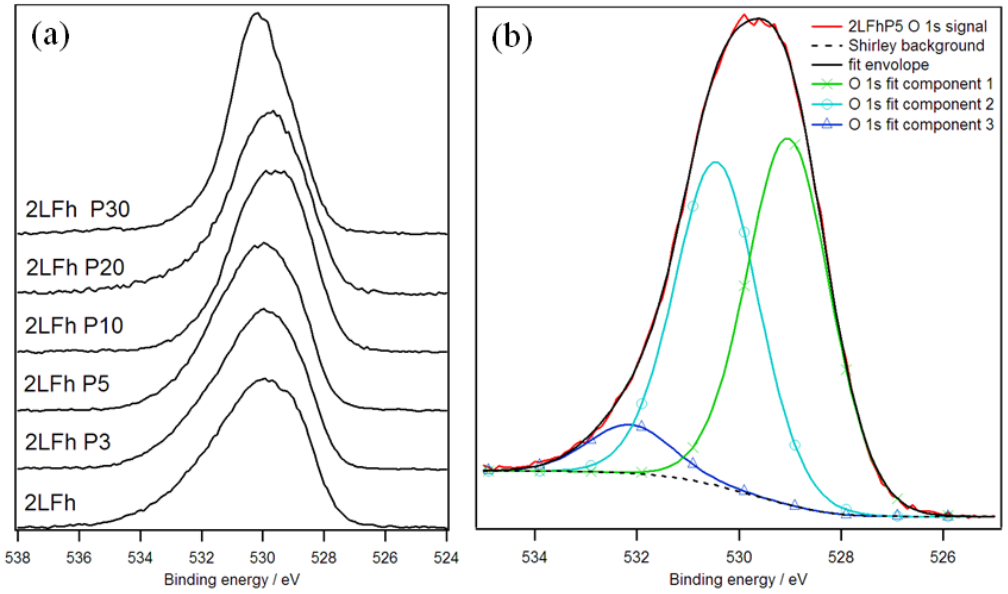

Figure 6.10 (a) X-ray photoelectron oxygen 1s peaks for the synthetic phosphorus doped two-line ferrihydrite series (2LFhPX defined in section 4.1.3.) and (b) an example of a three component fit to the oxygen 1s X-ray photoelectron peak of synthetic two-line ferrihydrite with 5% phosphorus doping (2LFhP5). The fitting routine used is explained in detail in section 4.2.3.

Table 6.4 Summary of X-ray photoelectron oxygen 1s peak fitting results for synthetic phosphorus doped two-line ferrihydrite series (2LFhPX defined in section 4.1.3.). The fitting routine is explained in detail in section 4.2.3.

Sample	Fitted Peak 1		Fitted Peak 2		Fitted Peak 3		FWHM
	centre (eV)	% Area	centre (eV)	% Area	centre (eV)	% Area	(eV)
2LFh	529.3	51	531.0	37	533.0	12	2.2
2LFh P3	529.3	49	530.8	37	532.6	14	2.1
2LFhP5	529.4	50	530.9	40	532.5	10	2.1
2LFhP10	529.0	50	530.4	44	532.1	7	1.9
2LFhP20	529.3	56	530.6	36	532.9	8	2.2
2LFhP30	529.2	28	530.4	64	532.4	7	1.8
Average =	529.3	-	530.7	-	532.6	-	2.1
Std Dev. =	0.1	-	0.3	-	0.3	-	0.2

In each case the centroid positions of the three fitting peaks were fairly stable, especially considering the possible errors in exact binding energy calibration, having average values of 529.5 ±0.1, 530.7 ±0.3 and 532.6 ±0.4 eV for components 1, 2, and 3 respectively. According to the literature, O (oxide) ~529.8 eV, OH ~531.2 eV and H_2O ~532.5 eV (Lin, Seshadri, & Kelber, 1997). In XPS it is generally the initial state which predominates in determining the binding energy of a given species. As such the greater the number of bonds with increasingly electronegative atoms the more positive the chemical shift for a given element (Watts & Wolstenholme, 2003). However, in this case the peak at 532.6 eV would be assigned to some PO species (most likely PO_4) which would be at odds with the relative peak contributions which from the table above clearly shows that the relative magnitude of peak 3 (~532.6 eV) is negatively correlated with P/Fe. In examining phosphate treated iron surfaces Stoch and Stoch (1989) assigned O1s peaks at 531.6 eV to P=O species and 532.9 eV to POH (Stoch & Stoch, 1989).

Core-Level XPS: P2p

A selection of P2*p* peaks from the 2LFhPX series is displayed in Figure 6.11. There is less of a pronounced systematic shift in the P2*p* peak than for the other peaks, however, the low SNR makes background estimations difficult for fine structure analysis.

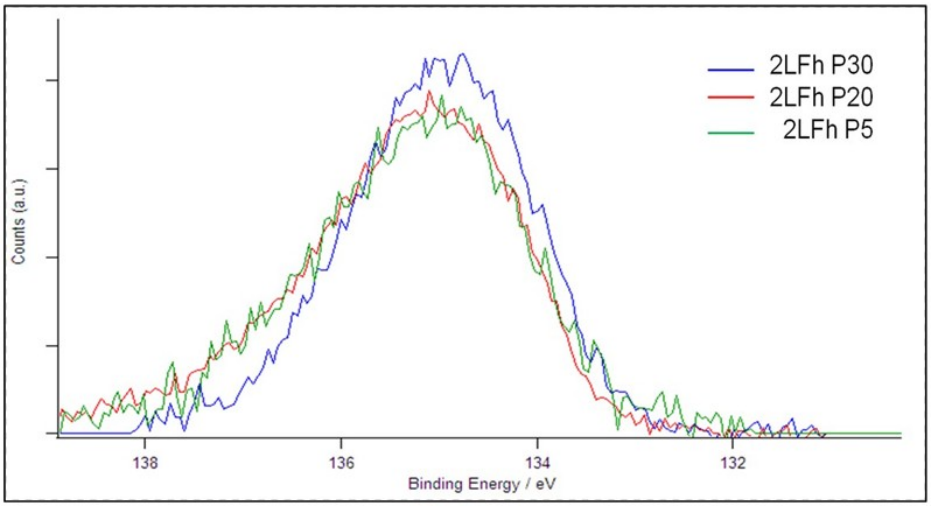

Figure 6.11 X-ray photoelectron phosphorus 2p peaks of selected synthetic phosphorus doped two-line ferrihydrites (2LFhPX defined in section 4.1.3.). For P/Fe levels below 0.20(P20) the peaks can be seen to be identical beyond this there is significant modification of peak profile indicating differences in bonding environment.

The same peak fitting analysis, as described in section 4.2.3 was performed on the P2*p* signal. In this case, the measured peaks were found to be well described by two fitted peaks, the results of which are summarised in Table 6.5.

Table 6.5 Summary of X-ray photoelectron phosphorous 2p peak fitting results for the synthetic phosphorus doped two-line ferrihydrite series (2LFhPX defined in section 4.1.3.). The fitting routine is described in detail in section 4.2.3.

Sample	Fitted peak 1		Fitted peak 2		FWHM
	centre (eV)	% Area	centre (eV)	% Area	(eV)
2LFhP5	132.5	88	134.4	12	2.1
2LFhP10	132.0	75	133.2	25	1.7
2LFhP20	132.0	89	134.1	11	1.8
2LFhP30	132.2	80	133.3	20	1.6
Average =	132.2	-	133.7	-	1.8
Std Dev. =	0.2	-	0.6	-	0.2

The lack of apparent systematic variation in the binding energy and profile of the P2*p* peak is consistent with the bonding environments being similar in each case.

6.6 Analytical Transmission Electron Microscopy

6.6.1 Beam Damage Assessment of 2LFh with 5% Phosphorous Doping

Figure 6.12 summarises the EELS Fe-*L* edge analysis of 2LFhP5 as a function of accumulated electron-fluence. As was the case with 2LFh (see section 5.4.1), error bars for the fitted ELNES data have been derived from the corresponding errors in the calculated fitting coefficient values. Over the fluence range 5.5 x 10^5 to 2.8 x 10^8

electrons nm^{-2} the ferric iron content is seen to remain fairly constant at around 85 ± 25% of the total iron present. Beyond 3.0 x 10^{8} electron nm^{-2} there is a marked drop in ferric iron content, which reaches a final value of approximately 20 ± 10% when a fluence of 4.1 x 10^{9} electron nm^{-2} had been reached. The ferric iron data has been fitted by an exponential function which, when extrapolated back to the zero-electron fluence limit, estimates 86 ± 25% of the total iron to be ferric. Over the course of the experiment, the average valence of the iron has been reduced from an initial starting value of 2.9 ± 1 to a final value of 2.2 ± 1. These results are very similar to those observed for 2LFh Fe-*L* EELS analysis given in section 5.4.1.

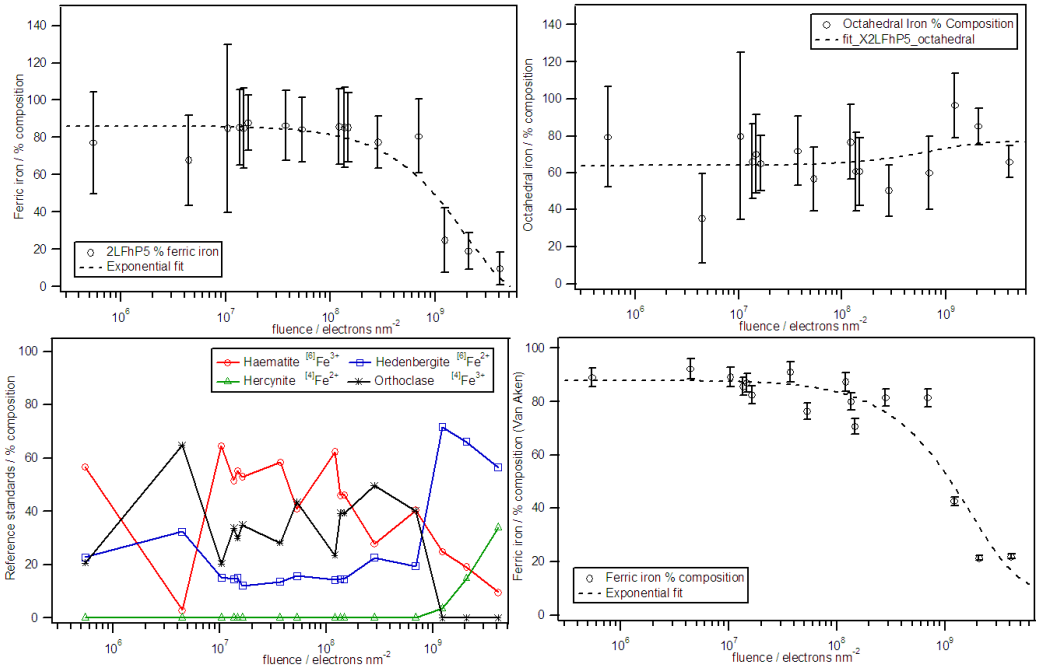

Figure 6.12 Summary of Fe-*L* energy-loss near edge structure analysis as a function of electron fluence applied to synthetic phosphorus doped two-line ferrihydrite with 5% phosphorus doping (2LFhP5). The onset of specimen damage can be seen to occur around 5 x 10^{7} electrons nm^{-2} as indicated by the drop in the ferric iron signal.

EDX analysis was used to monitor the elemental composition of the sample throughout the experiment, the results of which are summarised in Figure 6.13. Both the oxygen and phosphorus signals are seen to decrease after 2.5 x 10^{8} electron nm^{-2}, whereas the iron signal is seen to increase (relatively) at around the same fluence value, indicating the preferential loss of both oxygen and phosphorus from the material. This corresponds well with the point at which significant reduction of ferric iron is seen to occur and also the oxygen loss profile observed for 2LFh (section 5.4.1). Plotted in the bottom right-hand-side graph of Figure 6.13 is percentage change in the absolute oxygen, phosphorus and iron signals (normalised

by the copper signal) which again suggests that both oxygen and phosphorus are being preferentially removed from the material as a result of electron-beam irradiation.

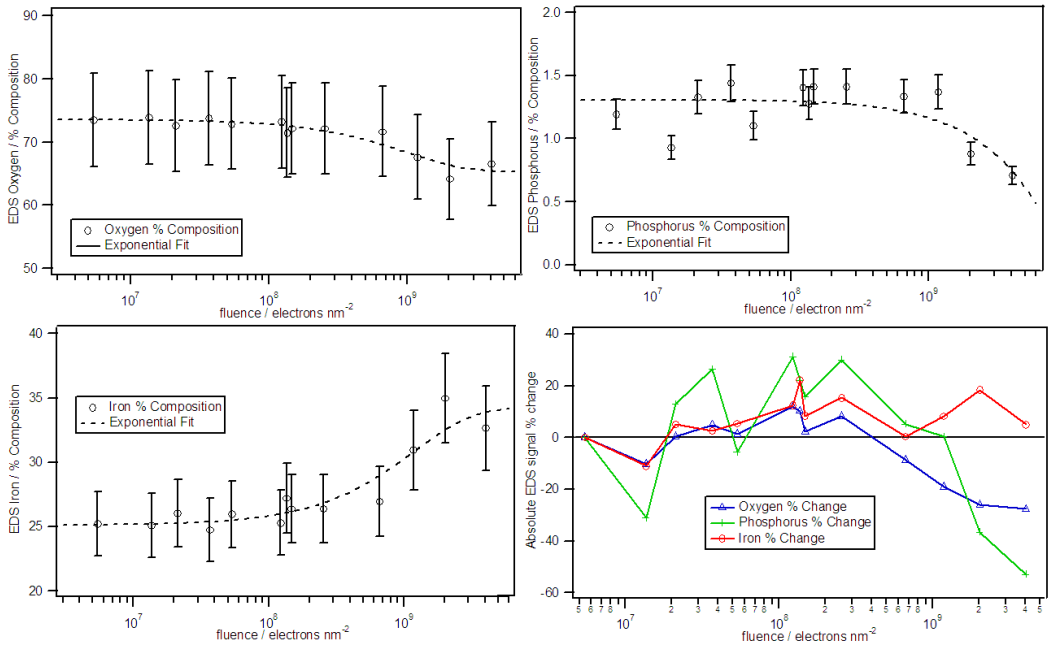

Figure 6.13 Summary of energy dispersive X-ray spectroscopic data acquired in the transmission electron microscope as a function of electon fluence for synthetic phosphorus doped two-line ferrihydrite with 5% phosphorus doping. (2LFhP5). Beyond 10^8 electrons nm^{-2} preferential loss of oxygen and phosphorous is observed. Exponential best fit lines are shown for illustration only. Error bars represent 10% of the base value.

A selection of SAED patterns acquired periodically throughout the experiment, are shown in Figure 6.14. The corresponding radially averaged patterns derived from these raw images are given in Figure 6.15. As was the case for 2LFh, upon increasing fluence the measured patterns were observed to evolve from ones in which two diffuse rings (typical of 2LFh) were seen at low-fluences (1.4 x 10^7 electrons nm^{-2}) to increasingly more *spotty* patterns at higher fluences (4.1 x 10^8 electrons nm^{-2}), indicating a coarsening of the sample and the presence of additional phases.

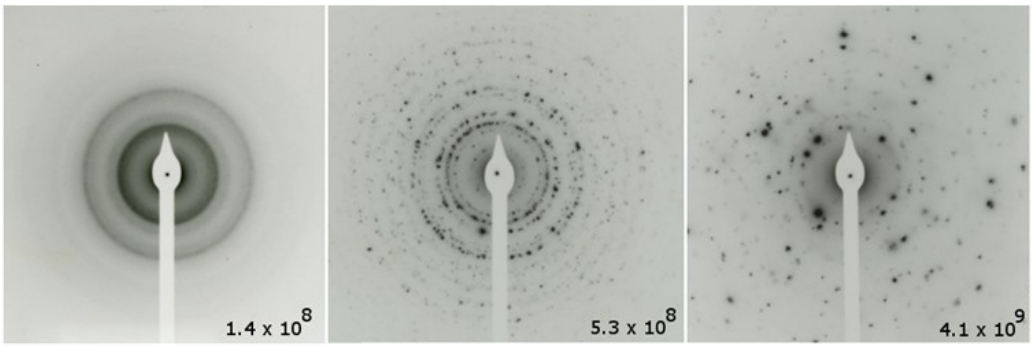

Figure 6.14 Selected-area electron diffraction patterns of synthetic 5% phosphorus doped two-line ferrihydrite (2LFhP5) acquired at various electron fluences. The effects of prolonged exposure to the electron beam can be clearly seen. Bold typeface numbers indicate electron fluence in electrons nm^{-2}.

It can be seen from these assignments and the stick-patterns shown in Figure 6.16 that a spinel phase (magnetite/maghemite) and wüstite are possible candidates for the conversion products of 2LFhP5 after being subjected to 4.1 x 10^9 electrons nm^{-2} (197 keV). A transformation of 2LFh to magnetite would involve the conversion of some ferric iron to ferrous and the increased probability of ferric iron occupying tetrahedral sites. A transformation to wüstite (FeO) would require the total reduction of the divalent state and an increase in Fe/O from approximately 0.5, a nominal value for 2LFh, to unity. These requirements are at least in part supported by the Fe-*L* edge and EDX data.

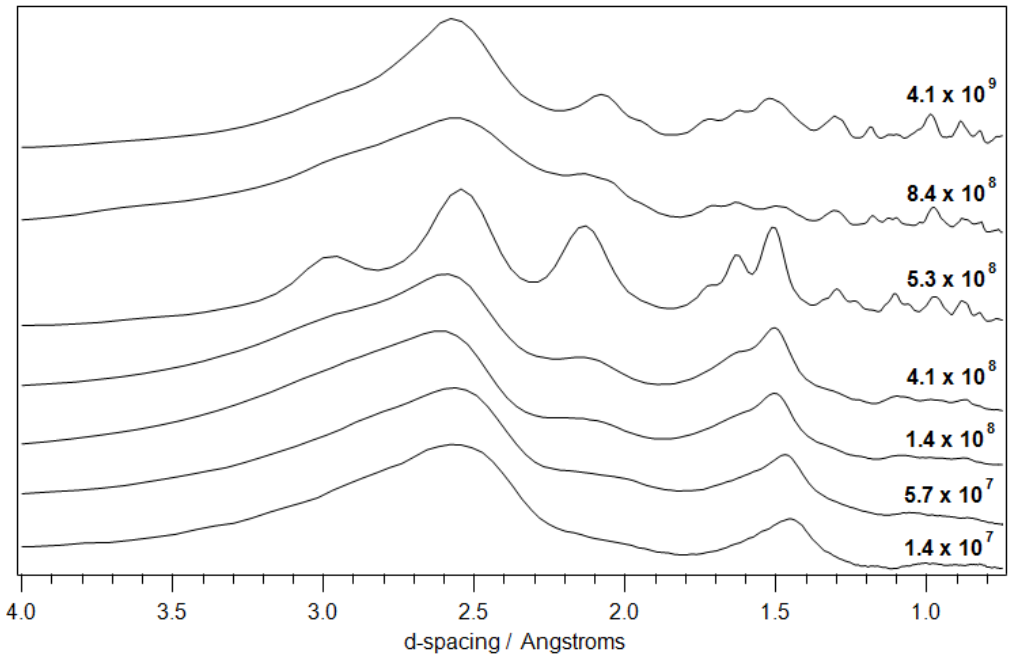

Figure 6.15 Radially-averaged selected area electron diffraction patterns of synthetic 5% phosphorus doped two-line ferrihydrite (2LFhP5) at various electron fluences showing an increase in the number of Bragg reflections with increasing fluence. Electron fluence values in units of electrons nm^{-2} are written in bold above each curve.

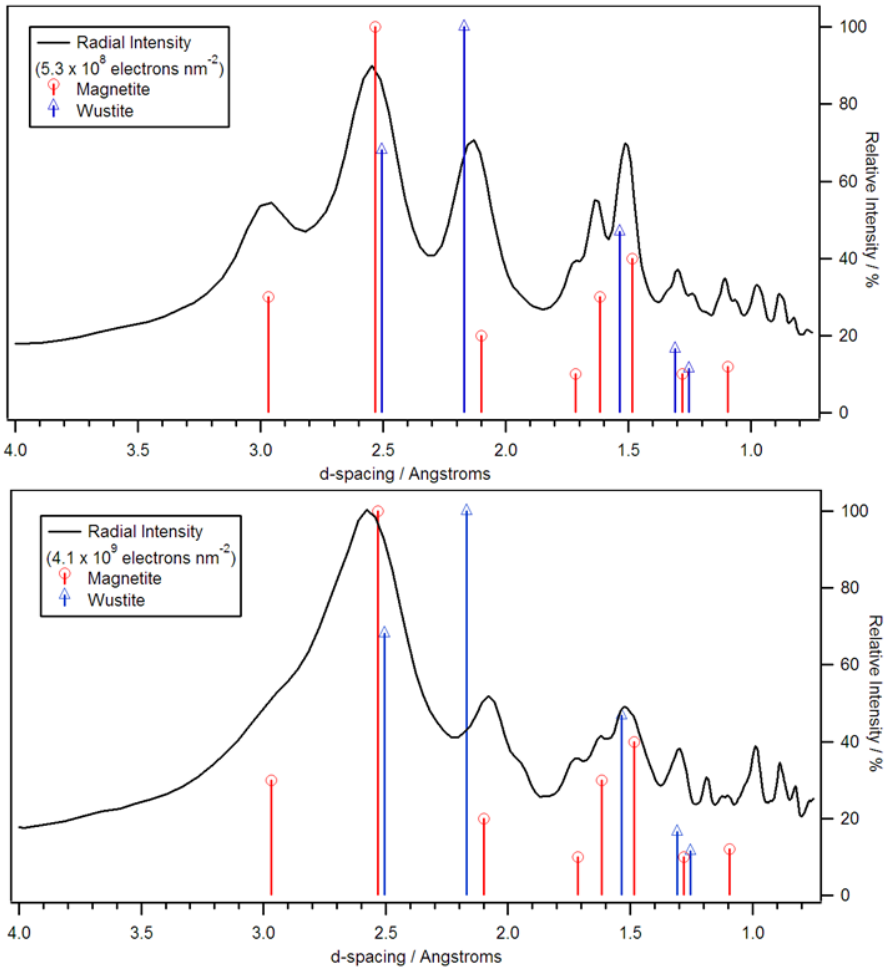

Figure 6.16 Radially-averaged selected area electron diffraction intensity profiles of synthetic 5% phosphorus doped two-line ferrihydrite (2LFhP5) as measured at fluences of 5.5 x 10^8 and 4.1 x 10^9 electrons nm^{-2}. Also shown for comparison the stick patterns of the most intense features (≥ 9% relative) for magnetite (JCPDS card 39-1349) and wüstite (JCPDS card 46-1312).

By the experiment's end (i.e. after an exposure to around 4.1 x 10^9 electrons nm^{-2}) the sample was seen to have changed from what was initially a large aggregate of small particles to an aggregate of larger particle with dimensions of 20-100 nm as is shown in Figure 6.17.

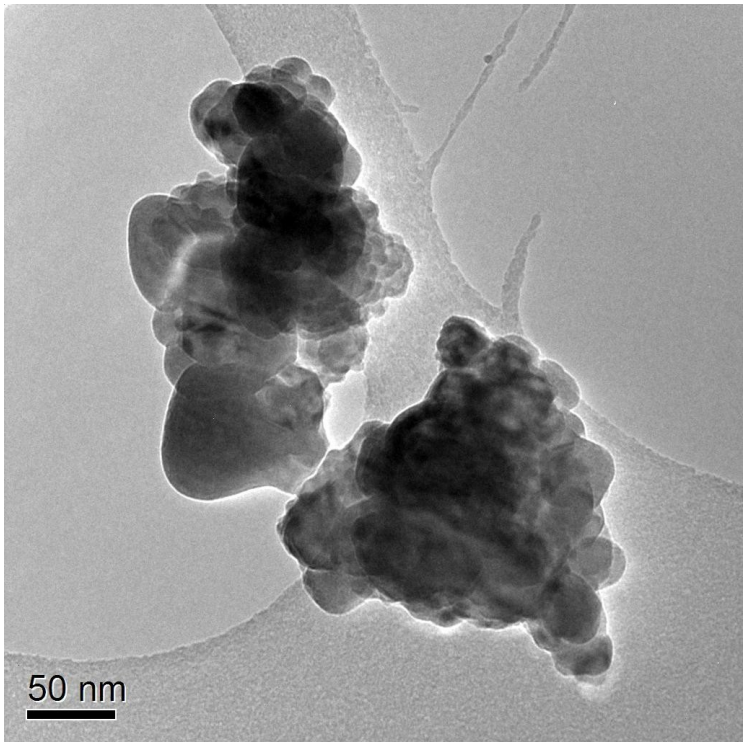

Figure 6.17 Bright-field transmission electron micrograph of synthetic 5% phosphorus doped two-line ferrihydrite (2LFhP5) after exposure to 4.1 x 10^9 electrons nm^{-2}. The effect of prolonged exposure to the electron beam can clearly be seen.

6.6.2 Beam Damage Assessment of 2LFh with 10% Phosphorous Doping

Figure 6.18 summarises the results of the EELS analysis as a function of increasing electron fluence for the 2LFhP10 sample. Again, as has been previously observed for the 2LFh and 2LFhP5 samples, there is a decrease in ferric iron content, the onset of which occurs at around 2 x 10^8 electrons nm^{-2}. The initial starting value for the ferric iron content as estimated from the NLLS fitting of the Fe-*L* peak is 75 ± 15% of the total iron content and falls to a final value of approximately 10 ± 10% at a fluence of approximately 10^{10} electrons nm^{-2}. Using the van Aken Fe-*L* white-line ratio method (see Appendix C) these values are slightly different being 93 ± 5% and 6 ± 5%, respectively. These values are identical with those obtained when the fitted exponential functions are extrapolated back to the zero-electron fluence limit. Over the course of the experiment (i.e. from 10^6 to 10^{10} electrons nm^{-2}), the average iron valence value has been reduced from 2.9 ± 1 to 2.1 ± 1. These results are very similar to those observed for 2LFh (section 5.4.1) and 2LFhP5 (section 6.6.1).

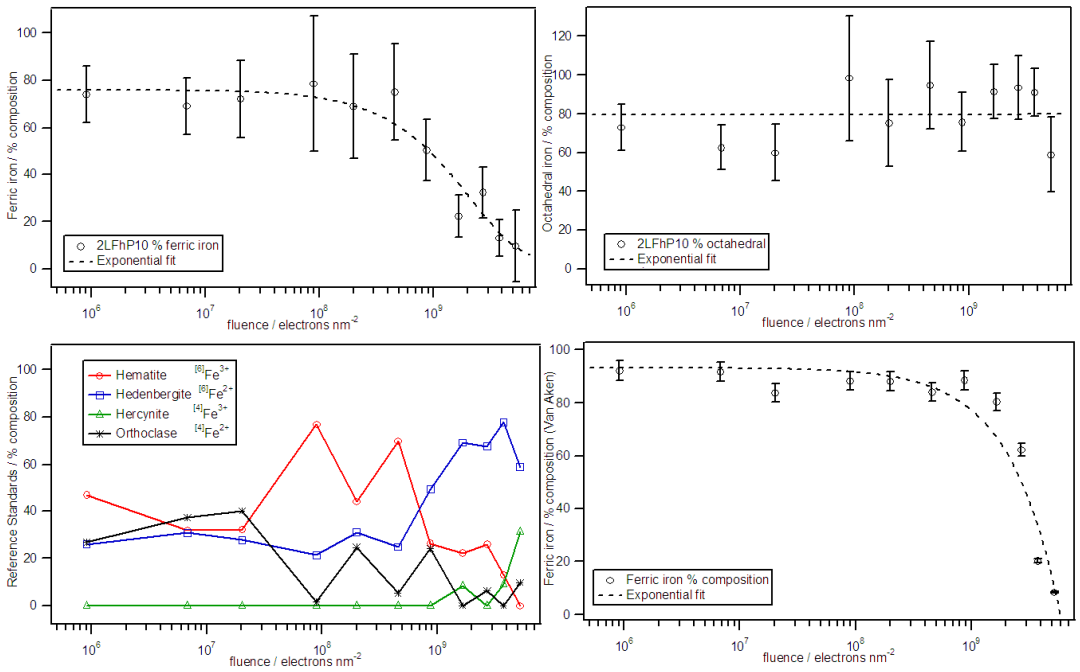

Figure 6.18 TEM-EELS Fe-*L* edge analysis for synthetic 10% phosphorus doped two-line ferrihydrite (2LFhP10) showing the derived ferric iron and octahedrally coordinated iron as a function of electron fluence. Exponential curves (dotted) are fitted for illustrative purposes. Error bars for fitted data are derived from the uncertainties provided by the fitting routine used for analysis of the Fe-*L* edge feature. Those for the van Aken method are in accordance with estimates derived in van Aken et al., (1998). The effect of prolonged exposure to the electron beam can be seen marked by a decrease in the ferric iron content beyond 10^8 electrons nm^{-2}.

Time-resolved compositional EDX analysis at progressively increasing fluence indicates that both oxygen and phosphorus are preferentially lost from the material to the vacuum whilst the iron (absolute) signal is seen to remain fairly constant (Figure 6.19). The onset of the loss of material occurs at approximately 3 x 10^8 electrons nm^{-2} and the data for each species are well fitted by exponential profiles. Analysis of the copper normalised absolute EDX signals indicate a similar percentage decreases for the oxygen and phosphorus signals. Zero-fluence estimates of the sample's composition as calculated by extrapolation give: oxygen 73.7 ±8%, iron 25.1 ±3% and phosphorus 1.3±1%, which by the experiment's end have changed to 65.4±7%, 33.9±4% and 0.7±1%, respectively.

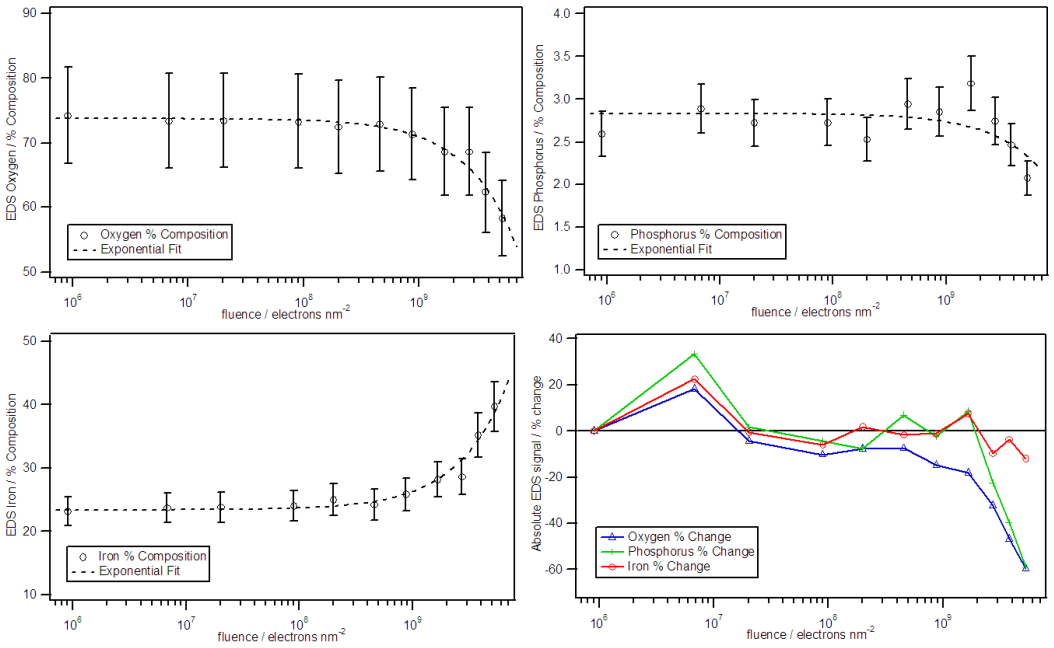

Figure 6.19 Summary of energy dispersive X-ray spectroscopic data for synthetic 10% phosphorus doped two-line ferrihydrite (2LFhP10) as a function of electron fluence acquired in the TEM. The onset of sample alteration can be seen to occur at an electron fluence of 10^8 electrons nm^{-2} as indicated by a marked decrease in both the oxygen and phosphorus specific signals.

BF-TEM micrographs of the sample at the experiment's end, after exposure to 5.4 x 10^9 electrons nm^{-2} are shown in Figure 6.20. It can be observed that the crystallinity of the sample has increased markedly in terms of both crystal order (extent and presence of extended lattice fringes) and crystallite size.

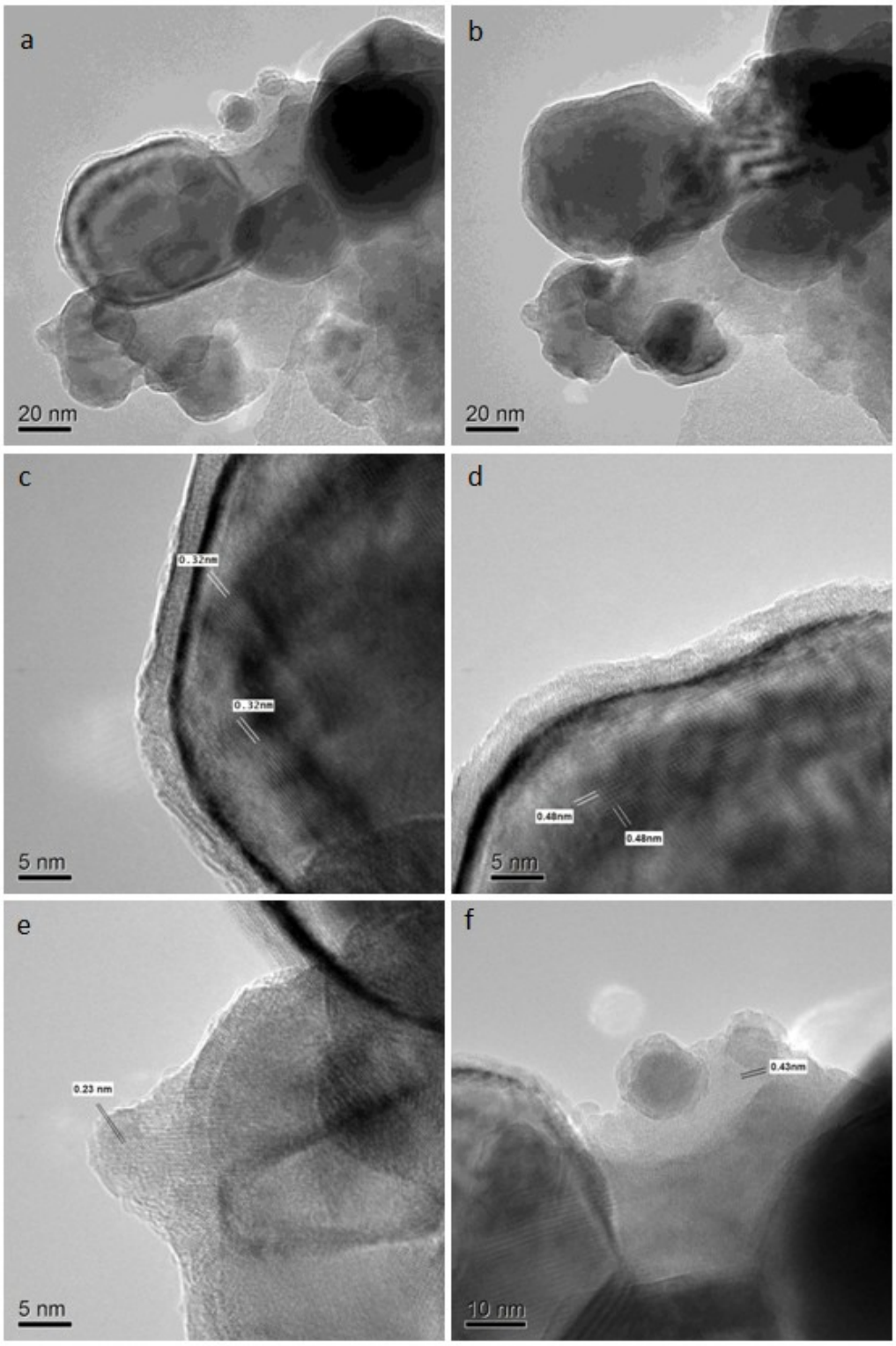

Figure 6.20 Bright-field transmission electron microscope images of synthetic 10% phosphorus doped two-line ferrihydrite (2LFhP10) after exposure to 5.4 x 10^9 electrons nm^{-2}. A significant increases in crystallinity (size and order) compared to the pristine product. Images (a) and (b) are tilted 15° with respect to one another. The fringe surrounding the crystalline areas, seen most prominantly in (c) and (d) is most likely due to serendipitous carbon fixed by the electron-beam. Lattice spacings of 0.32, 0.43 and 0.48 nm which are not typical of two-line ferrihydrite are indicated.

Radially averaged SAED patterns as a function of increasing fluence are shown in Figure 6.21. It can be seen that upon increasing fluence beyond 10^8 electrons nm^{-2} additional reflections are observed. Indicating the presence of additional phases.

Selected radially averaged SAED patterns are shown in Figure 6.22 along with the stick patterns of magnetite, wüstite and hematite for comparison. The presence of hematite is required to account for the feature at ~2.75 Å in the radially averaged SAED patterns acquired at 5.2 x 10^9 electrons nm^{-2} since it's most intense reflection is observed close to this *d*-spacing. As previously mentioned, a conversion to magnetite and wüstite is consistent with the EELS and EDX obtained here.

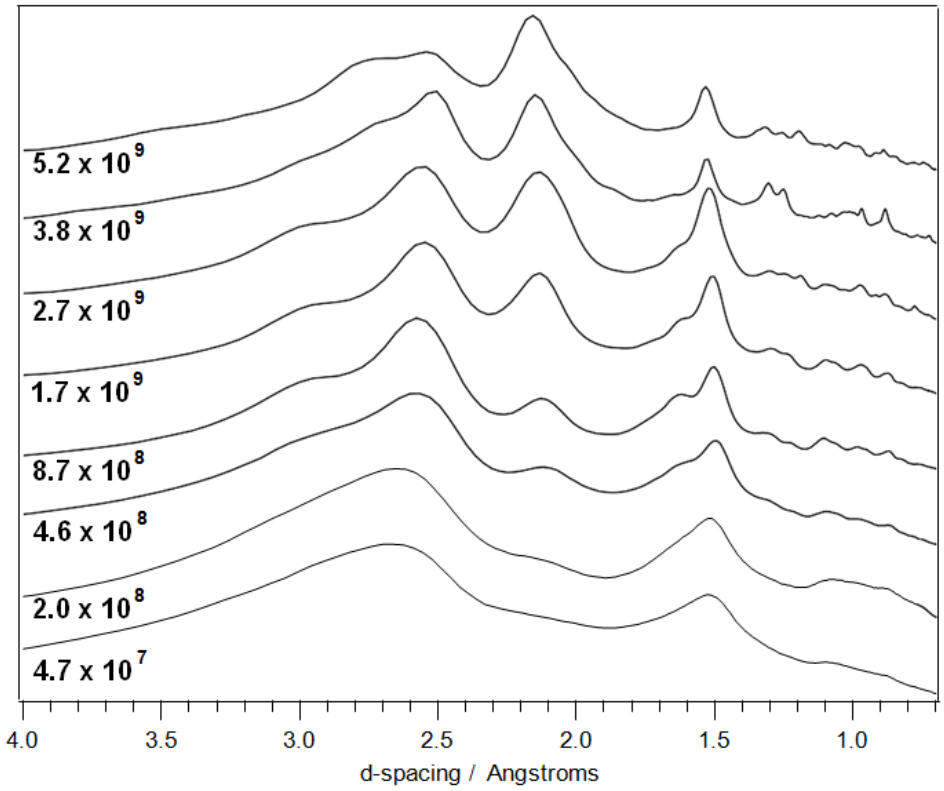

Figure 6.21 Radially averaged selected area electron diffraction profiles acquired from synthetic 10% phosphorus doped two-line ferrihydrite (2LFhP10) at progressively increasing electron fluences. Electron fluence values in units of electrons nm^{-2} are written in bold below each curve. An increase in crystallinity is observed with increasing fluence as indicated by the increasing number of increasingly sharp reflections.

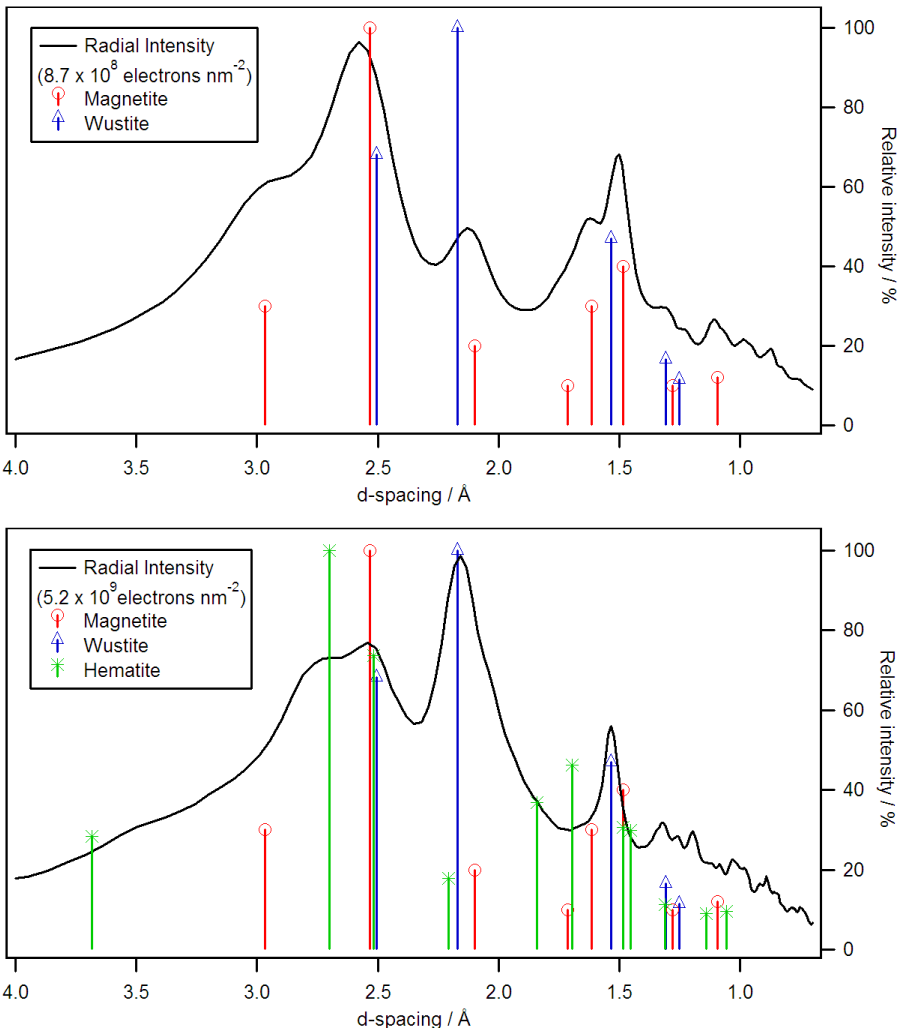

Figure 6.22 Radially averaged selected area electron diffraction profiles of acquired from synthetic 10% phosphorus doped two-line ferrihydrite (2LFhP10) as measured at electron fluences of 8.7 x 10^8 and 5.2 x 10^9 electrons nm^{-2}. Also shown for comparison are the stick patterns of the most intense features (≥9% relative) for for magnetite (JCPDS card 39-1349), wüstite (JCPDS card 46-1312) and hematite (JCPDS card 33-0664).

6.6.3 Beam Damage Assessment of 2LFh with 30% Phosphorous Doping

This section provides a brief description of the effect of electron beam exposure on the 2LFhP30 sample for which the P/Fe was the highest investigated.

Previous analysis outlined above for P/Fe ≥ 0.10(P10) suggests there is most likely a mixture of *pure* 2LFh and a separate iron-phosphate phase rather than a single phase intimately associated of 2LFh and phosphate. For this reason, a thorough assessment of the damage susceptibility of these samples was not performed. That said, as a matter, of course, a brief assessment was made and there was an apparent propensity to alteration when exposed to 197 keV electrons in the TEM. Figure 6.23(a & b) shows BF-TEM micrographs illustrating the changes as a result of exposing

2LFhP30 to fluences of 10^5 and 10^9 electron nm^{-2}. For comparison shown in Figure 6.23(c & d) are micrographs of $FePO_4 \cdot 2H_2O$ acquired at similar fluence which have been taken directly from the thesis of Pan (2006). What is apparent from these images is that unlike the 2LFhPX samples of P/Fe < 0.10(P10), exposure of 2LFhP30 or $FePO_4 \cdot 2H_2O$ to the electron beam of the TEM does not result in induced crystallisation. Rather it is seen that in the case of 2LFhP30 the sample is altered by the formation of pores (meso to macroporous) resulting in an amorphous product. On the other hand, the initially mesoporous $FePO_4 \cdot 2H_2O$ loses its pores in forming an amorphous end product. Although not conclusively compelling this suggests that 2LFhP30 is distinct from 2LFhPX, for $X \leq 10$(P10), and $FePO_4 \cdot 2H_2O$.

This concludes the consideration of electron beam damage.

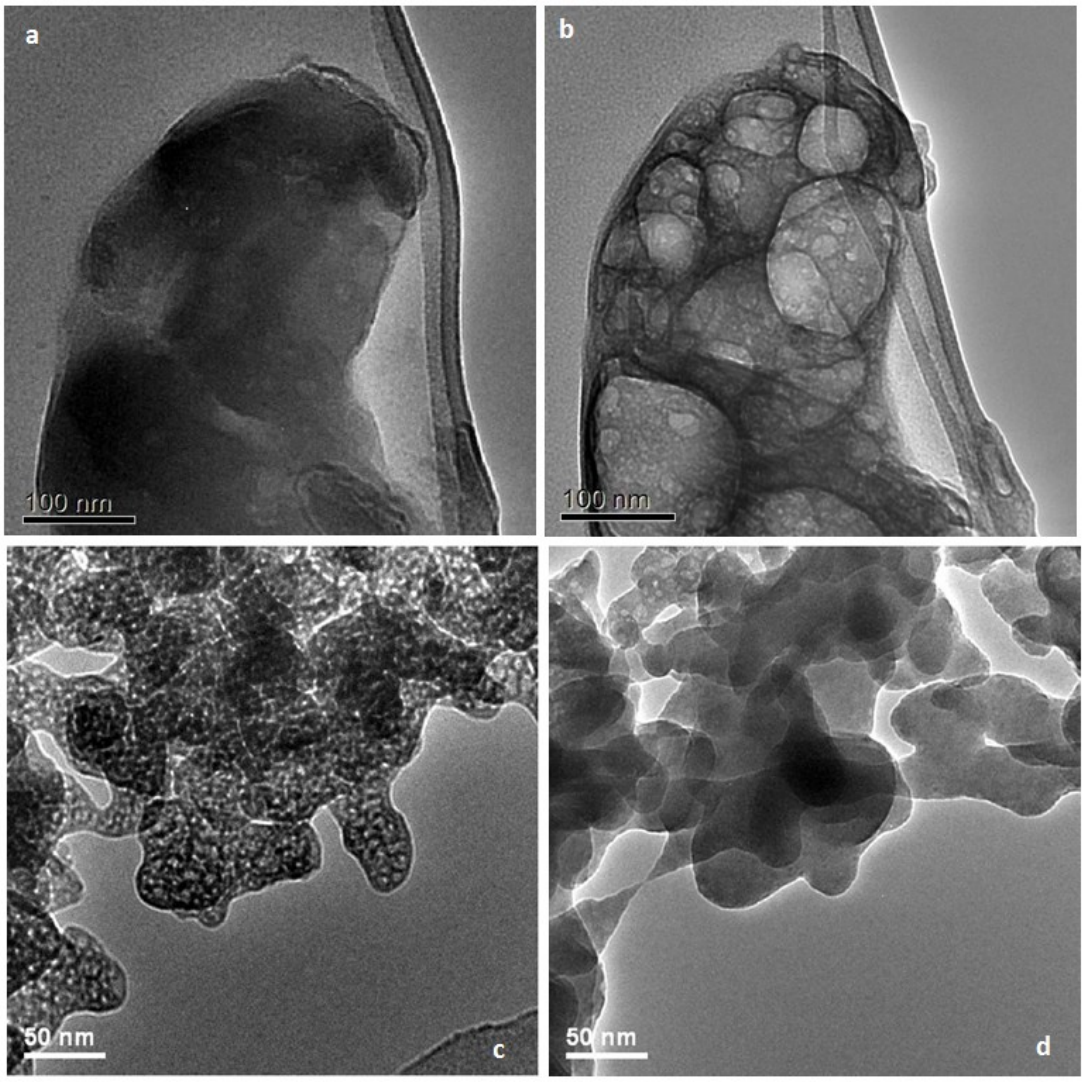

Figure 6.23 Bright-field TEM images of synthetic 30% phosphorus doped two-line ferrihydrite (2LFhP30) after exposure to approximately 10^5 (top left) and 10^9 electrons nm^{-2} (top right). Micrographs (c) and (d) are taken from the thesis of Pan (2006) and show FePO4•2H2O acquired at fluences similar to those for (a) and (b). Specimen alteration at high fluence is clearly different in each case.

6.6.4 EELS Oxygen-*K* edge of 2LFhPX

Displayed in Figure 6.24 are the O-*K* edge EEL spectra acquired from the 2LFhPX series along with that of $FePO_4 \cdot 2H_2O$ for means of comparison. Estimated fluences for each spectrum are 10^7 electrons nm^{-2} or less: below the *unsafe-fluence* threshold established in previous sections. Absolute energies were not measured and so edges have been aligned to the low energy pre-peak feature for comparison purposes, however, typically this feature is to within a few eV of 531 eV in the case of those Fe-O bearing minerals for which it is present (Colliex, Manoubi, & Ortiz, 1991; Grunes, Leapman, Wilker, Hoffmann, & Kunz, 1982). Upon increasing P/Fe there is a relative reduction in the intensity of the pre-peak and an accompanying decrease in the energy-loss separation between the pre-and main peaks. In the former case, the reduction of the pre-peak intensity as a function of P/Fe can be described well by a linear function. In the latter case, the separation of the pre-to-main peaks follows an exponential decrease upon increasing P/Fe. These relationships are given graphically, along with least-squares fits to the data, in Figure 6.25. From visual inspection of Figure 6.24, it is apparent that with increasing P/Fe the spectra evolve from being typical of 2LFh towards a more $FePO_4 \cdot 2H_2O$-like profile. Indeed, this relationship was confirmed by using 2LFh and $FePO_4 \cdot 2H_2O$ O-K EELS edges (as normalised by the continuum intensity between 515-525 eV) as reference endmembers and fitting the intermediate spectra as a linear combination of the two. This analysis showed that there is a linear increase (using the simplest approximation) in the $FePO_4 \cdot 2H_2O$ component with P/Fe.

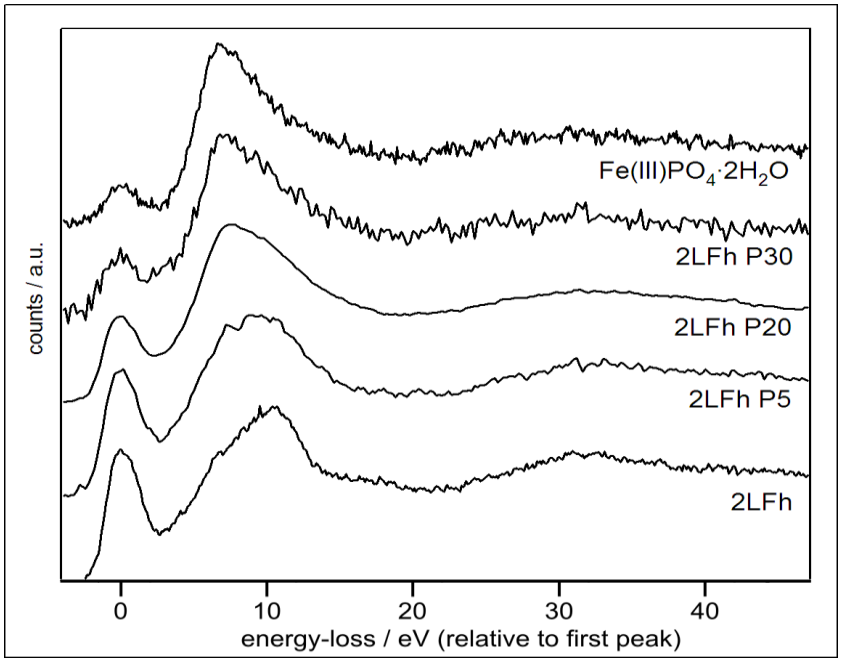

Figure 6.24 Comparison of oxygen-*K* edge electron energy-loss spectra for the synthetic phosphorus doped two-line ferrihydrite series (2LFhPX defined in section 4.1.3.) and $FePO_4 \bullet 2H_2O$. Absolute edge energies were not measured and so edges have been aligned to the low energy pre-peak feature for comparison purposes. A systematic evolution towards the $FePO_4 \bullet 2H_2O$ edge profile upon increased phosphorous-doping is clearly evident.

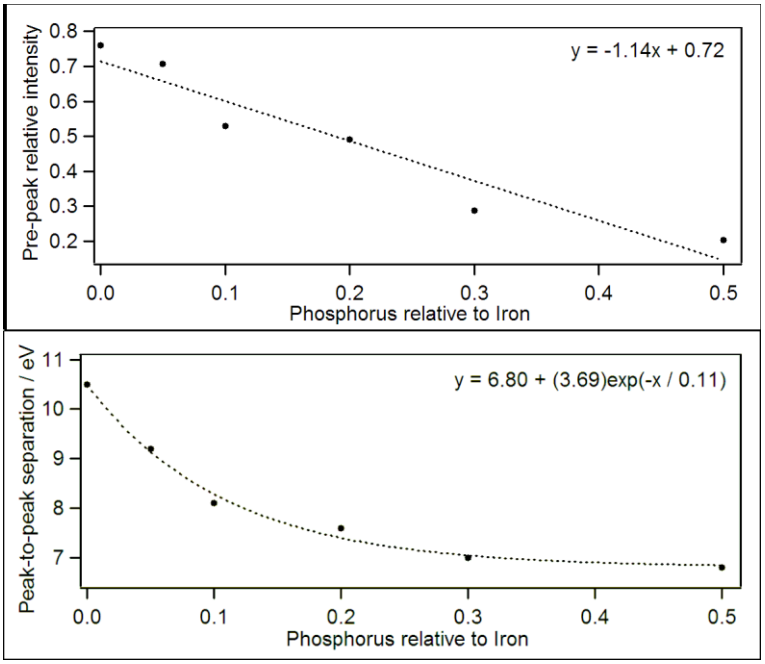

Figure 6.25 Oxygen-*K* edge electron energy-loss pre-peak relative intensity (top) and pre-to-main peak separation (bottom) as a function of phosphorus-doping relative to iron for the synthetic phosphorus doped two-line ferrihydrite series (2LFhPX defined in section 4.1.3.). Both trends can be well fitted by analytical expressions (dotted lines) indicating systematic variation in the atomic environment local to oxygen.

6.6.5 Bright-Field TEM Imaging Under Low Electron Fluence

Displayed in Figure 6.26 are some typical BF-TEM images of the P-doped 2LFh series (2LFhPX defined in section 4.1.3.) acquired at fluences less than 10^7 electrons nm^{-2}. In each case extended aggregations of poorly ordered ~4nm diameter crystallites can be observed. Since BF-TEM images do not carry chemical information no conclusion regarding composition can be drawn from such images.

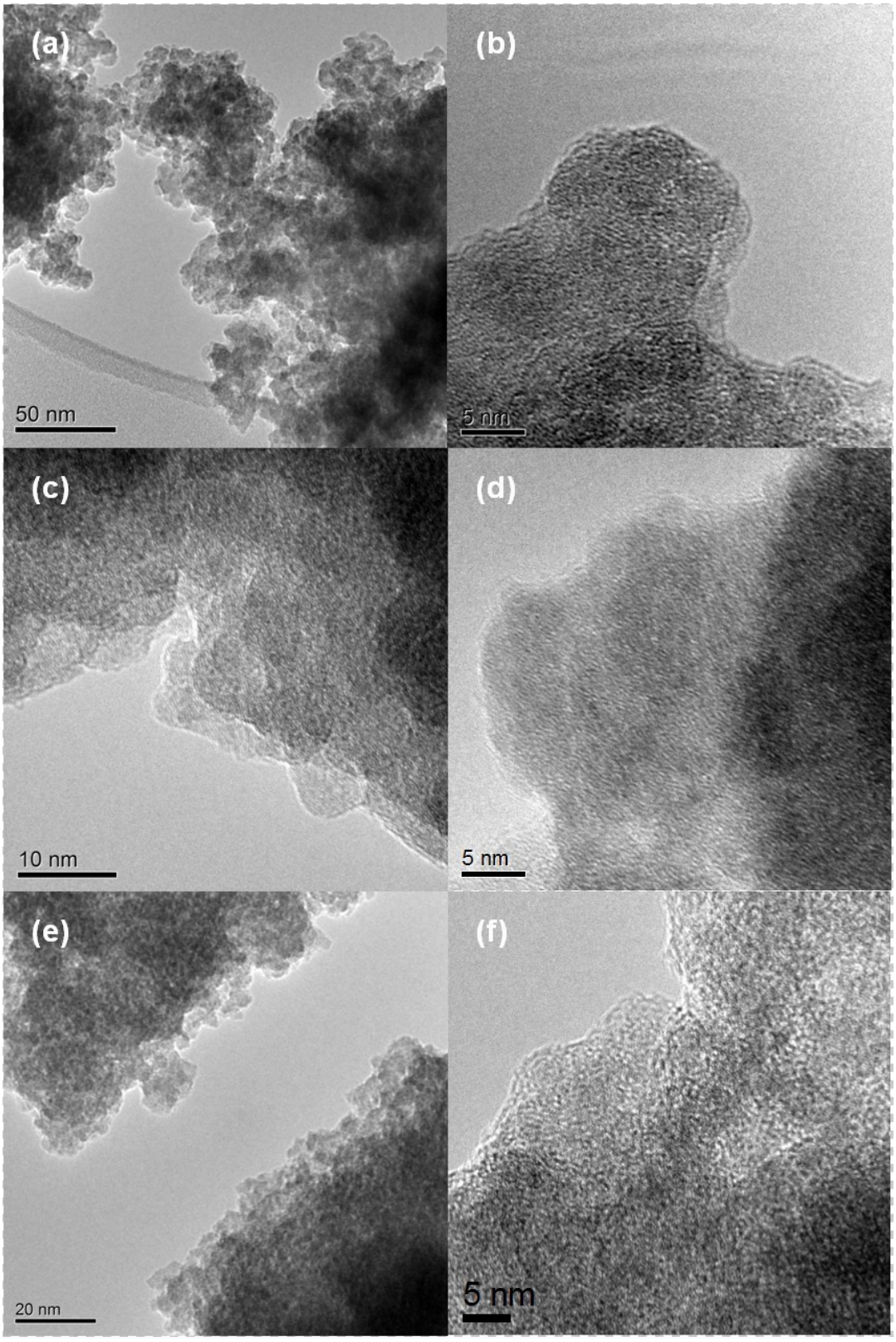

Figure 6.26 Bright-field TEM micrographs images of synthetic phosphorus doped two-line ferrihydrite for 30% 2LFhP30 (a & b), 20% 2LFhP20 (c & d) and 5% phosphorous-doping 2LFhP5 (e & f). Electron fluences are estimated to be less than 10^7 electrons nm^{-2}. In each case extended aggregations of poorly ordered ~4nm diameter crystallites can be seen.

6.7 Concluding Remarks

2LFh was precipitated in the presence of phosphate to achieve P/Fe levels of 0.01-0.30. Powder XRD analysis suggests the modification of 2LFh either by surface poisoning, structural incorporation or production of additional phases. A clear difference in the phosphate region (850 - 1150cm^{-1}) of the FTIR spectra of the products is observed with increasing P-levels. For levels above 0.10 the NO^{3-} anion has likely been replaced by the more strongly binding phosphate anion during hydrolysis. One cannot, however, rule out the presence of Fe-phosphate phases, therefore making it difficult to tell whether this is an indication of differing P-levels. Characterisation by Raman spectroscopy brings little extra evidence other than the products formed here are not $FePO_4.2H_2O$.

Thermal analysis of 2LFh is broadly similar to that previously reported in the literature, with perhaps less water content than that reported by Wenquin et al., (2011). It would appear that the addition of phosphate stabilises 2LFh against the phase transition to hematite. Below P/Fe levels of 0.10(P10) this transition is delayed occurring at higher temperatures with increasing P-level, however above this ratio it completely suppressed. XRD combined with TGA and DSC measurements estimates a compositional formula close to $Fe_2O_3 \cdot 2.2H_2O$ for 2LFh providing support for the most recent model for the structure of ferrihydrite as proposed by Michel et al. (2007, 2010).

Elemental quantification via XPS using the Tougarrd model function for background removal gives P % atomic values closer to the target P-levels, however, this method is possibly more surface sensitive.

The effect of exposure to the electron beam of TEM was studied for samples with P/Fe levels of 0.05(P5), 0.10(P10) and 0.30(P30). As for the undoped 2LFh, exposure to fluences below 10^8 electron nm^{-2} appeared to be a 'safe dose' for samples with P/Fe $\leq$ 0.10(P10). Exposure to fluences beyond this resulting in induced crystallisation of the specimen. Exposure of 2LFhP30 to higher fluences did not result in induced crystallisation, however, this sample was altered with the formation of meso/macro pores, resulting in an amorphous product. Beyond the 'safe dose' of electron fluence, the valency of iron in 2LFhP5 is closer to 2 than it's starting value of almost 3 at 10^6 electrons nm^{-2}, analogous to undoped 2LFh. Similar results were also obtained for 2LFhP10. EDX spectroscopy of 2LFhP5 and 2LFhP10

suggested that above fluences of 10^8 electron nm^{-2}, oxygen was preferentially lost from the material as a result of electron-beam irradiation. SAED patterns of 2LFhP5 and 2LFhP10 were indicative of the presence of extra phases at fluences of 10^8 electrons and beyond. In light of the EDX and EELS compositional data, EELS valence estimates and SAED crystallographic data it appears that the most likely candidate for the beam damage product is a magnetite-like phase.

Chapter 7 Characterisation of Thermally Ageing of Phosphorus-Doped Two-Line Ferrihydrite

The accelerated ageing of phosphorous-doped two-line ferrihydrite is investigated by means of *hydrothermal* and dry-air *annealing* treatments at 175°C. Preparation of the samples is described in sections 4.1.4 and 4.1.5. The resulting products are compared, with emphasis being given to the analysis of the hydrothermally treated samples since there has been considerable interest in such materials in recent years and potentially novel products have thus been formed. Structural and chemical analysis is presented which confirms the hydrothermally treated P-doped 2LFh samples studied here are consistent with those recently reported in the literature. Additional insight into the nature of these hydrothermal products is given by means of thorough analysis based on careful analytical transmission electron microscope observations from both aberration-corrected and uncorrected machines.

Table 7.1 provides an overview of the sample examined in the current chapter.

Table 7.1 Details of samples examined in Chapter 7.

Sample Full Name	**Abbreviated Name(s)**	**Sample Description**
Synthetic two-line ferrihydrite	2LFh	Two-line ferrihydrite synthesised *in vitro* according to the method provided in section 4.1.1.
Phosphorus doped synthetic two-line ferrihydrite	2LFhPX, P-doped 2LFh 2LFhP0 ≡ 2LFh (2LFhP1, 2LFhP3, 2LFhP5, 2LFhP10, 2LFhP20, 2LFhP30)	2LFh coprecipitated *in vitro* in the presence of phosphorus according to the method provided in section 4.1.3. Molar quantities of PO_4 were chosen to achieve a range of P/Fe levels (0.01, 0.03, 0.05, 0.10, 0.20 & 0.30). X is the atomic percent P with respect to Fe. e.g. for P/Fe = 0.20, X = 20 and the sample is denoted 2LFhP20
Hydrothermally treated (phosphorus doped) two-line ferrihydrite	PXhY (P3h12, P5h5, P5h11)	2LFh coprecipitated *in vitro* in the presence of phosphorus according to the method provided in section 4.1.3 was subject to hydrothermal treatment at 175°C according to the method provided in section 4.1.4. X in the abbreviated sample name is as defined above and in section 4.1.3 and Y is the time in hours the sample was subject to hydrothermal treatment.
Thermally annealed (phosphorus doped) two-line ferrihydrite	PXaY (P5a12)	2LFh coprecipitated *in vitro* in the presence of phosphorus according to the method provided in section 4.1.3 was subject to hydrothermal treatment at 175°C according to the method provided in section 4.1.5. X in the abbreviated sample name is as defined above and in section 4.1.3 and Y is the time in hours the sample was subject to thermal treatment.

Currently, there exists considerable controversy over the precise nature of what has been dubbed a new form of ferrihydrite with fundamental questions being raised regarding the correct interpretation of results obtained by high energy X-ray techniques which until recently have not been used in the characterisation of ferrihydrite.

Thermal Ageing of Phosphorus-Doped Two-Line Ferrihydrite

A series of P-doped 2LFh's (i.e. 2LFhPX but for brevity denoted here as PX) were prepared and dried according to the method outlined in section 4.1.1. These were then taken and subjected to elevated temperatures over extended periods of time either by annealing in air or by hydrothermal means. The protocols for each of these routes may be found in section 4.1.4 & 4.1.5. As a means of reference, undoped 2LFh was also subject to hydrothermal treatment at 175°C over a period of 12 hours. Their characterisation is as follows.

7.1 X-Ray Powder Diffraction

7.1.1 Hydrothermally Treated Two-Line Ferrihydrite

The X-ray powder diffraction patterns for undoped 2LFh which was hydrothermally treated at 175°C for 12 hours is presented below in Figure 7.1. The transformation product was found to be a mixture containing both hematite (JCPDS card 33-0664) and goethite (JCPDS card 29-713) in line with previous work documented in the literature (Cornell & Schwertmann, 2003). The predominant phase appears to be hematite for which the mean particle size is estimated to be 29 ± 3nm based on the estimate derived from the Scherrer relation applied to the eight most intense features.

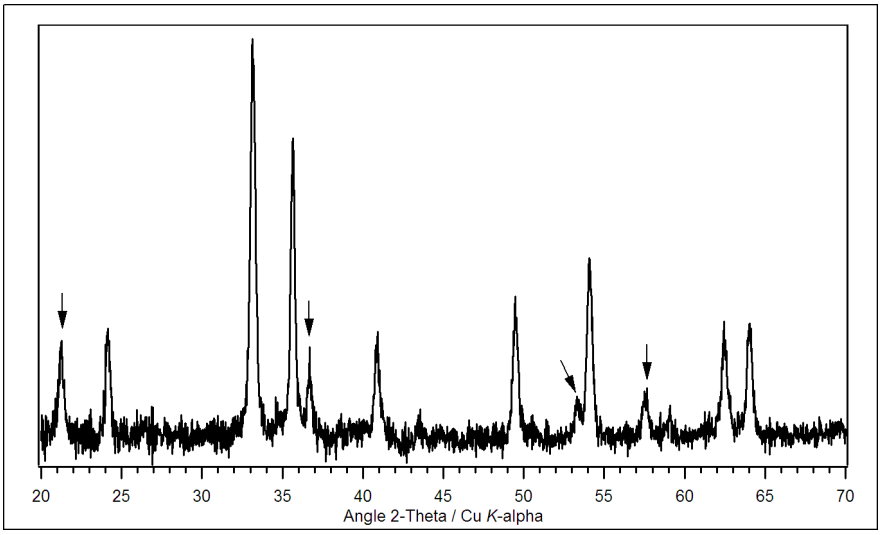

Figure 7.1 Powder X-ray diffraction profile of the transformation product formed following the hydrothermal treatment of synthetic two-line ferrihydrite at 175 °C over a period of 12 hours. Peaks marked with arrows can be assigned to goethite (JCPDS card 29-713) with all other being due to hematite (JCPDS card 33-0664).

7.1.2 Hydrothermally Treated P3h12 and P5h11

Presented in Figure 7.2 is the powder XRD data comparing the diffractograms of the unaged P5 sample with the twelve hour furnace annealed (P5a12) and the five and eleven hour hydrothermally treated (P5h5 & P5h11) samples. Also shown for comparison is a diffraction pattern taken from the literature of a hydrothermally aged (two weeks at 150 °C) P- doped (P/Fe = 0.0275) sample (Barrón et al., 2003).

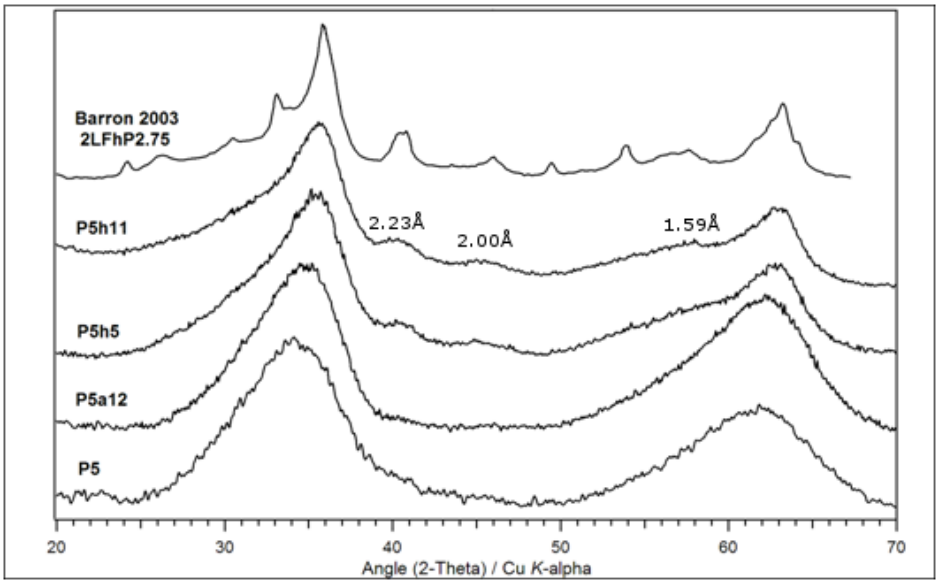

Figure 7.2 Powder X-ray diffraction profiles diffractograms comparing synthetic 5% phosphorus doped two-line ferrihydrite (P5) with five-hour furnace annealed (P5a12), five- and eleven-hour hydrothermally treated (P5h5 & P5h11) with the hydrothermally aged (150 °C, 2 weeks) P-doped (P/Fe = 0.0275) sample of Barrón et al., (2003).

Comparing 5% P-doped diffractogram (P5) with that of the five-hour furnace annealed sample (P5a5) reveals little difference between the two samples, save for a slight enhancement of the high angle peak about 62° 2θ. On the other hand, hydrothermal treatment, even after 5 hours (P5h5), exhibits significant modification of the diffraction profile compared to the unaged P5 sample. In particular, there is a notable sharpening of the peaks at ~1.5 Å and 2.5 - 2.6 Å (61.2 and 34.5 - 35.9 2θ Cu-$K\alpha$) indicative of particle growth. In addition to this sharpening there is a shift towards larger *d*-spacings (lower 2θ). It can also be seen that hydrothermal treatment has resulted in the appearance of extra intensities at *d*-spacing values of 2.23, 2.00 and 1.59 Å which are not present in either the unaged (P5) or twelve-hour annealed (P5a12) sample. These additional peaks, along with the principle maxima, correspond well with those seen in the data of Barrón et al., (2003), however, not observed for hydrothermally treated P5h11 are those peaks appearing at 3.40, 2.93, 2.97 and 1.84 Å (26.2, 30.5, 30.1 and 49.5 2θ for Cu-$K\alpha$) in the Barrón sample (Barrón et al., 2003). The absence of these peaks may indicate that the P5h11 sample had not matured to the same degree as that of Barrón or that the product at this point of the ageing is, in fact, different to that of Barrón. Support for this conjecture is provided by the fact that for the P5h11 sample, the breadth of the peaks would indicate that this sample is composed of crystallites which have coherent scattering domains significantly smaller than those of the Barrón sample.

Presented in Figure 7.3 is a comparison of the low-angle synchrotron X-ray scattering data for P3, and P5 along with that of their hydrothermal transformation products after 12 (P3h12) and 11 hours (P5h11) at 175°C, respectively.

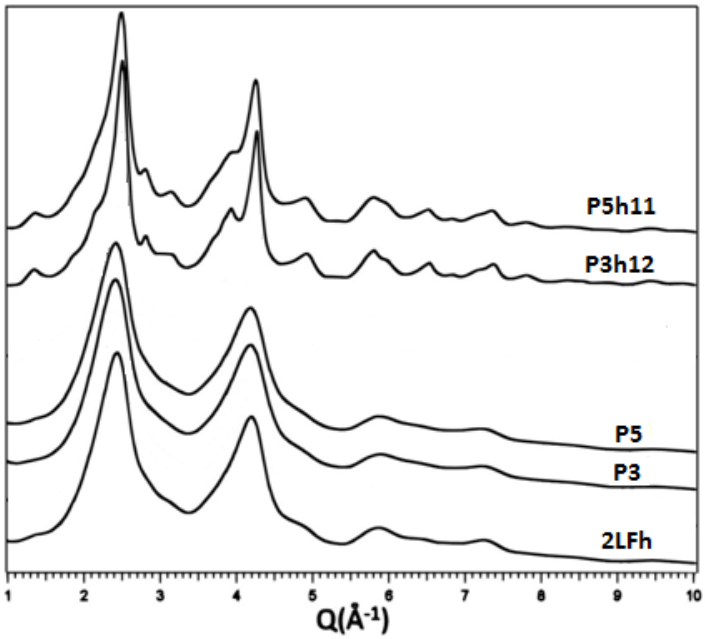

Figure 7.3 Low-angle synchrotron X-ray scattering data comparing synthetic two-line ferrihydrite (2LFh), 3% and 5% phosphorus doped 2LFh (P3 & P5) with their twelve and eleven hour 175ºC hydrothermally treated products (P3h12 & P5h11). The effect of hydrothermal treatment can clearly be seen with a sharpening of peaks and presence of additional peaks not seen for the untreated sample, consistent with an increase in both crystal size and atomic order.

From inspection of Figure 7.3, it is apparent that hydrothermal ageing has significantly modified the structure for each of the P-doped specimens. In each case a sharpening of the two major peaks around 1.5 Å and 2.5 - 2.6 Å (Q ~2.4 and 4.2 $Å^{-1}$) is consistent with the idea that the presence of phosphate during precipitation of 2LFh affects particle growth, presumably due to effects on the polymerization of Fe and/or surface poisoning of the growing particles. Additionally each of the hydrothermally treated samples exhibit extra peaks where only diffuse intensity was previously seen. This along with the sharpening of the diffraction features reflects both particle growth and atomic ordering.

When overlaid directly the hydrothermally treated samples are practically identical, with the P3h12 sample showing marginally sharper features and therefore having undergone the most change. For comparison Figure 7.4 shows the *ferrifh* (HYD7) phase taken from the Michel et al., (2010) study alongside the P5h11 sample of the present investigation. Good agreement is observed in terms of the positions and relative intensities of diffraction maxima. The breadth of the peaks in the P-doped sample suggests that this sample has smaller average particle sizes.

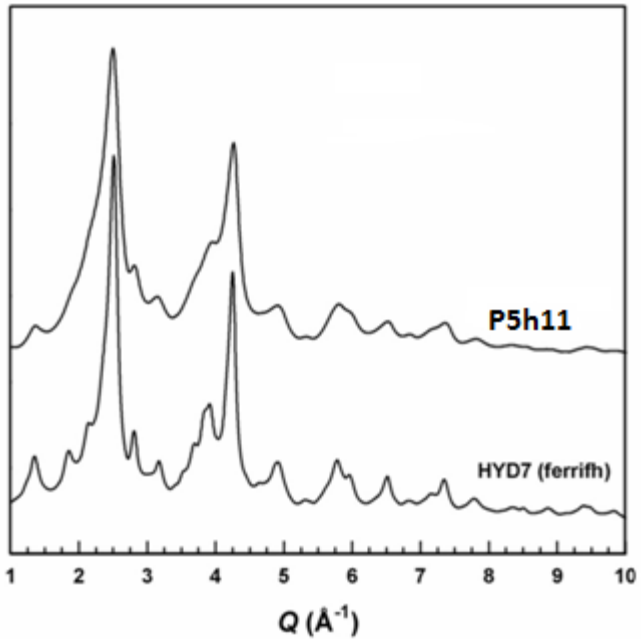

Figure 7.4 Comparison of low-angle synchrotron X-ray scattering data for the hydrothermally treated (eleven hours at 175ºC) 5% phosphorus doped synthetic two-line ferrihydrite sample (P5h11) with the hydrothermally treated (fourteen hours at 175ºC) 3% citrate associated two-line ferrihydrite (*ferrifh*) phase from Michel et al,. (2010). A broad correspondence between the two samples may be observed in terms of peaks positions, however, the increased breadth of features observed for P5h11 indicates a decreased overall particle size compared to the Michel *ferrifh* sample.

7.2 Total X-Ray Scattering Pair Distribution Function Analysis

7.2.1 Undoped Two-Line Ferrihydrite

The experimental PDF data for 2LFh acquired in this work, along with that of the Fhdy2 sample as reported by Michel et al., (2007), which was synthesised according to the same protocol used here, are displayed in Figure 7.5. Besides the high-frequency noise in the region $r < 1.7$ Å, which is an artifact (termination ripples) resulting from the Fourier transformation and the finite Q-range used to obtain the PDF, the PDFs of the two samples are very similar. The positions and relative intensities of the correlation peaks, which extend out to approximately $r = 20$ Å, when overlaid are practically indistinguishable.

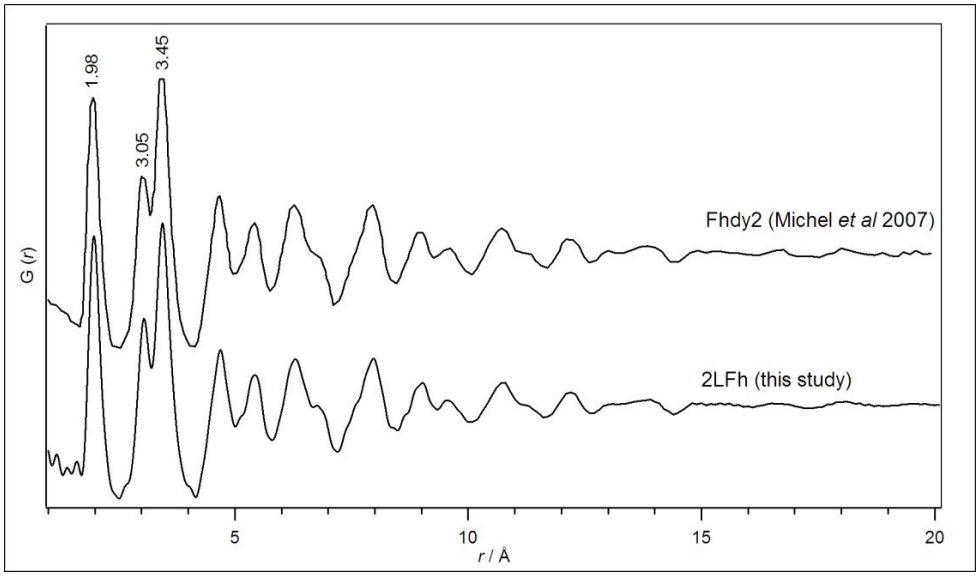

Figure 7.5 Comparison of the total X-Ray scattering PDF data for synthetic two-line ferrihydrite (2LFh) from this study and the synthetic two-line ferrihydrite Fhdy2 sample taken from the study of Michel et al., (2007). The atom-atom separations of the first three correlations, as determined from the 2LFh-PDF, are labelled in units of Ångstroms. Good agreement between the PDFs can been seen indicating the similarity between the two samples.

The first correlation in the PDF of 2LFh, at r = 1.98 Å, corresponds to the interatomic Fe-O, OH distances. This distance is typical of Fe in predominantly octahedral coordination with oxygens and/or hydroxyls (Michel et al., 2007) and has a similar value to the mean $^{[VI]}Fe^{3+}$-O_6 distance of 2.05 Å observed in maghemite (Shmakov, Kryukova, Tsybulya, Chuvilin, & Solovyeva, 1995). In their PDF analysis, Michel et al., (2007) note that currently it is not possible, based on this first-correlation, to estimate whether there exist tetrahedrally coordinated Fe sites in ferrihydrite for which the Fe-O distances would be expected to be shorter by some ~0.20 Å (Shmakov et al., 1995). If ideal $^{[IV]}Fe$-O_4 were indeed present in significant proportions, a low-r shoulder on the first correlation of the PDF would be expected. However, distorted octahedral sites which are expected to exist in ferrihydrite, would lead to a distribution of Fe-O distances about that predicted for ideal $^{[VI]}Fe$-O_6, leading to an increased breadth of the Fe-O correlation peak which may indeed conceal the shorter $^{[IV]}Fe$-O_4 correlations (Drits et al., 1993; Manceau & Gates, 2007; Michel et al., 2007). In the revised structural model for ferrihydrite (*ferrifh*) proposed by Michel et al., (2010), Fe occupying tetrahedral sites (Fe_3) is off-centered which leads to a range of Fe-O distances (1.931, 1.931, 1.932 and 1.816 Å) for this polyhedron. This position of Fe in *ferrifh* $^{[IV]}Fe$-O_4 has most probably been so constrained and thereby refined by the r-location of this first-correlation (Manceau 2009; Michel et al., 2010).

The second correlation, which lies at 3.05 Å, can be attributed to inter Fe-Fe distances between edge-sharing $^{[VI]}$Fe-(O,OH)$_6$ polyhedra (Combes, Manceau, Calas, & Bottero, 1989; Michel et al., 2007) which are observed in the *ferrihydrits* models for ferrihydrite (Drits et al., 1993). The inter Fe-Fe distance for edge-sharing $^{[VI]}$Fe-(O, OH)$_6$, due to electrostatic considerations, depends on the extent of protonation of the anions which contribute the shared edge: for example when two O^{2-} (hematite) form the shared edge *d*(Fe-Fe) = ~2.97 Å; one O^{-2} and one OH^- (goethite and akaganéite) give *d*(Fe-Fe) = 3.02 - 3.35 Å and a shared edge composed of two OH^- anions (goethite and akaganéite) give a *d*(Fe-Fe) = 3.30 - 3.52 Å (Manceau 2011). Based on these considerations it may be safe to assume that, in ferrihydrite, shared edges between Fe-octahedra are most probably O-OH type edge-linkages.

The third correlation at 3.45 Å has two possible assignments and is a cornerstone in support of tetrahedrally coordinated iron proposed in the Michel model for ferrihydrite. Firstly this distance is typical of double corner-sharing $^{[VI]}$Fe-(O, OH)$_6$ such as are observed in goethite and akaganéite (Manceau & Combes, 1988; Combes et al., 1989; Manceau 2011). The second possible assignment of this correlation is to the Fe-Fe distances in corner-sharing $^{[IV]}$Fe-O–$^{[VI]}$Fe-O polyhedra as is seen in maghemite (Manceau 2011) and importantly for the Michel model the Fe_{13} α-Keggin structure for which the *d*($^{[IV]}$Fe-O–$^{[VI]}$Fe-O) for the central Fe-O_4 tetrahedron is 3.46 Å (Bino, Ardon, Dongwann, Springler, & Lippard, 2002).

Somewhat controversially, the experimental PDFs do not exhibit an obvious correlation at 2.89 Å which would be expected for edge-sharing octahedra and are a constituent of the *f*-phase of the Drits' model, previously been confirmed to exist based on EXFAS measurements (Drits et al., 1993; Manceau & Drits, 1993). The absence of an obvious correlation at this position does not necessarily rule out face-sharing octahedra since they are expected to be few according to the Drits' models. Also found at approximately 2.90 Å are contributions from O-O correlations which may interfere with the face sharing Fe-Fe ones.

7.2.2 Phosphorus-Doped Two-Line Ferrihydrite

Upon hydrothermal treatment of P-doped 2LFh there is a modification of the PDF data (see Figure 7.6). Firstly it can be seen that the *r* position of correlations remain unaffected however, they now extend further out in *r* indicating an increase in the

average dimensions of particles which contribute to the data. The amplitudes of correlations are also observed to increase upon hydrothermal treatment, which again is consistent with a greater number of atom-atom correlations contributing to the PDF at larger *r* separations, due to an increase in particle dimensions. Besides the general increase in amplitude and *r* extent of the correlations, there is also a variation in their relative intensities, as determined relative to that of the first peak. This is highlighted in Figure 7.7 which presents an overlaid view of the data given in Figure 7.6. In particular, there is a substantial increase in the relative amplitude of the third correlation, the magnitude of which is greater for the P3h12 sample (1.60 relative units) than for P5h11 (1.46 relative units). This feature is predominantly due to Fe-Fe correlations and the increase in its relative intensity upon hydrothermal treatment was interpreted as vacancy filling in the Fe_2 (tetrahedral) and Fe_3 (octahedral) sites of the Michel structural model for ferrihydrite (Michel et al., 2010). The fact that its relative intensity is seen to be largest for the P3h12 sample lends credence to the previously asserted supposition, made on the basis of X-ray scattering data, that, due to hydrothermal treatment, this sample has undergone the most transformation from the original starting material.

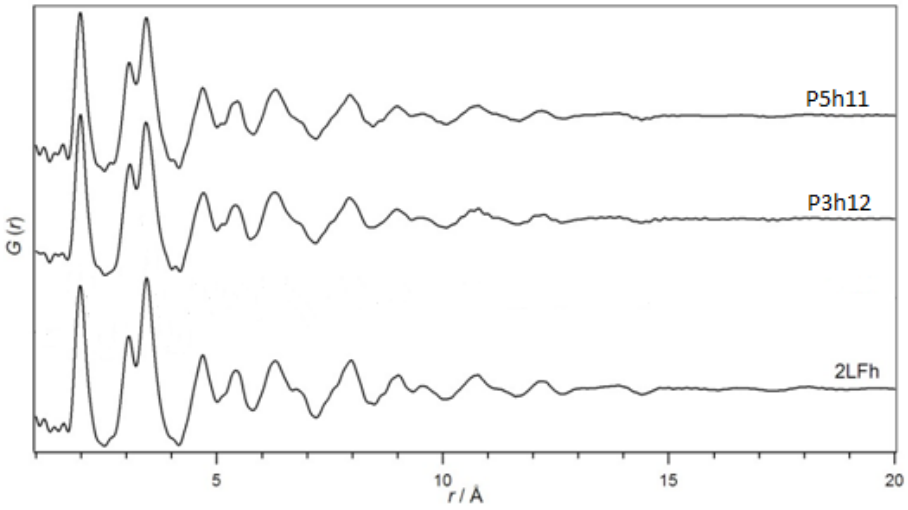

Figure 7.6 Comparison of X-ray PDF data for hydrothermally treated (twelve & eleven hours at 175ºC) phosphorus doped two-line ferrihydrite with 0% (2LFh), 3% (P3) and 5% (P5) levels of doping. The intensity scale has been normalised by the amplitude of the first Fe-O correlation at 1.98 Å.

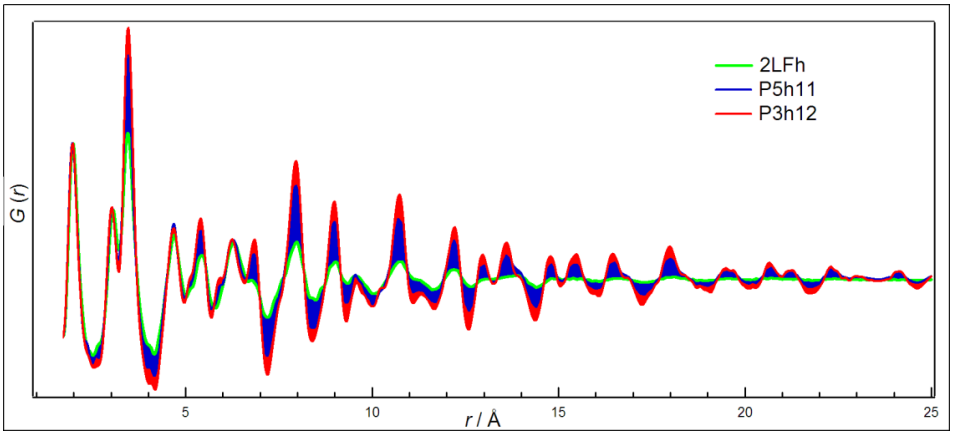

Figure 7.7 An overlay of the X-ray scattering derived PDF data for synthetic two-line ferrihydrite (2LFh) and hydrothermally treated (eleven hours at 175ºC) phosphorus doped two-line ferrihydrite with doping levels of 0% (2LFh), 3% (P3h12) and 5% (P5h10), highlighting the variation in relative intensities of the atom-atom correlations upon hydrothermal treatment. The effect of increased phosphorus doping can been seen to suppress the transformation.

7.3 Neutron Diffraction

Because the samples used here were not deuterated (i.e. not synthesised with deuterium, for which the incoherent scattering cross section is zero, but instead were hydrogen, for which the cross section is finite and negative) the data presented here consists of coherent nuclear Bragg reflections superimposed on an incoherent background due to neutron-proton scattering events. Since this background is difficult to estimate in the analysis which follows, only raw data will be presented unless otherwise specified.

Displayed in Figure 7.8 is the neutron diffraction data of undoped 2LFh acquired in this study compared with that previously acquired for synthetic 6LFh acquired by (Jansen, Kyek, Schäfer, & Schwertmann, 2002). For the 2LFh data, background removal has been performed by manual estimation of the incoherent signal underneath the Bragg peaks. The peak widths for 2LFh are significantly larger compared to those of 6LFh indicating smaller crystal sizes for the 2LFh sample. In terms of peak positions, there is a good correspondence between the two forms of ferrihydrite despite the extreme peak broadening observed for the 2LFh sample due to its inherent disorder, meaning that many of the 6LFh peaks cannot be resolved.

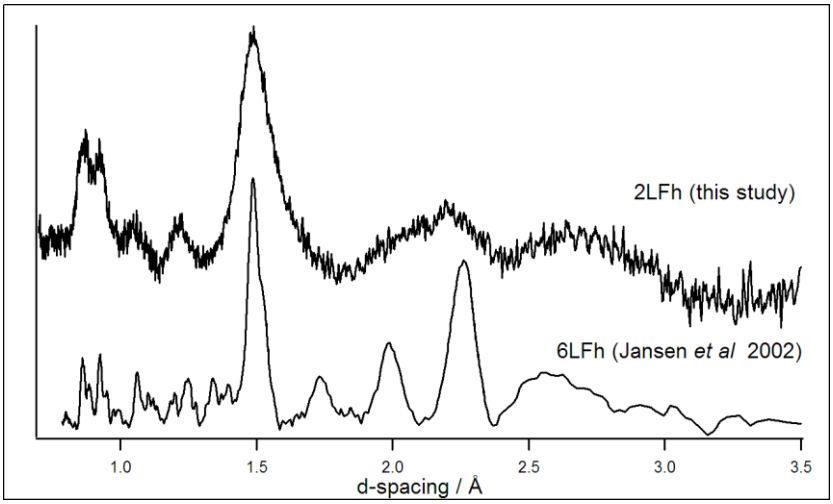

Figure 7.8 Neutron diffraction data comparing that of synthetic two-line ferrihydrite (2LFh) acquired in this study with that of synthetic six-line ferrihydrite (6LFh) acquired by Jansen et al., (2002). Both samples are un-deuterated. Background removal applied to the 2LFh data is described in the text.

Displayed in Figure 7.9 is the neutron diffraction data for the 2LFh and P3 samples. Also shown for comparison is the synchrotron X-ray diffraction data of 2LFh. The neutron diffraction patterns for 2LFh and 2LFhP3 are virtually identical being almost indistinguishable.

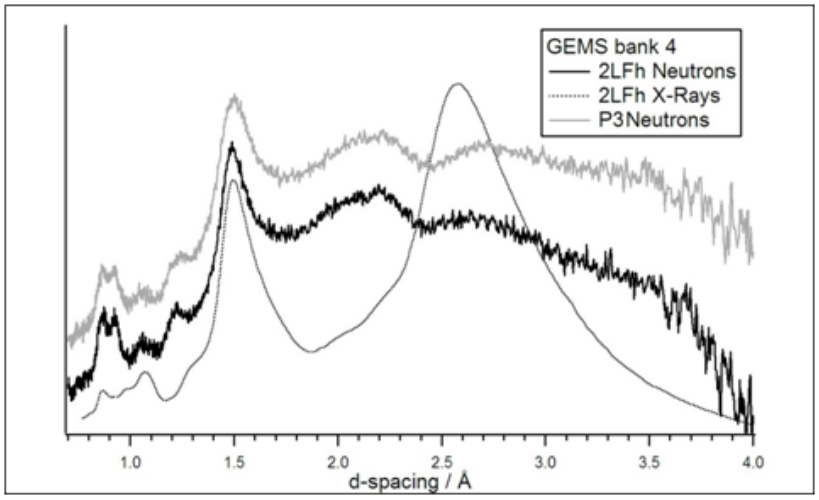

Figure 7.9 Neutron diffraction data comparing synthetic two-line ferrihydrite (2LFh) and synthetic 3% phosphorus doped two-line ferrihydrite (2LFhP3). Also for comparison, the low-angle synchrotron scattering data for 2LFh is shown. The profiles for both samples are practically identical.

Figure 7.10 compares the neutron diffraction data of P3 with that of P3h11. Apparent from the sharpening of the peaks upon ageing is the increased average crystal size of the hydrothermally treated sample when compared to its precursor.

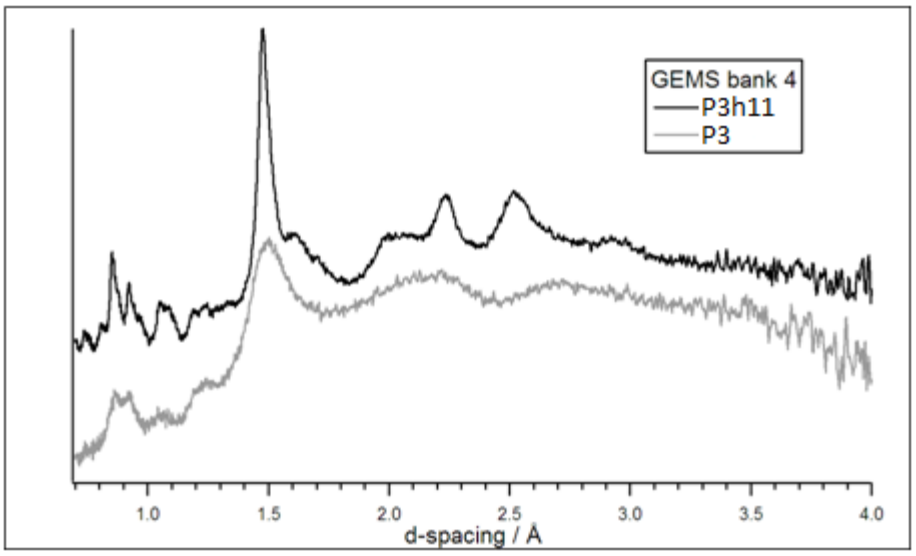

Figure 7.10 Neutron diffraction data for phosphorous doped (3% atomic) synthetic two-line ferrihydrite before (P3) and following hydrothermal treatment at 175ºC for twelve hours (P3h12). An increase in both crystal size and atomic order can been seen from the increased number of sharp reflections observed for the hydrothermally treated sample.

Hydrothermally treated P-doped 2LFh exhibits a Bragg peak as seen with both X-rays and neutrons at around 4.8 Å (see inset Figure 7.11) which is not observed in room temperature neutron measurements of the precursor material. In previous neutron diffraction studies of 6LFh and deuterated-2LFh this peak has been identified as being magnetic, since its intensity is inversely proportional to temperature, and has been assigned to antiferromagnetic alignment (+ – + –) on the (002) plane of the defect-free unit cell of the Drits model (Seehra, Babu, Manivannan, & Lynn, 2000; Jansen et al., 2002). Neutron diffraction studies of ferrimagnetic maghemite nanoparticles also identified a magnetic diffraction peak at around 4.8 Å which has been attributed to the antiferromagnetic sub-lattice of the bulk ferrimagnetic ordering of maghemite (Lefmann, Bodker, Klausen, Hansen, Clausen, Lindgård, & Morup, 2001).

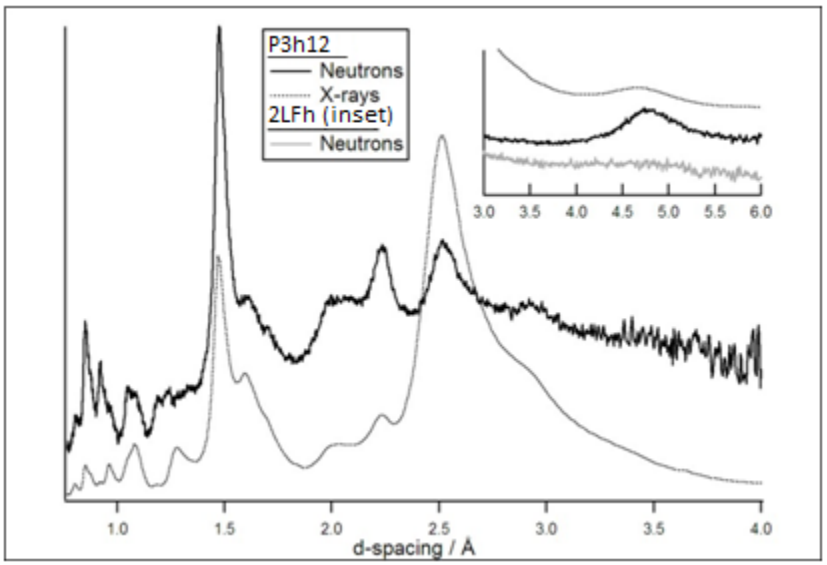

Figure 7.11 Comprison of neutron and X-ray diffraction data for phosphorous doped (3% atomic) synthetic two-line ferrihydrite following hydrothermal treatment at 175ºC for twelve hours (P3h12). Inset is the same data showing that at around 4.75 Å a peak common to both the neutron and X-ray data but is not observed in the neutron diffraction data of unaged undoped synthetic two-line ferrihydrite (2LFh).

7.4 Thermal Decompositional Analysis

Combined TGA and DSC data for the hydrothermally treated P5h11 and P3h12 samples are displayed below in Figure 7.12.

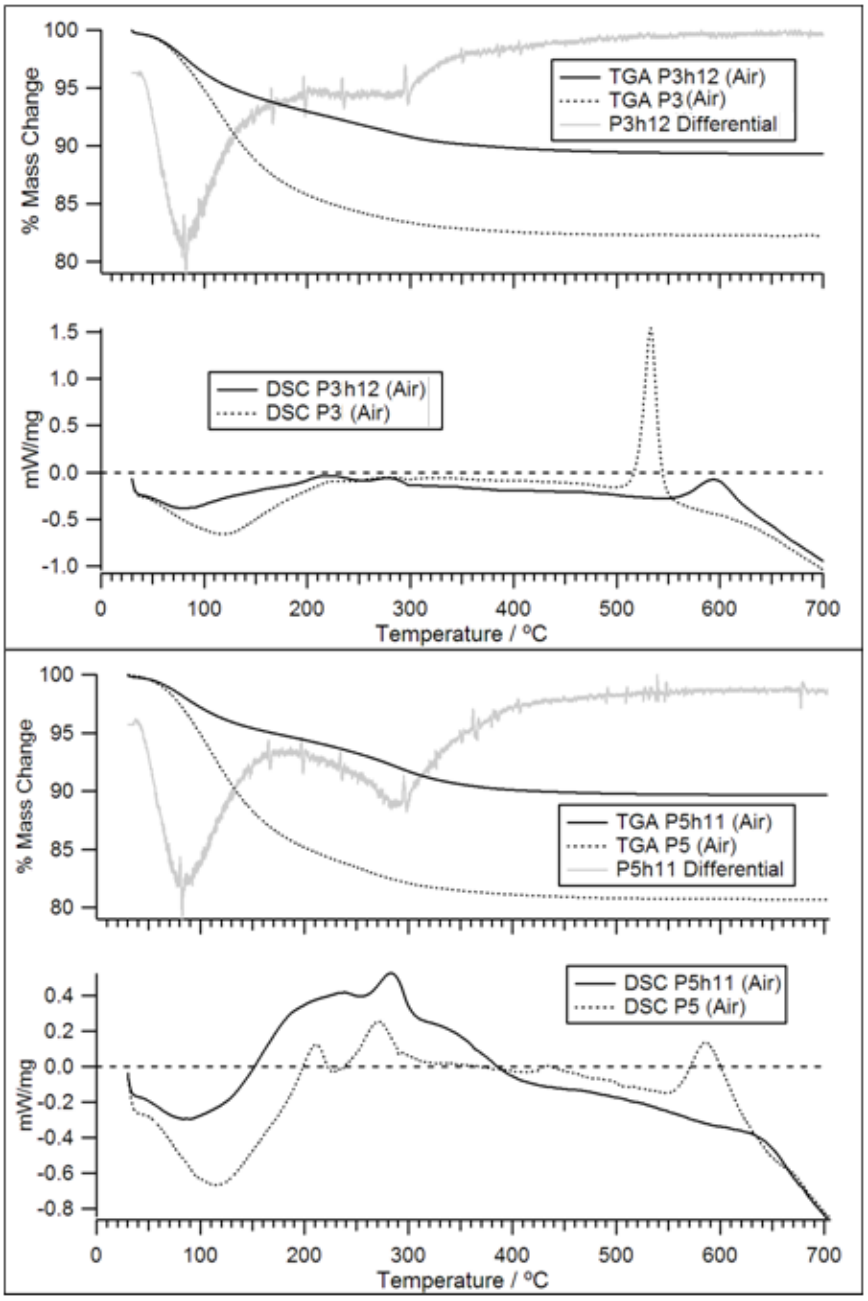

Figure 7.12 Thermogravimetric analysis (TGA) and differential scanning calorimetry (DSC) data of hydrothermally treated P3h11 (top) and P5h12 (bottom) using air purge gas. The grey curves on the TGA plots represent the differential mass-loss curves for the respective hydrothermally treated samples, as noted on the legend of each graph. Note that the intensity scales for normalised heat-flow for the DSC data are different in each case.

For both samples, the mass-loss at 700 °C is approximately 10%, half that lost by the precursor materials over the same temperature range. On the one hand, this may suggest that the hydrothermally treated samples contain less OH/H_2O compared to

their parent materials. Another possibility is that OH/H_2O is more tightly bound or incorporated in the structure of the hydrothermally treated materials.

DSC data of both P3h11 and P5h12 hydrothermally treated samples exhibit an endothermic peak region for temperatures in the sub 200 °C range as was observed for the P-doped parent materials. As previously discussed in section 6.4, this endothermic event can be associated with loss of OH and/or that of structural water (Schwertmann, 1991). Between 200 and 300 °C, two exothermic events are clearly observed for the P3h11 sample. The position and width of these features correspond well with weak exotherms observed in the DSC data of the P3 parent material. In the case of the P5h12 sample these exotherms are also present, however the intensity of the first, at around 225 ºC, is significantly suppressed when compared to that of the second. In addition to the suppression of the intensity of the first exotherm for the P5h12 sample, there is observed a delay in the onset of these events as gauged from the location of the peak maxima of the second exotherm relative to its temperature position for the parent material. These exothermic events have previously been observed for hydrothermally treated P-doped 2LFh and have somewhat tentatively been ascribed to OH loss and crystallinity changes during formation of the hydrothermal transformation product (Barrón et al., 2003). This assignment is, however, questionable since these exotherms are seen also in the DSC data of the P-doped parent samples, as presented in section 6.4, as well as in the data of Towe and Bradley (1967) for 6LFh.

Perhaps the most prominent difference between the DSC curves of the hydrothermally treated materials and those of their precursors is the suppression and delay of the high temperature exotherm with the peak location changing from around 520 to 680 °C for P3h12 and P5h11 respectively. This exotherm has previously been assigned to the phase transition of 2LFh to hematite, in section 6.4 for the P-doped 2LFh samples, and has been confirmed here for the hydrothermally treated samples with the aid of powder XRD. For the P3h12 sample, the delay and suppression of this high-temperature exothermic event is more pronounced than for that of the P5h11 sample. This is not surprising since this peak was already significantly suppressed for the P5 precursor material compared to those samples of lower P/Fe. The suppression of intensity of this feature may be explained by considering the accompanying increase in the breadth of this exotherm which would indicate that the temperature range over which the transition takes place is greater

for the hydrothermally treated samples and therefore the heat energy consumed during the transition is done so over a wider range of temperature. This naïve approach may, however, be misleading since the area under the peak for this transition in the P3h12 sample is approximately half that of the precursor material, perhaps suggesting that less of the hydrothermally treated material has undergone transformation. This, however, does not answer the question as to why hydrothermal treatment has resulted in a delay in the onset of the transformation. This may be in part due to the fact that the hydrothermally treated samples are composed of a mixture of extra phases in addition to the precursor P-doped 2LFh.

7.5 X-Ray Diffraction Analysis of 700 °C Annealed 2LFhPX

For the combined TGA-DSC analysis, the 2LFhPX samples were heated to 700 °C in air. In order to determine the transformation products of these samples, fresh samples of the 2FhPX series were heated in air to 700 °C (section 4.1.5) before analysis by XRD. Presented in Figure 7.13 are the XRD diffractograms of the transformation products of the annealed 2LFhPX samples. Also shown for comparison is that of $FePO_4 \cdot 2H_2O$ annealed according to the same method.

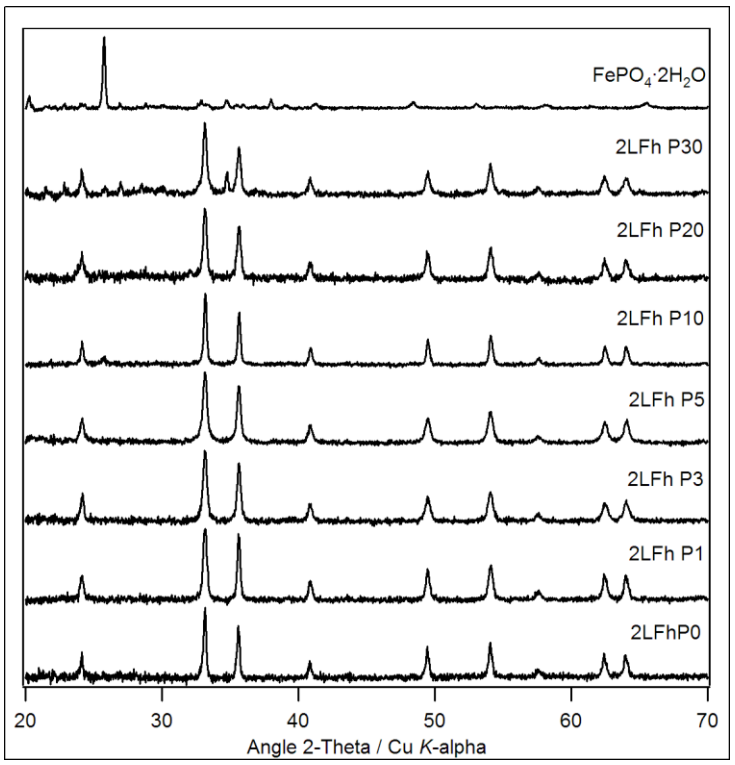

Figure 7.13 Powder X-ray diffraction data for the transformation products of the synthetic phosphorus doped two-line ferrihydrite series (2LFhPX) following annealing in air at 700 ºC for one hour. Also shown for comparison is that of FePO4•2H2O annealed according to the same protocol. For P/Fe levels of 0.20 and below the transformation products are practically identical with all features being indexable to hematite (JCPDS card 33-0664).

It can be seen from Figure 7.13 that for P/Fe levels of 0.20(P20) and below that the transformation products are essentially identical and can all be indexed to hematite. For 2LFhP10 an additional reflection is observed at 25.7 2θ which is not present in the profiles of the other 2LFhPX samples of P/Fe of 0.20(P20) and lower. This reflection may possibly due to either the (120) of goethite or the (116) of maghemite, however, these reflections have relative intensities (I/I_{max}) of only 0.10 and 0.07, respectively, and therefore would be expected to be accompanied by stronger reflections from each mineral phase. As can be seen from Figure 7.13, the transformation product of $FePO_4 \cdot 2H_2O$ has it maximum at 25.8 2θ, corresponding well with the position of this extra peak in the 2LFhP10 transformation product's diffractogram. This may indicate that at least part of the precursor 2LFhP10 material has been transformed to that of $FePO_4 \cdot 2H_2O$'s transformation product. The fact that this peak is not present in the transformation product of 2LFhP20 may be that the SNR of this diffractogram is poorer than that in 2LFhP10 case and therefore relatively weak reflections are not so apparent. In the XRD pattern of 2LFhP30's transformation product, in addition to those peaks which have been assigned to hematite for P/Fe = 0.20(P20) and lower, additional peaks can be seen, the most prominent of which lie at 21.6, 22.8, 25.8, 26.9 and 34.7 2θ. As was the case for 2LFhP5 the 22.8 2θ reflection may be due to the $FePO_4 \cdot 2H_2O$ transformation product. The other reflections may possibly be assigned to goethite or maghemite. The most intense of the extra features observed in the 2LFhP10 transformation product's diffractogram, which lies at 2.6 Å (34.5 2θ), is a spacing which is common to most iron oxides and hydroxides and therefore cannot be uniquely assigned to any.

Application of the Scherrer relationship, using a shape-factor equal to 0.89, to the seven most intense reflections between 30 and 65 2θ for each of the respective diffractograms of the 2LFhPX series gives estimates of average crystallite sizes, as shown in Figure 7.14. Error bars are equal to the standard deviation of the seven crystal size estimates calculated for each diffractogram. For P/Fe $\leq$ 0.05(P5) there is a strong negative correlation, which is well described by an exponential function, between average crystal size and P/Fe. This result is consistent with the notion that the presence of phosphate hinders the growth of hematite from the precursor 2LFhPX by surface poisoning of the growing particles. For P/Fe = 0.10(P10) the result, which in terms of the other P/Fe levels is somewhat anomalous, indicates that

average crystallite sizes for this sample are similar to that of the undoped 2LFh. For P/Fe = 0.20(P20) and 0.30(P30), average crystallite sizes are approximately 28% less than that of undoped 2LFh however, these values are some 5 nm or so larger than would be expected if the exponential relationship, which is observed for P/Fe ≤ 0.05(P5), is extrapolated to these P/Fe levels.

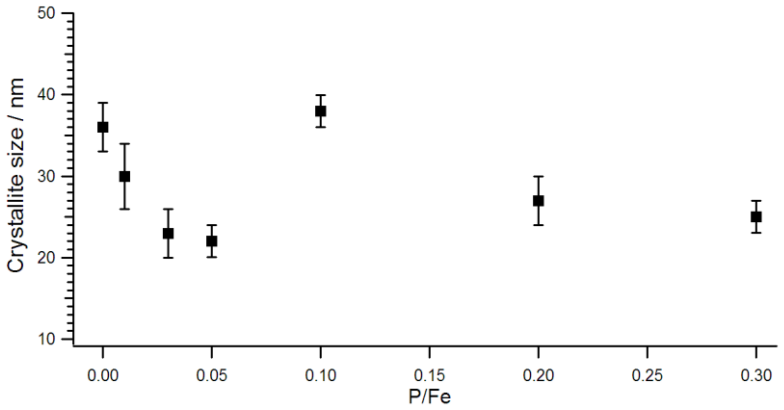

Figure 7.14 Average crystallite size estimated from the Scherrer relationship as applied to the powder X-ray diffractograms of synthetic phosphorus doped two-line ferrihydrite series (2LFhPX defined in section 4.1.3.) after annealing at 700 °C as displayed in Figure 7.13. Error bars represent the standard deviation of the size estimates as calculated from the seven most intense reflections between 30 and 65 2θ for each diffractogram.

7.6 *In situ* Heating and Combined XRD Analysis of 2LFhP3

Displayed in Figure 7.15 are the results of the *in situ* XRD heating experiment for 2LFhP3 (procedure outlined in section 4.2.1). It was observed that from ~25 °C to 317 °C the sample remained essentially unchanged with the measured scattering signal being typical of 2LFh. Between 317 °C and 368 °C occurs the onset of the phase transition of 2LFhP3 to hematite with the all the Bragg reflections beyond 418 °C being attributable to hematite (JCPDS card 33-0664). At 368 °C the diffractograms can clearly be seen to be composed of two distinct phases (2LFhP3 & hematite) whereas beyond this temperature (i.e. at 418 °C) the diffractograms consist predominantly of hematite save for some residual background intensity between 31–37 and 61–65 2θ, due to residual 2LFhP3 which becomes negligible at the temperature increases beyond 418 °C.

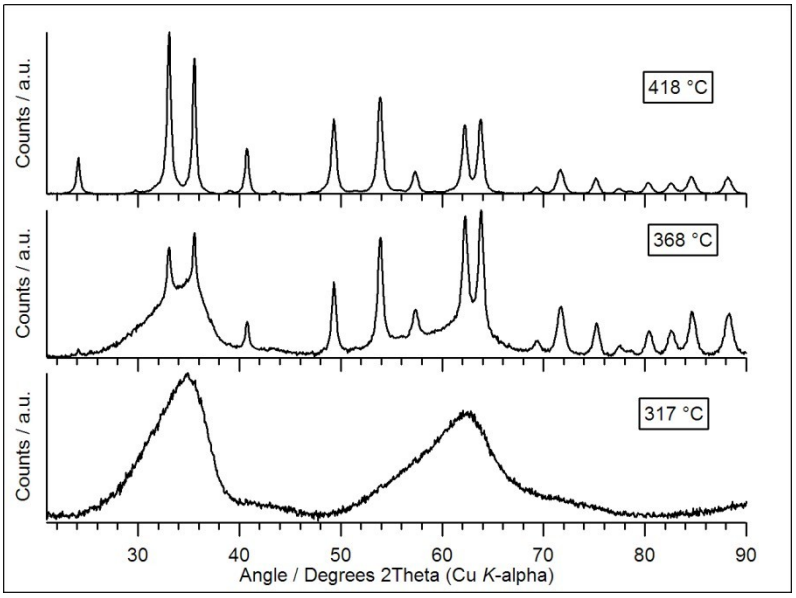

Figure 7.15 *In situ* heating powder X-ray diffraction analysis of 3% phosphorus doped synthetic two-line ferrihydrite (2LFhP3) showing a phase transition to hematite between 317 - 368 ºC. Beyond 418 ºC the major phase is that of hematite (JCPDS card 33-0664).

More subtle than the phase change observed at 368 °C is a systematic variation in the relative intensity of the low-angle (~35 2θ) maxima to that of the high-angle (~65 2θ) maxima occurring in the temperature interval ~25 to 266 °C. Shown in Figure 7.16 is the variation of intensity of the low-angle diffraction maxima, as normalized by the intensity of the high-angle maxima, upon heating of the sample. The temperature range over which the relative intensity of these two diffraction features is observed to vary corresponds well with the region of mass loss (OH/H_2O) as observed in the TGA analysis (see Figure 7.12). A similar result has been previously observed for sintered Si-associated 2LFh particles and was taken as evidence of the onset of hematite formation (Glasauer, Hug, Weidler, & Gehring, 2000).

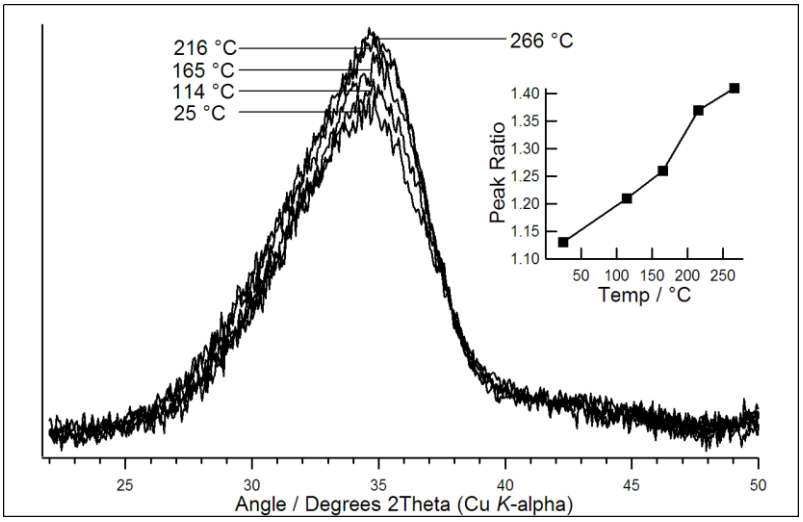

Figure 7.16 Variation of the intensity of the low-angle powder X-ray diffraction maxima (~35 2θ) relative to the high-angle maxima (~65 2θ) for 3% phosphorus doped synthetic two-line ferrihydrite (2LFhP3) as a function of sample temperature. Data have been normalised by the intensity of the high-angle maxima. Inset is the variation in peak ratio as a function of temperature.

7.7 Fourier Transform Infrared Spectroscopy

The FTIR spectra of P3 and hydrothermally treated P3h12 samples are shown in Figure 7.17. Also presented in the bottom half of Figure 7.17 is a magnified view of the 1150 - 820 cm^{-1} P-O stretching excitation region of the infrared spectrum.

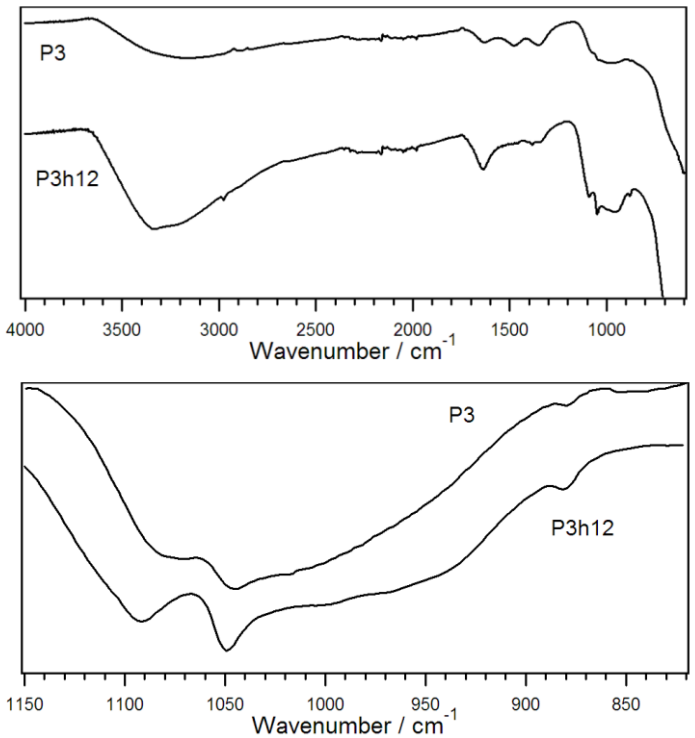

Figure 7.17 (top) Fourier transform infrared spectra for 3% phosphorus doped synthetic two-line ferrihydrite before (P3) and after hydrothermal treatment at 175ºC for twelve hours (P3h12) (bottom). A magnified view of the P-O stretching region for the same samples highlighting increased structural order upon hydrothermal treatment.

The first observation to make, based on the signal intensities in the 2500 - 3600 cm^{-1} region and at 1622 cm^{-1}, is that the extent of hydration of the hydrothermally treated sample would appear to be enhanced when compared to that of its P3 precursor. TGA data presented in Figure 7.12 demonstrated that hydrothermal treatment resulted in a product which, upon heating to 700 °C, lost 50% less mass compared its precursor material. Based on these combined observations it would appear that hydrothermal treatment has resulted in a product which is more hydrous in which the OH/H_2O content is more tightly associated with the crystal structure at ambient temperatures. One possibility is that as crystals have ripened and grown from the parent material the accompanying reduction in surface area (to volume ratio) has resulted in fewer surface sites for the binding of loosely associated OH/H_2O and the volume fraction of OH/H_2O has increased in which more tightly bound OH/H_2O may be expected to reside.

Between 1800 - 1300 cm^{-1} the P3 FTIR spectrum exhibits three clearly defined absorptions bands which are typical of ferrihydrite (Cornell & Schwertmann, 2003). These bands are however not visible in the FTIR spectrum of the P3h12 sample, being most probably obscured by the overlap of the 1622 cm^{-1} hydroxyl ion absorption feature.

Perhaps the most interesting difference between the P3 and P3h12 samples is the modification that hydrothermal treatment has on the P-O stretching region (1150 - 820 cm^{-1}). For the P3 sample, this region appears to be composed of several overlapping absorption bands with clearly defined, relatively narrow, features at 1075, 1050 and 880 cm^{-1}. Hydrothermal treatment results in a significant sharpening of these features and also a shifting of the 1175 cm^{-1} to higher wavenumbers ~1090 cm^{-1}. This result may suggest that phosphate associated with the surface of the P3h12 crystallites, which are on average larger and more well defined, has a more regular bonding geometry compared to that associated with, what is likely a more disordered, surface structure of P3. Another possibility is that as the crystallites have grown during hydrothermal treatment some of the phosphorous has been incorporated within the lattice structure. This may also account for the shifting of the high wavenumber feature, at 1175 cm^{-1}, to 1090 cm^{-1} for the P3h12 sample.

7.8 X-Ray Photoelectron Spectroscopy

Displayed in Figure 7.18 are the O 1*s* and Fe 2*p* XPS peaks for P3 and P3h12. Unfortunately due to an error with the automated acquisition routine the P 2*p* peaks for both samples were not acquired. Following the procedure outlined in section 4.2.3, the O 1*s* peaks were decomposed into three Voigt profiles the results of which are given in Table 7.2. From the inspection of Figure 7.18a, it can be seen that there exist slight differences between the area normalised O 1*s* peaks for the two samples. Upon hydrothermal treatment, the distribution of intensity of the O 1*s* peaks is weighted more strongly about ~531 eV than for the precursor P3 specimen. This shift in intensity can also be seen from the results of the peak fitting given in Table 7.2 which shows an increase in the proportion of the fitted peak at ~530.8 eV which is accompanied by a decrease in that at 532.5 eV.

The Fe 2*p* peaks for both samples are typical of iron in the ferric state and do not show any change upon hydrothermal ageing.

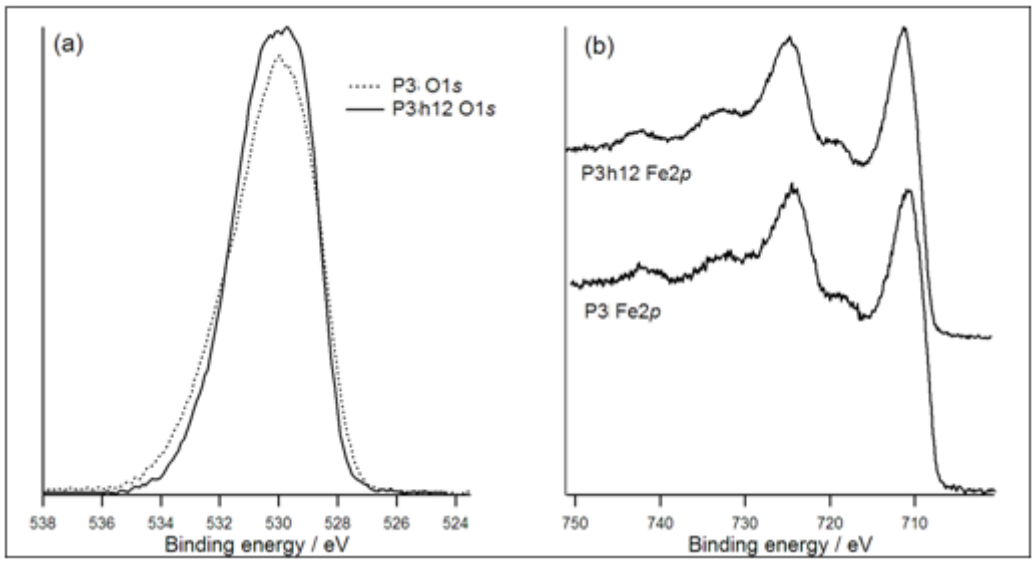

Figure 7.18 X-ray photoelectron spectra for 3% phosphorus doped synthetic two-line ferrihydrite before (P3) and following hydrothermal treatment at 175ºC for twelve hours (P3h12) comparing background subtracted (Shirley) area normalised oxygen 1s peaks (a) and raw unprocessed iron 2p peaks (b). A slight modification of the oxygen 1s binding energy profile can be observed.

Table 7.2 X-ray photoelectron oxygen 1s peak fitting results for 3% phosphorus doped synthetic two-line ferrihydrite before (P3) and following hydrothermal treatment at 175ºC for twelve hours (P3h12). The fitting routine is described in section 4.2.3.

Sample	Fitted Peak 1		Fitted Peak 2		Fitted Peak 3		FWHM (eV)
	centre (eV)	% Area	centre (eV)	% Area	centre (eV)	% Area	
P3	529.3	49.2	530.8	36.9	532.6	13.9	2.1
P3h12	529.4	47.7	530.9	41.5	532.5	10.8	2.1

7.9 Magnetic Characterisation

Magnetisation curves and blocking temperature (T_b) measurements were acquired for both the hydrothermally treated and annealed P5 samples. Displayed in Figure 7.19 are the magnetic hysteresis loops (M vs. H) of the hydrothermally treated P5 sample showing the evolution of the loops as a function of ageing time. Summarised in Figure 7.20 are maximum magnetisations (M_{max}), as measured at an applied field strength H equal to 5 T (the maximum field strength of the VSM equipment), for the hydrothermally treated and annealed P5 samples as a function of heat treatment time. Figure 7.21 presents the zero-field-cooled M vs. T curves for the P5 samples illustrating the effect of hydrothermal heat treatment as a function of increasing treatment time. Summarised in Table 7.3 are the T_b values, estimated from the zero-field cooled M vs. T data, for both the hydrothermally treated and annealed samples as a function of heat treatment time. Magnetic data was also collected for the hydrothermally treated P3h12 sample which is not shown here but will be discussed in the text which follows. The sample magnetisations M have been normalised by the mass of the sample, which was typically 100 mg, and as such M is given in SI units of emu per gramme (A m^2 kg^{-1}).

After being subject to an applied field strength of 5 T, the unaged 2LFh sample is characterised by a coercively of ~0.1 T, a remnant magnetisation of ~1.3 T and M of some 10.4 T. In the case of the unaged P5 sample these values are 0.2, 1.6 and 11.5 T, respectively.

Hydrothermal treatment of the P5 sample was found to result in an increase in coercivity, remnant magnetism and M_{max} with increasing hydrothermal treatment time. By eleven hours ageing time these values were found to increase by 1.3, 4.8 and 2.2 times their initial values for the unaged sample. Hysteresis loops measured at five and eleven hours ageing time were found to be almost identical. This may suggest that beyond five hours ageing time either no further enhancement of the magnetic properties takes place or that there is an enhancement in the magnetic

properties which is followed by a subsequent drop upon approaching eleven hours. In their study on hydrothermal treated citrate-associated 2LFh, Michel et al. (2010) found that the M_{max} of the material initially increased reaching a maximum around eight hours ageing time before rapidly dropping below that of the starting material as significant amounts of hematite began to form (Michel et al., 2010).

In contrast to hydrothermal treatment, annealing of the P5 sample results in a reduction in coercivity, remnant magnetisation and M_{max}. This effect is seen to increase with annealing time. This result in itself is interesting considering that powder XRD structural analysis was unable to detect a significant change for the annealing temperatures and times used here.

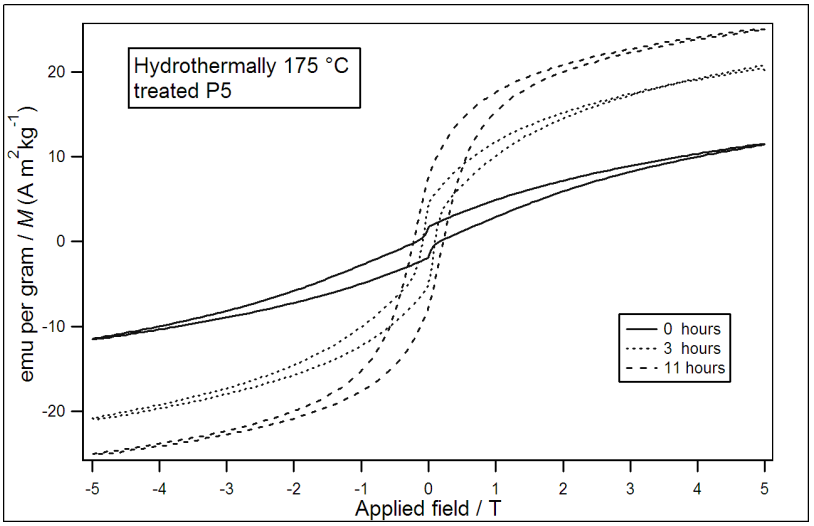

Figure 7.19 Magnetic hysteresis-loops for 5% phosphorus doped synthetic two-line ferrihydrite (P5) following hydrothermal treatment at 175ºC for zero, three and eleven hours showing the evolution of the loops with ageing time. An increase in magnetic coercivity and saturation with increasing treatment time can be clearly observed.

From inspection of the magnetic hysteresis loops presented in Figure 7.19 it can be seen that, even at the maximum values of applied field strength, magnetic saturation of the samples was not achieved. Since the magnitude of the applied fields are relatively high (± 5T) this behaviour suggest a significant fraction of the material is ferrimagnetic. Ferromagnetic materials, on the other hand, would be expected to reach saturation with applied fields of 2-2.5T or lower.

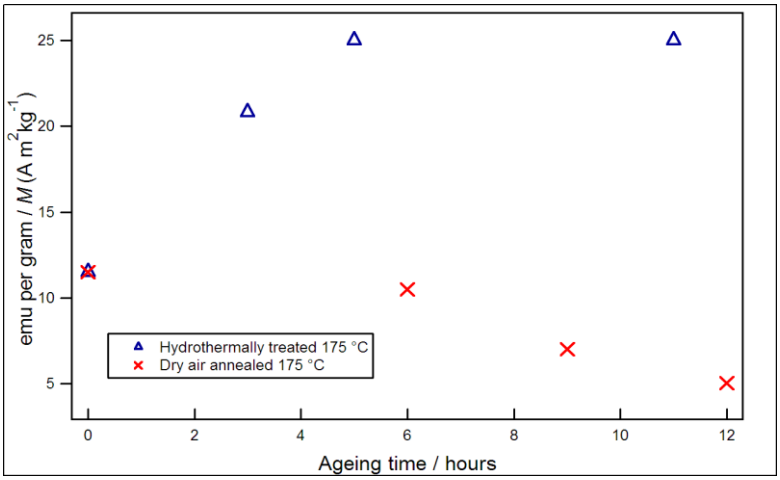

Figure 7.20 Comparison of the maximum magnetization (Mmax) for hydrothermally aged and annealed (at 175ºC) 5% phosphorus doped synthetic two-line ferrihydrite (2LFhP5) as a function of ageing time measured at an applied field strength of 5 T at a temperature of 5 K. An increase in maximum magnetization is observed with increasing hydrothermal treatment time, whereas, a decrease in magnetization is observed with increasing annealing time.

Measurement of the magnetic blocking-temperature (T_b) indicates a slight increase from around 47 Kelvin for unaged P5 to a value of 54 Kelvin for the 11 hours hydrothermally treated sample (see Figure 7.21). In addition to this slight increase in T_b, the *M* vs. T curve for the 11 hours sample exhibited a conspicuous hump around 99 K. Since the T_b is affected by particle size as well as magnetic anisotropy the appearance of this extra feature suggests the hydrothermally treated P5 is composed of a bimodal distribution of particle sizes and/or anisotropies. An additional observation which can be made is that the breadth of the main peak in the *M vs.* T plot increases with increasing ageing time. This again may be explained by considering that during the hydrothermal ageing process, the precursor material is transformed into one composed of an ensemble of different crystallites, be that in terms of size, anisotropy, phase or a combination thereof.

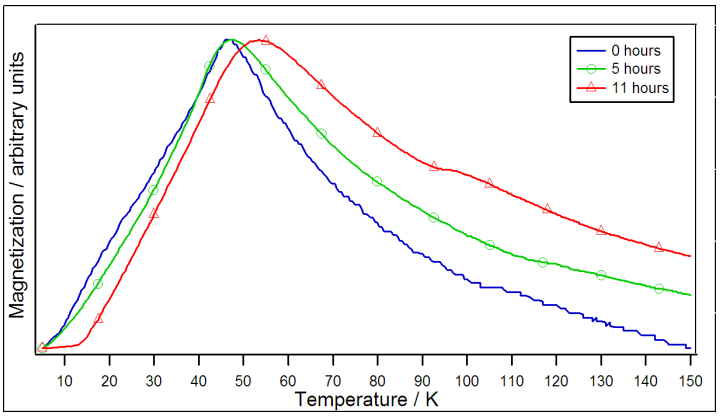

Figure 7.21 Zero-field cooled M vs. T curves (5mT) for hydrothermally treated (at 175ºC) 5% phosphorus doped synthetic two-line ferrihydrite (2LFhP5). An increase in the magnetic blocking temperature can be seen for increasing hydrothermal treatment time.

The M *vs.* T data for the annealed P5 sample also exhibited an increase in T_b which was somewhat more pronounced than for the hydrothermally treated sample. The results of this analysis, along with that of the hydrothermally treated sample, are summarised in Table 7.3. Due to a measurement error, the Tb for 3 hours hydrothermal ageing time could not be determined.

Table 7.3 Summary of M vs. T data measured at 5mT for the 5% phosphorus doped synthetic two-line ferrihydrite (P5) sample comparing the results of annealing and hydrothermal treatment at 175ºC.

Annealing time (hours)	Blocking Temp. (k)	Hydrothermal time (hours)	Blocking Temp (k)
0	47.8	0	47.8
6	65.8	3	-
9	67.0	5	46.9
12	72.9	11	52.5

7.10 Analytical Transmission Electron Microscopy

7.10.1 Bright-Field TEM Imaging

BF-TEM imaging of the hydrothermally treated P-doped samples revealed a marked increase in crystallinity compared to the precursor material (see Figure 7.23). The presence and abundance of crystallites exhibiting well defined faceted edges and lattice fringes which cover the extent of the crystallite surface has increased.

Similar to the precursor, this sample also has a strong propensity to form large aggregates tens to hundreds of nanometres in extent. Particle size analysis, based on measurements of the dimensions of 70 crystallites, estimates an average crystallite size of 3.6 ± 0.9nm (Figure 7.22). What's more the distribution appear to be log-normal implying coalescence of crystallites. Compared with the Michel et al., (2010) study, in which by 11 hours ageing crystallites had grown to an average size of ~ 9 ± 2nm (~310% increase), it would appear that phosphorous has allowed an increase in atomic ordering with minimal ripening of particles for the hydrothermal treatment times used here.

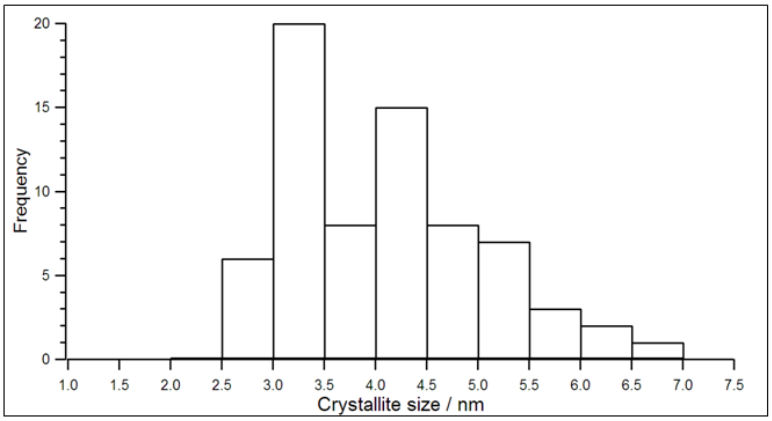

Figure 7.22 Histogram of hydrothermally treated (eleven hours at 175ºC) 5% phosphorus doped synthetic two-line ferrihydrite (P5h11) crystallite sizes as estimated from the direct measurement of seventy crystals observed in bright-field TEM micrographs.

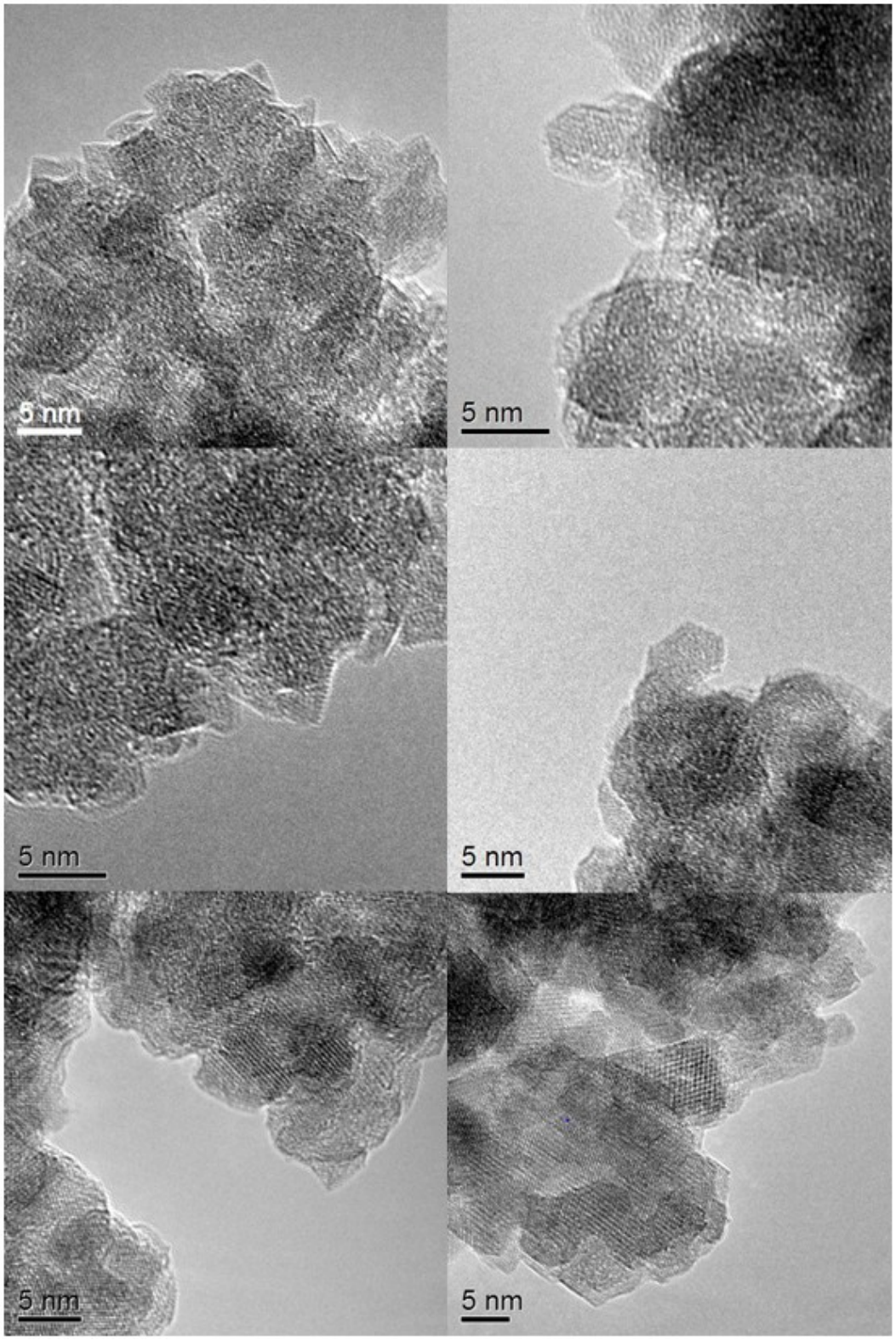

Figure 7.23 High magnification bright-field TEM micrographs of hydrothermally treated (eleven hours at 175ºC) 5% phosphorus doped synthetic two-line ferrihydrite (P5h11). An increase in both crystallite size and atomic order can been seen compared with the untreated sample (see Figure 6.26).

Direct phase identification from BF-TEM micrographs is always a difficult and uncertain task. For example, displayed in Figure 7.24a is a BF-TEM micrograph,

recorded from the edge of an aggregate of P5h11 acquired close to Scherzer defocus. This field of view contains several overlapping faceted crystallites. One of these crystallites (marked with a red box) appears to be oriented such that it is viewed along a low-order zone-axis; a serendipitous alignment which provides the best opportunity for of phase identification. A magnified view of this *boxed* area is given in Figure 7.24b from which it can be seen that the image intensities describe a regular square patterning of white dots, with dark interstices, separated by distances of approximately 2.6 Å along the base of the square. One possible crystallographic assignment for this crystallite is one of the Fe_2O_3 spinels (maghemite/magnetite) as viewed down the [001] zone-axis. Figure 7.24c and d show the maghemite structure (ICSD 79196) as viewed along the [001] direction and a simulated BF-TEM image of a 6 nm slab of maghemite viewed in this projection. Microscope parameters used for the image simulation were chosen to match those of the microscope (Philips CM200) used to acquire the image (see section 4.2.8). It can be seen that there is a good correspondence between the simulated (Figure 7.24d) and experimental (Figure 7.24b) micrographs. It should be noted that the other spinel phase magnetite would be indistinguishable from that of maghemite based on BF-TEM imaging alone. Wüstite, as viewed down one of the <100> cube-face normal axes, has Fe and O arranged in a square motif with similar spacings to those observed for the maghemite <100> projection. A BF-TEM micrograph of this phase viewed down one of these zone-axes is again almost identical to that of the spinels.

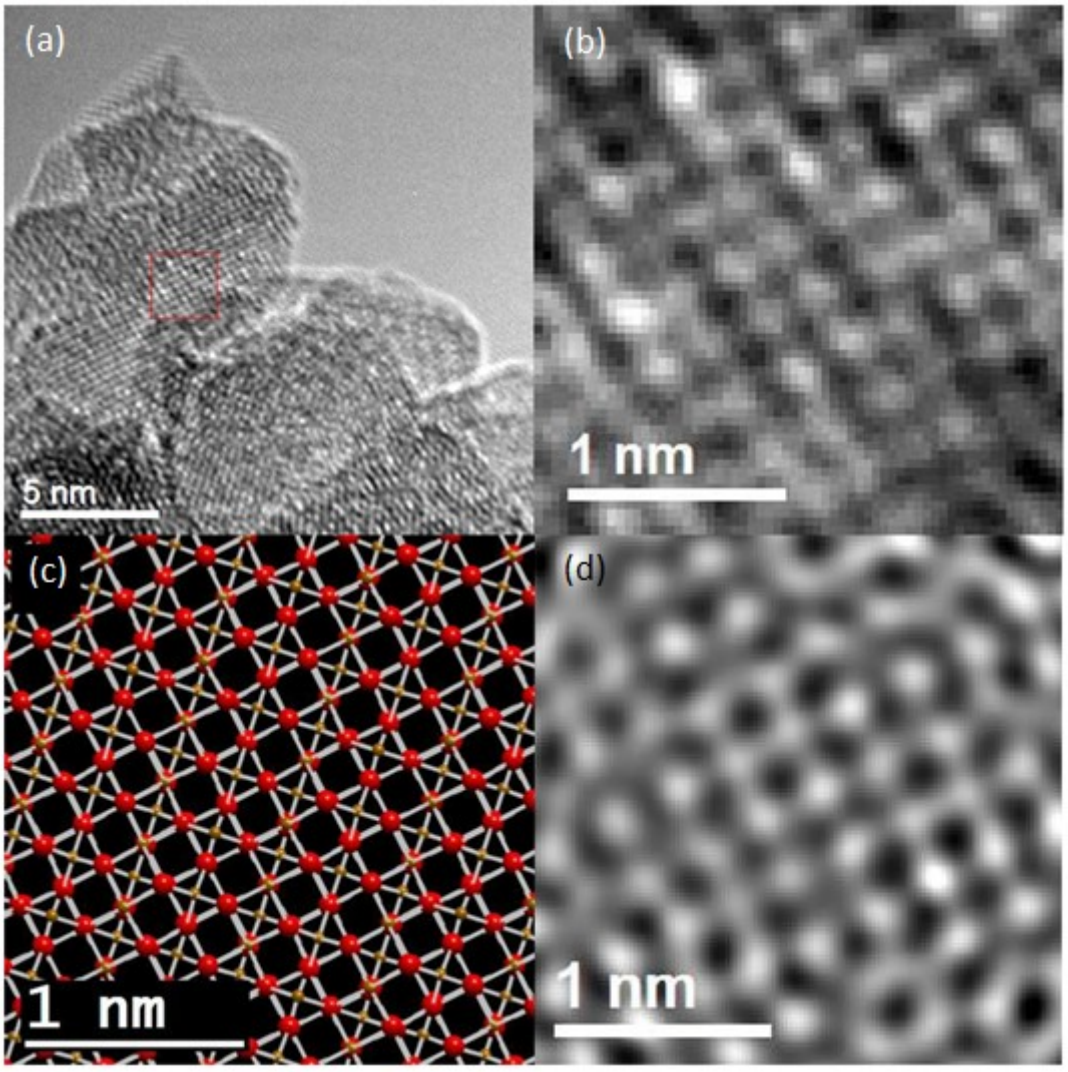

Figure 7.24 (a) High magnification bright-field TEM micrograph of hydrothermally treated (eleven hours at 175ºC) 5% phosphorus doped synthetic two-line ferrihydrite (P5h11) showing a well crystalline area view down a low-order zone axis (red-boxed) (b) a magnified view of the area indicated in 'a' (c) maghemite (ICSD 79196) viewed down the [001] zone-axis. O atoms (large) are coloured red and Fe atoms (small) orange. (d) a BF-TEM image simulation of the projection in 'c' calculated for a 6 nm slab of material. Simulation parameters are given in section 4.2.8.

As illustrated above it is sometimes difficult to use BF-TEM imaging alone for unambiguous phase identification; especially when dealing with multi-phase nanocrystalline systems which have a strong propensity to aggregate. A somewhat simpler means of high-magnification BF-TEM micrograph interpretation is to measure lattice spacings and attempt to assign these to crystallographic planes of known crystal structures. It should be noted, however, that due to the poor sampling statistics of TEM lattice fringes observed in one area may not be representative of the material as a whole. On the other hand in powder XRD, where the number of crystallites examined is large (approaching infinity) and in the absence of texture all crystal orientations are considered to be equally likely, the relative scattering

intensities of atomic planes are important. In high-magnification (S)TEM on the other hand, for which the area under observation contains a small number of randomly oriented crystallites, the relative scattering intensities are of less importance. In the limiting case we could imagine a single crystal which, in the absence of *in situ* specimen tilting, will be oriented randomly with respect to the beam direction. In this situation all crystallographic directions will be equally likely and by implication only those planes which lie near or on axis will contribute to the image or diffraction pattern. In this case the symmetry of a particular crystal structure becomes important, with those possessing higher symmetry (e.g. cubic, fcc, bcc, *etc.*) having a greater number of equivalent axes, and so atomic planes. However, from inspection of BF-TEM micrographs it is clear that other phases exist in addition to that of ferrihydrite.

7.10.2 TEM EEL Spectroscopy

Estimates the of ferric iron and octahedrally coordinated iron content, for 2LFhP5h11 as derived from TEM-EELS fitting analysis of the Fe-*L* edge, as a function of increasing electron-fluence are presented in Figure 7.25. Estimated from least-squares fitting analysis at fluences of around 5 x 10^5 electrons nm^{-2}, ferric iron comprises between 65-90% of the total iron present (81% if we go by the exponential function fitted to the data). The van Aken method estimates close to 100%. At the same fluence, the octahedral iron content represents 53-75% (68% by the fitted line) of the total iron present. At around 10^8 electrons nm^{-2} the ferric iron content is seen to decrease whereas within errors the octahedral iron fraction remains constant. By the experiments end, ferric- iron accounts for approximately 30% and octahedrally coordinated iron for 90% of the total iron present. If we compare these estimates to the same values for the precursor P5 sample, which were presented and duly discussed in section 6.6, we see that the initial estimates of percent ferric-iron and octahedrally coordinated iron are very similar for both samples. In the case of the octahedral iron data for the P5 sample, with reference to Figure 6.12 in section 6.6.1 it can be seen that there is a large scatter of the data points and the corresponding error bars are significantly larger that those presented here for P5h11. This indicates that there is a larger uncertainty in the best-fit solutions for P5 than for the P5h11 sample. The low-fluence estimate of octahedral-iron content for P5 is between 55-100 % whereas, for P5h11 it is 53-73%.

Therefore, within errors, P5 may feasibly contain 100% six-fold coordinated iron whereas the upper limit on octahedral iron in the hydrothermally treated P5h11 is 73%. This goes some way to substantiate the conclusion of Michel et al., (2010) that hydrothermal treatment results in an increase in the probability of tetrahedral-iron site occupancy.

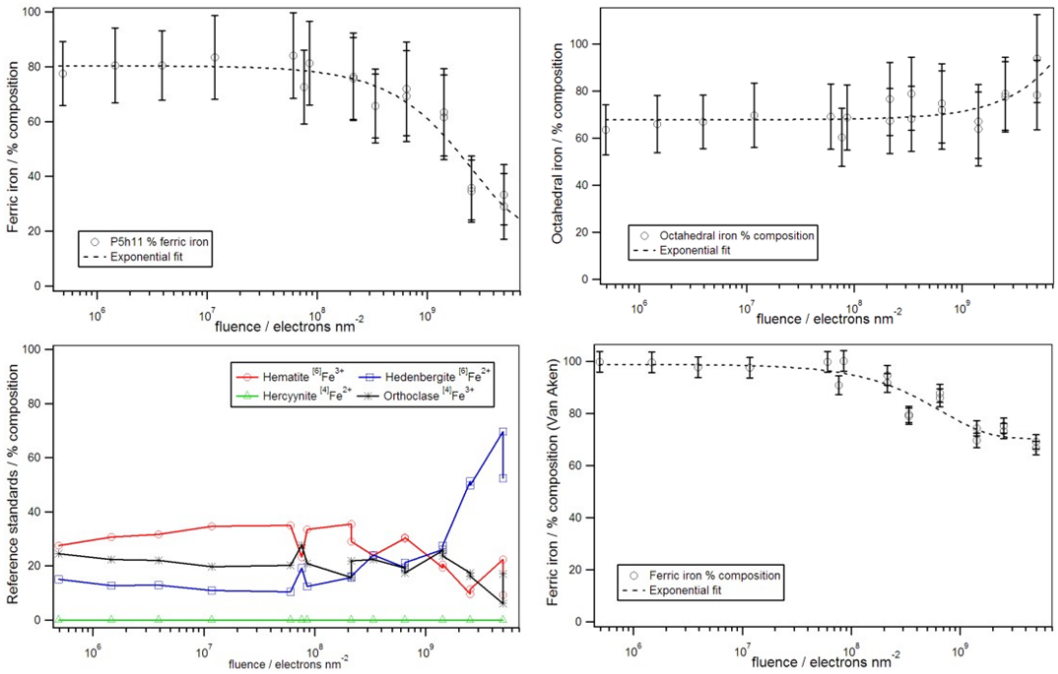

Figure 7.25 TEM-EELS Fe-*L* edge analysis for hydrothermally treated (eleven hours at 175ºC) 5% phosphorus doped synthetic two-line ferrihydrite (P5h11) showing the derived ferric iron and octahedrally coordinated iron content as a function of electron fluence. Exponential curves (dotted) are fitted to both data sets. Error bars for fitted data are derived from the uncertainties provided by the fitting routine used for analysis of this Fe-L edge feature. Those for the van Aken method are in accordance with estimates derived in van Aken et al. (1998). The effect of prolonged exposure to the electron beam can be seen marked by a decrease in the ferric iron content beyond 10^8 electrons nm^{-2}.

7.10.3 Aberration Corrected STEM Imaging

AC-STEM HAADF imaging of the P3h12 sample was carried out using the NION UltraSTEM (SuperSTEM2) at the SuperSTEM laboratories (UK). The same analysis of the P5h11 sample was performed using the same model of microscope (actually a later build with some of the problems of previous builds ironed out) housed at the Oak Ridge Laboratories (USA). Great care was taken to ensure that fluence levels were kept to a minimum despite the fact that fluences typically required for the acquisition of the micrographs are of the order of 10^7-10^8 electrons nm^{-2} (significantly higher than those encountered in conventional TEM imaging), however, still at or below the fluence damage threshold determined in the previous section for 200 keV electrons.

AC-STEM HAADF imaging of the hydrothermally treated samples (Figure 7.26) reveal an increase in average crystallite size and a corresponding increase in crystallinity. In cases where crystallites are favorably oriented with respect to the optical axis, atomic ordering can be observed extending over the entirety of the particles (see Figure 7.26c & d for an example). Regions may be identified in which the projected Fe-atomic arrangement describes interlocking hexagonal motifs with Fe-Fe distances and relative orientations, which are consistent with both hematite and the defective phase of the Drits' structure as viewed down the [001] direction (Figure 89a and b). Other regions are seen to contain crystallites for which the Fe projected positions bear resemblance the structures of either maghemite of magnetite viewed down an axis close to the [1 1 2] (see Figure 7.26f and Figure 7.27b, c, d and f for examples of this).

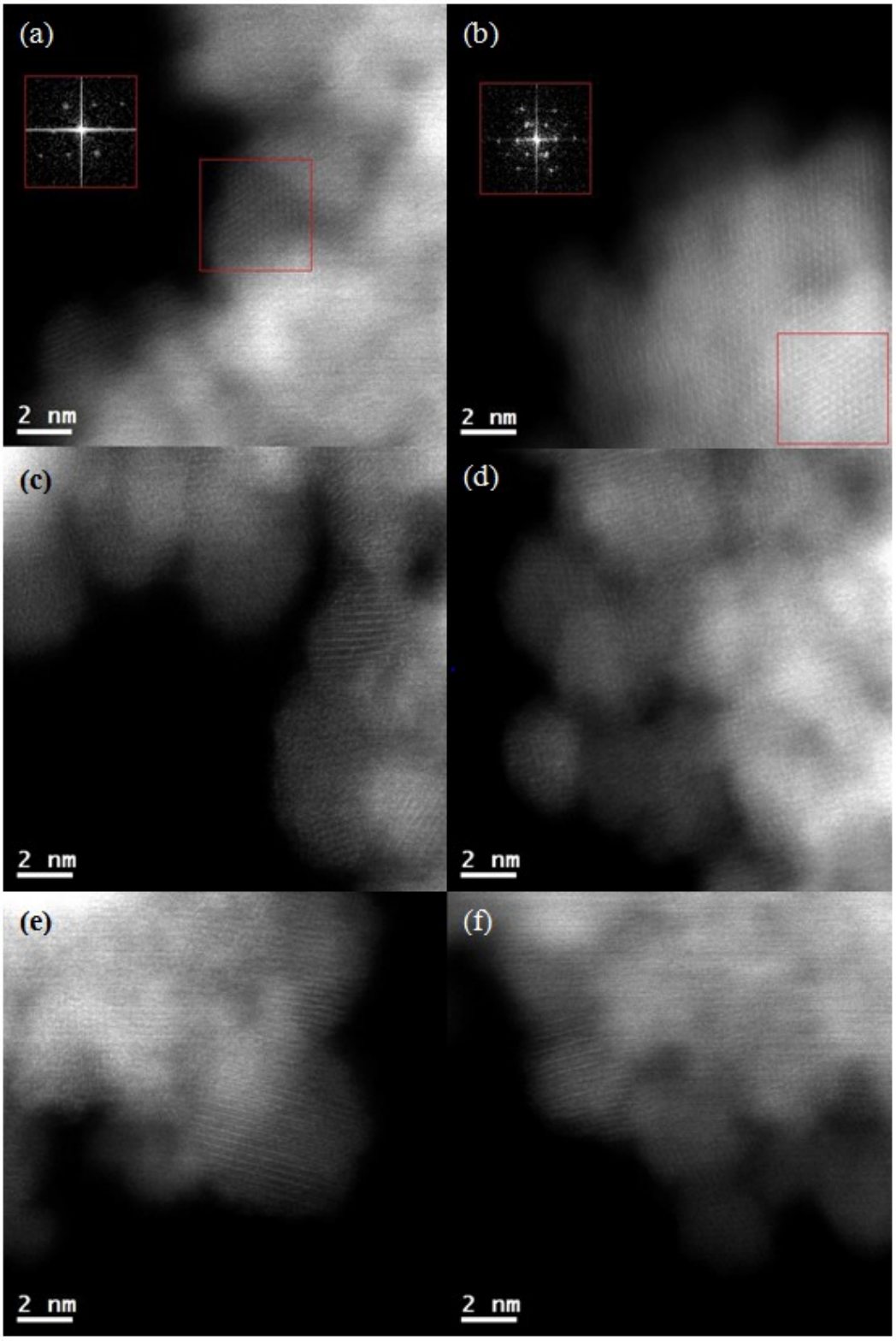

Figure 7.26 Aberration corrected HAADF STEM micrographs of hydrothermally treated (twelve hours at 175ºC) 3% phosphorus doped synthetic two-line ferrihydrite (P3h12) collected at fluences below ~10^8 electrons nm^{-2}. Images (a) and (b) clearly show a projected hexagonal arrangement of Fe-atoms. Close inspection reveals atomic structural order extending over ~4-8 nm.

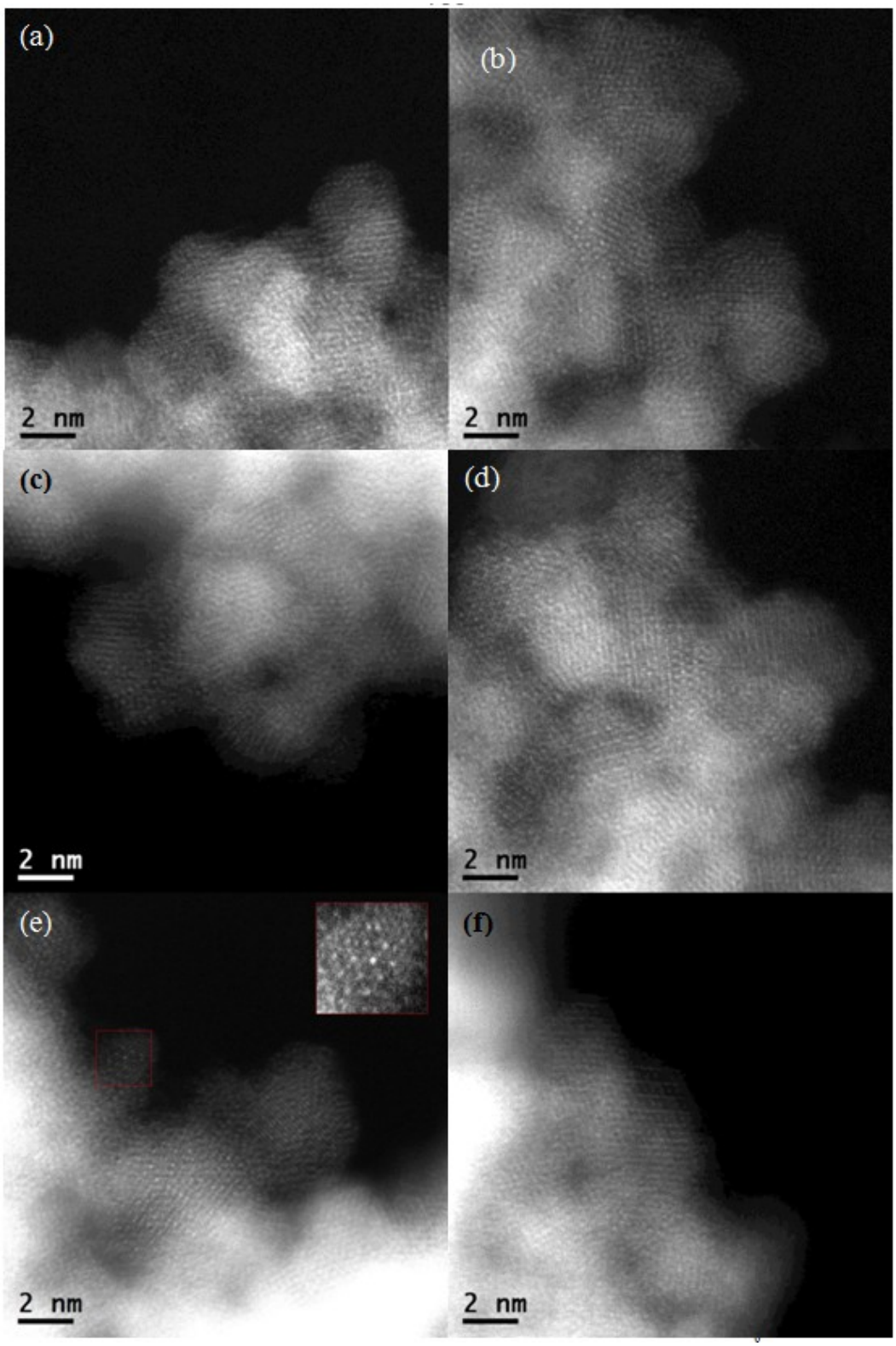

Figure 7.27 Aberration corrected HADDF STEM micrographs of hydrothermally treated (eleven hours at 175ºC) 5% phosphorus doped synthetic two-line ferrihydrite (P5h11) collected at fluences below ~10^8 electrons nm^{-2}. Inset in (e) is a zoomed and contrast adjusted view of the red-boxed area which shows hexagonal arrangement typical of Fe-atomic arrangement of hematite and the Drits' defective-phase as viewed down the [0 0 1] zone-axis.

Displayed in Figure 7.27a is an AC-HAADF micrograph of sample P5h11 in which periodic arrangement of projected Fe-atomic positions may be observed. This

pattern is typical of the projected Fe-atom arrangement of spinel iron oxides (magnetite/maghemite) as viewed down the [1 1 2] zone-axis. Shown in Figure 7.28b is a simulated HAADF image of the maghemite structure as viewed down this zone-axis. The simulation was performed using microscope specific parameters set to match those of the NION UltraSTEM used for the acquisition of the experimental micrographs (see section 4.2.8). Assuming the particles to be approximately spherical, a slab thickness of ~4 nm was chosen for the simulation, that is the spatial extent of the magnetite-like [1 1 2] Fe arrangement observed in the experimental micrographs. The calculated image shows excellent agreement with the experimental Fe atom arrangement observed in the experimental micrographs.

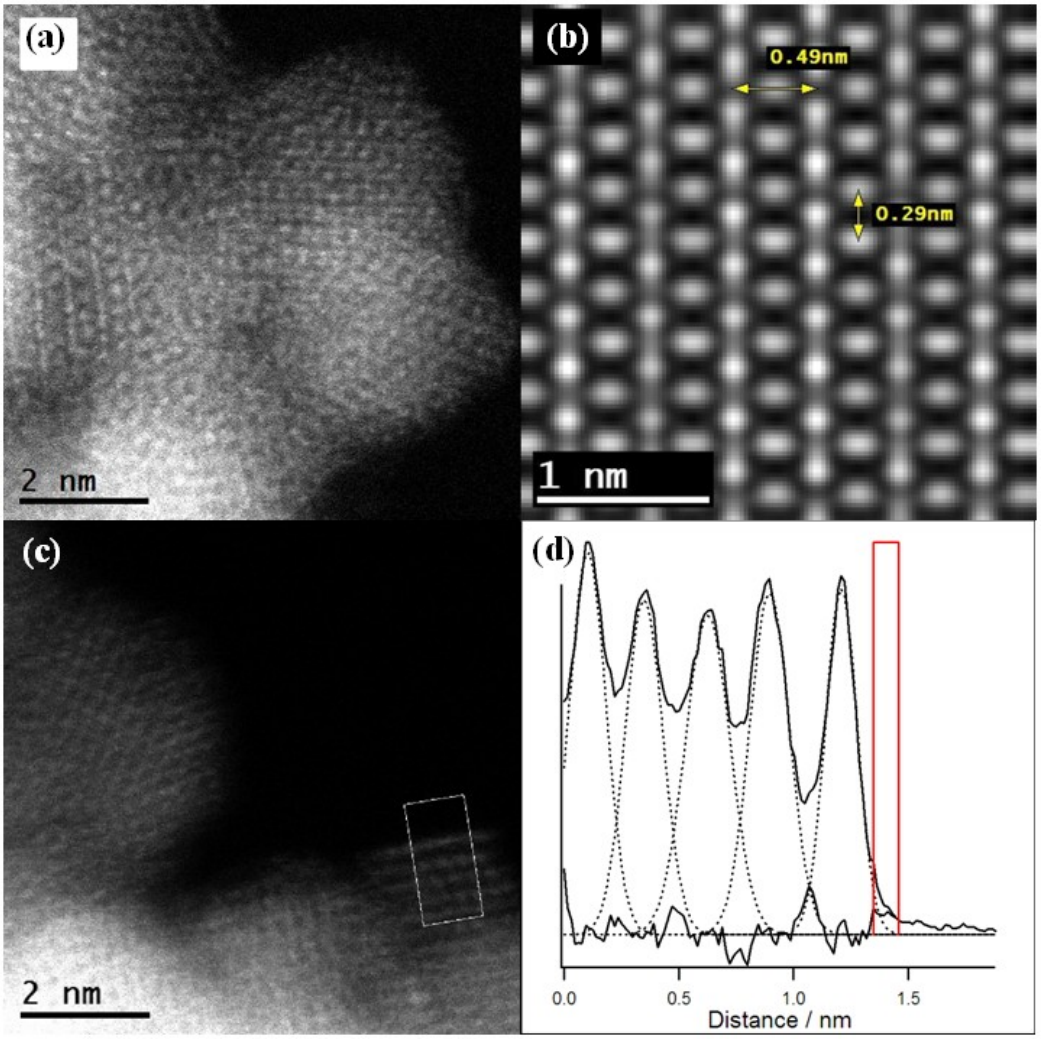

Figure 7.28 (a) Aberration corrected HAADF micrograph of hydrothermally treated (eleven hours at 175ºC) 5% phosphorus doped synthetic two-line ferrihydrite (P5h11) (fluence of $< 10^8$ electrons nm^{-2}). (b) Simulated AC-HAADF micrograph of a 3.9 nm thick slab of maghemite viewed down the [1 1 2] zone-axis. (c) A favourably oriented crystal of P5h11 showing atomically sharp edges and (d) Pixel intensity profile is taken from boxed area in (c) showing atomically sharp edge of the crystal. The red boxed area in (d) has a width of 0.11 nm; approximately equal to the STEM probe–width of the UltraSTEM used to acquire images (a) and (c) highlighting well defined crystals.

Shown in Figure 7.28c is a favourably oriented ~2 nm crystal from which the AC-HAADF intensity profile has been extracted and displayed in Figure 7.28d. The pixel intensity profile shows clearly that this crystal terminates with an atomically sharp surface with no sign of surface modification. Additionally, the intensity profile, which has been fitted with a series of Gaussians, indicates that within the first four (Fe) atomic layers the crystal is approximately of uniform thickness.

7.10.4 AC-STEM-EELS Compositional Analysis of P5h11

AC-STEM EEL spectroscopic measurements were made for P5h11 using the Oak Ridge NION UltraSTEM. Since the routines for smart-EELS acquisition are, at the time of writing, still under development at the SuperSTEM facility, controlled, low fluence EEL spectroscopy was performed in the following manner. Conventional EEL spectrum images were acquired from a given area of the sample using a signal integration time of 0.5 seconds per pixel and a pixel-size which varied between 1.6 and 25.0 $Å^2$, depending on the area of sample being scanned. A spectrometer dispersion of 0.3 eV/channel was used in order that both the O-*K* and Fe-*L* edges were simultaneously projected across the CCD array. In order to reduce fixed pattern CCD noise between each pixel acquisition, a small random offset was applied to the drift-tube voltage and the *unshifted* spectrum image was reconstructed offline, post-acquisition. Sub-pixel scanning was employed during acquisition to ensure a uniform illumination of the sample. A single integrated spectrum was extracted from the spectrum-image for subsequent analysis. Using this protocol all EEL spectra were acquired using fluences of approximately 2×10^9 electrons nm^{-2}.

In total, nineteen spectra were used for compositional analysis for which an average value of O/Fe = 1.4 ±0.1 was found. A typical spectrum-image region and the corresponding Fe-*L* and O-*K* EEL edges acquired from that area are shown in Figure 7.29(a & b). The O-*K* edge (Figure 7.29b) is characteristic of a number of iron-(hyd)oxides and therefore it does not provide unique phase identification. The Fe-*L* edge, for which the principal maxima exhibits a low-energy shoulder, is characteristic of predominantly ferric iron in six-fold coordination and again is a common structural-chemical environment common to many iron (hyd)oxides.

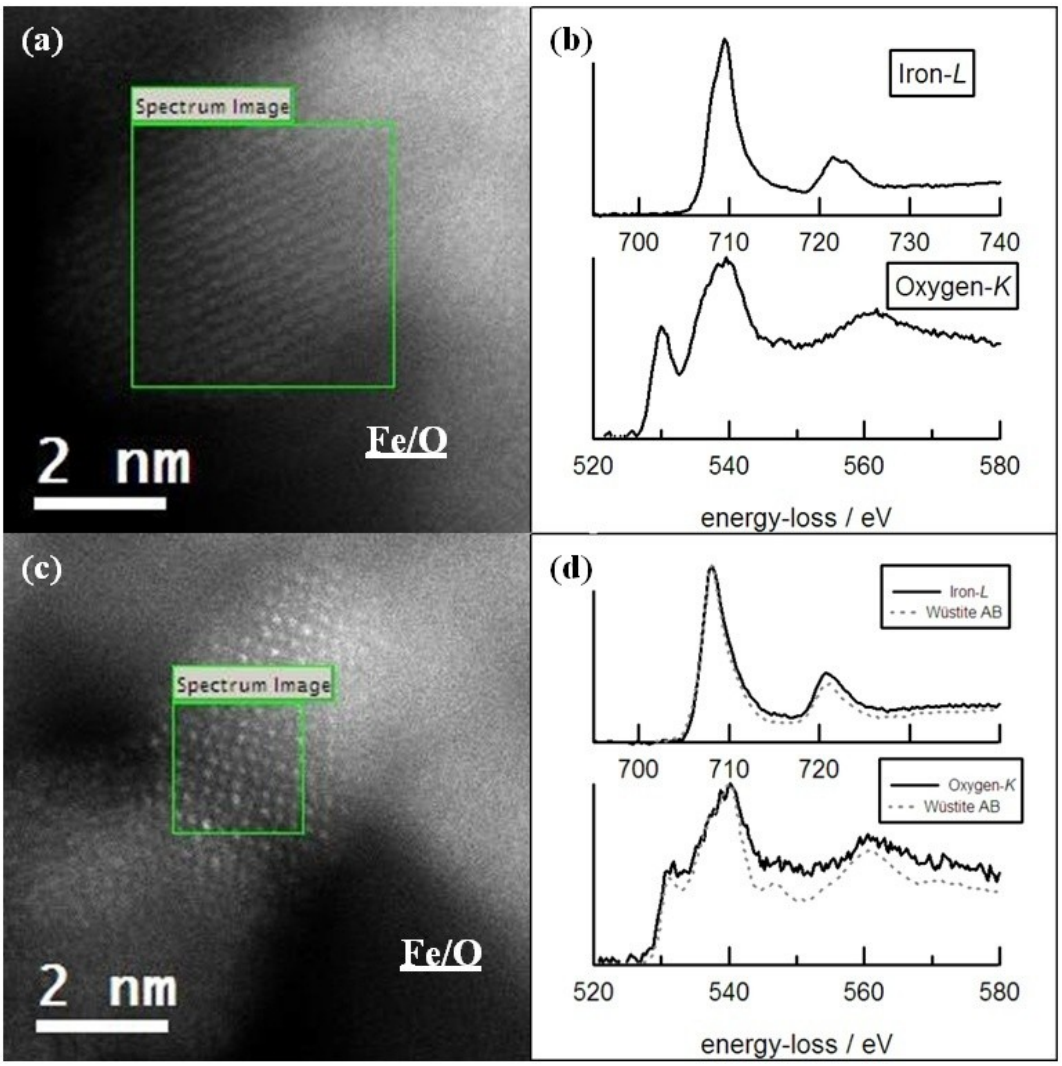

Figure 7.29 AC-STEM EELS compositional analysis of hydrothermally treated (eleven hours at 175ºC) 5% phosphorus doped synthetic two-line ferrihydrite (P5h11). (a & c) examples of a typical spectrum-image regions used for compositional analysis and the corresponding typical Fe-*L* and O-*K* EEL edges (b from a and d from c). Shown in (c) is a spectrum image survey image of an area of sample displaying Fe-atom positions typical of wüstite as viewed down one of the cube face-normal zone-axis of the cubic unit-cell i.e. <1 0 0>. Also shown for comparison in (d) are the EELS edges for wüstite as acquired on a CM200-TEM by Brown et al. (2001). It is clear the P5h11 sample appears to be inhomogeneous.

One spectrum-image, not included in the above compositional analysis, was found to have an anomalously high value of O/Fe being equal to unity. It is thought that this single region is a single crystal of wüstite (see Figure 7.29(c & d)). As may be seen in Figure 7.29c, the spectrum-image has been acquired from a region in which the HAADF intensity is typical of the projected Fe-Fe distances in wüstite as viewed down one of the <1 0 0> zone-axes. Further evidence that this crystal may indeed be wüstite comes from the ELNES of both the O-*K* and Fe-*L* edges, both of which are shown in Figure 7.29d along with TEM-EEL spectra of wüstite taken from the literature for comparison (Brown et al., 2001). In particular, the weak pre-peak of the O-*K* edge and the low energy-loss weighting of both the Fe-L_2 and Fe-L_3 edges

are wüstite-typical EELS fingerprints. It should be noted that the spectra acquired here have not been corrected for the effects of multiple scattering since no corresponding low-loss spectrum was acquired, and as such beyond the first ~ 10 eV there is some divergence between the edges that are compared in Figure 7.29d. The presence of the wüstite-like minor phase may be a result of beam damage to the specimen however, extreme care was taken here to avoid irradiation induced sample alteration with regions being minimally scanned and even abandoned if it was deemed that beam damage may have occurred. Of the forty-five micrographs acquired for this sample, along with the many more areas seen in preview-scan mode, this was the only area to exhibit cubic symmetry and therefore it can be assumed that wüstite, if indeed present in the pristine material, is only a minor phase.

7.10.5 AC-STEM Analysis of Michel et al., 2010's "*ferrifh"* Sample

As part of the AC-STEM analysis carried out in this study, the citrate associated hydrothermally treated (11 hours at 175 ºC) 2LFh sample of Michel et al., (2010) – from which the *ferrifh*, ferrimagnetic model for ferrihydrite, was derived (Michel et al., 2010) – was also examined. As observed for the hydrothermally treated P-doped samples, *ferrifh* exhibits a pronounced increase in crystallinity compared to 2LFh; and by implication, its parent, citrate associated, material. The crystallinity of the *ferrifh* sample, from AC-STEM HAADF imaging, is seen to be somewhat more crystalline, than the P-doped samples studied here, with larger crystals often being observed. The size of these crystallites were observed to extend over tens of nanometers and display atomic ordering over the entirety of their extent. For example, the reader is referred to Figure 7.30. Like the P-doped hydrothermally treated samples, some of the AC-STEM HAADF micrographs of *ferrifh* contain regions in which resemble the projected Fe atom distribution of either maghemite or magnetite viewed down the [1 1 2] zone-axis. . An example of such a particle, which is slightly off the [1 1 2] zone-axis, is shown in Figure 7.30. Since this crystallite is slightly off zone, correspondence is most apparent only at the thin edge of the crystal.

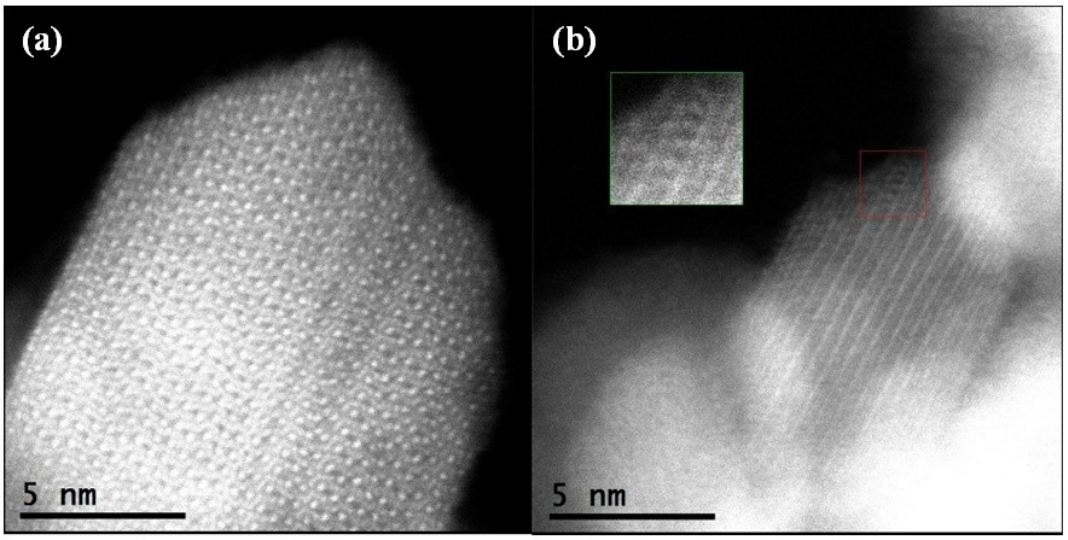

Figure 7.30 AC-HAADF STEM micrographs of the ferrifh, ferrimagnetic ferrihydrite, first presented and discussed in Michel et al., (2010). Shown in (b) is a crystallite which may possibly be either maghemite or magnetite viewed close to the [1 1 2] zone-axis. At the thin edge of this crystal (red-boxed and seen magnified in the green box) the Fe-atomic arrangement similar to maghemite/magnetite as viewed down the [1 1 2] can be observed.

AC-STEM EELS compositional data was also acquired for the *ferrifh* sample using the same protocol outlined in section 5.4 with fluences estimated to be the same as for that analysis. As determined from fourteen EEL spectra, the O/Fe atomic ratio is 1.4 with a standard deviation of 0.1. This value is in good agreement with the O/Fe ratio for both magnetite and maghemite which ideally are 1.3 (Fe_3O_4) and 1.5 (γ-Fe_2O_3), respectively. However, as the electron-beam sensitivity measurements have shown, preferential loss of oxygen is to be expected as a consequence of irradiation damage, therefore the actual value of O/Fe may be higher if indeed has damage occurred.

7.11 Concluding Remarks

P-doped (P/Fe = 0.03(P3) and 0.05(P5)) 2LFh samples were subject to two different methods of heat treatment, *viz.* hydrothermal and (dry-air) annealing, at 175 °C for times ranging from zero to twelve hours. Atomic structure analysis (powder XRD, X-ray PDF and neutron scattering) indicates that hydrothermal treatment results in a significant ripening of particles with an accompanying increase in crystallinity. On the other hand, annealing has little discernible effect on the overall atomic structure. Comparison of the atomic PDFs of the hydrothermally treated samples with those in the literature for hydrothermally treated citrate-associated 2LFh indicates that the products of such treatment are essentially the same. However, in the case of the P-doped samples studied here, average crystallite sizes are smaller. Magnetic

measurements (VSM) point to the formation of a magnetically enhanced phase upon hydrothermal treatment whereas annealing results in a slight decrease in magnetic susceptibility. Measurement of the magnetic (un)blocking temperature points to an increase in average particle size (or anisotropy), which is also accompanied by an increase in the distribution of particle sizes with increased hydrothermal treatment time.

Thermal analysis (TGA & DSC), between 28 and 700 °C, reveal a 50% reduction in total mass-loss for the hydrothermally treated samples when compared to their parent materials. Powder XRD analysis, following the thermal analysis, confirms the transformation of the hydrothermally treated samples to hematite. FTIR spectroscopic measurements point to an increased ordering of the phosphate molecular configuration upon hydrothermal treatment. This is most probably a result of the increase in both the overall atomic ordering and crystallite size which accompanies such treatment. XPS of the O 1*s* level indicates a slight modification of the average oxygen environment reflecting the structural differences between the hydrothermally treated product and its parent material. BF-TEM imaging confirms the increase in average particle size, particle faceting and overall crystallinity upon hydrothermal treatment. Additionally, measurements of lattice-spacings seen in BF-TEM micrographs confirm the presence of new phases not present in the parent materials. EELS measurements performed in the TEM confirm the hydrothermal transformation product to be predominantly ferric with a significantly higher tetrahedral site occupancy than 2LFh. EELS compositional analysis, employed using 100 keV electrons with a fluence ~2 x 10^9 electrons nm^{-2}, indicate the hydrothermally treated sample have an atomic ratio O/Fe equal to 1.4 ±0.1, similar to that of the parent material. Finally AC-HAADF imaging, performed at fluences lower than 10^8 electrons nm^{-2} (i.e. below the damage threshold), reveal crystallites exhibiting increased crystallinity, well-defined edges and perhaps the presence of a spinel iron oxide (Fe_3O_4, γ-Fe_2O_3) phase along with either hematite and/or the defective phase from the Drits' model (Drits et al., 1993).

Chapter 8 Characterisation of Horse Spleen Ferritin

This Chapter describes preliminary work towards linking the structure and morphology of ferrihydrite to the development of the mineral core of the iron storage molecule ferritin. The former has been extensively explored in this thesis thus far. The latter has a long history of analysis by electron microscopy and quite recently the group here at Leeds demonstrated that ferritin mineral cores within human liver tissue possess distinct sub-unit morphology (Pan et al., 2009). It was postulated by Pan et al. (2009), that the sub-unit structure results from the eight channels in the protein shell that are known to facilitate the transport of iron ions into the protein cavity (Chasteen & Harrison, 1999). If correct then sub-unit structure should be present in all ferritins, natural or synthetic. The preliminary work described here will concentrate on the production and characterisation of reconstituted mineral cores of ferritin molecules extracted from horse spleen. The aim is to progressively increase the iron loading in the reconstituted mineral cores and observe the development (or lack of) sub-unit morphology. Samples were synthesised according to the method outlined in section 4.1.6. Table 8.1 provides an overview of samples examined in the current chapter.

Table 8.1 Details of samples examined in Chapter 8.

Sample Full Name	**Abbreviated Name(s)**	**Sample Description**
Reconstituted (*in vitro*) Ferritin mineral cores	F1125, F2225, F3375, F4500	Horse spleen holo-ferritins were reconstituted *in vitro* from apo-ferritins prepared from commercially bought horse spleen ferritin according to the method provided in section 4.1.6. Iron-to-protein ratios of 4500, 3375, 2225 and 1125 were chosen since these values correspond to cores filled to *maximum, ¾, ½* and *¼* of their nominal capacity for iron.

8.1 Overview of Sub-Unit Structure

It is well established that ferritin sequesters iron in a ferrihydrite-like nanoparticulate structure at the centre of the molecule (Clegg et al., 1980). As already discussed, recent HAADF-STEM work has shown regular sub-unit structure within mineral cores of human liver ferritin (Pan et al., 2009). Subunit structure is seen in a three-dimensional reconstruction of an 'averaged' core, containing ~1600 iron atoms, produced by averaging 2D projections of ~750 individual, randomly oriented cores.

This reconstructed core is composed of eight near spherical subunits packed within the ferritin cavity such that each one lies at the vertex of an imaginary cube. The sub-unit packing reflects the cubic point group symmetry of the protein shell, resulting in a region of relatively lower density at the core's centre and has stimulated a new model for the growth of the mineral core Figure 8.1.

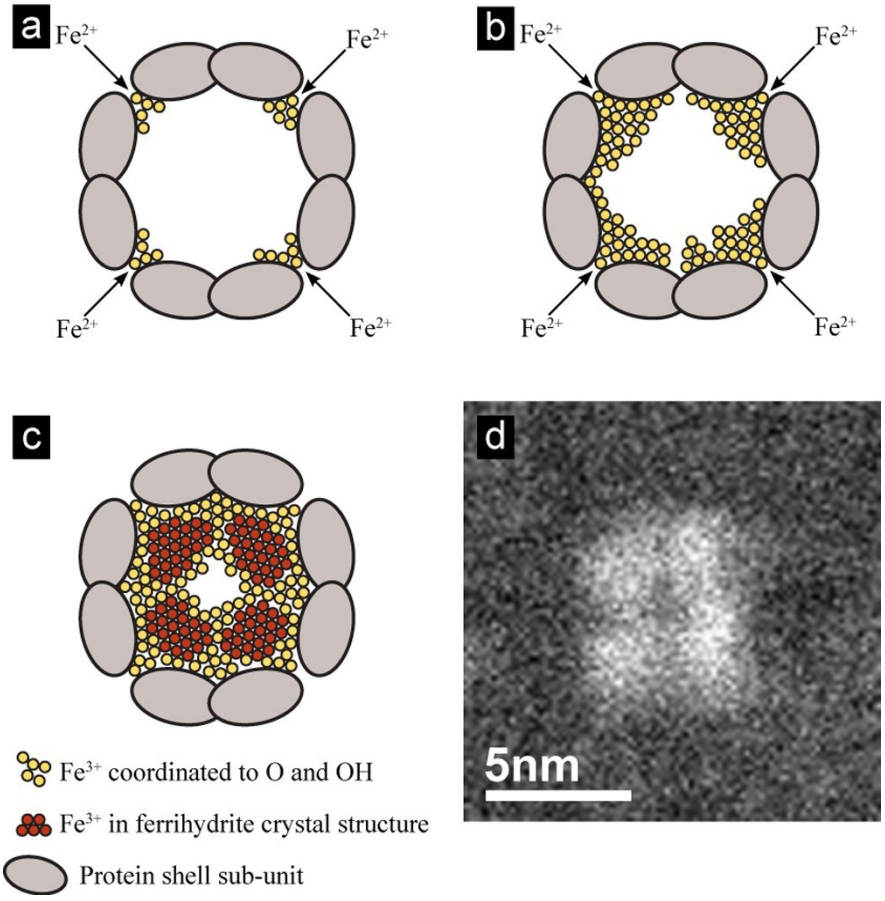

Figure 8.1 "Schematic cross section (viewing direction: parallel to one of the four-fold symmetry channels in the protein shell) of a hepatic ferritin core depicting our proposed formation mechanism. This is a modification of a schematic of core formation by Lewin et al., (2005). (a) Early stage of iron deposition in the ferritin central cavity. The sites near the ends of the three-fold symmetry iron entry channels (where the protein shell subunits, shown as grey lobes, have specific oxidation sites) are favourable for the incoming Fe^{2+} to deposit and be oxidised. The yellow circles represent oxidised iron (Fe^{3+}). (b) As the iron cellular concentration increases, more Fe^{2+} is shuffled into the molecule and may rapidly deposit and oxidise on the surface of any existing Fe^{3+} deposits near the entry channels; consequently, core subunits are formed. (c) With higher iron-filling, a cubic-like core structure with eight-subunits (only four of which are shown) develops. Oxidation of further incoming Fe^{2+}, results in the early deposited Fe^{3+} diffusing inwards forming closely packed crystalline structures of ferrihydrite (dark red circles in contrast to the loosely packed Fe^{3+} (yellow circles)), the atomic structure of such a subunit structure is seen experimentally in Figure 97d. The surface of each core subunit is disordered facilitating dynamic load and release activities consistent with the 'last-in first-out' hypothesis (Hoy et al., 1974). (d) An example of a commonly observed HAADF image of a single ferritin core of similar iron loading and lying in a similar orientation to the schematic; the four- fold symmetry arrangement of the subunits and a low density central region are clearly evident." – Pan et al., 2009.

If this model is valid, sub-unit structure should be present in all ferritins but would vary according to iron loading (which is itself a function of the ratio of heavy (H) to

light (L) subunits that compose the protein shell and iron availability). In a parallel piece of work by the Leeds group, Dr Kasim Sader has imaged (using HAADF-STEM) subunit structure in human liver and spleen (L subunit rich) and placenta and heart (H subunit rich) ferritin mineral cores, as well as in standard horse spleen ferritin preparations. The work is currently being drafted for publication however the key point here is that ferritin preparations extracted from horse spleen also demonstrate subunit structure.

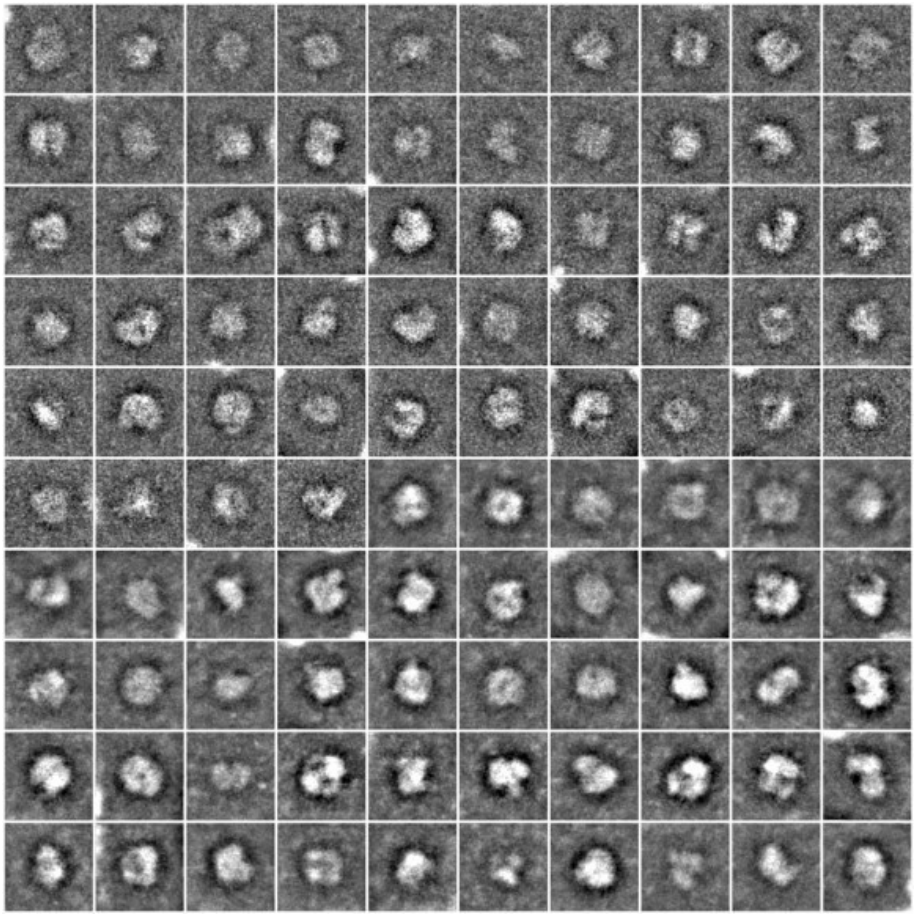

Figure 8.2 A tableau of HAADF-STEM images (SuperSTEM 1) of extracted and purified HoSF mineral cores (Sigma-Aldrich, UK). Sub-unit structure is evident. Images were acquired and processed (background normalised and Fourier filtered) by Kasim Sader following the procedure outline in Pan et al. (2009).

Confirmation of sub-unit morphology in native horse spleen ferritin (HoSF) cores supports the work of Pan et al. (2009), however, it remains to be seen whether sub-unit morphology is still present in cores formed outside of the finely tuned biochemical environment of the donor organism. Thus, the main objectives of this preliminary work are to:

a) Establish a method for the *in vitro* reconstitution of ferrihydrite cores within apo-ferritins (ferritin protein macromolecules without a mineral core). For

this extracted and demineralised HoSF will be used;

b) Obtain a series of *in vitro* iron-reconstituted HoSF (ivHoSF) samples with different iron loading by controlling the amount of iron available for uptake during reconstitution.

HAADF-STEM characterisation of the ivHoSF cores will be then used to explore core morphology.

8.2 Preparation for (S)TEM Observation

For (S)TEM observation, a single drop of ivHoSF solution (prepared via the method outlined in section 4.1.6) was drop-cast onto standard holey carbon film on copper TEM support grids. To ensure that a sufficiently thin layer of the sample was deposited on the grid, excess sample was removed immediately following deposition by blotting with the whiskers of a freshly torn filter paper before setting it aside and allowing time for it to air-dry.

For both low-magnification BF-TEM and non-aberration corrected ADF-STEM observations, as-prepared samples could be observed without rapid hydrocarbon contamination build-up, provided images were acquired quickly and where possible at low electron fluence. For AC-STEM observations, as is so often the case, it was found that contamination build up was a significant and limiting factor. Plasma-cleaning (≤7 seconds) was found to alleviate but not eliminate this problem. It was suggested that exposure to the cleaning plasma for a duration of ten seconds or less would not cause significant alteration to ferritin samples, at least from the point of view of the overall core morphology (Kasim Sader personal communication). Thus for observations made using SuperSTEM2 plasma-cleaning for ~7 seconds (in a Fischione plasma cleaner) was performed immediately prior to the sample entering the microscope's specimen airlock. For AC-STEM HAADF imaging of samples, using the UltraSTEM at the Oak Ridge National Laboratories, plasma cleaning was not available and therefore baking was resorted to as a means of removing hydrocarbon contamination. The samples were heated in a custom build oven the chamber which may be evacuated independently of the heating program. With the samples inserted, the oven chamber was evacuated and the pressure maintained against a rotary pump. After a few minutes, once rotary pressure was achieved the heating elements were switched on until the temperature reached approximately 80 ˚C. At this point, power to the heating elements was cut and the oven allowed to

return to ambient temperatures overnight whilst still under vacuum. Baking of the specimens in this manner was found to almost completely eliminate hydrocarbon contamination allowing suitable conditions for observation within the microscope. Although not ideal it is deemed that this procedure would have resulted in minimal alteration of the specimen since it is known that the protein of ferritin is resilient to such elevated temperatures (Meldrum et al., 1991).

8.3 Analytical (S)TEM Observations

The main point to address in this preliminary study was whether the inorganic core of ferritin could be reconstituted *in vitro* with the same morphology as is observed for ferritin cores loaded in the finely tuned biochemical environment of the host organism. Direct confirmation of core loading (i.e. Fe-(oxy)hydroxide material present within the confines of the protein shell), by means of imaging in the electron microscope, would require the simultaneous acquisition of signals specific to both the protein structure and the Fe-rich core. In both cases, the intensities of these signals would need to be sufficiently high (significantly) above the background signal originating from the material used as support. Additionally, both signals must fall below the saturation limits of the detector system. In this study standard, holey-carbon support films were used. The detection of protein structures suspended on these supports is all but impossible, given the thickness of the support (~30 nm) and the compositional similarity to organic proteins (i.e. carbon). Graphene has been explored as a support material since it is thinner and more rigid than amorphous carbon (Pantelic, Meyer, Kaiser, Baumeister, & Plitzko, 2010). Graphene was investigated here, however, after initial trials, it was abandoned due to of the lack of few *versus* multi-layered regions within a given "graphene" sample and the lack of extent of continuous layers. Finally, holy-carbon film was used as a support material.

8.3.1 Confirmation of *in vitro* Iron Loading

Indirect evidence confirming the success of the *in vitro* core-reconstitution method used here came about as the result of the formation of a precipitate decorating the outer surface of the molecules. Whilst such decoration indicates incomplete uptake of iron by the ferritin molecules it does help to identify individual ferritin cores and highlights the associated protein shell.

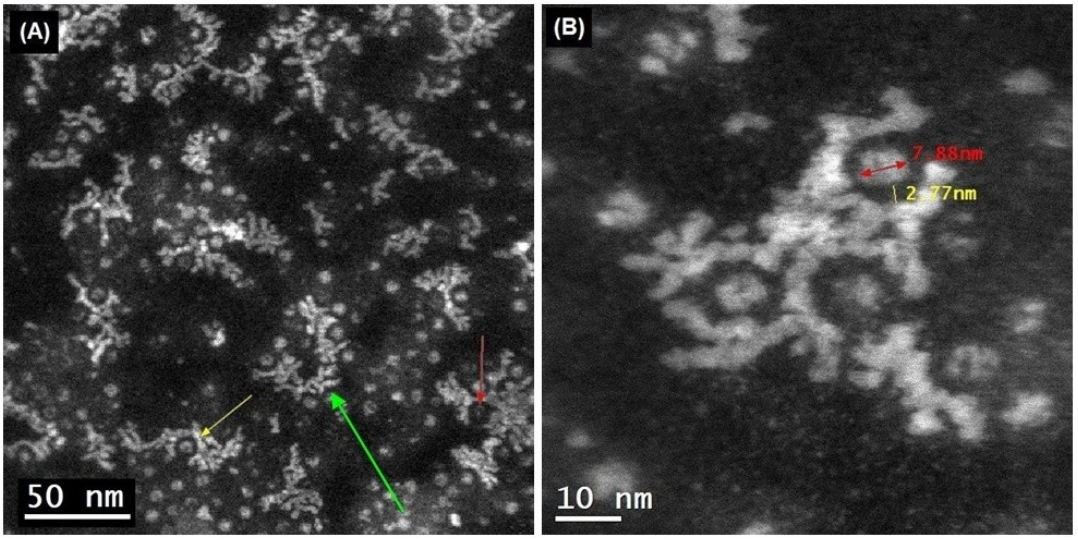

Figure 8.3 HAADF STEM images of ferritin sample F1125 supported on an amorphous carbon film. Sub-spherical regions of ~7 nm in diameter along with an irregular decoration of material 3 or so nm outside this are visible (red and yellow arrows) all with apparently similar HAADF intensity suggesting the presence of holo-ferritin. The decoration of precipitate around a 12 nm diameter circle (green arrow) suggests the presence of apo-ferritin too.

Displayed in Figure 8.3 are two ADF micrographs of ferritin sample F1125 in which ferritin cores may be seen in close association with the aforementioned precipitate. Apparent is the distinct separation - or stand-off - between the sub-spherical ferritin cores and the boundary of the precipitate. This annular separation is approximately 3nm thick (see Figure 8.3b), i.e. the known thickness of the protein shell (Massover, 1993). Based on the similarity of the ADF signal intensities of the precipitate and ferritin cores' both must be of similar projected Z/thickness suggesting that they are the same type of mineral/phase. Such a decoration would suggest the precipitate to have formed during the drying of the sample subsequent to deposition on the support film i.e. by aggregation of solids upon evaporation of the solution.

8.3.2 Bright-Field TEM Imaging

Figure 8.4 compares two conventional BF-TEM micrographs of synthetic ferritin cores (F1125) taken at two different levels of defocus. These are simply presented at this point as a means of illustrating the sensitivity of apparent FMC structure to defocus in *conventional* bright-field imaging. This has been discussed in more detail in Pan et al. (2009) but is shown again here to re-highlight why ADF-STEM imaging is a preferred choice for imaging substructure in FMCs since there is no focus sensitive phase-contrast information in an in focus ADF image.

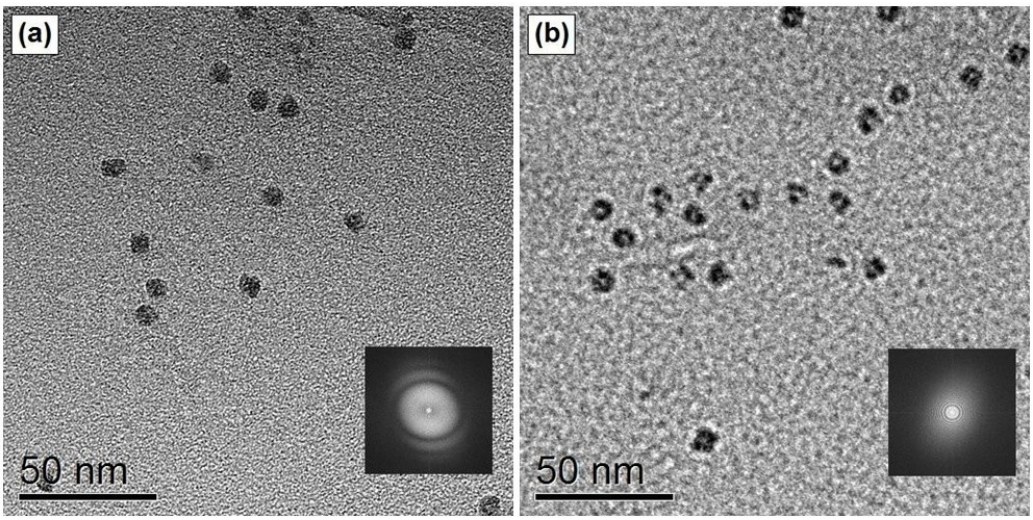

Figure 8.4 BF-TEM micrographs of synthetic ferritin cores (F1125) suspended on a holey carbon-support film. Both images are taken at 7300x magnification at different levels of defocus as indicated by the whole image FFTs (inserted). The defocus in image (b) is greater in magnitude than that of (a) (for which there is also some degree of objective astigmatism). Corresponding to the increase in defocus is an apparent increase in the sub-unit structure and coarseness of the granularity of the support film due to clipping of high-frequency information i.e. this is dominated by artifact.

In Figure 8.4 the effect defocus has on the perceived morphology of FMCs is apparent as was first identified by Haydon (1969). Increasing the defocus of the objective lens affects the contrast transfer function (CTF) of the microscope by lowering the extent out to which both the first contrast-reversal and the information limit extend out in *k*-space (Williams & Carter, 1996). In this way, defocusing results in blurred, low-pass images from which high-frequency information has been clipped and artifacts are introduced. This does not occur in the formation of an in-focus bright field TEM image or HAADF image, however, the contrast is very low in the focused BF image (making interpretation difficult) and much stronger in the HAADF image (see Fig 2b and c of Pan et al., 2009). Thus an in-focus HAADF image of an FMC is straightforwardly interpretable without any ambiguity.

8.3.3 Selected Area Electron Diffraction

SAED data confirmed the similarity between the atomic structure of the synthetic ferritin mineral cores and that of 6LFh. Figure 8.5 compares a powder XRD pattern of 6LFh with a poly-crystalline SAED pattern (radially averaged) of synthetic ferritin core sample F4500. The correspondence between the patterns is obvious rendering further expansion superfluous. For display purposes the two-dimensional SAED pattern has been radially averaged, background stripped and transformed, along the scattering axis (i.e. in *k*) only, to simulate the use of $\lambda = 1.54$ Å radiation

such as was used in the acquisition of the powder XRD data.

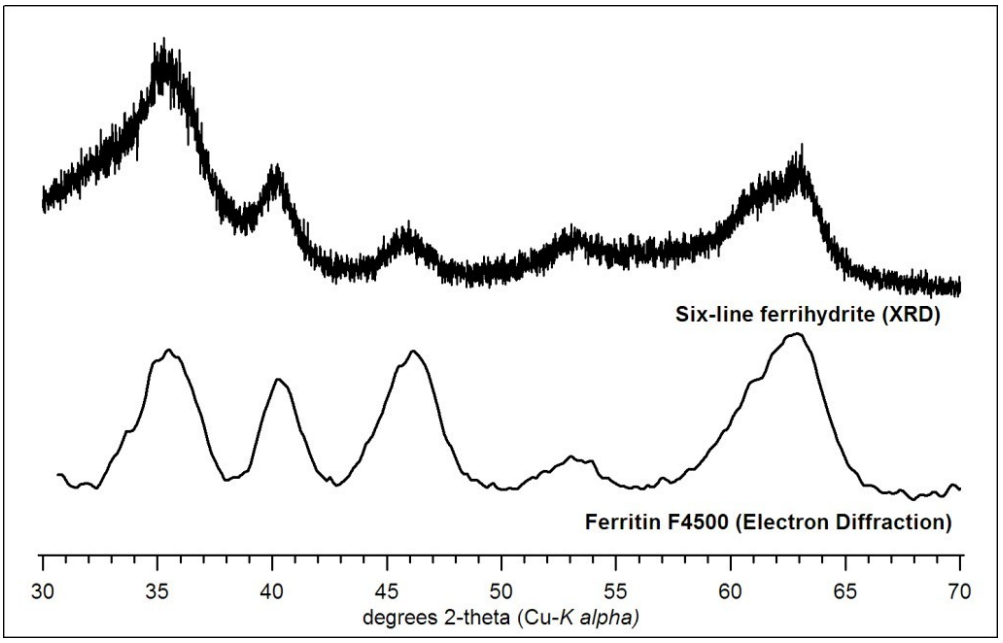

Figure 8.5 Comparison of powder XRD patterns of 6LFh (top) and a poly-crystalline SAED pattern of synthetic ferritin mineral core sample F4500 (bottom). The SAED pattern of ferritin cores has been transformed to the same scattering angle axis as the XRD pattern (i.e. a source radiation wavelength equivalent to that of Cu K-α used for the acquisition of the powder XRD of 6LFh). The similarity between the two patterns is clear.

8.3.4 Compositional Analysis by STEM-EELS

EEL spectrum imaging in the STEM was used to map the composition of an individual core (Figure 8.6). It can be seen that the Fe elemental signal (Fe-*L* edge) co-localised very strongly with the HAADF intensity (labeled Analog) as one might expect.

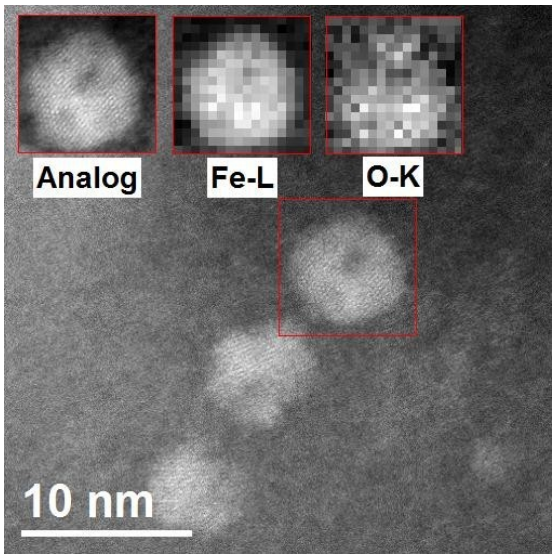

Figure 8.6 HAADF STEM micrograph showing three iron rich ferritin cores. Inset are EELS images showing iron and oxygen signals to be correlated with the HAADF signal intensity (inset labelled “Analog”).

8.3.5 Annular Dark-Field STEM Imaging

For the assessment of the core morphologies of the synthetic FMCs, the Tecnai F20 microscope was used in STEM mode for the acquisition of high angle annular dark-field imaging data. The aim here was to answer the question of how the growth of the core proceeds from the initial deposition of material within an apo-ferritin protein cage to one which is full to capacity.

Thus far the synthetic FMC samples have been referred to by their nominal iron loading level during reconstitution. However, this is misleading as it implies all ferritins within a given sample have identical core loadings. Since the ADF signal intensity correlates with the iron content of an individual mineral core (Figure 8.6), it may be used to assess the distribution of iron loading across ferritins reconstituted at a given nominal iron loading. The results of this analysis are given in histogram form on a per sample basis Figure 8.7.

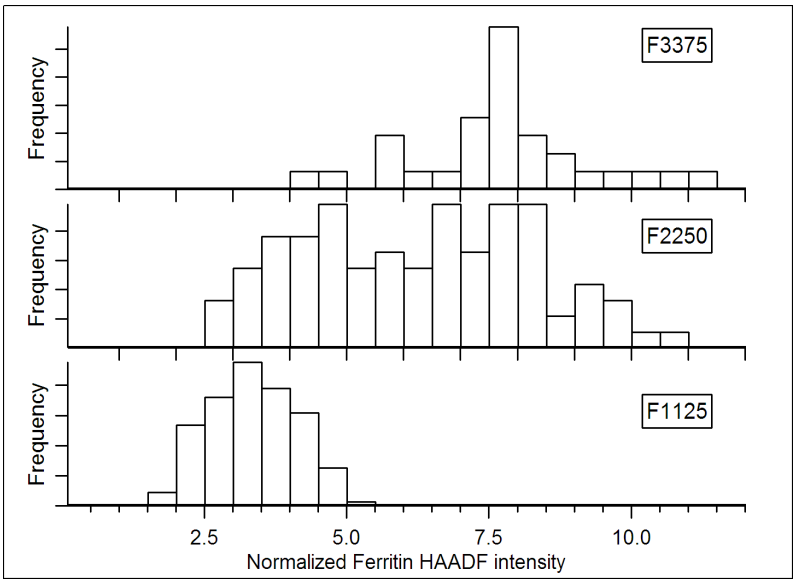

Figure 8.7 Histograms of normalised ADF signal intensities integrated over whole ferritin cores with X and Y nominal iron loading, following the procedure outlined in Pan et al., (2009).

Immediately apparent from inspection of Figure 8.7 is that upon increasing the Fe/protein ratio both the mean normalised intensity and the width of the distribution (or the variance in the mean) increase. Additionally, the significant overlap in intensity distribution (and the variance in the mean) between samples indicates that one cannot identify significantly distinct populations of FMCs but rather a continuum of loadings. It is suggested here that in future experiments some other method of post-synthesis fractionalization (such as disk centrifuge separation) be used to reduce the variance of core-loading to achieve distinct and well-defined

populations of samples.

Tableaus of representative ADF images of cores from each reconstitution experiment are shown in Figure 8.8, Figure 8.9 and Figure 8.10.

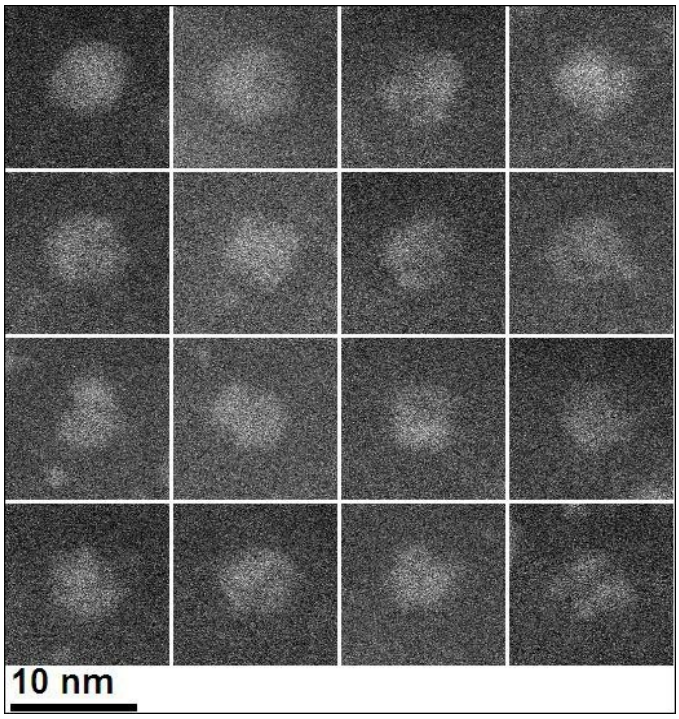

Figure 8.8 ADF STEM micrographs of HoSF cores reconstituted with nominal Fe/protein = 1125 (F1125).

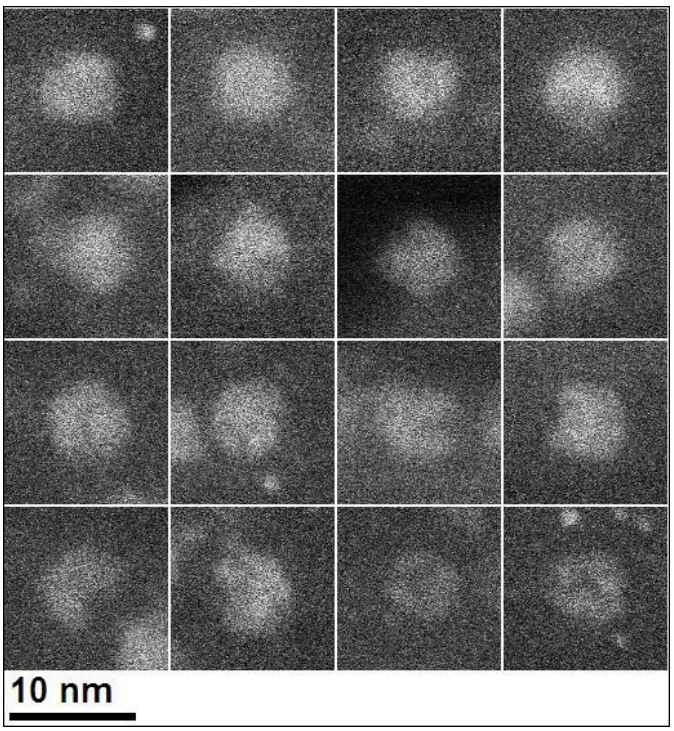

Figure 8.9 ADF STEM micrographs of HoSF cores reconstituted with nominal Fe/protein = 2225 (F2225).

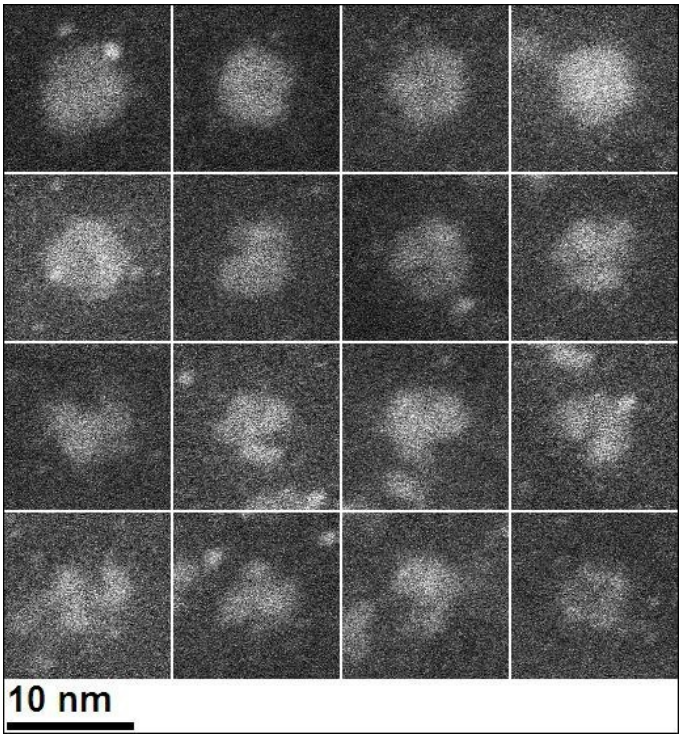

Figure 8.10 ADF STEM micrographs of HoSF cores reconstituted with nominal Fe/protein = 3375 (F3375).

We should not expect dramatic differences between the shape/form of the FMC images from the different reconstitution experiments since the means and distributions of the HAADF intensities are not very different. In overall summary these images suggest:

1) Subunit structure is evident in some images of all the reconstituted series but not in every case.

2) The overall projected shape of the cores is not consistent with strictly cubic core morphology for all stages of core growth.

8.3.6 Aberration Corrected High-Angle Annular Dark-Field Imaging

The imaging has been extended to better resolution to investigate the degree of poly-crystallinity within individual cores. Whether core growth proceeds from a single nucleation point or by the coalescing of several sub-cores each originating from individual sites of nucleation is explored. Also, the degree of crystallographic alignment or coherency between individual sub-units within a given core is investigated. What unfolded is a mixed picture in which cores, for which sub-unit structure is apparent, display varying degrees of coherency in terms of the relative orientation of each sub-unit crystallites in terms of the core as a whole. Given the biological context of ferritin and the implications this may have for iron liability this

might not be unsurprising. What follows in Figure 8.11–Figure 8.13 is a selection of atomic-resolution HAADF STEM micrographs of reconstituted cores. What is apparent is variable/random column occupancy of Fe sites as per the disordered nature of ferrihydrite.

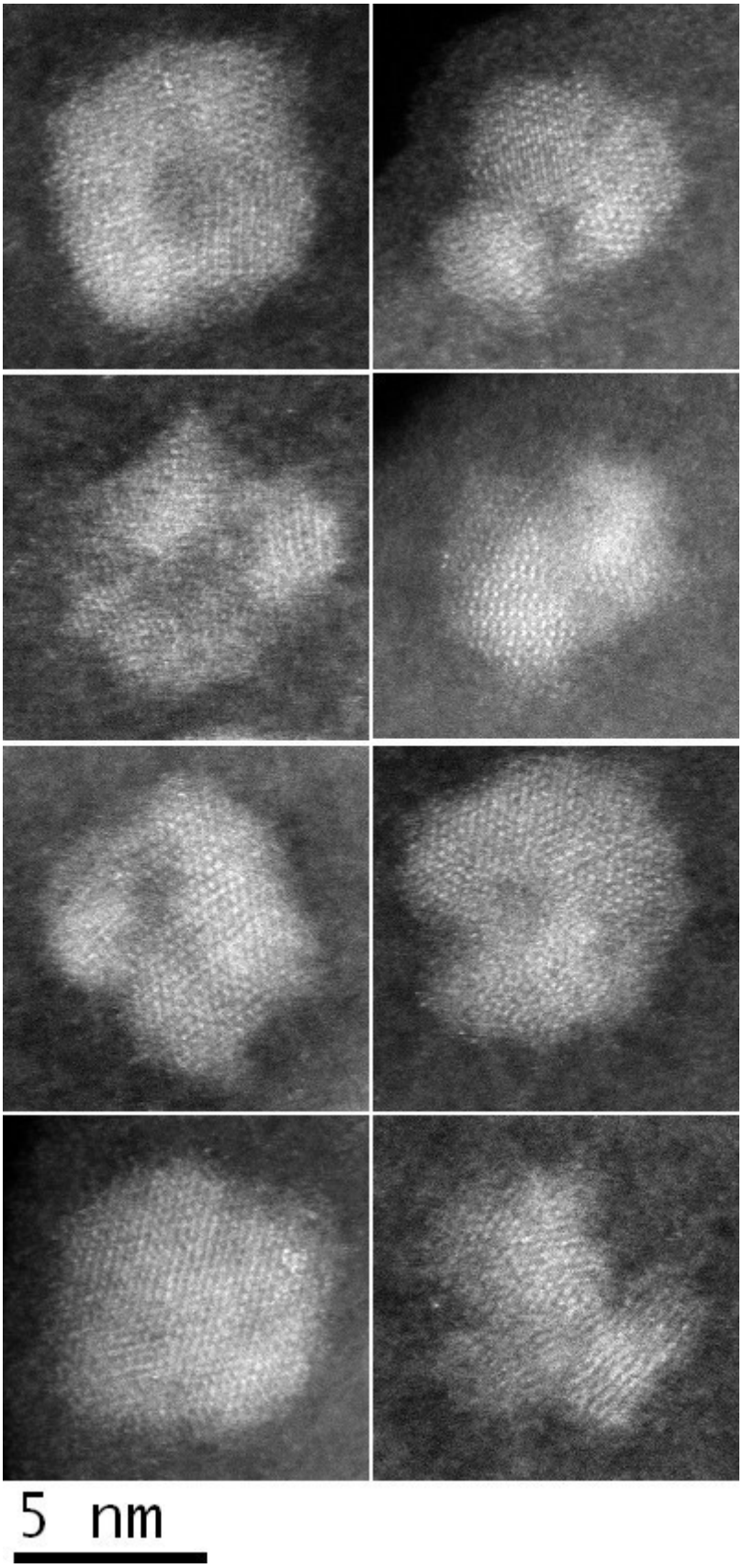

Figure 8.11 A selection of atomic-resolution HAADF STEM micrographs of reconstituted HoSF cores with nominal Fe/protein = 1125 (F1125).

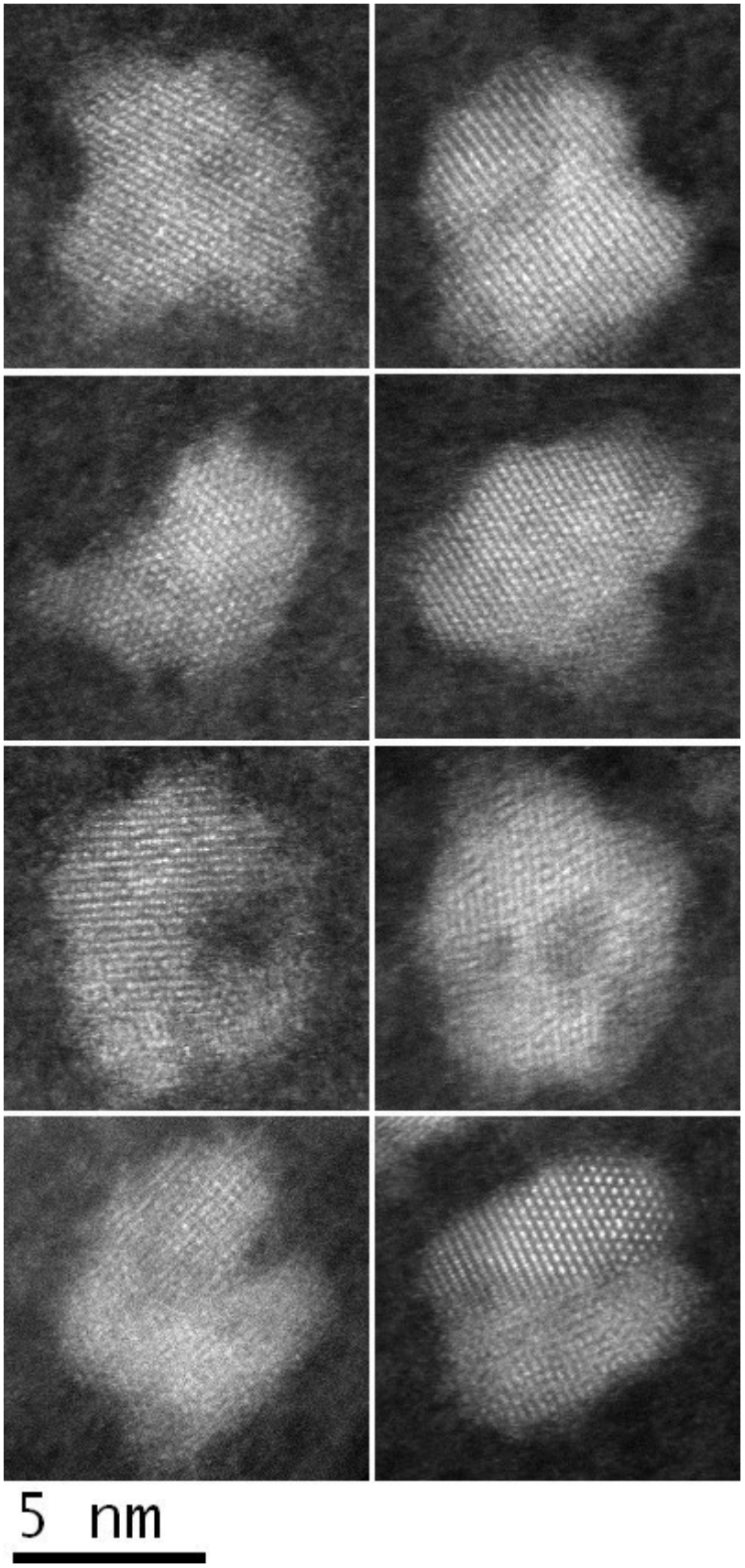

Figure 8.12 A selection of atomic-resolution HAADF STEM micrographs of reconstituted HoSF cores with nominal Fe/protein = 2225 (F2225).

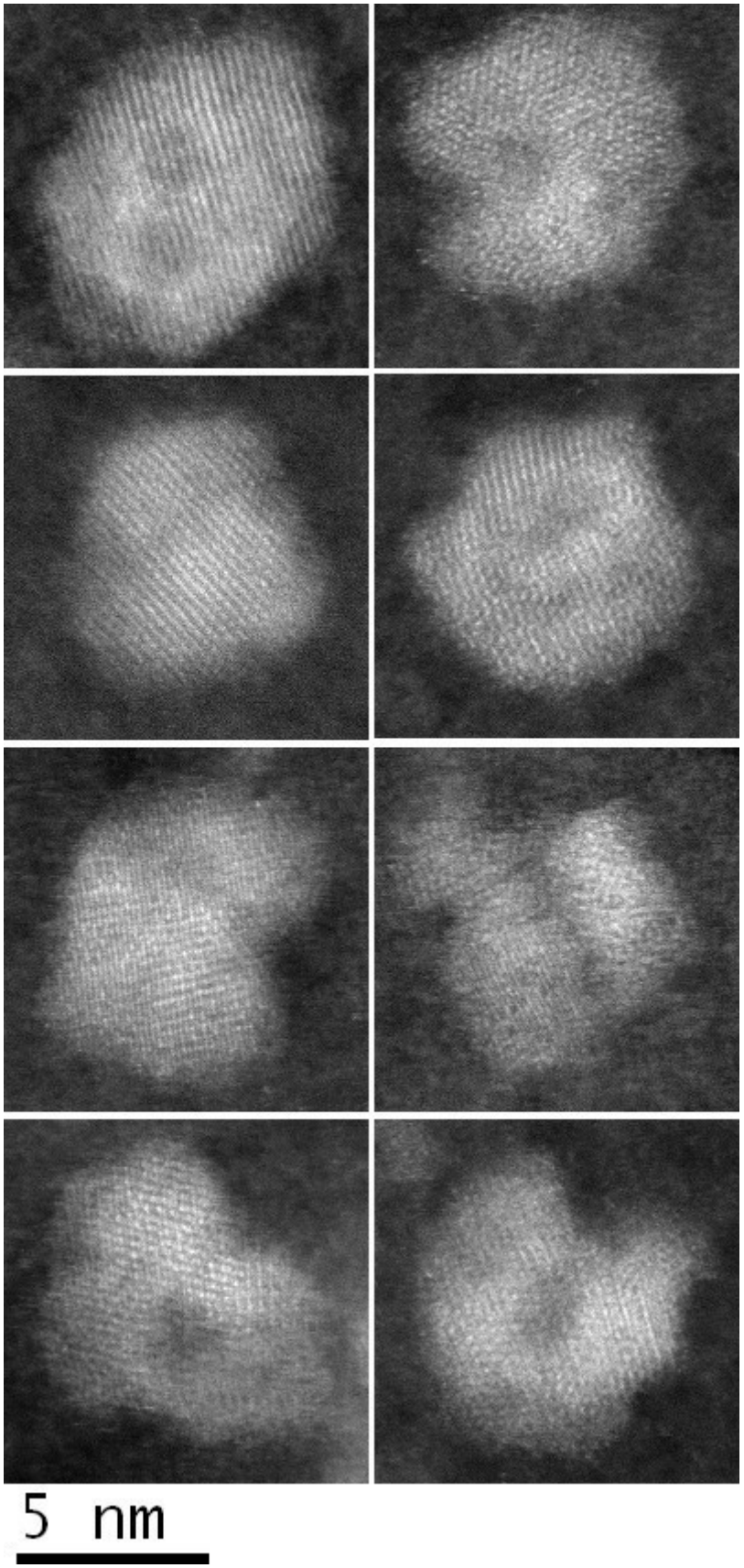

Figure 8.13 A selection of atomic-resolution HAADF STEM micrographs of reconstituted HoSF cores with nominal Fe/protein = 3375 (F3375).

8.4 Concluding Remarks

Horse spleen ferritin mineral cores have been reconstituted *in vitro* following a previously documented method of preparation (Meldrum et al., 1991). The iron-richness of the resulting cores has been confirmed by EELS and shown to have six-line ferrihydrite character using selected-area electron diffraction. High-angle annular dark field STEM imaging with an uncorrected probe has been used to demonstrate proportionality between nominal Fe/protein ratios used for preparation and HAADF signal-intensity. Aberration-corrected HAADF imaging has shown cores to poses sub-unit structure with highly variable morphology and crystalline structure at the atomic level.

Chapter 9 Conclusions and Future Outlook

This work has demonstrated the application of the latest generation of aberration corrected electron microscopes to the structural and chemical characterisation of ferrihydrite (2LFh & 6LFh) produced both *in vitro* and within the protein cage of ferritin. 2LFh, coprecipitated in the presence of varying concentrations of phosphorus and subject to hydrothermal and dry air annealing heat treatments, has also been investigated. By way of a thorough characterisation additional physicochemical characterisation techniques have applied to confirm the phase purity of specimens and benchmark them against those reported in the literature.

This chapter provides a brief summary of the major results presented in previous chapter and concludes by outlining some important points which would be worthwhile considering in any future continuation of this work.

9.1 Conclusions

The effects of prolonged exposure to the 200keV electron beam of TEM has been investigated by the simultaneous acquisition of Fe-*L* and O-*K* edge EELS data, EELS and EDX compositional data and SAED. A safe fluence level of 10^8 electrons nm^{-2} has been established, below which both 2LFh and P-doped 2LFh can be observed in their pristine state. Beyond the safe fluence limit alteration of both pristine 2LFh and the phosphorus associated 2LFh specimens proceeds by preferential loss of oxygen, reduction of iron and concomitant phase transformation to a material with characteristics similar to that of magnetite.

With the aim of reducing the impact of high energy electron irradiation induced damage, a novel low electron-fluence method of STEM EELS acquisition (SmartAcquisition) has been developed and its applicability to the characterisation of ferrihydrite nanoparticles proven.

Results here demonstrate that of the major iron-oxides, the EELS ELNES of the O-*K* edge of ferrihydrite is most similar to that of either maghemite or magnetite (Brown et al., 2007). The Fe-*L* signal is typical of a predominantly Fe(III) bearing iron-oxide material in which the iron atoms reside in six-fold coordination with oxygens and/or hydroxyls (Grunes et al., 1982; Colliex et al., 1991; van Aken at al., 1998; van Aken & Liebscher, 2002; Brown et. al, 2001). Support for the newly proposed Michel model for ferrihydrite (Michel at al., 2007) comes from Fe-*L* edge EELS analysis

which allow for a significant proportion (93 ± 25%) of tetrahedrally coordinated iron in the pristine structure of 2LFh.

XRD combined with TGA and DSC measurements estimates a compositional formula close to $Fe_2O_3 \cdot 2.2H_2O$ for 2LFh providing support for the most recent model for the structure of ferrihydrite as proposed by Michel et al. (2007, 2010).

Hydrothermal treatment of P-doped 2LFh results in a product which is extremely similar to hydrothermally treated citrate-associated 2LFh as reported by Michel et al. (2010). Atomic structure analysis (powder XRD, X-ray PDF and neutron scattering) indicate a significant ripening of particles with an accompanying increase in crystallinity. Magnetic measurements (VSM) point to the formation of a magnetically enhanced ferrimagnetic phase. Thermal analysis (TGA & DSC), between 28 and 700 °C, reveal a 50% reduction in total mass-loss for the hydrothermally treated samples when compared to their parent materials. FTIR spectroscopic measurements point to an increased ordering of the phosphate molecular configuration. XPS of the O 1*s* level indicates a slight modification of the average oxygen environment. BF-TEM imaging confirms the increase in average particle size, particle faceting and overall crystallinity. Measurements of lattice spacings seen in BF-TEM micrographs confirm the presence of new phases not present in the parent materials. EELS measurements performed in the TEM confirm the hydrothermal transformation product to be predominantly ferric with a significantly higher tetrahedral site occupancy than 2LFh. EELS compositional analysis, indicate the hydrothermally treated sample have an atomic ratio O/Fe equal to 1.4 ± 0.1, similar to that of the parent material. AC-HAADF imaging reveals crystallites exhibiting increased crystallinity, well defined edges and perhaps the presence of a spinel iron oxide (Fe_3O_4, γ-Fe_2O_3) phase along with either hematite and/or the defective phase from the Drits' model (Drits et. al, 1993).

Ferritin mineral cores have been reconstituted *in vitro* and charecterised using aberration corrected HAADF imaging with controlled fluence levels below the damage threshold. By varying the ratio of Fe/protein during reconstitution, ferritins with variable core iron content have been produced. ADF STEM imaging has been used to confirm this. Atomically resolved sub-unit structure is observed by means of HAADF AC-STEM imaging, with individual cores comprising several crystalline units which appear to have nucleated independently of one another. SAED has been

used to confirm the similarity of ferritin mineral core and 6LFh.

9.2 Future Outlook

Analysis of the Fe-$L_{2,3}$ EEL core-loss edge for the estimation of iron's coordination and valence relied on spectra acquired from four reference minerals. These spectra have been inherited from a previous PhD study and unfortunately, they are not accompanied by the corresponding O-*K* and Fe-$M_{2,3}$ edges. Therefore new EELS measurement will be made both on the CM200 and the SuperSTEM to characterise these minerals and to obtain full EELS data sets extending from the low-loss region up to the Fe-$L_{2,3}$ edge at ~709eV energy loss.

Low electron fluence EELS experiments monitoring the changes in the Fe-$L_{2,3}$ ELNES of 2LFh in the CTEM have led to the conclusion that the lowest feasible dose limit for statistically sound data is $\sim 10^6$ electrons nm^{-2}: something which has been already demonstrated for 6LFh (Pan et al. 2006). It would be desirable to make EELS measurements at lower fluences as it is unclear where the fluence threshold for beam damage of FHY lies. One possibility would be to use the Fe-$M_{2,3}$ edge which displays a chemical shift, between the main peak and its pre-peak, which can be used to monitor the valence of iron. This edge has a much lower energy threshold (~ 54eV) than the Fe-$L_{2,3}$ edge and therefore possesses a larger interaction cross section meaning significantly lower fluences will be required to obtain statistically sound data. Another advantage of using this edge to monitor iron's valence is that absolute energy calibration would not be necessary as it is the relative energy separation between the main peak and its pre-peak which is of interest.

The preliminary SmartAcquisition experiments have proven the general applicability of this technique however it is very much still under development. There are several important problems which first must be addressed before this technique can be used routinely for the acquisition of data of sufficiently high quality for the analysis of ELNES. These problems are discussed below. The chemical shift in the Fe $L_{2\text{-}3}$ ELNES associated with the change in valence from Fe(II) to Fe(III) results in an absolute energy-loss shift of around +2eV. It is therefore necessary that spectra be energy calibrated with an accuracy better than this in order that correct fitting of the spectra may be performed. This, in the case of core-loss EELS, is usually done by including an edge of known, none variable, energy within the same spectrum. If an

energy resolution of say 0.3eV/channel were employed then the O *K* edge would be an ideal calibration candidate. Unfortunately, this is not possible since at such energy resolutions it is not possible to fully exploit the information present in the ELNES. Another possibility, which is currently under investigation, would be to superimpose a short exposure of the low-loss region over the core-loss acquisition thereby allowing the position of the ZLP, along with the drift-tube bias values, to be used for energy calibration. This method will require the development of a DMS routine for the control of the drift tube bias. Finally, another solution may be to include small amount of another metal (e.g. Ni or Co) on the TEM sample holder along with FHY so that its *L*-edge may be used as a calibration reference. This last point as yet has not been investigated and a search for an ideal candidate (i.e. one which does not exhibit a chemical shift in its *L*-edge) will need to be undertaken.

Sample drift can be a major problem in HRTEM and has been one of the biggest problems affecting the preliminary experiments outlined here. There is little that can be done to mitigate the effects of sample drift other than allowing the sample to 'sit' in the microscope for an extended period of time prior to analysis. As it stands the SmartAcquisition technique requires a time consuming pre-acquisition setup process during which time the sample is likely to have drifted. Work needs to be done to streamline the process, by tying together several currently separate routines, so that the time between the initial preliminary scan and acquisition may be minimised.

Finally, the recent introduction of electron microscopes with milli-electron Volt monochromated sources offer exciting opportunities for EEL spectroscopic analysis which would be worthwhile investigating.

Bibliography/References

Allen, L., Findlay, S., Lupini, a., Oxley, M., & Pennycook, S. (2003). Atomic-Resolution Electron Energy Loss Spectroscopy Imaging in Aberration Corrected Scanning Transmission Electron Microscopy. *Physical Review Letters*, *91*(10), 1–4. doi:10.1103/PhysRevLett.91.105503

Amelinckx, S., Dyck, D. V., Landuyt, J. V., & Tendeloo, G. V. (1997). *Electron Microscopy Principles and Fundamentals*. Wiley VCH.

Andrews, S. C., Robinson, A. K. & Rodriguez-Quinones, F. (2003). Bacterial iron homeostasis. *FEMS Microbiology Reviews*. 27(2) 215-237 doi: 10.1016/S0168-6445(03)00055-X

Antelo, J., Fiol, S., Pérez, C., Mariño, S., Arce, F., Gondar, D. & López, R. (2010). Analysis of phosphate adsorption onto ferrihydrite using the CD-MUSIC model. *Journal of Colloid and Interface Science*. 347(1) 112-119 doi:10.1016/j.jcis.2010.03.020

Arai, Y. & Sparks, D. L. (2001) ATR-FTIR Spectroscopic Investigation on Phosphate Adsorption Mechanisms at the Ferrihydrite-Water Interface. *Journal of Colloid and Interface Science.* 241(2) 317-326. doi:10.1006/jcis.2001.7773

Barbara, H. (2004). *Infrared spectroscopy: Fundamentals and applications*. *Analytical Techniques in the Science*. John Wiley & Sons, Ltd.

Barrón, V., Torrent, J., & Michel, F. (2012). Critical evaluation of the revised akdalaite model for ferrihydrite—Discussion. *American Mineralogist*, *97*(2010), 14071.

Beagley, B., Cruicksank, D. W. J., Pinder, P. H., Robiette, A. G. & Sheldrick, G. M. (1969). The molecular structure of $Fe(CO)_5$ in the gas phase. *Acta Crystallographica Section B*. B25 737-744 doi:10.1107/S0567740869002901

Billinge, S. J. L., & Kanatzidis, M. G. (2004). Beyond crystallography: the study of disorder, nanocrystallinity and crystallographically challenged materials with pair distribution functions. *Chemical communications (Cambridge, England)*, (7), 749–60. doi:10.1039/b309577k

Billinge, Simon J.L. (2008). Nanoscale structural order from the atomic pair distribution function (PDF): There's plenty of room in the middle. *Journal of Solid State Chemistry*, *181*(7), 1695–1700. doi:10.1016/j.jssc.2008.06.046

Bino, A., Ardon, M., Dongwann, L., Springler, B. & Lippard, S. J. (2002). Synthesis and structure of [Fe13O4F24(OMe)12]5-: The first Open-Shell Keggin ion. *Journal of the American Chemical Society: 124*(17). 4578-4579 doi:10.1021/ja025590a

Bou-Abdallah, F. (2010). The iron redox and hydrolysis chemistry of the ferritin. *Biochimica et Biophysica Acta*. 1800(8) 719-731 doi:10.1016/j.bbagen.2010.03.021

Bradley, S. M & Kydd, R. A. (1993). Comparison of the species formed upon base hydrolyses of gallium(III) and iron(III) aqueous solutions: the possibility of existence of an $[FeO_4Fe_{12}(OH)_{24}(H_2O)_{12}]^{7+}$ Polyoxocation. *Journal of the Chemical Society, Dalton Transactions*. 15 2407-2413 doi:10.1039/DT9930002407

Brown, M. E. (1988). *Introduction to Thermal Analysis. Techniques and applications*. Chapman and Hall. ISBN 978-0-306-4804-9

Brown, A., Moore, R. G. C., Evans, S. D., & Brydson, R. (2001). Characterisation of iron oxide nanoparticles using EELS. *Journal of Physics: Conference Series*, *126*(1).

Brydson, R. (2001). Electron Energy Loss Spectroscopy. *Taylor & Francis.* ISBN:1-859996-134-7

Carlson, L. & Schwertmann, U. (1981). Natural ferrihydrites in surface deposits from Finland and their association with silica. *Geochimica at Cosmochimica Acta.* 45 421-429

Carta, D., Casula, A., Corrias, A., Falqui, G., Navarra, G. & Pinna, G. (2009). Structural and magnetic characterisation of synthetic ferrihydrite nanoparticles. *Materials Chemistry and Physics*. 113(1) 349-355 doi:10.1016/j.matchemphys.2008.07.122

Casey, W. H. (2006). Large Aqueous Aluminum Hydroxide Molecules. *Chemical Reviews*. 106(1) 1-16 doi:10.1021/cr040095d

Chasteen, N. D., & Harrison, P. M. (1999). Mineralization in ferritin: an efficient means of iron storage. *Journal of structural biology*, *126*(3), 182–94. doi:10.1006/jsbi.1999.4118

Chupas, P. J., Qiu, X., Hanson, J. C., Lee, P. L., Grey, C. P., & Billinge, S. J. L. (2003) Rapid-acquisition pair distribution function (RA-PDF) analysis. *Journal of Applied Crystallography.* 36 1342-1347 doi:10.1007/S002218898030175964

Clegg, G. A, Fitton, J. E., Harrison, P. M., & Treffry, A. (1980). Ferritin: molecular structure and iron-storage mechanisms. *Progress in biophysics and molecular biology*, *36*(2-3), 56–86.

Cliff, G., & Lorimer, G. W. (1975). The quantitative analysis of thin specimens. *Journal of Microscopy*, 103(2), 203-207. doi:10.1111/j.1365-2818.1975.tb03895x

Colliex, C., Manoubi, T., & Ortiz, C. (1991). Electron-energy-loss-spectroscopy near-edge fine structures in the iron-oxygen system. *Physical Review B*, *44*(20), 402–411. doi:10.1103/PhysRevB.44.11402

Collman, J.P. (1975). Disodium tetracarbonylferrate, a transition metal analog of a Grignard reagent. *Accounts of Chemical Research*, *8*(10), 342-374 doi:10.1021/ar50094a004

Colquhoun, H.M., Holton, J., Thompson, D. J. & Twigg, M. V. (1984). New Pathways for Organic Synthesis - Practical Applications of Transition Metals. *Plenum Press, New York*, doi:10.1007/978-1-4613-2651-9

Combes J. M., Manceau A., Calas G. & Bottero J. Y. (1989) Formation of ferric oxides from aqueous solutions : a polyhedral approach by X-ray absorption spectroscopy. I. Hydrolysis and formation of ferric gels. *Geochimica et Cosmochimica Acta*, 53, 583-594

Cornell, R. M., & Schwertmann, U. (2003). *The Iron Oxides: Structure, Properties, Reactions, Occurrences and Uses* (Second., pp. 3–527). Darmstadt: WILEY-VCH.

Cullity, B. D. (1956). *Elements of X-ray Diffraction* (p. 531). Addison-Wesley, Inc.

Cullity, B. D., & Graham, C. D. (2011). Introduction to magnetic materials, Second Edi. John Wiley & Sons, Inc.

de Broglie, L. (1924) Recherches sur la théorie des quanta. *Ph.D Thesis.*

Davisson, C. J., & Germer, L. H. (1928). Reflection of Electrons by a Crystal of Nickle. *Proceedings of the National Academy of Sciences.* 14(4) 317-322

Descostes, M., Mercier, F., Thromat, N., Beaucaire, C. & Gautier-Soyer, M. (2000). Use of XPS in the determination of chemical environment and oxidation state of iron and sulfur samples: constitution of a data basis in binding energies for Fe and S reference compounds and applications to the evidence of surface species of an oxidized pyrite in a carbon medium. *Applied Surface Science*. 165, 288-302

Drits, V. A., Sakharov, B. A., Salyn, A. L., & Manceau, A. (1993). Structural model for ferrihydrite. *Clay Minerals*, 185–207.

Egami, T., & Billinge, S., J., L. (2003). *Underneath the bragg peaks: Structural analysis of complex materials*. (R. W. Cahn, Ed.). Pergamon Press.

Egerton, R. F. (2003). New techniques in electron energy-loss spectroscopy and energy-filtered imaging. *Micron*, *34*(3-5), 127–139. doi:10.1016/S0968-4328(03)00023-4

Egerton, R. F. (2005). *Physical Principles of Electron Microscopy*. Springer.

Egerton, R. F. (2007). Limits to the spatial, energy and momentum resolution of electron energy-loss spectroscopy. *Ultramicroscopy*, *107*(8), 575–86. doi:10.1016/j.ultramic.2006.11.005

Egerton, R. F. (2009). Electron energy-loss spectroscopy in the TEM. *Reports on Progress in Physics*, *72*(1), 016502. doi:10.1088/0034-4885/72/1/016502

Egerton, R. F. (2011). *Electron Energy-Loss Spectroscopy in the Electron Microscope* (Third Edit., p. 503). Boston, MA: Springer US. doi:10.1007/978-1-4419-9583-4

Egerton, R. F. (2012). TEM-EELS: a personal perspective. *Ultramicroscopy*, *119*, 24–32. doi:10.1016/j.ultramic.2011.11.008

Egerton, R. F. (2013). Control of radiation damage in the TEM. *Ultramicroscopy*, *127*, 100–8. doi:10.1016/j.ultramic.2012.07.006

Egerton, R. F., Li, P., & Malac, M. (2004). Radiation damage in the TEM and SEM. *Micron (Oxford, England : 1993)*, *35*(6), 399–409. doi:10.1016/j.micron.2004.02.003

Egerton, R. F., McLeod, R., Wang, F., & Malac, M. (2010). Basic questions related to electron-induced sputtering in the TEM. *Ultramicroscopy*, *110*(8), 991–997. doi:10.1016/j.ultramic.2009.11.003

Egerton, R. F., Qian, H., & Malac, M. (2006). Improving the energy resolution of X-ray and electron energy-loss spectra. *Micron (Oxford, England : 1993)*, *37*(4), 310–5. doi:10.1016/j.micron.2005.11.005

Eggleton, R. A., & Fitzpatrick, R. W. (1988). New Data and a Revised Structural Model for Ferrihydrite. *Clay and Clay Minerals*, *36*(2), 111–124.

Fairley, N. (2001). CASAXPS Software, version 2.0.17.

Faivre, D. (2016). Iron Oxides: From Nature to Applications. *Wiley-VCH Verlag.* doi:10.1002/9783527691395

Farrow, C. L., Juhás, P., Liu, J. W., Bryndin, D., Božin, E. S., Bloch, J., Proffen, T. & Billinge, S. J. L. (2007) PDFfit2 and PDFgui: computer programs for studying nanostructure in crystals. *Journal of Physics: Condensed Matter.* 19

Farrow, C L (2009). PDFgui user guide. www.diffpy.org/doc/pdfgui/pdfgui.pdf

Farrant, J. L. (1954). An electron microscopic study of ferritin. *Biochimica et biophysica acta*, *13*, 569–576. doi:10.1016/0006-3002(54)90376-5

Fischbach, F. A., Harrison, P. M., & Hoy, T. G. (1969). The structural relationship between ferritin protein and its mineral core. *Journal of molecular biology*, *39*(1), 235–238.

Flynn, C. M. (1984). Hydrolysis of inorganic iron(III) salts. *Chemical Reviews.* 84 31-41 doi:10.1021/cr00059a003

Foner, S. (1959). Versatile and Sensitive Vibrating-Sample Magnetometer. *The Review of Scientific Instruments*, *30*(7), 548–557. doi:10.1063/1.1716679

Foner, S. (1967). Vibrating Sample Magnetometer (VSM) Patent US3496459A.

Frau, D., Addari, D., Atzei, R., Biddau, R., Cidu, R., & Rossi, A. (2011) Influence of major anions on As(V) adsorption by synthetic 2-line ferrihydrite. Kinetic investigation and XPS study of the competitive effect of bicarbonate. *Water, Air and Soil Pollution*. 205(1) 25-41 doi:10.1007/s11270-009-0054-4

Frost, R. L., Martens, W., Williams, P. A., & Kloprogge, J. T. (2002). Raman and Infrared Spectroscopic Study of the Vivianite-Group Phosphates, Barcite and Bobierrite. *Mineralogical Magazine*, *66*(6), 1063–1073. doi:10.1080/0026461026660077

Fultz, B., & Howe, J. (2012). *Transmission Electron Microscopy and Diffractometry of Materials*. Springer.

Gálvez, N., Barrón, V., & Torrent, J. (1999). Effect of phosphate on the crystallisation of hematite, goethite, and lepidocrocite from ferrihydrite. *Clay and Clay Minerals*, *47*(3), 304–311.

Garratt-Reed, A. J., & Bell, D. C. (2003) Energy-Dispersive X-Ray Analysis in the Electron Microscope. *Bios Scientific.* ISBN: 1-85996-109-6

Garvie, L. A. J., & Buseck, P. R. (1998). Ratios of ferrous to ferric iron from nanometre-sized areas in minerals. *Nature*, *396*(December), 667–670. doi:10.1038/25334

Gebauer, D., Kellermeier, M., Gale, J. D., Bergström, L. & Cölfen, H. (2014). Pre-nucleation clusters as solute precursors in crystallisation. *Chemical Society Reviews*, 43, 2348-2371 doi:10.1039/C3CS60451A

Gilbert, B., Lu, G. & Kim, C. S. (2007). Stable cluster formation in aqueous suspensions of iron oxyhydroxide nanoparticles. *Journal of Colloid and Interface Science*, 313(1), 152-159 doi:10.1016/j.jcis.2007.04.038

Glasauer, S. M., Hug, P., Weidler, P. G, & Gehring, A. U. (2000). Inhibition of Sintering by Si During the Conversion of Si-Rich Ferrihydrite to Hematite. *Clays and Clay Minerals*, *48*(1), 51–56. doi:10.1346/CCMN.2000.0480106

Goodhew, P. J. (2008). *Electron Microscopy and Analysis*. Taylor & Francis.

Grady, J. K., Zang, J., Laue, T. M., Arosio, P., & Chasteen, N. D. (2002) Characterisation of the H- and L-subunit ratios of ferritins by sodium dodecyl sulfate-capillary gel electrophoresis. *Analytical biochemistry*, *302*(2), 263–8. doi:10.1006/abio.2001.5561

Griffith, W. P., Lewis, J. & Wilkinson, G. (1958). Some Nitric Oxide Complexes of Iron and Copper. *Journal of the Chemical Society.* 3993-3998 doi:10.1039/JR9580003993

Grunes, L., Leapman, R., Wilker, C., Hoffmann, R., & Kunz, A. (1982). Oxygen K near-edge fine structure: An electron-energy-loss investigation with comparisons to new theory for selected 3d Transition-metal oxides. *Physical Review B*, *25*(12), 7157–7173. doi:10.1103/PhysRevB.25.7157

Gubbens, A., Barfels, M., Trevor, C., Twesten, R., Mooney, P., Thomas, P., & Menon, N. (2010). The GIF Quantum, a next generation post-column imaging energy filter. *Ultramicroscopy*, *110*(8), 962–970. doi:10.1016/j.ultramic.2010.01.009

Hammersley, A. P. (1997) FIT2D: An Introduction and Overview. *ESRF Internal Report.* ESRF97HA02T

Hanesch, M. (2009). Raman spectroscopy of iron oxides and (oxy)hydroxides at low laser power and possible applications in environmental magnetic studies. *Geophysical Journal International*, *177*(3), 941–948. doi:10.1111/j.1365-246X.2009.04122.x

Harrison, P., & Arosio, P. (1996). The ferritins: molecular properties, iron storage function and cellular regulation. *Biochimica et Biophysica Acta (BBA) - Bioenergetics*, *1275*(3), 161–203. doi:10.1016/0005-2728(96)00022-9

Hawkes, P. W. (1990) Ernst Ryska. *Physics Today.* 43(7) 84-85

Haydon, G. (1969). Visualization of substructure in ferritin molecules: an artifact. *Journal of microscopy*, *89*(2), 251–261. doi:10.1111/j.1365-2818.1969.tb00672.x

Heqing, H., Watt, R. K., Frankel, R. B. & Watt, G. D. (1993) Role of phosphate in Fe^{2+} binding to horse spleen holoferritin. *Biochemistry*, 32(6) 1681–1687

House, J. E. (2008). Inorganic Chemistry. *Academic Press, Elsevier.* ISBN:978-0-12-356786-4

Humphreys, C. (1991). 100 keV electron beam damage of metals and oxides. *Micron and Microscopica Acta*, *22*(1/2), 147–148.

Hunt, J. A., Leapman, R & Williams, D. B. (1993). Low-dose EELS and Imaging Stratergies in the STEM. *Microbeam Analysis*

Isaacson, M., & Ohtsuki, M. (1980). Scanning transmission electron microscopy of small inhomogeneous particles, applications to Ferritin - part7. *Scanning electron microscopy*, *80*, 73–79.

Jambor, J. L., & Dutrizac, J. E. (1998). Occurrence and Constitution of Natural and Synthetic Ferrihydrite, a Widespread Iron Oxyhydroxide. *Chemical Reviews*, *98*(7), 2549–2585.

Janney, D. E., Cowley, J. M., & Buseck, P. R. (2000a). Transmission Electron Microscopy of Synthetic 2- and 6- Line Ferrihydrite. *Clay and Clay Minerals*, *48*(I), 111–119.

Janney, D. E., Cowley, J. M., & Buseck, P. R. (2000b). Structure of synthetic 2-line ferrihydrite by electron nanodiffraction. *American Mineralogist*, *85*(1967), 1180–1187.

Janney, D. E., Cowley, J. M., & Buseck, P. R. (2001). Structure of synthetic 6-line ferrihydrite by electron nanodiffraction. *American Mineralogist*, *86*(1967), 327–335.

Jansen, E., Kyek, A., Schäfer, W. & Schwertmann, U. (2002). The structure of six-line ferrihydrite. *Applied Physics A*, *74*(1), 1004–1006.

Jiang, N., & Spence, J. C. H. (2012). On the dose-rate threshold of beam damage in TEM. *Ultramicroscopy*, *113*, 77–82. doi:10.1016/j.ultramic.2011.11.016

Johnson, J. L., Cannon, M., Watt, R. K., Frankel, R. B. & Watt, G .D. (1999) Forming the phosphate layer in reconstituted horse spleen ferritin and the role of phosphate in promoting core surface redox reactions. *Biochemistry* 38(20) 6706–6713

Jolivet, J., Chanéac, C. & Tronc, E. (2004). Iron oxide chemistry. From molecular clusters to extended solid networks. *Chemical Communications.* 5 591-597 doi:10.1039/b304532n

Kaufmann, E. N. (2003). Characterisation of Materials. Vols 1 & 2. (E. Kaufmann, Ed.) (p. 1413). Wiley-Interscience.

Kinniburgh, D. G., Jackson, M. L. & Syers, J. K. (1976). Adsorption of alkaline earth, transition, and heavy metal cations by hydrous oxide gels of iron and aluminum. *Soil Science Society of America Journal.* doi:10.2136/sssaj1976.03615995004000050055x

Kirkland, E. J. (2009). Advanced Computing in Electron Microscopy, Second Edition. *Springer, New York.* ISBN: 978-1-4419-6532-5

Khare, N., Hesterburg, D., Beauchemin, S. & Wang, S. (2004). XANES Determination of Adsorbed phosphate Distribution between Ferrihydrite and Boehmite in Mixtures. *Soil Science Society of America, Journal*, 68(2), 460-469 doi:10.2136/sssaj2004.4600

Khare, N., Martin, J. D. & Hesterberg, D. (2007). Phosphate bonding configuration on ferrihydrite based on molecular orbital calculations and XANES fingerprinting. G*eochimica et Cosmochimica Acta*, 71(18), 4405-4415 doi:10.1016/j.gca.2007.07.008

Klie, R. F., & Zhu, Y. (2005). Atomic resolution STEM analysis of defects and interfaces in ceramic materials. *Micron (Oxford, England : 1993)*, *36*(3), 219–31. doi:10.1016/j.micron.2004.12.003

Knight, R. J. & Sylva, R. N. (1974). Precipitation in hydrolysed iron(III) solutions. *Journal of Inorganic and Nuclear Chemistry.* 36(3) 591-597 doi:10.1016/0022-1902(74)80119-3

Koch, C. (2002). Determination of Core Structure Periodicity and Point Defect Density Along Dislocations. *Unpublished Thesis*, Arizona State University

Krivanek, O. L. (1989). Improved parallel-detection Electron-Energy-Loss Spectrometer. *Ultramicroscopy*, *28*(1-4), 118–121. doi:10.1016/0304-3991(89)90282-9

Krivanek, O. L., Ahn, C. C., & Keeney, R. B. (1987). Parallel detection electron

spectrometer using quadrupole lenses. *Ultramicroscopy*, *22*(1-4), 103–115. doi:10.1016/0304-3991(87)90054-4

Krivanek, O. L., Corbin, G. J., Dellby, N., Elston, B. F., Keyse, R. J., Murfitt, M. F., Own, C. S. et al., (2008). An electron microscope for the aberration-corrected era. *Ultramicroscopy*, *108*(3), 179–95. doi:10.1016/j.ultramic.2007.07.010

Kujawa, S., Freitag, B., & Hubert, D. (2005). An Aberration Corrected (S)TEM Microscope for Nanoresearch. *Microscopy Today*.

Kwon, K. D. & Kubicki, J. D. (2004). Molecular Orbital Theory Study on Surface Complex Structures of Phosphates to Iron Hydroxides: Calculation of Vibrational Frequencies and Adsorption Energies. *Langmuir*, 20(21), 9249-9254 doi:10.21/la0487444

Lefmann, K, Bodker, F., Klausen, S. N., Hansen, M. F., Clausen, K. N., Lindgård, P. A., & Morup, S. (2001). A Neutron Scattering Study of Spin Precession in Ferrimagnetic Maghemite Nanoparticles. *EPL Europhysical Letters* , *54*(4), 526. doi:10.1209/epl/i2001-00279-7

Legg, B. A., Mengqiang, Z., Comolli, L. R., Gilbert, B. & Banfield, J. F. (2014A). Determination of the Three-Dimensional Structure of Ferrihydrite Nanoparticle Aggregates. *Langmuir.* 30(33) 9931-9940 doi:10.1021/la502128d

Legg, B. A., Mengqiang, Z., Comolli, L. R., Gilbert, B. & Banfield, J. F. (2014B). Impacts of Ionic Strength on Three-Dimensional Nanoparticle Aggregate Structure and Consequences for Environmental Transport and Deposition. *Environmental Science and Technology.* 48(23) 13703-13710 doi:10.1021/es502654q

Levi, S, Santambrogio, P., Cozzi, A., Rovida, E., Corsi, B., Tamborini, E. & Spada, S. (1994). The Role of the L-Chain in Ferritin Iron Incorporation: Studies of Homo and Heteropolymers. *Journal of Molecular Biology*, *238*(5), 649–654. doi:10.1006/jmbi.1994.1325

Lin, T.-C., Seshadri, G., & Kelber, J. A. (1997). A consistent method for quantitative XPS peak analysis of thin oxide films on clean polycrystalline iron surfaces. *Applied Surface Science*, *119*(1-2), 83–92. doi:10.1016/S0169-4332(97)00167-0

Lindegren, M. & Persson, P. (2010) Competitive adsorption involving phosphate and benzenecarboxylic acids on goethite-Effects of molecular structures. *Journal of Colloid and Interface Science,* 343(1), 263−270, doi:10.1016/j.jcis.2009.11.040

Loan, M., Parkinson, G., Newman, M. & Farrow, J. (2002). Iron oxy-hydroxide crystallisation in a hydrometallurgical residue. *Journal of Crystal Growth.* 432(1-4) 482-488 doi:10.1016/S0022-0248(01)01791-2

Lopes, L., de Laat, J. & Legube, B. (2002). Charge Transfer of Iron(III) Monomeric and Oligomeric Aqua Hydroxo Complexes: Semiempirical Investigation into Photoactivity. *Inorganic Chemistry.* 41(9) 2505-2517 doi:10.21/ic011029m

Lupini, A., & Pennycook, S. (2002). Initial Results from Aberration Correction in STEM. Microscopy and Microanalysis (Vol. 8, pp. 2–3).

Loretto, M. H. (1994). Electron Beam Analysis of Materials. (2002). Chapman & Hall.

Lorimer, G. W. (1987). Quantitative X-ray Microanalysis of Thin Specimens in the Transmission Electron Microscope; A Review. (1987) *Mineralogical Magazine.* 51(359) 49-60. doi:10.1180/minmag.1987.051.359.05

Lupini, A., & Pennycook, S. (2002). Initial Results from Aberration Correction in STEM. *Microscopy and Microanalysis* (Vol. 8, pp. 2–3).

Mallet, M., Barthélémy, K., Ruby, C., Renard, a, & Naille, S. (2013). Investigation of phosphate adsorption onto ferrihydrite by X-ray Photoelectron Spectroscopy. *Journal of colloid and interface science*, *407*, 95–101. doi:10.1016/j.jcis.2013.06.049

Manceau, A., Drits, V. A. (1993) Local structure of ferrihydrite and feroxyhite by EXAFS spectroscopy. *Clay Minerals*, 28, 165-184

Manceau, A., Gates, W. P. (2007). Surface structural model for ferrihydrite. *Clays and Clay Minerals*, *45*(3), 448–460.

Manceau, A (2009) Evaluation of the structural model for ferrihydrite derived from real-space modeling of high-energy X-ray diffraction data. *Clay Minerals.* 44, 19-34

Manceau, A. (2011). Critical evaluation of the revised akdalaite model for ferrihydrite. *American Mineralogist*, *96*(4), 521–533. doi:10.2138/am.2011.3583

Manceau, A. (2012). Critical evaluation of the revised akdalaite model for ferrihydrite -Reply. *American Mineralogist*, *97*(1), 255–256. doi:10.2138/am.2012.3954

Mann, S., Bannister, J. V., & Williams, R. J. (1986). Structure and composition of ferritin cores isolated from human spleen, limpet (Patella vulgata) hemolymph and bacterial (Pseudomonas aeruginosa) cells. *Journal of molecular biology*, *188*(2), 225–32.

Massover, W. H. (1993). Ultrastructure of ferritin and apoferritin: A review. *Micron*, *24*(4), 389–437. doi:10.1016/0968-4328(93)90005-L

May, M., & Fish, W. (1978). The UV and Visible Spectral Properties of Ferritin. *Archives of Biochemistry and Biophysics.* 190(2) 720-725

May, P., & Williams, D. (1980). *Inorganic Biochemistry of Iron Metabolism*. *Iron in biochemistry and medicine* (Vol. 1). John Wiley & Sons.

Mayo, D., Miller, F., & Hannah, R. (2004). *Course notes on the interpretation of infrared and Raman spectra*.

Mazzetti, L. & Thistlewaite, P. J. (2002). Raman spectra and thermal transformations of ferrihydrite and schwertmannite. *Journal of Raman Spectroscopy.* 33(2) 104-111. doi:10.1002/jrs.830

McIntyre, N. S. & Zetaruk, D. G. (1977). X-ray photoelectron spectroscopic studies of iron oxides. *Analytical Chemistry.* 49(11) 1521-1529. doi:10.1021/ac50019a016

Meldrum, F. C., Wade, V. J., Nimmo, D. L., Heywood, B. R. & Mann, S. (1991). Synthesis of Inorganic Nanophase Materials in Supramolecular Protein Cages. *Nature.* 349 684-687 doi:10.1038/349684a0

Melikhov, I. V., Kozlovskaya, E. D., Berliner, L. B & Prokofiev, M. A. (1987). Kinetics of hydroxide Fe(III) Solid Phase Formation. *Journal of Colloid and*

Interface Science. 117(1) 1-9 doi:10.21/0021-9797(87)90162-7

Michel, F M, Ehm, L., Antao, S. M., Lee, P. L., Chupas, P. J., Liu, G., Strongin, D. R., Schoonen, M. A. A., Phillips, B. L. & Parise, J. B. (2007). The structure of ferrihydrite, a nanocrystalline material. *Science*, *316*, 1726–9. doi:10.1126/science.1142525

Michel, F. M, Ehm, L., Liu, G., Han, W. Q., Antao, S. M., Chupas, P. J., Lee, P. L. et al., (2007). Similarities in 2- and 6-Line Ferrihydrite Based on Pair Distribution Function Analysis of X-ray Total Scattering. *Chemistry of Materials*, *35*(6), 1489–1496.

Michel, F. M., Barrón, V., Torrent, J., Morales, M. P., Serna, C. J., Boily, J. F., Liu, Q. (2010). Ordered ferrimagnetic form of ferrihydrite reveals links among structure, composition, and magnetism. *Proceedings of the National Academy of Sciences of the United States of America*, *107*(7), 2787–92. doi:10.1073/pnas.0910170107

Miller, F. A., & Wilkins, C. H. (1952). Infrared Spectra and Characteristic Frequencies of Inorganic Ions. *Analytical Chemistry*, *24*(8), 1253–1294. doi:10.1021/ac60068a007

Muller, D. A., & Silcox, J. (1995). Delocalization in inelastic scattering. *Ultramicroscopy*, *59*(1-4), 195–213. doi:10.1016/0304-3991(95)00029-Z

Nakamoto, K., & Brown, C. W. (2003). *Introductory Raman Spectroscopy* (pp. 406–421). Elsevier.

Nelson, P.G. (1991). Important elements. *Journal of Chemical Education*, *68*(9), 732-737 doi:10.1021/ed068p732

Pan, Y.-H. (2006). Electron Microscopy of Mineral Cores in Ferritin and Haemosiderin. *Thesis, University of Leeds*

Pan, Y., Brown, A., Brydson, R., Warley, A., Li, A., & Powell, J. (2006). Electron beam damage studies of synthetic 6-line ferrihydrite and ferritin molecule cores within a human liver biopsy. *Micron (Oxford, England : 1993)*, *37*(5), 403–11. doi:10.1016/j.micron.2005.12.009

Pan, Y.-H., Sader, K., Powell, J. J., Bleloch, A., Gass, M., Trinik, J., Warley, A., Li, A., Brydson, R. & Brown, A. (2009) 3D morphology of the human hepatic ferritin mineral core: New evidence for a subunit structure revealed by single particle analysis of HAAD-STEM images. *Journal of Structural Biology.* 166(1) 22-31 doi:10.1016/j.jsb.2008.12.001

Pan, Y.-H., Vaughan, G., Brydson, R., Bleloch, A., Gass, M., Sader, K., & Brown, A. (2010). Electron-beam-induced reduction of Fe^{3+} in iron phosphate dihydrate, ferrihydrite, haemosiderin and ferritin as revealed by electron energy-loss spectroscopy. *Ultramicroscopy*, *110*(8), 1020–1032. doi:10.1016/j.ultramic.2010.01.008

Pantelic, R. S., Meyer, J. C., Kaiser, U., Baumeister, W., & Plitzko, J. M. (2010). Graphene oxide: a substrate for optimizing preparations of frozen-hydrated samples. *Journal of structural biology*, *170*(1), 152–6. doi:10.1016/j.jsb.2009.12.020

Parfitt, R. L., Atkinson, R. J., & Smart, R. S. C. (1975). The Mechanism of Phosphate Fixation by Iron Oxides. *Soil Science Society of America Journal*,

39(5), 837. doi:10.2136/sssaj1975.03615995003900050017x

Pennycook, S J, & Varela, M. (2011). New views of materials through aberration-corrected scanning transmission electron microscopy. *Journal of electron microscopy*, *60 Suppl 1*(Supplement 1), S213–23. doi:10.1093/jmicro/dfr030

Pennycook, Stephen J, Varela, M., Lupini, A. R., Oxley, M. P., & Chisholm, M. F. (2009). Atomic-resolution spectroscopic imaging: past, present and future. *Journal of electron microscopy*, *58*(3), 87–97. doi:10.1093/jmicro/dfn030

Piao, X., Zeng, G. M., Huang, D. L., Feng, C. L., Shuang, H., Zhao, M. H., Lai, C. Wei, Z. Huang, C., Xie, G. X. & Liu, Z. F. (2012). Use of iron oxide nanomaterials in wastewater treatment: A review. *Science of The Total Environment.* 1-10 doi:10.1016/j.scitotenv.2012.02.023

Qiu, X., Thompson, J. W., & Billinge, S. J. L. (2004) PDFgetX2: A GUI driven program to obtain the pair distribution function from X-ray powder diffraction data. *Journal or Applied Crystallography.* 37 678-678

Quintana, C. & Gutierrez, L. (2010). Could a dysfunction of ferritin be a determinant factor in the aetiology of some neurodegenerative diseases?. *Biochimica et Biophysica Acta*, 1*800*(8), 770-782 doi:10.1016/j.bbagen.2010.04.012

Reyes-Gasga, R. (2002). Analysis of the electron-beam radiation damage of TEM samples in the acceleration energy range from 0.1 to 2MeV using the standard theory for fast electrons. *Radiation Physics and Chemistry*. 64(5-6), 359–367. doi:10.1016/S0969-806X(01)00578-3

Richter, G. W., & Walker, G. F. (1967). Reversible Association of Apoferritin Molecules. Comparison of Light Scattering and Other Data. *Biochemistry*. 6(9) 2871-2881 doi:10.1021/bi00861a031

Ristić, M., De Grave, E., Musić, S., Popović, S., & Orehovec, Z. (2007). Transformation of low crystalline ferrihydrite to α-Fe2O3 in the solid state. *Journal of Molecular Structure*. 834-836, 454–460. doi:10.1016/j.molstruc.2006.10.016

Rose, H. H. (2008). Optics of high-performance electron microscopes. *Science and Technology of Advanced Materials*, *9*(1), 014107. doi:10.1088/0031-8949/9/1/014107

Rose, A. L., Blight, M. W. Collins, R. N & Waite, D. T. (2014).Resolving Early Stages of Homogeneous Iron(III) Oxyhydroxide Formation from Iron(III) Nitrate Solutions at pH 3 Using Time-Resolved SAXS. *Langmuir*, 30(12), 3548-3556 doi:10.1021/la404712r

Rowland, R., & Lewis, D. (1951). Furnace atmosphere control in differential thermal analysis. *American Minerologist*, (10), 80–91.

Russell, J. D. (1979). Infrared Spectroscopy of Ferrihydrite: Evidence for the Presence of Structural Hydroxyl Groups. *Clay Minerals*, *14*(2), 109–114. doi:10.1180/claymin.1979.014.2.03

Sader, K., Schaffer, B., Vaughan, G., Brydson, R., Brown, A., & Bleloch, A. (2010). Smart acquisition EELS. *Ultramicroscopy*, *110*(8), 998–1003. doi:10.1016/j.ultramic.2010.01.012

Sadeghi, O., Zakharov, L. N. & Nymann, M. (2015). Aqueous formation and

manipulation of the iron-oxo Keggin ion. *Science.* 347(6228) 1359-1362. doi:10.1126/science.aaa4620

Schwertmann, U. (2004). Formation and properties of a continuous crystallinity series of synthetic ferrihydrites (2-to 6-line) and their relation to FeOOH forms. *Clays and clay …*, *52*(2), 221–226.

Schwertmann, U., & Cornell, R. M. (1993). Iron Oxides in Laboratory: Preparation and Charecterization. *Wiley-VCH* doi:10.1097/00010694-199311000-00012

Schwertmann, U., Friedl, J. & Stanjek, H. (1999). From Fe(III) ions to Ferrihydrite and then to Hematite. *Journal of Colloid and Interface Science.* 209(1) 215-223 doi:10.1002/jcis.1998.5899

Seerhra, M. S., Babu, V. S. Manivannan, A. & Lynn, J. W. (2000). Neutron scattering and magnetic studies of ferrihydrite nanoparticles. *Phys Rev B* 61(5). doi:10.1103/PhysRevB.61.3513

Silver, J. (1993) Chemistry of Iron. *Springer Science and Buisness Media, Dordrecht.* ISBN 978-94-010-4948-1

Shaik, S., Kumar, D., de Visser, S. P, Altun, A. & Theil, W. (2005). Theoretical perspective on the Structure and mechanism of cytochrome P450 enzymes. *Chemical Reviews.* 105(6) 2279-2328 doi:10.1021/cr030722j

Shmakov, A. N., Kryukova, G. N., Tsybulya, S. V., Chuvilin, A. L. & Solovyeva, L. P. (1995). Vacancy Ordering in γ-Fe_2O_3: Synchrotron X-ray Powder Diffraction and High-Resolution Electron Microscopy Studies. *Journal of Applied Crystallography.* 28, 141-145. doi:10.1107/S0021889894010113

Shmueli, U. (2007). Theories and techniques of crystal structure determination. *Oxford University Press.* ISBN: 978-0199213504

Shuman, H. (1981). Parallel recording of electron energy loss spectra. *Ultramicroscopy*, *6*(1), 163–167. doi:10.1016/S0304-3991(81)80194-5

Smith, E., & Dent, G. (2004). *Modern Raman Spectroscopy - A Practical Approach*. Chichester, UK: John Wiley & Sons, Ltd. doi:10.1002/0470011831

Spence, J. C. H. (2002). *High-resolution electron microscopy*. *Advances in Imaging and Electron Physics*. Oxford University Press.

Speyer, R. F. (1994). *Thermal Analysis of Material*. (R. F. Speyer, Ed.). New York: Marcel Dekker, Inc.

Spiro, T. G., Allerton, S., Renner, J., Terzis, A., Bils, R., & Saltman, P. (1966). The hydrolytic polymerization of iron (III). *Journal of the American Chemical Society.* 88(12) 2721-2726. doi:10.1021/ja00964a020

Spiro, T. G., Lehto, S., Valkiers, S., Bièvre, P., Selgrad, O., Flegel, U. & Kruk, T.(1998). Microscale Synthesis of $Fe(PF_3)_5$ for Gas Source Mass Spectrometry. *Analytical Chemistry.* 1033-1035 doi:10.1021/ac970523y

Stoch, A., & Stoch, J. (1989). XPS studies of chemical interaction between modified phosphate coatings and iron. *Solid State Ionics*, *34*, 17–20.

Tanaka, S. (1992). Theory of power-compensated DSC. *Thermochimica Acta*, *210*, 67–76. doi:10.1016/0040-6031(92)80277-4

Taylor, P. D. P., Lehto, S., Valkiers, S., Bièvre, P., Selgrad, O., Flegel, U. & Kruk, T. (1998). Microscale Synthesis of $Fe(PF_3)_5$ for Gas Source Mass Spectrometry.

Analytical Chemistry. 1033-1035 doi:10.1021/ac970523y

Tejedor-Tejedor, M. I. & Anderson, M. A. (1990). The protonation of phosphate on the surface of goethite as studied by CIR-FTIR and electrophoretic mobility. *Langmuir. 6(3)* 602-611 doi: 10.1021/la00093a015

Thibault, P.-J., Rancourt, D. G., Evans, R. J., & Dutrizac, J. E. (2009). Mineralogical confirmation of a near-P:Fe=1:2 limiting stoichiometric ratio in colloidal P-bearing ferrihydrite-like hydrous ferric oxide. *Geochimica et Cosmochimica Acta*, *73*(2), 364–376. doi:10.1016/j.gca.2008.10.031

Thomson, J. J. (1897) Cathode Rays. *Philosophical Magazine.* 44 293

Towe, K. M., & Bradley, W. F. (1967). Mineralogical constitution of colloidal "hydrous ferric oxides." *Journal of Colloid and Interface Science*, *24*(3), 384–392. doi:10.1016/0021-9797(67)90266-4

Towe, K. M. (1969). Substructure in the iron core of ferritin molecules. *Journal of Microscopy.* 90(3) 279-281. doi:10.1111/j.1365-2818.1969.tb00714.x

Treffry, A., Zhao, Z., Quail, M. A., Guest, J. R. & Harrison, P. M. (1998) How the presence of three iron binding sites affects the iron storage function of the ferritin (EcFtnA) of *Escherichia coli*. *FEBS Letters.* 432(3) 213-218 doi:10.1016/S0014-5793(98)00867-9

Trefry, A, & Harrison, P. M. (1978). Incorporation and release of inorganic phosphate in horse spleen ferritin. *The Biochemical journal*, *171*(2), 313–20.

van Aken, P., Liebscher, B., & Styrsa, V. (1997). Quantitative determination iron oxidation states in minerals using Fe L_{23}-edge electron energy-loss near-edge spectra. *Physics and Chemistry of Minerals.* 25 323-327 doi:10.1007/s002690050122

van Aken, P. & Liebscher, B. (2002). Quantification of ferrous/ferric ratios in minerals: new evaluation schemes of Fe L_{23} electron energy-loss near-edge spectra. *Physics and Chemistry of Minerals.* 29 188-200 doi:10.1007/s00269-001-0222-6

van der Heide, P (2011). X-Ray Photoelectron Spectroscopy. An Introduction to Principles and Practices. *John Wiley & Sons, Inc.* ISBN:978-1-118-06253-1

Vilgé-Ritter, A., Rose, J., Maison, A., Bottero, J. -Y. & Lainé, J. -M. (1999). Chemistry and Structure of Aggregates formed with Fe-salts and natural Organic Matter. *Colloids and Surfaces A.* 147(3) 5297-308 doi:10.1016/S0927-7757(98)00325-2

Violante, A., Ricciardella, M., del Gaudio, S. & Pigna, M. (2006). Coprecipitation of Arsenate with Metal Oxides: Nature, Mineralogy, and Reactivity of Aluminum Precipitates. *Environmental Science and Technology.* 4961-4967 doi:10.1021/es052321m

Wade, V. J., Levi, S., Arosio, P., Treffry, A., Harrison, P. M. & Mann, S. (1991) Influence of site-directed modifications on the formation of iron cores in ferritin. *Journal of Molecular Biology.* 221(4) 1443-1452 doi:10.1021/es401301z

Wagner, C. D., Riggs, W. M., Davis, L. E., Moulder, J. F., & Muilenberg, G. E. (1979). Handbook of X-ray Photoelectron Spectroscopy: A Reference Book of Standard Spectra for Identification and Interpretation of XPS Data. *Perkin-Elmer Corporation.*

Wang, X., Li, W., Harrington, R., Liu, F., Parise, J. B., Feng, X. & Sparks, D. L. (2013). Effect of Ferrihydrite Crystallite Size on Phosphate Adsorption Reactivity. *Environmental Science and Technology.* 47(18) 10322-10331 doi:10.1016/0022-2836(91)90944-2

Watt, R. K., Hilton, R. J. & Graff, D. M. (2010) Oxido-reduction is not the only mechanism allowing ions to traverse the ferritin protein shell. *Biochimica et Biophysica Acta.* 1800(8) 745–759 doi:10.1016/j.bbagen.2010.03.001

Watts, J., & Wolstenholme, J. (2003). *An introduction to surface analysis by XPS and AES*. John Wiley & Sons.

Wavemetrics. (2007). *Igor Pro 6 (Software)*. www.wavemetrics.com

Wenqian, X., Hausner, D. B., Harrington, R., Lee, P. L., Strongin, D. R., & Parise, J. B. (2011) Structural water in ferrihydrite and constraints this provides on possible structural models. *American Mineralogist.* 96(4) doi:10.2138/am.2011.3460

Williams, D B, & Carter, B. C. (1996). *Transmission Electron Microscopy - Spectrometry IV*. New York, NY: Plenum Press.

Williams, D. B., & Carter, C. B. (2009). *Transmission Electron Microscopy*. Boston, MA: Springer US. doi:10.1007/978-0-387-76501-3

Xu, P., Zeng, G. M., Huang, D. L., Feng, C. L., Hu, S., Zhao, M. H., Lai, C., Wei, Z., Huang, C., Xie G. X. & Liu, Z. F. (2012). Use of Iron Oxide Nanomaterials in Wastewater Treatment: a Review. *Science of the Total Environment.* 424 1-10 doi:10.1016/j.scitotenv.2012.02.023

Yuwono, V. M., Burrows, N. D. Soltis, J. A., Do, T. A., & Penn, R. L. (2012). Aggregation of Ferrihydrite Nanoparticles in Aqueous Systems. *Faraday Discussions.* 159, 235-245 doi:10.1039/C2FD20115A

Zhao, G., Bou-Abdallah, F., Arosio, P., Levi, S., Janus-Chandler, C. & Chasteen, N. D. (2003) Multiple pathways for mineral core formation in mammalian apoferritin. The role of hydrogen peroxide. *Biochemistry*. 42(10) 3142-3150 doi:10.1021/bi027357v

Zhou, W., Pennycook, S. J., & Idrobo, J.-C. (2012). Localization of inelastic electron scattering in the low-loss energy regime. *Ultramicroscopy*, *119*, 51–6. doi:10.1016/j.ultramic.2011.11.013

Zhu, M., Puls, B. W. Frandsen, C., Kubicki, J. D, Zhang, H. & Waychunas, G. A. (2013). In Situ Structural Characterisation of Ferric Iron Dimers in Aqueous Solution: Identification of μ-Oxo Species. *Inorganic Chemistry.* 52(12) 6788-6797 doi:10.1021/ic302053w

Appendix A Computer Code for Smart EELS-Acquisition

The Smart EELS-Acquisition routine requires an HAADF image with thresholding applied to create a binary mask-image defining the areas to be scanned during the EELS exposure. Some pre-processing of the image may be required to account for noise which typically involves smoothing. Both thresholding and smoothing may be performed within DigitalMicrograph™ using the appropriate built-in menu functions. The code section below may be used to convert a thresholded-image to a binary mask-image.

```
/*
**      Image should be smoothed and thresholded
**      prior to running this script
*/

// Smoothed and thresholded image
Image img_orig := GetFrontImage()
// The binary mask image
Image mask := RealImage("", 4, 1024, 1024)

try{
        // Check thresholding of image
        if(img_orig.ImageGetImageDisplay(0).RasterImageDisplayIsThresholdOn() != 1){
                OkDialog("Image is not thresholded!")
                exit(0)
                img_orig.ImageGetImageDisplay(0)
                        .RasterImageDisplayAddThresholdToMask(mask, 0, 0, 1024, 1024)
                mask.SetName(img_orig.GetName() + " (SAMASK)")
                mask.ShowImage()
}catch{
        OkDialog("Please have the thresholded image formost");
        exit(0)
}
```

The binary mask-image is then converted to a coordinates file (comma separated variable) ready to be used as input for the main EELS acquisition routine. This could be done using DM-scripting however since it is an interpreted script language this approach is prohibitively slow. To account for this limitation a custom DM-scripting plugin was developed which utilises the C++ DM-scripting software development kit (SDK) which is available from by request from Gatan Inc. The code below is written in C++ and provides the custom scripting functionality for saving a binary mask-image to a coordinate file.

```
/*
**    This code reads a thresholded image as a binary mask
**    image and outputs the masked pixel coordinates to a
**    comma separated variable UTF-8 file. This code
**    compiles against the Gatan DigitalMicrograph SDK-382
*/

#define _GATAN_USE_STL_STRING

#define _GATANPLUGIN_USES_LIBRARY_VERSION 2
#include "DMPlugInBasic.h"

#define _GATANPLUGIN_USE_CLASS_PLUGINMAIN
#include "DMPlugInMain.h"

using namespace Gatan;

#include <cassert>
#include <string>
#include <fstream.h>
#include <vector>

class CreateAndSaveCoordinatesPlugIn : public
Gatan::PlugIn::PlugInMain
{
      virtual void Start();
      virtual void Run();
      virtual void Cleanup();
      virtual void End();
};

/*
      This function is used to create an x-y text output given a
mask image
      (Ineger 4 Signed) and a threshold level.
      The function's operation is modified using the switch-flag.
      Parameters:
            return value - the number of x-y-pairs
                           (pixels fulfilling the threshold criteria)
            mask_image  - this is the original mask image.
                          This must be of
                          data type : "Integer 4 Signed"
            full_file_save_path - file location where the
                                  x-y data will be stored.
            Threshold           - the threshold pixel value.

            SwitchExactAboveBelow   - a switch flag which modifies
                                      the thresholding logic.
                                      Possible values are:
                        0 - the x-y coordinate will be output if
                           ( pix_val == Threshold )

                        1 - the x-y coordinate will be out put if
                           ( pix_val <= Threshold )
                        2 - the x-y coordinate will be out put if
                           ( pix_val < Threshold )
                        3 - the x-y coordinate will be out put if
                           ( pix_val >= Threshold )
                        4 - the x-y coordinate will be out put if
                           ( pix_val > Threshold )
```

```
                        neither of the above values then default
                        logic
                        ( pix_val == Threshold )
*/
float CreateAndSaveCoordinates(
            const DM::Image &mask_image,
            DM_StringToken full_file_save_path,
            float Threshold,
            float SwitchExactAboveBelow ){

      // Return value
      float retVal = 0;

      PLUG_IN_ENTRY

      std::string str
            = DM::String(full_file_save_path).get_string();

      //
      PlugIn::gResultOut << std::endl;
      PlugIn::gResultOut      << "Creating coordinate image...";
      PlugIn::gResultOut << std::endl;
      PlugIn::gResultOut << str << std::endl;

      // START:
      DM::Image src_img;
      if ( mask_image.GetDataType() != ImageData::REAL4_DATA )
      {
            src_img = mask_image.Clone();
            src_img.ChangeDataType( ImageData::REAL4_DATA );

      }

      ulong xsize = src_img.GetDimensionSize( 0 );
      ulong ysize = src_img.GetDimensionSize( 1 );

      PlugIn::ImageDataLocker src_img_l( src_img,
      PlugIn::ImageDataLocker::lock_data_CONTIGUOUS );

      ulong x_src_img_len
            = src_img_l.get_image_data().get_dim_length(0);
      ulong y_src_img_len
            = src_img_l.get_image_data().get_dim_length(1);

      float32 *src_img_data = reinterpret_cast<float32 *>(
            src_img_l.get_image_data().get_data() );

      ofstream out(str.c_str());

      sint16 pix_val;

      for( ulong y_idx = 0; y_idx < y_src_img_len; ++y_idx ){

            // The end points are special cases
            for( ulong x_idx = 0; x_idx < x_src_img_len ; ++x_idx ){
                  pix_val = (sint16) ( src_img_data[x_idx]);
                  switch ( (int)SwitchExactAboveBelow ){
                        case 0:
                              if(pix_val == Threshold){
                                    out <<x_idx<<","<<y_idx<<"\n";
                                    retVal++;
                              }
```

```
                              break;
                        case 1:
                              if(pix_val <= Threshold){
                                    out <<x_idx<<","<<y_idx<<"\n";
                                    retVal++;
                              }
                              break;
                        case 2:
                              if(pix_val < Threshold){
                                    out <<x_idx<<","<<y_idx<<"\n";
                                    retVal++;
                              }
                              break;
                        case 3:
                              if(pix_val >= Threshold){
                                    out <<x_idx<<","<<y_idx<<"\n";
                                    retVal++;
                              }
                              break;
                        case 4:
                              if(pix_val > Threshold){
                                    out <<x_idx<<","<<y_idx<<"\n";
                                    retVal++;
                              }
                              break;
                        default:
                              if(pix_val == Threshold){
                                    out <<x_idx<<","<<y_idx<<"\n";
                                    retVal++;
                              }
                  }
            }
            src_img_data += x_src_img_len;
      }
      out.close();

      PlugIn::gResultOut << ".......image created and saved.";
      PlugIn::gResultOut << std::endl;
      // End

      PLUG_IN_EXIT

      return retVal;
}
*/

/*
**    Make an alias function
*/
float A_CreateAndSaveCoordinates(
      DM_ImageToken src_img,
      DM_StringToken str_in,
      float aThreshold,
      float aSwitchExactAboveBelow ){
      return CreateAndSaveCoordinates(
            src_img,
            str_in,
            aThreshold,
            aSwitchExactAboveBelow );
}
/*
**    Define the PlugIn's Run method
```

```
*/
void CreateAndSaveCoordinatesPlugIn::Start()
{
	AddFunction(
		"float SA_CreateAndSaveCoordinates( BasicImage
mask_image, dm_string  full_file_save_path, float Threshold, float
SwitchExactAboveBelow)", &A_CreateAndSaveCoordinates );
}

CreateAndSaveCoordinatesPlugIn gCreateAndSaveCoordinatesPlugIn;
```

Once the coordinate file has been created the main Smart-EELS acquisition may be performed using the following DM-script.

```
// $BACKGROUND$

/*
**	This script requires a x-y coordinate csv ascii file as input
*/
// Images
image		img, coord_image, imageofspectrum, spectra
// Image-Display
imagedisplay imgDisp
// Regions-of-Interest
roi		 SmartROI
roi		tempROI
roi		beamROI,tracerROI
// ROI identifiers
number		numROI,id_beamROI
// Beam positions
number		x_Beam,y_Beam
// Temp numeric variables
number		i,x,y,j,k,r,g,sx,sy,ex,eyn,px,py,val,ySize, xSize, ii, jj,tsleep

/*
** Get user inputs
*/
void GetUserInputs(){
	// Get the coordinate image
	string img_name
	getstring("Enter the coordinate image","", img_name)
	getnamedimage(coord_image, img_name)
	// Get the dwell time
	getnumber("Enter dwell time (s) of the beam",0,tsleep)
	// Get time per spectrum
	getnumber("Enter the time per spectrum",0,t_per_spec)

}

/*
**	Get control of beam
*/
void GetControlOfBeam(){
	getfrontimage(img)
	imgDISP = img.ImageGetImageDisplay(0)
	numROI=imgDisp.ImageDisplayCountROIs()
	result("\n Image		: '"+img.getname()+"'")
	result("\n Number of ROIS : "+numROI)

	for (i=0;i<numROI;i++){
	tempROI=imgDisp.ImageDisplayGetROI(i);
	if (tempRoi.ROIIsPoint()){
			result("\n Beam is")
			beamROI=imgDisp.ImageDisplayGetROI(i);
```

```
                beamROI.ROIGetPoint(x_Beam,y_Beam)
                id_beamROI = beamROI.ROIGetID()
                        result("\t\t ("+id_beamROI+")")
                        result("\t\t@ ("+x_Beam+","+y_Beam+")")
                }
        }
}

/*
**      Update beam position on image
*/
void WriteCurrentPosition(number x, number y){
                        tracerROI= NewROI()
                ROISetRange(tracerROI, x, y)

                        tracerROI.ROIaddVertex(x, y-1)
                tracerROI.ROIaddVertex(x-1, y)
                        imgDisp.ImageDisplayAddROI(tracerROI)
                        updateimage(img)
}

/*
**      Move beam
*/
void MoveBeamToNextPixel(number index){
                number x_pos, y_pos
                x_pos=GetPixel(coord_image,0,index);
                y_pos=GetPixel(coord_image,1,index);
                DSPositionBeam( img, x_pos,y_pos) //Uses direct digiscan positioning
}

/*
**      Acquire EELS
*/
void GetEELS(Number t_exp, String aTitle){
        image img
        img := sscgainnormalizedbinnedacquire(t_exp, 1, 479, 0, 479 + 48, 1024 )
        realimage out := Realimage(aTitle, 4, 1024, 1)
        out[icol, 0] += img

        // Calibrate spectrum
        Number drift = IFCGetDriftTubeVoltage()
        NUmber dispersionno = IFCGetActiveDispersion()
        Number dispersion
        if(dispersionno==1) dispersion=1
        if(dispersionno==2) dispersion=0.5
        if(dispersionno==3) dispersion=0.3
        if(dispersionno==4) dispersion=0.2
        if(dispersionno==5) dispersion=0.1
        if(dispersionno==6) dispersion=0.05
        out.ImageSetDimensionOrigin( 0, drift - 15.0 )
        out.ImageSetDimensionScale( 0, dispersion )
        out.ImageSetDimensionUnitString(0, "eV")

        return img
}

void MainScript(){
        // Get user inputs for coordinate image
        GetUserInputs()
        number N = coord_image.ImageGetDimensionSize(1)

        // Establish beam control
        GetControlOfBeam()
        // Start acquisition
        Image eels = GetEELS( 20, "")
        sleep(0.5)
        // Iterate beam positions
        for(number loop = 1; loop < N; loop++){
                MoveBeamToNextPixel( loop )
        }
        eels.ShowImage()
}
// Main script start
MainScript()
```

Appendix B Energy Shifts in Scanned EELS Spectra: Implications for Averaging EELS Signals from Spatially Extended Areas

In what follows consideration is only given to EELS acquisition in the STEM. The following experiment was performed on the UltraSTEM (SuperSTEM2) microscope.

When the STEM-probe is scanned over a sample in the x-y plane the beam-optical-axis necessarily subtends an angle with respect to the microscope's true optical-axis. The magnitude of this angle will depend on a combination of the probe position in the x-y plane and the operating magnification of the microscope. When projected through the microscopes optical system (if pre-spectrometer coupling lenses are indeed present) this offset will result the EEL signal entering the EEL spectrometer at varying angles. This will ultimately manifest itself as a shift along the energy-axis of the EEL spectrum as the probe is scanned across the sample. This effect has been previously noted in the STEM-EELS community as being an issue which must be dealt with especially when integrating EEL signals from extended areas of a sample (Hunt 1993).

To investigate this effect and its dependence on the operating magnification of the microscope a series of EEL spectrum-images were acquired, in the absence of a specimen. Since no specimen was present only the intense zero-loss peak was collected, the position of which on the CCD was used to monitor the spectrum energy-shift and a function of beam position. Four EEL-spectrum images (50x50 pixels) were acquired at four different operating magnifications covering fields-of-views of 250, 200, 100 and 50nm. The spectrometer dispersion was set to 0.05 eV per channel and the energy-axis was arbitrarily calibrated by setting the starting ZLP position close to the centre of the CCD array. Exposure times of 0.05 seconds were used so as not to saturate the CCD. The energy-spread of the system (source-limited), as estimated from the width of the ZLP taken from a signal pixel location in a spectrum-images, was determined to be 0.6 eV.

Post acquisition a DigitalMicrograph script was used to reduce the 3D spectrum images into 2D maps displaying the ZLP energy-shift in units of eV (see Figure A.1). The first pixel (x, y = 0, 0) of each spectrum-image was chosen as a reference against which the relative energy-shift of the ZLPs in the remaining pixels of the

spectrum-image were defined. This choice of reference is arbitrary however, the consistency of its use allows comparison to be made between the four datasets.

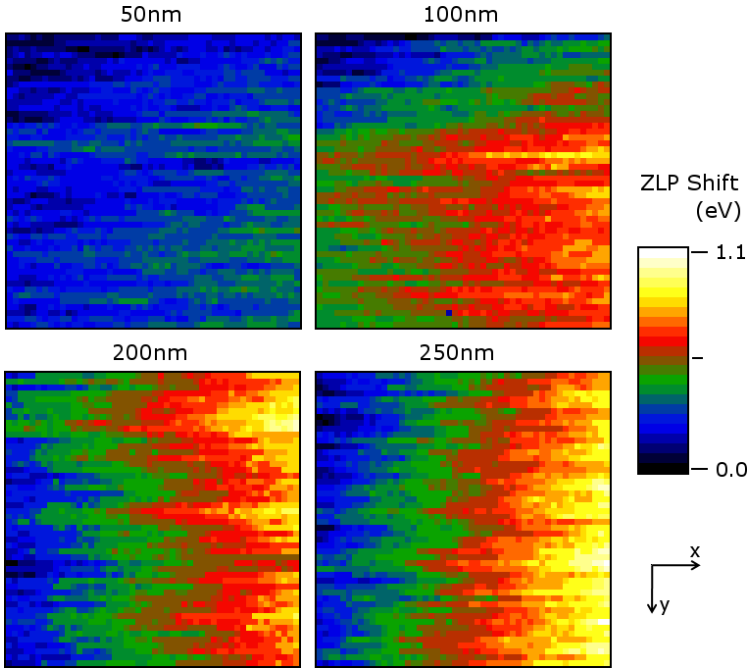

Figure A.1 Maps of energy-shift (eV) relative to the first-pixel (0,0) of the EELS spectrum-image. Field-of-view dimensions of the scan region are given in nm above the respective maps and energy-shift in eV is shown on the temperature scale

It can be seen from Figure A.1 that as the field-of-view range is increased (magnification lowered) the magnitude of the maximum energy-loss shift is increase. The second thing to note is that in the case of the 200 and 250 nm FOV scans windows, for a given x- position the magnitude of the energy-shift is approximately constant (i.e. y- invariant). If, as would be expected, the energy-shift depended purely on the absolute relative-offset of the beam from the reference pixel in the x-y plane (i.e. $\propto \sqrt{[x^2 + y^2]}$) then the energy-shift map would be expected to resemble the 100 nm FOV in which the energy-shift is observed to increase from the top-left to the bottom-right of the map. This result is due to the complicated, and somewhat none intuitive, manner in which the EEL signal is dispersed by the spectrometer optics and projected upon the CCD array.

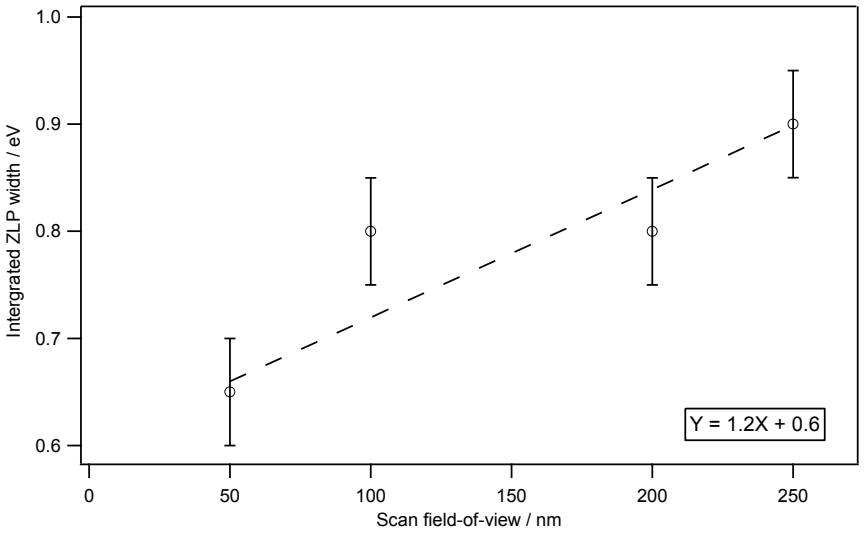

Figure A.2 Width of the ZLP integrated from the 50x50 spectrum-image as a function of scan-window field-of-view. Dashed-line represents linear fit to data where y-intercept has fixed at 0.6eV in accordance with the source-limited ZLP energy-width. Error-bars represent 0.05eV corresponding to the spectral energy dispersion.

In order to further assess the degradation of the energy-resolution as a function of microscope magnification the spectral-signal was integrated from each of the spectrum-images and the resulting integrated zero-loss peak energy-widths were determined. It can be seen from inspection of Figure A.2that there exists an approximate linear proportionality between the integrated ZLP width and the scan-FOV.

It should now be clear that if a single STEM-EEL spectrum acquisition is made whilst the probe is being scanned over an extended area of sample that the energy-resolution of the resulting spectrum will be degraded from that of a source-limited point-analysis spectral acquisition. It is clear from Figure A.2 that the magnitude of this degradation will depend on the operating magnification as well as the extent of the current field-of-view being averaged over. In the case of an online-area-averaging STEM-EELS acquisition method such as smart-acquisition EELS as described in this work the only solution would be to use the drift-tube to add a compensating de-scan bias on a pixel-by-pixel basis. Knowing the appropriate compensating voltage would require the proper characterisation of the relationship between the energy-shift, magnification and probe position of a given system. In addition to this some form of beam- of spectrometer-blanking would need to be employed whilst the drift-tube voltage is being adjusted as suggested by Hunt *et al.,* 1993.

Appendix C DigitalMicrograph Script for Calculating Fe-*L* White-Line Ratios as per van Aken et al., 1998

The script below allows the user to calculate Fe-L edge white line ratios as per the method of Van Aken *et al.,* 1998. The script requires an EELS spectrum containing a energy calibrated, background extracted, deconvoluted Fe-*L* edge.

After the script has been executed for the first time settings are saved as persistent tags in DigitalMicrograph's which can be viewed and edited via the persistent notes dialog. In principle the user can change these setting to adapt the script to work with *L-edge* white line features of other elements.

```
// $BACKGROUND$
/*
**      This assumes that the spectra have been energy calibrated,
**      deconvoluted extracted from the power-law like background.
**      Calculate the first derivate, find the first inflection points
**      after the peak positions the finally find the averaged height
**      (signal) in an window of width a1 (a2) centred about this position
*/

number PI = 3.14159265

/*
**      Find the interpeak inflection
*/
void FindHeightBehindPeaks(Image spec, number &h1, number &h2, number a1, number
a2, number &e1, number &e2, number &i1, number &i2, number fixed){
        image spec_deriv
        number origin, scale
        string units
        spec.ImageGetDimensionCalibration(0, origin, scale, units, 0)
        number e1_uc = (e1 - origin)/scale  // Uncalibrated x-axis
        number e2_uc = (e2 - origin)/scale  // Uncalibrated x-axis

        spec.SelectImage()
        //
        ChooseMenuItem(
                "Spectrum", "Numerical Filters", "First derivative")
        spec_deriv := GetFrontImage()
        //
        if(fixed != 1){
                //      Search for the first inflextion point
                for(number loop = e1_uc; loop < e1_uc + 100; loop++){
                        if((spec_deriv.GetPixel(loop, 0) > 0) &&
                        (spec_deriv.GetPixel(loop - 1, 0) < 0)){
                                i1 = loop - 1
                                break
                        }
                }
                //      Search for the second inflextion point
                for(number loop = e2_uc + 10; loop < e2_uc + 100; loop++){
                        if((spec_deriv.GetPixel(loop, 0) > 0) &&
                                (spec_deriv.GetPixel(loop - 1, 0) < 0)){
                                i2 = loop - 1
                                break
                        }
                }
        }else{
                i1 = (i1 - origin)/scale
                i2 = (i2 - origin)/scale
        }

        ROI roi1 = NEWROI()
        roi1.ROISetRange(i1, i1)
        spec.ImageGetImageDisplay(0).ImageDisplayAddROI(roi1)
        roi1.ROISetLabel("Min 1")
```

```
        ROI roi2 = NEWROI()
        roi2.ROISetRange(i2, i2)
        spec.ImageGetImageDisplay(0).ImageDisplayAddROI(roi2)
        roi2.ROISetLabel("Min 2")

        h1 = 0
        number n = 0
        for(number loop = i1 - (a1/2); loop < i1 + (a1/2); loop++){
                h1 += spec.GetPixel(loop, 0)
                n++
        }
        h1 /= a1
        h2 = 0
        for(number loop = i2 - (a2/2); loop < i2 + (a2/2); loop++){
                h2 += spec.GetPixel(loop, 0)
        }
        h2 /= (a2 + 0)
        e1 = e1_uc
        e2 = e2_uc
        spec_deriv.CleanImage()
        spec_deriv.DeleteImage()
        //result("\ni1, i2 = " + i1 + ", " + i2)
        i1 = (i1*scale) + origin
        i2 = (i2*scale) + origin

}

/*
**      Calculate the double arctan background
*/
number dbl_atan(number h1, number h2, number e1, number e2, number w1, number w2,
number E){
        number retVal = 0;
        retVal += ((h1/PI)*(atan((PI/w1)*(E - e1)) + (PI/2)))
        //retVal += (h1/PI)
        retVal += ((h2/PI)*(atan((PI/w2)*(E - e2)) + (PI/2)))
        //retVal += (h2/PI)
        return retVal
}

/*
** Calculate the extracted white-line signal
*/
Image WhiteLines(Image sub, number w1, number w2){
        Image ret := sub.ImageClone()
        number width, height, origin, scale
        string units
        sub.ImageGetDimensionCalibration(0, origin, scale, units, 0)

        number w1_uc = (w1 - origin)/scale
        number w2_uc = (w2 - origin)/scale

        ret.GetSize(width, height)
        for(number loop = 0; loop < width; loop++){
                if((loop >= w1_uc) && (loop <= (w2_uc))){
                        ret.SetPixel(loop, 0, sub.GetPixel(loop, 0))
                }else{
                        ret.SetPixel(loop, 0, 0)
                }
        }
        return ret
}

/*
**      Get & Set persistent notes
*/
void GetSetPersistentNotesVanAken1998(number &e1, number &e2, number &a1,
         number &a2, number &w1_start, number &w1_end, number &w2_start,
         number &w2_end, number &i1, number &i2, number &fixed){
        if(!GetPersistentNumberNote(
                "CustomEELS:FeLRatios:VanAken1998:Inflex1",e1)){
                e1 = 708.95
                SetPersistentNumberNote(
                        "CustomEELS:FeLRatios:VanAken1998:Inflex1",e1)
```

```
	}
	if(!GetPersistentNumberNote(
		"CustomEELS:FeLRatios:VanAken1998:Inflex2",e2)){
		e2 = 721.65
		SetPersistentNumberNote(
			"CustomEELS:FeLRatios:VanAken1998:Inflex2",e2)
	}
	if(!GetPersistentNumberNote(
		"CustomEELS:FeLRatios:VanAken1998:HeightWidth1",a1)){
		a1 = 3
		SetPersistentNumberNote(
		"CustomEELS:FeLRatios:VanAken1998:HeightWidth1",a1)
	}
	if(!GetPersistentNumberNote(
	"CustomEELS:FeLRatios:VanAken1998:HeightWidth2",a2)){
		a2 = 3
		SetPersistentNumberNote(
		"CustomEELS:FeLRatios:VanAken1998:HeightWidth2",a2)
	}
	if(!GetPersistentNumberNote(
	"CustomEELS:FeLRatios:VanAken1998:PeakStart1",w1_start)){
		w1_start = 708.5
		SetPersistentNumberNote(
		"CustomEELS:FeLRatios:VanAken1998:PeakStart1",w1_start)
	}
	if(!GetPersistentNumberNote(
	"CustomEELS:FeLRatios:VanAken1998:PeakEnd1",w1_end)){
		w1_end = 710.5
		SetPersistentNumberNote(
		"CustomEELS:FeLRatios:VanAken1998:PeakEnd1",w1_end)
	}
	if(!GetPersistentNumberNote(
		"CustomEELS:FeLRatios:VanAken1998:PeakStart2",w2_start)){
		w2_start = 719.7
		SetPersistentNumberNote(
		"CustomEELS:FeLRatios:VanAken1998:PeakStart2",w2_start)
	}
	if(!GetPersistentNumberNote(
		"CustomEELS:FeLRatios:VanAken1998:PeakEnd2",w2_end)){
		w2_end = 721.7
		SetPersistentNumberNote(
		"CustomEELS:FeLRatios:VanAken1998:PeakEnd2",w2_end)
	}
	if(!GetPersistentNumberNote(
		"CustomEELS:FeLRatios:VanAken1998:MinPos1",i1)){
		i1 = 718.0
		SetPersistentNumberNote(
		"CustomEELS:FeLRatios:VanAken1998:MinPos1",i1)
	}
	if(!GetPersistentNumberNote(
		"CustomEELS:FeLRatios:VanAken1998:MinPos2",i2)){
		i2 = 727.0
		SetPersistentNumberNote(
		"CustomEELS:FeLRatios:VanAken1998:MinPos2",i2)
	}
	if(!GetPersistentNumberNote(
		"CustomEELS:FeLRatios:VanAken1998:FixedYesNo",fixed)){
		fixed = 0
		SetPersistentNumberNote(
		"CustomEELS:FeLRatios:VanAken1998:FixedYesNo",fixed)
	}
}

/*
**	Main routine
*/
void CalcVanAken1998(){
	Image spec, atan_bkg, sub, WL1, WL2

	number h1, h2				// the step height of the bkg
	number a1 = 10				// the window overwhich to average
	number a2 = 10
	number e1 = 708.65			// fixed inflection points
```

```
	number e2 = 721.65			//
	number w1_start = 708.5			//	White Line Integration Windows
	number w1_end  = 710.5			//
	number w2_start = 719.7			//
	number w2_end  = 721.7			//
	number w1 = 1
	number w2 = 1
	number width, height
	number fixed = 0
	number i1, i2

	GetSetPersistentNotesVanAken1998(e1, e2, a1, a2, w1_start, w1_end,
		w2_start, w2_end, i1, i2, fixed)

	spec := GetFrontImage().ImageClone() // work on a copy of the original
	spec.GetSize(width, height)
	spec.ShowImage()

	// find the parameters for the background
	FindHeightBehindPeaks(spec, h1, h2, a1, a2, e1, e2, i1, i2, fixed)

	atan_bkg := RealImage("", 4, width, 1)

	for(number loop = 0; loop < width; loop++){
		atan_bkg.SetPixel(loop, 0, dbl_atan(h1, h2 - h1, e1, e2, w1, w2,
			loop))
	}

	sub := spec.ImageClone()
	spec.SetName(spec.GetName() + " (WL)")
	sub = spec - atan_bkg

	spec.ImageGetImageDisplay(0).ImageDisplayAddImage(atan_bkg, "atanbkg")
	spec.ImageGetImageDisplay(0).ImageDisplayAddImage(sub, "sub")
	WL1 := sub.ImageClone()
	WL1 = WhiteLines(sub, w1_start, w1_end)

	WL2 := sub.ImageClone()
	WL2 = WhiteLines(sub, w2_start, w2_end)

	spec.ImageGetImageDisplay(0).ImageDisplayAddImage(WL1, "FeL3")
	spec.ImageGetImageDisplay(0).ImageDisplayAddImage(WL2, "FeL2")

	string msg = ""
	msg += "\n\nWhite Line Ratios\n\t" + spec.GetName()
	result("\nw1_start, w1_end = " + w1_start + ", " + w1_end)
	result("\nw2_start, w2_end = " + w2_start + ", " + w2_end)
	if(fixed == 1){
		msg += "\nfixed inflex = yes"
	}else{
		msg += "\nfixed inflex = no"
	}
	msg += "\n\tinflex1 = " + i1
	msg += "\n\tinflex2 = " + i2
	msg += "\n\th1, h2 = " + h1 + ", " + h2
	msg += "\t\nL3/L2  = "
	msg    += "" + (WL1.Sum()/WL2.Sum())
	result(msg)
}
// Start main routine

CalcVanAken1998()
```